

**THEORETICAL STUDIES ON PHASE
TRANSFORMATIONS AND RELEVANT
THERMAL PROPERTIES OF Zr- AND
ThO₂-BASED NUCLEAR MATERIALS**

By

Partha Sarathi Ghosh

Enrollment No.: PHYS01201104018

Bhabha Atomic Research Centre, Trombay, Mumbai, INDIA

*A thesis submitted to the
Board of Studies in Physical Sciences
In partial fulfillment of requirements
for the Degree of*

DOCTOR OF PHILOSOPHY

of

HOMI BHABHA NATIONAL INSTITUTE



December 2017

Homi Bhabha National Institute

Recommendations of the Viva Voce Board

As members of Viva Voce Board, we certify that we have read the dissertation prepared by “**Partha Sarathi Ghosh**” entitled “**Theoretical Studies on Phase Transformations and Relevant Thermal Properties in Zr- and ThO₂-based Nuclear Materials**” and recommend that it may be accepted as fulfilling the dissertation requirement for the award of Degree of Doctor of Philosophy.

Chairman- Dr. G. K. Dey
Bhabha Atomic Research Centre
Trombay, Mumbai, Maharashtra 400085, India

_____ **Date:**

Guide/Convener- Dr. A. K. Arya
Bhabha Atomic Research Centre
Trombay, Mumbai, Maharashtra 400085, India

_____ **Date:**

Examiner- Dr. U. V. Waghmare
Theoretical Sciences Unit, Jawaharlal Nehru Centre for Advanced Scientific Research, Jakkur, Bangalore, Karnataka 560064, India

_____ **Date:**

Member- Dr. S. C. Gupta
Bhabha Atomic Research Centre
Trombay, Mumbai, Maharashtra 400085, India

_____ **Date:**

Member- Dr. I. Samajdar
Department of Metallurgical Engineering and Materials Science
Indian Institute of Technology Bombay, Powai, Mumbai, Maharashtra 400076, India

_____ **Date:**

Final approval and acceptance of this dissertation is contingent upon the candidate's submission of the final copies of the dissertation to HBNI.

I hereby certify that I have read this dissertation prepared under my direction and recommend that it may be accepted as fulfilling the dissertation requirement.

Date:

Dr. A. K. Arya

Place: Mumbai

Guide

STATEMENT BY AUTHOR

This dissertation has been submitted in partial fulfillment of requirements for an advanced degree at Homi Bhabha National Institute (HBNI) and is deposited in the Library to be made available to borrowers under rules of the HBNI.

Brief quotations from this dissertation are allowable without special permission, provided that accurate acknowledgment of source is made. Requests for permission for extended quotation from or reproduction of this manuscript in whole or in part may be granted by the Competent Authority of HBNI when in his or her judgment the proposed use of the material is in the interests of scholarship. In all other instances, however, permission must be obtained from the author.

Partha Sarathi Ghosh

DECLARATION

I, *Partha Sarathi Ghosh*, hereby declare that the investigation presented in the thesis has been carried out by me. The work is original and has not been submitted earlier as a whole or part for a degree/diploma at this or any other Institution/University.

Partha Sarathi Ghosh

Acknowledgements

I would like to thank the following people without whom this thesis would not have been possible. First of all, I would like to thank my supervisor Dr. Ashok Arya, not just for introducing me to the world of first-principles simulations, but also for his excellent supervision and guidance throughout this work. I would also like to thank him for helping me in organization of the thesis and for marathon proofreading preceding the submission of this work. I would like to thank Dr. G.K. Dey, Director Materials Group, for his support and encouragement throughout. This thesis wouldn't have been possible without the help and support of Dr. P.S. Somayajulu, Radio-metallurgy Division, BARC, for conducting experiments on (Th,Ce)O₂, (Th,Pu)O₂ and (Th,U)O₂ MOX fuels. I would also like to acknowledge Kaushik Ghoshal for his help in preparing (Th,U)O₂ MOX samples and providing technical assistance to characterize MOX samples.

I would like to thank Dr. Robin Grimes, Imperial College London, for giving excellent ideas in setting up two-phase melting simulations, suggesting changes and corrections in (Th,U)O₂-(Th,Pu)O₂ MOX melting and ThO₂ superionic transition papers. Dr. N. Kuganathan and C.O.T. Galvin from atomistic simulation group, Imperial College London, are also acknowledged for their support for those two papers. The members of doctoral committee, Dr. G.K. Dey, Dr. I. Samajdar, Dr. S.C. Gupta and Dr. N. Choudhury are also acknowledged for their suggestions and guidance during the course of Ph.D. I would also like to thank Kawsar Ali for his technical support and delightful discussions we had.

Finally, I want to thank my parents, my wife Sangita and my daughter Aratrika for being constantly by my side.

Abstract

This study attempts to systematically study the thermodynamic stability and detailed atomistic mechanism involved in the phase transformations in the pure Zr, ThO₂ and their alloys using atomistic simulation techniques. Zr-based alloys are the basic components of the structural materials in pressurized heavy water reactors and ThO₂ based mixed oxides are excellent alternative fuels for the current light water reactors and upcoming advanced heavy water reactors. These materials show variety of phase transformations of displacive, mixed-mode (diffusive-cum-displacive) and superionic nature. Thermo-physical and mechanical properties of these materials are governed by the phases present in their parent matrix and subsequent phases that arise during the thermal treatment of the alloys.

In this thesis, ab-initio estimation of formation energies of chemically ordered ω phases, *viz.*, Zr₂Al, Zr₃Al₂Nb and Zr₄AlNb show that a pure displacive $\beta \rightarrow \omega$ transformation is not energetically favorable for chemically disordered bcc (β) phase at these compositions. Density functional theory (DFT) calculated ground state energy landscape suggested that for the ω like collapse to occur, a certain degree of chemical ordering is a pre-requisite. This study also presents a systematic theoretical investigation of most energetically favorable atomistic pathways for $\alpha \rightarrow \omega$ transformation in pure Zr out of many experimentally proposed pathways. The lowest barrier pathway is a suitable combination of smallest strains and atomic shuffle, an essential criterion for diffusionless displacive transformation. The most favorable transformation pathway has a $C2/c$ common space group along the transition pathway with an enthalpy barrier of 22 meV/atom at 0 K.

With increasing temperature, ThO₂ shows “superionic transitions” where the material allow the macroscopic movement of oxygen ions through its structure, leading to exceptionally high (liquid-like) values of ionic conductivity whilst in the solid state. This behavior typically occurs at elevated temperatures ($\sim 0.8 \times$ melting temperature) and is characterized by the rapid diffusion of a significant fraction of

oxygen ions within an essentially rigid framework formed by the Th sublattice. This study evaluates the most probable directions of diffusion and actual diffusion paths of the oxygen atoms in the superionic regime using atomistic simulations. Moreover, the calculated diffusion barriers indicate that $\langle 001 \rangle$ is the easy direction for anion migration in superionic state. With further increase of temperature, B_{1u} phonon mode continues to soften and become imaginary at a temperature of 3430 K (below melting temperature of ~ 3600 K). The calculated temperature variation of single crystal elastic constants shows that the fluorite phase of ThO_2 remains elastically stable in the superionic regime, though the B_{1u} phonon mode becomes imaginary in that state. This leads to anionic disorder at elevated temperature. Tracking of anions in the superionic state as a function of time suggests a hopping model in which the oxygen ions migrate from one tetrahedral site to another via octahedral interstitial sites.

The melting behavior of ThO_2 , UO_2 and PuO_2 as well as $(\text{Th,U})\text{O}_2$ and $(\text{Th,Pu})\text{O}_2$ mixed oxides (MOX) is studied using molecular dynamics (MD) simulations. The MD calculated melting temperatures of ThO_2 , UO_2 and PuO_2 using two-phase simulations, lie between 3650-3675 K, 3050-3075 K and 2800-2825 K, respectively, which match well with experiments. The variation of enthalpy increments and density with temperature, for solid and liquid phases of ThO_2 , PuO_2 as well as the ThO_2 rich part of $(\text{Th,U})\text{O}_2$ and $(\text{Th,Pu})\text{O}_2$ MOX are also reported. The MD calculated melting temperatures of $(\text{Th,U})\text{O}_2$ and $(\text{Th,Pu})\text{O}_2$ MOX show good agreement with the ideal solidus line in the high thoria section of the phase diagram and an evidence for a minimum is identified around 5 atom% of ThO_2 in the phase diagram of $(\text{Th,Pu})\text{O}_2$ MOX.

PuO_2 is emulated by CeO_2 in many laboratory scale experiments as CeO_2 and PuO_2 have quite similar physico-chemical properties. This thesis also presents a systematic study of thermal properties of $(\text{Th,Ce})\text{O}_2$, $(\text{Th,Pu})\text{O}_2$ and $(\text{Th,U})\text{O}_2$ MOX. In this study, we employ classical MD simulations to calculate the thermal expansion and thermal conductivity of these MOX and our calculated values are compared with available experimental data. We also present the experimental work done to validate some of our calculated results. Our combined MD simulations and

dilatometry/high temperature XRD measurements indicate that incorporation of CeO_2 , PuO_2 and UO_2 in ThO_2 systematically increases coefficient of thermal expansion. Similarly, the MD calculated and laser-flash measured thermal conductivity values indicate that incorporation of PuO_2 in ThO_2 (by 6 wt.%) reduces thermal conductivity between $0.6\text{-}1.2 \text{ Wm}^{-1}\text{K}^{-1}$ in the $973\text{-}1613 \text{ K}$ temperature range compared to pure ThO_2 . Similarly, the incorporation of UO_2 in ThO_2 (by 6 wt.%) reduces thermal conductivity values between $0.5\text{-}1.1 \text{ Wm}^{-1}\text{K}^{-1}$ in the temperature range between $873\text{-}1873 \text{ K}$. The MD calculated thermal property results show good agreement with experimental results wherever available. Though, the factors like porosity, sample inhomogeneity, *etc.*, have not been taken into our calculations. The chapter concludes that using the present MD simulation methodology, the thermal properties of $(\text{Th,Pu})\text{O}_2$ and $(\text{Th,U})\text{O}_2$ MOX could be predicted over a wide temperature and composition range and complement experimental observations.

List of Publications

Journals

1. Ab-initio study on the formation of chemically ordered Zr_2Al phase by coupled replacive-displacive transformation
P.S. Ghosh, A. Arya, R. Tewari, U.D. Kulkarni and G.K. Dey,
Philosophical Magazine 92 (2012) 4040-4055.
2. Alpha to omega martensitic phase transformation pathways in pure Zr
P.S. Ghosh, A. Arya, R. Tewari, G.K. Dey,
Journal of Alloys and Compounds 586 (2014) 693-698.
3. Prediction of ordered omega phase formation by coupled replacive-displacive processes in Zr_3Al_2Nb and Zr_4AlNb alloy: a first-principles study
P.S. Ghosh, A. Arya and G.K. Dey,
Philosophical Magazine 95 (2015) 1201-1220.
4. Thermal expansion and thermal conductivity of $(Th,Ce)O_2$ mixed oxides: A molecular dynamics and experimental study
P.S. Ghosh, P.S. Somayajulu, A. Arya, G.K. Dey, B.K. Dutta,
Journal of Alloys and Compounds 638 (2015) 172-181.
5. Thermal expansion and thermal conductivity of $(Th,U)O_2$ mixed oxides: A molecular dynamics and experimental study
P.S. Ghosh, P.S. Somayajulu, K. Krishnan, N. Pathak, A. Arya, G.K. Dey,
Journal of Alloys and Compounds 650 (2015) 165-177.
6. Experimental and molecular dynamics study of thermo-physical and transport properties of ThO_2 -5wt.% CeO_2 mixed oxides
P.S. Somayajulu, **P.S. Ghosh**, J. Banerjee, K.L.N.C. Babu, K.M. Danny,
B.P. Mandal, T. Mahata, P. Sengupta, S.K. Sali, A. Arya,
Journal of Nuclear Materials 467 (2015) 644-659.
7. Thermal expansion and thermal conductivity of $(Th,Pu)O_2$ mixed oxides: A molecular dynamics and experimental study
P.S. Somayajulu, **P.S. Ghosh**, A. Arya, K.V. Vrinda Devi, D.B. Sathe, J. Banerjee, K.B. Khan, G.K. Dey, B.K. Dutta,
Journal of Alloys and Compounds 664 (2016) 291-303.

8. Melting Behavior of (Th,U)O₂ and (Th,Pu)O₂ Mixed Oxides
P.S. Ghosh, N. Kuganathan, C.O.T Galvin, A. Arya, G.K. Dey, B.K. Dutta and R.W. Grimes
Journal of Nuclear Materials 479 (2016) 112-122.
9. A Computational Study on Superionic Behaviour of ThO₂
P.S. Ghosh, A. Arya, N. Kuganathan, G.K. Dey and R.W. Grimes
Physical Chemistry Chemical Physics 18 (2016) 31494-31504.

Conference Proceeding

1. “Determination of thermal properties pure ThO₂ using classical molecular dynamics simulations”; **P.S. Ghosh**, Karamvir Kaur, K Ali, A Arya, GK Dey; AIP Conference Proceedings 1731, 140029 (2016);
doi: <http://dx.doi.org/10.1063/1.4948195>.
2. “Ab-initio study of replacive-displacive phase transformations in Zr₂Al-Nb alloys” **P.S. Ghosh**, A. Arya and G.K. Dey; Proceedings of the conference on advances in refractory and reactive metals and alloys (ARRMA-2016), Mumbai, India; January 27-29; 2016; p. 135.
3. “Determination of thermal expansion, thermal conductivity and melting temperature of ThO₂ using classical molecular dynamics simulations” **P.S. Ghosh**, N. Kuganathan, C.O.T. Galvin, A. Arya, B. K. Dutta, G. K. Dey and R. W Grimes; Proceedings of the International Thorium Energy Conference 2015 (ThEC15), October 12-15, 2015 Mumbai, India.
4. “Determination of thermo-physical properties of (Th,Ce)O₂ MOX using classical molecular dynamics simulations” **P.S. Ghosh**, A. Arya, G.K. Dey, P.S. Somayajulu; Proceedings of the International Thorium Energy Conference 2015 (ThEC15), October 12-15, 2015 Mumbai, India.
5. “HCP to omega martensitic phase transformation pathway in pure Zr” **P.S. Ghosh**, A. Arya and G.K. Dey; AIP Conference Proceedings 1512, 48 (2013);
doi: <http://dx.doi.org/10.1063/1.4790904>

Contents

1	Introduction	2
1.1	Background	2
1.2	Motivation	4
1.3	Objectives	7
1.4	Organization of the Thesis	7
2	Historical Perspective	9
2.1	Phase Transformations and its Pathways	9
2.1.1	Displacive Transformation in pure Zr	9
2.1.2	Diffusive-Displacive Transformation in Zr-Al alloys	17
2.1.3	Superionic Transition in ThO ₂	22
2.1.4	Melting Behavior of (Th,U)O ₂ and (Th,Pu)O ₂ MOX	26
2.2	Thermal Properties of ThO ₂ based MOX	28
2.2.1	Experimental Studies	28
2.2.2	Computational Studies	30
3	Theoretical Methodologies	32
3.1	Introduction	32
3.2	Electronic Structure Theory	33
3.2.1	Density Functional Theory (DFT)	35
3.2.2	Kohn-Sham equations	40

3.2.3	Approximations to Exchange-Correlation functionals	41
3.2.4	DFT+ U and Hybrid Functionals	42
3.2.5	The plane-wave basis set	44
3.2.6	The pseudopotential approximation	46
3.2.7	Projector Augmented Wave	49
3.2.8	Hellmann-Feynman Forces	50
3.3	Self-consistent Iterative Optimization	52
3.4	First-principles Lattice Dynamics Theory	54
3.5	Empirical Pair Potential based Classical Molecular Dynamics Calculations	59
3.5.1	The Born Interpretation of Interatomic Forces	62
3.5.2	Ensembles	66
3.5.3	Temperature and Pressure Control	67
3.6	Thermal Properties from MD Simulations	70
3.6.1	Thermal Expansion	70
3.6.2	Thermal Conductivity by Green-Kubo method	70
4	Finding Lowest Energy Barrier Pathway for $\alpha \rightarrow \omega$ Martensitic Transformation in Zr	72
4.1	Introduction	72
4.2	Computational Details	73
4.3	Atomistic Details and Enthalpy Barriers of Experimentally Proposed Pathways	74
4.3.1	UZ Pathway [42]	74
4.3.2	RTB Pathway [43]	76
4.3.3	SG Pathway [26]	76
4.4	COMSUBS Generated Pathways	79
4.5	Precursor to $\alpha \rightarrow \omega$ transformation	82

4.6	Summary	84
5	$\beta \rightarrow$ ordered-ω Phase Transformation Pathways in Zr-Al Alloys	85
5.1	Introduction	85
5.2	Disordered $\beta \rightarrow$ ordered- ω Athermal Transformation Pathway in Zr ₂ Al alloy	86
5.2.1	Description of Crystal Structures	87
5.2.2	Computational Methodology	87
5.2.3	Relative Stability of the Phases	89
5.2.4	Ordered ω Phase Formation: Replacive <i>versus</i> displacive process	90
5.3	Disordered $\beta \rightarrow$ ordered- ω Athermal Transformation Pathways in Zr ₂ Al-Nb Alloys	93
5.3.1	Phase Stability and bcc \rightarrow ω Transformation	93
5.3.2	Mechanical Stability of ω' -Zr ₃ Al ₂ Nb, ω -Zr ₄ AlNb and B8 ₂ -Zr ₂ Al alloys	101
5.3.3	Bond Stability and Bond Strength	105
5.3.4	Chemical Ordering <i>versus</i> Displacive Tendencies	106
5.4	Summary	108
6	Superionic Transition in ThO₂	109
6.1	Introduction	109
6.2	Computation Methodology	110
6.3	Ground State Properties of ThO ₂	112
6.4	Lattice Dynamical Properties of ThO ₂	113
6.5	Lattice Dynamical Properties as a function of isotropic strain	116
6.6	B_{1u} and E_u phonon mode softening at the X point	119
6.7	Transition to Superionic State: The Pathway	121
6.7.1	Anion Conduction Mechanism	121

6.7.2	Migration Barrier for Oxygen Movement	122
6.7.3	Position-Time plot for oxygen migration	123
6.8	Temperature variation of single crystal elastic constants	126
6.9	Summary	128
7	Melting Behavior of (Th,U)O₂ and (Th,Pu)O₂ MOX	129
7.1	Introduction	129
7.2	Computational Methodology	129
7.2.1	Modeling of random solid solutions	129
7.2.2	(Th,U)O ₂ and (Th,Pu)O ₂ MOX interatomic potentials	130
7.2.3	MD simulations of thermodynamic properties	132
7.2.4	Two-phase simulations of melting temperatures	133
7.3	Melting Temperatures of pure oxides	134
7.3.1	ThO ₂	134
7.3.2	UO ₂	135
7.3.3	PuO ₂	136
7.4	Enthalpies and densities of pure oxides	138
7.4.1	ThO ₂	138
7.4.2	UO ₂	141
7.4.3	PuO ₂	142
7.5	Melting Temperatures of (Th,U)O ₂ MOX	144
7.6	Melting Temperatures of (Th,Pu)O ₂ MOX	146
7.7	Enthalpies and Densities of Th rich (Th,U)O ₂ and (Th,Pu)O ₂ MOX	150
7.8	Summary	150
8	Thermal Properties of (Th,Pu)O₂ and (Th,U)O₂ MOX	154
8.1	Introduction	154
8.2	MD simulation methodology	155

8.3	(Th,Pu)O ₂ MOX	156
8.3.1	Thermal Expansion	156
8.3.2	Thermal Conductivity	158
8.4	(Th,U)O ₂ MOX	161
8.4.1	Experiments	162
8.4.2	Thermal Expansion	163
8.4.3	Thermal Conductivity	171
8.5	Summary	173
9	Conclusions and Future Scopes	174
9.1	Summary of Results and Conclusions	174
9.1.1	Phase Transformation Pathways	174
9.1.2	Thermodynamic Parameters of ThO ₂ based MOX	176
9.2	Limitations and Future Scope of this work	178
	Appendices	181
A	Superionic Transition in ThO₂	182
B	Thermal Properties of (Th,Ce)O₂ MOX	187
B.1	Determination of Buckingham-type (Th,Ce)O ₂ MOX Interatomic Potentials	187
B.1.1	Thermal Expansion	190
B.1.2	Thermal Conductivity	193
C	Experimental Techniques	199
C.1	Preparation of ThO ₂ -X wt% CeO ₂ (X = 0, 5 and 8) solid solutions	199
C.2	Preparation of ThO ₂ -X wt% UO ₂ (X = 0, 6, 13, 25 and 30) solid solutions	200
C.3	ICP-AES	201

C.3.1	Sample preparation for ICP analysis	201
C.3.2	Instrument and operating conditions	202
C.4	Thermogravimetry	202
C.5	High Temperature XRD	202
C.6	Dilatometry	203
C.7	Thermal Conductivity Measurements	203
Bibliography		204

List of Figures

- 2.1 A schematic representation of the atoms on the basal plane for α and ω . Two inequivalent lattice sites are shown as solid and open circle. 11
- 2.2 A schematic representation of the phase diagram of Zr. Three main phases: the room temperature α (hexagonal-closed packed), the high temperature β (body-centered cubic), and the high pressure ω (hexagonal structure) can be identified. The $\alpha \rightarrow \omega$ transformation and its reverse $\omega \rightarrow \alpha$ are strongly hysteric; the finish transformations are indicated by the dashed lines. At room temperature, when Zr is pressurized to ω and then returned to atmospheric pressure, there is retained ω phase in the α phase. The ω phase is removed by annealing at $T_{\omega \rightarrow \alpha} = 470$ K. The $\omega \leftrightarrow \alpha$ room temperature equilibrium pressure $P_{\alpha \rightarrow \omega}$ of 2.2 GPa is found at the discontinuity in shear strength under pressure (caused by ω particles in α). The dotted line continues the $\omega \leftrightarrow \alpha$ equilibrium line from the triple point (P_t, T_t) down to atmospheric pressure to guide the eye. (reproduced from Sikka *et al.* [18]) 12

2.3	Schematic diagram showing stacking of the $(222)_{bcc}$ planes of the bcc (cubic symmetry) (a) ω' structure (partial collapse of the planes, trigonal symmetry) (b) and ω (AlB_2) structure (full collapse of two of the planes, hexagonal symmetry). Systematic collapse of the bcc planes (marked as 1 and 2) into a single plane (-1.5) generates AlB_2 structure. Planes marked as 0 remain stationary. The parameter Z is a measure of the movement of the second and third plane along with their Wyckoff counterparts.	17
3.1	A schematic representation of the potentials (red lines) and wave functions (blue lines) for an atom. The real potential and wave function are shown with thin lines, while the pseudopotential and wave function are shown in thick lines. Outside the cutoff region (vertical black lines) the two are identical.	48
3.2	Flowchart illustrating the iterative scheme for the calculation of ground state electron density using Kohn-Sham approximation.	53
4.1	Energy barrier of $\beta \rightarrow \omega$ transformation for possible range of atomic shuffles. Normalized atomic shuffle parameter $6z = 0$ and 1 correspond to β and ω structure, respectively.	75

4.2 **The RTB pathway:** in each $(0001)_\alpha$ stacking plane three neighboring closed-pack $[\bar{1}\bar{2}10]_\alpha$ atomic rows are displaced by a distance $\frac{a_\alpha}{4}$ along $[\bar{1}\bar{2}10]_\alpha$ direction and the next three parallel atomic rows are displaced by the same distance along the opposite direction $[\bar{1}2\bar{1}0]_\alpha$ produces atomic arrangement corresponds to that of $[\bar{1}\bar{2}10]_\omega$ plane of distorted ω structure. An additional small atomic shuffle of $\frac{a_\alpha\sqrt{3}}{24}$ along $[\bar{1}010]_\alpha$ direction is also required to produce ideal ω structure. This shuffle is accompanied by strain components of -2.97% along $[\bar{1}\bar{2}10]_\alpha$ direction, -2.14% along $[0001]_\alpha$ direction and 3.94% along $[\bar{1}010]_\alpha$ direction to produce a hexagonal ω structure with correct c/a ratio. The orientation relations connecting the α and ω supercells are $(0001)_\alpha \parallel (\bar{1}\bar{2}10)_\omega$; $[\bar{1}2\bar{1}0]_\alpha \parallel [0001]_\omega$ 77

4.3 **The SG pathway:** in each stacking $(0001)_\alpha$ plane atoms of label 1, 3, 5 and atoms of label 2, 4, 6 are moved by $\frac{a_\alpha\sqrt{3}}{12}$ along $[10\bar{1}0]_\alpha$ and $[\bar{1}010]_\alpha$ directions, respectively. This shearing movement can be decomposed into two equal movements by a fraction $\pm\frac{1}{12}$ along A_1 and A_2 (as described in Table 1). Additionally, atoms of level 2, 3 and 3, 4 are shifted by a fraction $-\frac{1}{12}$ and $\frac{1}{12}$ of A_3 lattice vector along A_3 , respectively. In this process $(0001)_\alpha$ plane transforms into $(10\bar{1}1)_\omega$ plane. The arrows indicate atom movements along the $(0001)_\alpha$ plane only. This shuffle is accompanied by lattice strain ϵ such that $A'(\omega) = \epsilon A(\alpha)$ to produce a hexagonal ω structure with correct c/a ratio. The supercell lattice vectors are also shown (as described in Table 1) in this figure. The atomic arrangements in this figure are depicted according to our choice of supercell. The orientation relations connecting the α and ω supercells are $(0001)_\alpha \parallel (0\bar{1}11)_\omega$; $[11\bar{2}0]_\alpha \parallel [01\bar{1}1]_\omega$ 78

4.4	GGA-PBE Calculated enthalpy barrier versus reaction co-ordinate as a function of pressure for the RTB and SG pathway using ab-initio NEB method with 9 intermediate images. At 0 GPa enthalpy barrier for the SG pathway is almost 3 times lower than the RTB pathway. With increasing pressure barrier for the SG pathway also decreases and even at 17.13 GPa barrier is not zero.	79
4.5	Variation of calculated potential energy versus zone center phonon mode (E_{2g}) in terms of normalized atomic displacement as a function of volume compression. The inset figure shows variation of the calculated zone center phonon frequencies and calculated values of C_{44} as a function of volume compression. The calculated values of $\nu_{E_{2g}} = 79.3 \text{ cm}^{-1}$ and $C_{44} = 24.8 \text{ GPa}$ at ambient pressure are in good agreement with respective experimental values of 87 cm^{-1} [47] and 33 GPa [215] (room temperature). Solid boxes show experimental values of $\nu_{E_{2g}}$ as a function of pressure [47].	83
4.6	Band structure of α Zr along high symmetry directions at ambient pressure (solid line), at 9.363 GPa (large dotted line) and distorted hcp lattice to simulate a zone center TO E_{2g} mode (small dotted line) at ambient pressure.	84
5.1	(a) Stacking of the $(222)_{\beta}$ planes of the bcc Zr_2Al phase, (b) ω'' structure (partial collapse of the planes), (c) ω structure (full collapse of two of the planes). The parameter Z is a measure of the movement of the second and third plane along with their Wyckoff counterparts. When all planes are equidistant, $Z = 0$, and the first plane is at a distance $1/6$ of c/a above the lowest plane. As the shuffle progresses to completion, this plane moves up by $1/12$ of c/a (the plane above it simultaneously moves down by $1/12$ of c/a).	88
5.2	All possible arrangements ($\{a\}$ - $\{h\}$) of Zr and Al atoms on the bcc lattice corresponding to bcc Zr_2Al alloy. Dark gray and light gray circles represent Zr and Al atoms, respectively.	91

5.3	The variation of energy difference ($E - E_{\Gamma} - Zr_2Al$) as a function of magnitude of ω -type collapse of atomic planes for all configurations corresponding to bcc- Zr_2Al phase (see Figure 5.2), where $E_{\Gamma} - Zr_2Al$ is cohesive energy of the most stable configuration Γ . Here, the ω and bcc structures correspond to normalized displacement parameter equals to 1.0 and 0.0, respectively.	92
5.4	Total and partial density of states (DOS) of Zr_2Al structure for (i) configuration {b} with $Z=0$ (ii) configuration b with $Z=1/12$ (iii) configuration Γ and (iv) $B8_2$ showing strong interaction between Zr-d and Al-p states.	94
5.5	Different arrangements of the atoms for Zr_3Al_2Nb alloy with an underlying bcc structure. Black, white and gray atoms show Zr, Al and Nb, respectively. Systematic collapse of the bcc planes (marked as 2, 3 and 5, 6) into a single plane (2-3 and 5-6) generates ω structure while keeping planes marked as 1 and 4 stationary. This is true for all the configuration.	95
5.6	Different arrangements of the atoms for Zr_4AlNb alloy with an underlying bcc structure. Black, white and gray atoms show Zr, Al and Nb, respectively. Systematic collapse of the bcc planes (marked as 2, 3 and 5, 6) into a single plane (2-3 and 5-6) generates ω structure while keeping planes marked as 1 and 4 stationary. This is true for all the configuration.	96
5.7	Calculated total energy as a function of atomic displacement for 6 distinct Zr_3Al_2Nb configuration.	98
5.8	Calculated total energy as a function of atomic displacement for 10 distinct Zr_4AlNb configuration. Energy values in the y axis are given with respect to configuration (i).	99
5.9	Total and partial DOS of (a) Γ and (b) ω' - Zr_3Al_2Nb . Fermi energy (E_F) is represented by vertical line.	101

6.1	Variation of equilibrium lattice constant (a_0), bulk modulus (B_0) and electronic energy-gap (E_g) as a function of U_{eff} calculated for LDA+ U . Experimental values are presented as horizontal solid lines in the graph. In this graph we also show pure GGA calculated values of a_0 and B_0 for comparison with LDA+ U calculated values. For the calculation of bulk modulus Birch-Murnaghan equation of state was employed as shown in B_0 vs. U_{eff} plot.	114
6.2	Phonon dispersion curve of ThO ₂ calculated using GGA and LDA+ U compared with inelastic neutron scattering data [261] and Raman scattering measured data [265] at room temperature. Solid and dotted line represents LDA+ U and GGA calculated phonon frequencies, respectively. Solid circles present experimentally measured data. The notation of the special points is Γ (0,0,0), X (0,0,1), W (1,1,0) and L (1,1,1).	116
6.3	Phonon dispersion curve of ThO ₂ calculated using LDA+ U and $3\times 3\times 3$ (81 atoms) as well as $4\times 4\times 4$ (192 atoms) supercell compared with inelastic neutron scattering data at room temperature. Solid and dotted line represents calculated phonon frequencies for $3\times 3\times 3$ and $4\times 4\times 4$ supercell, respectively. Solid points are neutron scattering data as reported by Clausen <i>et al.</i> [261].	117
6.4	Phonon dispersion curve and density of states for ThO ₂ calculated using GGA at lattice strain (a) $\epsilon = 0.0$, (b) $\epsilon = 0.04$, (c) $\epsilon = 0.045$ and using LDA+ U at lattice strain (d) $\epsilon = 0.0$, (e) $\epsilon = 0.05$, (f) $\epsilon = 0.06$. Red, blue and black lines in DOS plot shows partial DOS of Th, O and total DOS, respectively.	119
6.5	GGA, LDA+ U and HSE06 calculated E_u (empty points) and B_{1u} (solid points) mode frequencies at the X point as a function of linear lattice strain. Solid lines are drawn only for visual guidance	120

6.6	GGA, LDA+ U and HSE06 calculated variation of potential energy versus zone center phonon mode B_{1u} in terms of normalized atomic displacement of O atoms as a function of isotropic dilational lattice strains. Actual motion of the O atoms in the ThO ₂ unit cell is also shown.	121
6.7	MD calculated migration barrier along [001], [110] and [111] high symmetry directions. Solid lines and fill points present MD NEB calculated migration path for $a = 5.6 \text{ \AA}$ (correspond to normal state). Similarly, dotted lines and open points present MD NEB calculated migration path for $a = 5.8 \text{ \AA}$ (corresponds to superionic state). . . .	124
6.8	Snapshot of the movement of given oxygen atoms (atom A and atom B) for 20 ps time duration in the XY and YZ plane calculated using molecular dynamic simulations at 3000 K. Oxygen atoms preferentially occupy and migrate through tetrahedral positions.	126
6.9	LDA+ U , GGA and MD calculated single crystal elastic constants (C_{11} , C_{12} and C_{44}) are shown as a function of lattice strains (temperatures) and experimentally measured room temperature values are also shown (measured by Macedo <i>et al.</i> [260] from single crystal ThO ₂). Similar symbol with color black, red and blue represents C_{11} , C_{12} and C_{44} , respectively.	127
7.1	Snapshots of the two-phase MD simulation in the NPT ensemble with (a) T=3650 K (left panel) and (b) 3675 K (right panel). The red spheres represent O atoms and the blue spheres represent Th atoms. (a) Initial state of the simulation box, which contains both liquid and solid phases. (b) Intermediate state of the simulation box (at 0.6-0.7 ns), where the solid phase propagates to the liquid (at 3650 K) and liquid phase propagates to the solid phase (at 3675 K). (c) Final state of the simulation box (at 1.7-1.9 ns), when the entire system has turned into a solid phase (at 3650 K) and vice-verse (at 3675 K).	134

7.2	MD calculated enthalpy increments (a) and density variation (b) as a function of temperature in the 300-6000 K range for ThO ₂ are compared with experimental values.	138
7.3	MD calculated enthalpy increments (a) and density variation (b) as a function of temperature in the 300-6000 K range for UO ₂ are compared with experimental values reported by Fink <i>et al.</i> [119].	140
7.4	MD calculated enthalpy increments (a) and density variation (b) as a function of temperature in the 300-6000 K range for PuO ₂ are compared with experimental values.	142
7.5	MD calculated melting temperatures of (Th,U)O ₂ MOX are compared with ideal solidus and liquidus line as well as experimentally reported values.	144
7.6	MD calculated melting temperatures of (Th,Pu)O ₂ MOX are compared with ideal solidus and liquidus line as well as experimentally reported values by Böhler <i>et al.</i> [123]. Ideal behavior represented by (a) and (b) is after Bruycker <i>et al.</i> [112] and Bakker <i>et al.</i> [6], respectively.	147
7.7	MD calculated enthalpy increments of (a) Th _{0.9375} U _{0.0625} O ₂ (b) Th _{0.875} U _{0.125} O ₂ (c) Th _{0.8125} U _{0.1875} O ₂ and (d) Th _{0.6875} U _{0.3125} O ₂ MOX are compared with experimental values reported by Dash <i>et al.</i> [115] and Fischer <i>et al.</i> [287].	152
7.8	MD calculated enthalpy increments of (a) Th _{0.97} Pu _{0.03} O ₂ (b) Th _{0.92} Pu _{0.08} O ₂ (c) Th _{0.80} Pu _{0.20} O ₂ (d) Th _{0.70} Pu _{0.30} O ₂ MOX are compared with experimental values reported by Valu <i>et al.</i> [124] at the same compositions.	153
8.1	MD calculated lattice parameter variation as a function of temperature ($a(T)$) of ThO ₂ , Th _{0.9375} Pu _{0.0625} O ₂ and Th _{0.875} Pu _{0.125} O ₂ is compared with HT-XRD determined values of ThO ₂ , Th _{0.96} Ce _{0.04} O ₂ and Th _{0.92} Ce _{0.08} O ₂ MOX. MD values are calculated in the 300-3000 K temperature range in 100 K interval.	157

8.2	Thermal conductivity calculated by MD simulations as a function of temperature for ThO_2 and $\text{Th}_{0.9275}\text{Pu}_{0.0625}\text{O}_2$ compared with our experimental values of ThO_2 , ThO_2 -1 wt.% PuO_2 (POP and CAP pellets) and ThO_2 -6 wt.% PuO_2 POP pellet (95% TD). These values are also compared with reported values of ThO_2 , ThO_2 -3 wt.% and ThO_2 -8 wt.% PuO_2 by Cozzo <i>et al.</i> [142]. Solid lines are only for visual guidance.	160
8.3	XRD patterns of ThO_{2-x} wt.% UO_2 ($x = 0, 6, 13, 25$ and 30) MOX at room temperature. Lines at 40.47° and 47.12° are due to Pt-Rh sample carrier (marked as \star in the figure).	164
8.4	XRD patterns of ThO_2 -6wt.% UO_2 (POP) at different temperatures. Lines at 40.47° and 47.12° are due to Pt-Rh sample carrier.	165
8.5	Comparison of lattice parameter (a) and thermal conductivity (b) variation as a function of temperature of pure ThO_2 calculated by classical MD simulation and reported experimental values. The lattice parameters are calculated form 300-3000 K in 100 K interval and the error bars in the calculated lattice parameters are ± 0.0008 Å. The thermal conductivity values are calculated at 300, 400, 500, 750, 1000, 1250, 1500, 1750 and 2000 K temperature.	167
8.6	Variation of lattice parameter of $\text{Th}_{1-x}\text{U}_x\text{O}_2$ ($x = 0, 0.0625, 0.125, 0.1875, 0.25$ and 0.3125) in the 300-1300 K temperature range along with our HT-XRD data. The lattice parameters are calculated form 300-3000 K in 100 K interval and the error bars in the calculated lattice parameters are ± 0.0008 Å.	168
8.7	Variation of lattice parameter of $\text{Th}_{1-x}\text{U}_x\text{O}_2$ ($x = 0, 0.0625, 0.125, 0.1875, 0.25$ and 0.3125) in the 300-3000 K temperature range along with HT-XRD data of $\text{Th}_{0.94}\text{U}_{0.06}\text{O}_2$ [127], $\text{Th}_{0.87}\text{U}_{0.13}\text{O}_2$ [129] and $\text{Th}_{0.80}\text{U}_{0.20}\text{O}_2$ [130]. The lattice parameters are calculated form 300-3000 K in 100 K interval and the error bars in the calculated lattice parameters are ± 0.0008	169

8.8	Thermal conductivity as calculated by MD simulations as a function of temperature for ThO_2 and $\text{Th}_{0.9375}\text{U}_{0.0625}\text{O}_2$ compared with our experimental values of ThO_2 and ThO_2 -6wt.% UO_2 (POP and CAP) pellet (both corrected to 95 % TD). These values are also compared with reported values of ThO_2 -2wt.% UO_2 by Pillai <i>et al.</i> [132]. The thermal conductivity values are calculated at 300, 400, 500, 750, 1000, 1250, 1500, 1750 and 2000 K temperature and solid lines are only for visual guidance.	171
A.1	Illustration of oxygen migration directions towards a vacant oxygen site A (black atom) in a 2x2x2 supercell (96 atoms). Atoms B, C and D migrate to position A along [001], [110] and [111] directions, respectively. This supercell is taken only to show 3 migration direction and actual calculation was performed in a 10x10x10 supercell (12000 atoms).	182
A.2	MD calculated MSD curve for oxygen between 2500 K and 3200 K (100 K interval). Superionic transition is visible above 2900 K. . . .	183
A.3	MD calculated diffusivity plot for oxygen between 2500 K and 3300 K (100 K interval). The jump in the diffusivity value appears at 3000 K and above.	183
A.4	MD calculated RDF plot for O-O pair at 2500 K and 3000 K. Below the fast ionic regime, simulated at 2500 K, RDF of O-O show succession of well-defined peaks, while in the fast ionic regime O-O RDF peaks are less-well defined from 2 nd nearest neighbours onwards. This indicates a diffuse O sub-lattice because of intensive ionic motion. . .	184
A.5	MD calculated total displacement ($\sqrt{(dx^2 + dy^2 + dz^2)}$) from equilibrium position is plotted as a function of simulation time for atom A (upper panel) and atom B (lower panel) at 3000 K temperature. Inset figures show simulation time corresponding to which anionic transition occurs from one tetrahedral position to the other.	185

A.6	MD calculated total displacement ($\sqrt{(dx^2 + dy^2 + dz^2)}$) from equilibrium position is plotted as a function of simulation time for atom A (upper panel) and atom B (lower panel) at 2900 K temperature. Inset figures show simulation time corresponding to which anionic transition occurs from one tetrahedral position to the other.	186
B.1	Calculated (a) Thermal expansion and (b) isothermal compressibility of ThO ₂ is compared with available experimental data in the literature [130, 141, 259, 296, 297].	189
B.2	Calculated (a) Thermal expansion and (b) isothermal compressibility of CeO ₂ is compared with available experimental data in the literature [141, 307].	189
B.3	MD calculated (using Buck (solid line) and BMM (dotted line) model) unit cell dimension of pure ThO ₂ , Th _{0.9375} Ce _{0.0625} O ₂ and Th _{0.875} Ce _{0.125} O ₂ MOX in the 300-3000 K temperature range is compared with HT-XRD data [141]. The lattice parameters are calculated from 300-3000 K in 100 K interval. Black, red and blue lines are for ThO ₂ , Th _{0.9375} Ce _{0.0625} O ₂ and Th _{0.875} Ce _{0.125} O ₂ MOX, respectively.	191
B.4	Normalized heat current auto correction function (HCACF) for C_{xx} as a function of time for ThO ₂ at 500 K and 1500 K.	193
B.5	Normalized heat current auto correction function (HCACF) for C_{xx} as a function of time for CeO ₂ at 500 K and 1500 K.	194
B.6	Thermal conductivity calculated by MD simulations as a function of temperature for ThO ₂ compared with experimental values. Solid line is only for visual guidance.	195
B.7	Thermal conductivity calculated by MD simulations as a function of temperature for CeO ₂ compared with experimental values. Solid line is only for visual guidance.	195

B.8 Thermal conductivity calculated by MD simulations as a function of temperature for ThO_2 , $\text{Th}_{0.9275}\text{Ce}_{0.0625}\text{O}_2$ and $\text{Th}_{0.875}\text{Ce}_{0.125}\text{O}_2$ compared with our experimental values of ThO_2 and ThO_2 -5wt% CeO_2 for POP as well as CAP pellets sintered in Ar+ H_2 and Air atmosphere (95 % TD). These values are also compared with reported values of ThO_2 , ThO_2 -3wt% and ThO_2 -8wt% PuO_2 by Cozzo *et al.* [142]. Lines are only for visual guidance. Black, red and blue lines show MD calculated values of ThO_2 , $\text{Th}_{0.9275}\text{Ce}_{0.0625}\text{O}_2$ and $\text{Th}_{0.875}\text{Ce}_{0.125}\text{O}_2$ MOX. Solid and dotted lines show MD calculated values using Buckingham and BMM potential. 197

List of Tables

2.1	Summary of literature data on thermal expansion coefficient and thermal conductivity of ThO ₂ and (Th,U)O ₂ MOX	30
4.1	Details of the α and ω supercell generated to study RTB and SG pathway. The strains required to produce the ω lattice with correct c/a ratio from α shown in the table are our PAW-PBE calculated values.	80
4.2	Maximal common subgroup (G) of the two phases $G_1 = P6_3/mmc$ and $G_2 = P6/mmm$ of Zr. G provides a possible path for the transition from G_1 to G_2 as $G_1 \rightarrow G \rightarrow G_2$. We give the atomic positions and supercell lattice vectors of G_1 and G_2 in terms of the conventional lattice vectors $a_1 = a_0(\frac{1}{2}\hat{x} - \frac{\sqrt{3}}{2}\hat{y})$, $a_2 = a_0(\frac{1}{2}\hat{x} + \frac{\sqrt{3}}{2}\hat{y})$, $a_3 = c_0\hat{z}$ of G_i (a_0 and c_0 are the respective equilibrium lattice parameters of G_i). In the last column an estimate of the approximate barrier height is given.	81
5.1	DFT-GGA ground-state properties of Zr-Al system along with pure Zr (hcp) and Al (fcc) phases. Experimental (in parenthesis) and other calculated ab-initio values in braces are also given.	90

5.2	Difference between cohesive energies of possible configurations of the bcc-Zr ₂ Al composition compared to the Γ -Zr ₂ Al configuration ($E_{\Gamma-Zr_2Al}$) and number of first and second nearest neighbour (nn) Zr-Al, Zr-Zr and Al-Al bonds. Bond lengths (in brackets (Å)) of these 1st and 2nd nn bonds of configurations {a}, {b} and {c} in their bcc and ω' (24% plane collapse) structures are also enlisted.	91
5.3	Difference between energy of possible distinct configurations and the most stable configuration and number of first nearest neighbor Zr-Al and Zr-Nb bonds. Though energetically degenerate configurations, <i>viz.</i> , (a), (g) and (i) of Zr ₄ AlNb structure are symmetrically equivalent in the bcc structure, but these configurations behave differently during ω -type collapse.	97
5.4	DFT-GGA ground-state properties of Zr ₃ Al ₂ Nb (Γ, ω' and B8 ₂), ω -Zr ₄ AlNb along with pure Nb (bcc) phase. Experimental (in parentheses) and other calculated ab-initio values in braces are also given. References [77] enlist experimental values of a and c/a for Zr ₅₉ Al ₂₀ Nb ₂₁ alloy.	100
5.5	The listing of strains (e_i) used for the calculation of elastic constants at 0 K for the ω' -Zr ₃ Al ₂ Nb, ω -Zr ₄ AlNb and B8 ₂ -Zr ₂ Al (the unlisted e_i 's = 0).	102
5.6	Calculated values of elastic constants for the ω' -Zr ₃ Al ₂ Nb, ω -Zr ₄ AlNb and B8 ₂ -Zr ₂ Al.	105
6.1	Calculated structural, elastic and dielectric properties of ThO ₂ are compared with previous experimental and theoretical results in the literature. (* = our HT-XRD study)	115
6.2	GGA, LDA+ U and HSE06 calculated phonon mode frequencies of ThO ₂ at high symmetry points of the Brillouin zone (Γ , X and L) are compared with inelastic neutron scattering and Raman scattering measured phonon frequencies. The results are shown for isotropic lattice strain (ϵ) of 0.00.	118

7.1	Pair and multisite correlation functions ($\Pi_{k,m}$) of SQS-96 structures for mimicking ideal random $\text{Th}_{1-x}\text{U}_x\text{O}_2$ solid-solution ($x = 1/6, 2/16, 3/16, 4/16, 5/16$ and $6/16$).	131
7.2	MD calculated melting temperatures of pure ThO_2 , UO_2 and PuO_2 are compared with experimentally measured values available in the literature.	137
7.3	MD calculated enthalpy of fusion of pure ThO_2 , UO_2 and PuO_2 are compared with experimentally measured values available in the literature.	139
7.4	MD calculated enthalpy increments (in J/mole) of solid and liquid phases of $(\text{Th,U})\text{O}_2$ and $(\text{Th,Pu})\text{O}_2$ MOX are fitted to equation 7.7 and 7.8, respectively and coefficients are enlisted.	148
7.5	MD calculated density (in g/cm^3) of solid and liquid phases of $(\text{Th,U})\text{O}_2$ and $(\text{Th,Pu})\text{O}_2$ MOX are fitted to equation 7.9 and 7.10, respectively and coefficients are enlisted.	149
8.1	MD Calculated and experimentally measured thermal expansion coefficients of ThO_2 and $(\text{Th,Pu})\text{O}_2$ MOX are compared with available experimental data for $(\text{Th,Ce})\text{O}_2$ MOX. ThO_2 -5wt% CeO_2 and ThO_2 -8wt% CeO_2 corresponds to compositions $\text{Th}_{0.9253}\text{Ce}_{0.0747}\text{O}_2$ and $\text{Th}_{0.8823}\text{Ce}_{0.1177}\text{O}_2$, respectively. (TD=Theoretical Density)	158
8.2	Constants A and B of the equations $\kappa = \frac{1}{A+BT}$ for ThO_2 and $(\text{Th,Pu})\text{O}_2$ MOX calculated from MD simulations and experimental measurements.	161
8.3	Impurity content analysis by ICP-AES	163
8.4	Variation of lattice parameter a (\AA) for ThO_2 and ThO_{2-x} wt.% UO_2 MOX ($x = 6, 13, 25$ and 30) with temperature as measured using HT-XRD.	165
8.5	Characteristics of experimental pellets used for thermal property studies.	166

8.6	MD Calculated and experimentally measured thermal expansion coefficients of ThO ₂ and (Th,U)O ₂ MOX compared with available experimental data in the literature.	170
8.7	Constants A and B of the equations $\kappa = \frac{1}{A+BT}$ for ThO ₂ and (Th,U)O ₂ MOX calculated from MD simulations and experimental measurements.	172
B.1	Parameters of the pair-wise interactions described by equation B.1.	188
B.2	Relative lattice energies of different AB ₂ polymorphs with respect to fluorite structure calculated from our interaction parameters for ThO ₂ and CeO ₂ in eV/atom. ‘F’ indicates the structures optimized to the same energy as the fluorite structure.	190
B.3	MD Calculated and experimentally measured thermal expansion coefficients of ThO ₂ and (Th,Ce)O ₂ MOX are compared with available experimental data in the literature. ThO ₂ -5wt%CeO ₂ and ThO ₂ -8wt%CeO ₂ corresponds to compositions Th _{0.9253} Ce _{0.0747} O ₂ and Th _{0.8823} Ce _{0.1177} O ₂ , respectively. The Buckingham (Buck) and Buckingham-Morese-manybody (BMM) models correspond to the potential model employed in those calculations	192
B.4	Supercell size dependence of thermal conductivity of ThO ₂ at 1250 K.	196
B.5	Constants A and B of the equations $\kappa = \frac{1}{A+BT}$ for ThO ₂ and (Th,Ce)O ₂ MOX calculated from MD simulations and experimental measurements.	198
C.1	Characteristics of starting ThO ₂ and UO ₂ powders.	201

Chapter 1

Introduction

1.1 Background

Phase stability and phase transformations are of utmost importance for physicist, chemists, metallurgist, ceramists and others involved in the study of solids. This multi-disciplinary field is not only academically important but also has technological relevance. Accompanying a phase transformation, there are changes in some physical properties and structure of the material. Often, transformed structures show deleterious change in physical and mechanical properties in the desired pressure and temperature range. Hence, there is always a motivation to tailor material properties by controlling their phase transformation behavior in the desired temperature and/or pressure range. In order to do so, it is necessary to understand the mechanistic details of phase transformation or “*phase transformation pathway*” (PTP). The study of PTP gives us a vivid picture of actual microscopic phase transformation (PT) mechanism and enable us to tune PT behavior by suitable addition of alloying elements and/or change in alloy treatment environments. Moreover, knowledge of basic thermodynamic properties over the temperature and/or pressure range is necessary to understand structural and mechanical stability of the phases. The study of phase stability and phase transformation becomes even more important and challenging for materials commonly utilized in nuclear industry as structural components and basic fuels.

In recent times, the world has witnessed a renewed interest in nuclear energy as it is the only CO₂-free source of energy at the gigawatt scale. Presently, nuclear energy provides only 15% of the total global energy requirements [1,2]. Major hindrances to increase this number come mainly from disposal of radioactive waste and limited resources of natural uranium, among many other. This exorbitant amount

of waste with the presence of weapon-grade plutonium is a major concern leading to nuclear proliferation [3–6]. A potential solution to this problem lies in the use of thorium-based, rather than uranium-based, fuel cycle in working commercial nuclear power plants. Thorium fuel cycle itself has several potential advantages over uranium-plutonium fuel cycles as it tends to reduce the proliferation of spent fuel and plutonium production. It reduces the long-lived minor actinides production compared with the uranium-plutonium cycle, which is certainly an ecological advantage. The waste generated from thorium fuel cycle has lesser amounts of actinides and the rate of decrease of radio-toxicity level is much faster compared to that in uranium fuel cycle [3]. Therefore, thorium based fuels have an attractive prospect mainly due to its abundance, to reduce the need for enrichment in the fuel cycle, the high conversion ratios achievable, less radioactive fission product generation and also due to other neutron and thermal physical properties.

The engineering designs of nuclear reactors are largely governed by materials properties of fuel, their cladding, fuel elements and their structural components [7]. Zirconium based alloys have been established as vital materials in reactor technology, functioning as fuel cladding, pressure tubes and fuel spacer grid materials due to their good oxidation, corrosion and creep resistance. The requirement of thermal neutron transparency accounts for the rejection of many established materials used for structural applications at high temperature and corrosive environments [7]. Among all the existing alloys zirconium-based alloys like zircaloy-2, zircaloy-4 and Zr-2.5%Nb, which are currently being used for reactor core structural applications, qualify best with regard to the desired properties. One of the major problems faced with these materials is related to the hydrogen pick up and irradiation growth. Due to the very limited solubility of hydrogen in these structural materials, various hydride phases precipitate on thermal cycling and particularly during the shutting down of the reactors. The problem of irradiation growth, resulting in undesirable change in the macroscopic dimensions of the components, is again associated with the anisotropy of the low temperature α phase crystal structure. Thus a material having an isotropic cubic matrix with high solubility for interstitial hydrogen would be better suited for structural applications in nuclear reactor.

There is a constant search for new materials which can be used as alternate nuclear fuels as well as materials which have suitable combination of properties in reactor environment as structural components. A limited number of elements satisfy the criterion of a low thermal neutron absorption cross-section, the number of alloys suitable for reactor core structural applications are very few. Since the early days of zirconium technology it was known that alloys based on the Zr-Al system

are stronger than most of the other zirconium based alloys [8]. The dilute alloys of this binary system, however, showed catastrophic failure due to enhanced corrosion caused by the aluminium bearing porous oxide film [8]. Later on, Schulson *et al.* [9–13] showed that Zr_3Al based alloys is a potential material for structural components of reactors. Basic thermal and physical properties of these fuel and structural component material are influenced by their phase transformation behavior and thermodynamic parameters of product and parent phases.

The knowledge of basic thermal properties of relatively new fuel materials is also important for fuel design, performance modeling and assessment of safety issues. The fuel materials always possess inherent radioactivity. Therefore, experimental determination of thermal properties requires extensive safety precautions and remote handling of samples. Experiments can be performed in a limited temperature and/or composition range. Similarly, the experimental evaluation of PTP may be hindered due to differing time scales between microscopic processes and experimental observations.

Over the last few decades there has been a significant increase in the usage of simulation tools within the scientific community for the basic and applied research. With rapidly growing computational processing power and continuing development of basic algorithms, atomic scale modeling has become a valuable tool to provide useful insights into the behavior of atoms on spatial and temporal scales often inaccessible to traditional experimental investigations. This thesis adopts atomic scale simulation techniques to expand our understanding of phase transformation pathway and to determine thermodynamic properties of Zr and ThO_2 based materials.

1.2 Motivation

Zirconium aluminides have been actively considered as potential candidate materials for structural components in nuclear industry because of their suitable combination of properties like high strength, good corrosion and oxidation resistance [14, 15]. However, one of the major problems in their applications is their low ductility in the low-to-intermediate temperature region due to the presence of unwanted omega (ω) derivative phases which embrittle the Zr_3Al based alloy [16]. Other inherent problems like, inadequate control over the distribution of undesirable phases [10], irradiation induced amorphization [13], *etc.*, prevented Zr_3Al based materials to be used for structural applications in nuclear reactors. Schulson [11] reviewed the work on Zr_3Al and showed that some of these problems could be solved by altering the

initial microstructures by controlling the grain size and shapes and by introducing new phases. In this connection, a ternary addition (*e.g.* Nb) in Zr_3Al was thought to be beneficial. The effect of Nb on the transformation behavior in Zr_3Al alloys has not been well studied. A systematic study of the effect of Nb addition is desired to explore their potential as a structural material in nuclear reactors.

Moreover, group IV elements exhibit two distinct allotrimorphs - stable low-temperature hexagonal close-packed (hcp) α and stable high-temperature body-centered cubic (bcc) β phases. Alloys of these elements, containing a critical concentration of β -stabilizing elements, form a metastable, non-closed-packed hexagonal ω phase upon rapid cooling from the high-temperature single β phase field followed by isothermal/athermal annealing [17, 18]. The ω phase forms by displacive mechanism involving periodic displacement of lattice planes. Importantly, the formation of the ω phase has been actively studied over a decade due to its complex formation mechanism and its deleterious influence on mechanical and superconducting properties [14–17, 19–24], especially in Zr and Zr-rich Zr-Al alloys. For these reasons, the mechanism of ω formation is of high relevance in these alloys for controlling its formation mechanism.

In zirconium aluminides, one often encounters another ω transformation in which the disordered β transforms to *ordered* ω structures where chemical ordering of the ω -lattice occurs through diffusional atomic movements. The overall process can be viewed as superimposition of displacive and diffusive processes. The quantitative determination of thermodynamic tendencies leading to diffusive and/or displacive processes at different stages of the transformation delineates the actual pathway on the free energy landscape. This study aims to investigate the formation mechanism and basic thermodynamic tendencies in ω phase formation in pure Zr, Zr-rich Zr-Al binary and Zr-Al-Nb ternary alloys using a computational approach.

Investigations of thorium ^{232}Th as a fuel for nuclear power reactors started in parallel with those of uranium and plutonium. Thorium seemed an attractive prospect mainly due to its abundance, the opportunity to reduce the need for enrichment in the fuel cycle, the high conversion ratios (to ^{233}U) achievable in a thermal neutron spectrum and other neutron and thermal physical properties studied at the early stages of nuclear power program. Despite this rather long list of advantages and fast depletion of uranium resources, thorium is not yet challenging the use of uranium fuel on a commercial basis, although research efforts regarding the thorium fuel cycle continue [2–5]. In nature, ^{232}Th is fertile, and by absorbing slow neutrons in the reactor environment it can transmute to ^{233}U [3], which is fissile. Therefore, ^{232}Th based fuels need a fissile material as a ‘driver’ (such as ^{235}U

or ^{239}Pu) to facilitate a nuclear chain reaction. Thus, ^{232}Th based mixed oxides (MOX) ($(\text{Th,U})\text{O}_2$ and $(\text{Th,Pu})\text{O}_2$) are considered as a potential fuel for various reactor systems (*viz.*, conventional pressurized water reactors (PWR), advanced heavy water reactors (AHWR) and thermal breeder reactors) [2–5]. It has already been established that $(\text{Th,Pu})\text{O}_2$ MOX fuel can be used in PWRs without any significant change in the reactor design [2–5]. Nevertheless, since it has not been widely used, a number of thermo-physical properties that are available to designers and regulators of UO_2 based fuels are not so well established for ThO_2 based fuels.

To predict the in-pile behavior and performance of $(\text{Th,U})\text{O}_2$ and $(\text{Th,Pu})\text{O}_2$ MOX fuels, a primary knowledge of their phase transformation behavior and thermo-physical and transport properties such as thermal expansion, melting point, elastic modulus (bulk, shear and Young modulus), ionic conductivity, heat capacity and thermal conductivity is of utmost importance. The melting and superionic behavior of ThO_2 based MOX are important to assess their thermodynamical and structural stability. The melting temperature is also an important engineering parameter for nuclear fuel design and safety assessment, as it defines operational limits of nuclear fuel in its application environment and it limits the power that can be extracted from the fuel elements.

Thermal expansion values, on the one hand, decide the extent of thermal stresses the fuel is going to experience during burn-up in the reactor, while on the other hand, these are crucial in determining the fuel assembly-clad gap and the effective heat transport. The temperature variation of bulk, shear and Young modulus gives an estimation of the mechanical stability of fuels in the reactor operating condition. Further, thermal conductivity of nuclear fuels is one of the most important properties which influences the processes such as swelling, grain growth and fission gas release and limits the linear power of the reactor. The temperature of nuclear fuels is controlled by its specific heat capacity as well as thermal conductivity.

Determination of these properties of $(\text{Th,Pu})\text{O}_2$ MOX by experimental means is very difficult due to associated radiotoxicity, high specific activity and proliferation risk of PuO_2 based systems and require extensive and expensive safety precautions [3, 4, 6]. As a result, the number of experimental studies addressing the thermo-physical and thermodynamical properties of $(\text{Th,Pu})\text{O}_2$ MOX is limited. This study aims also to investigate important thermal properties of $(\text{Th,U})\text{O}_2$, $(\text{Th,Pu})\text{O}_2$ MOX using a computational approach followed by validation of those results through experimental measurements.

1.3 Objectives

There are range of issues that atomic scale simulation can be used to investigate with regard to thermodynamics of Zr and ThO₂ based nuclear materials. The “equilibrium” phase stability of pure Zr and ThO₂ and their alloys is well studied by experiments. Initial work in the transformation of phases focused on orientation relationships between initial phase and final product, [17, 18, 25–27] and measurements of some thermodynamic property (electrical conductivity, thermal diffusivity, *etc.*) showing discontinuous change across the transition temperature and/or pressure [28–32]. Actual “atomistic pathway” which is operative in the transformation of phases have never been explored. A major hindrance to study “atomistic pathway” by experimental means is the fast moving transformation front. This study attempts to systematically study the detailed atomistic mechanism involved in the phase transformations in the pure Zr, ThO₂ and their alloys whether the nature of transformation is pure displacive, mixed-mode (diffusive-cum-displacive), superionic or melting using atomistic simulation techniques. The quantitative determination of thermodynamic tendencies for these transformations at different stages of transformation enables delineation of the actual pathway on the free energy landscape. This thesis covers the following phase transformation studies:

- (a) Evolution of omega (ω) phase from ground state alpha (α) phase in pure Zr by displacive transformation mechanism,
- (b) Evolution of chemically ordered omega (ω) phase from disordered bcc (β) phase in Zr-rich Zr₂Al and Zr₂Al-Nb alloys by diffusive-displacive transformation pathway,
- (c) Evolution of *superionic* phase in ThO₂ at elevated temperature and
- (d) Melting behavior of (Th,Pu)O₂ and (Th,U)O₂ MOX fuels

Moreover, the study of thermal properties (*e.g.*, thermal expansion, thermal conductivity, enthalpy, *etc.*) of ThO₂ based MOX (*e.g.* (Th,Ce)O₂, (Th,Pu)O₂ and (Th,U)O₂) as a function of temperature is also covered in this work.

1.4 Organization of the Thesis

The rest of the thesis is chapter-wise organized as follows:

- Chapter 2:** A detailed survey of the literature (experimental and theoretical) relevant to this work is presented in this chapter
- Chapter 3:** A brief description of the theoretical simulation tools (First-principles, classical molecular dynamics, *etc.*) used in this work is presented in this chapter
- Chapter 4:** A first-principles study of the evolution of omega (ω) phase from ground state alpha (α) phase in Zr by pure displacive transformation pathway is presented in this chapter
- Chapter 5:** A first-principles study of the evolution of chemically ordered omega (ω) phase from disordered bcc (β) phase in Zr-rich Zr_2Al and Zr_2Al-Nb alloy by replacive-displacive transformation pathway is presented in this chapter
- Chapter 6:** A combined first-principles and molecular dynamics study of the evolution of the *superionic* phase in ThO_2 is presented in this chapter
- Chapter 7:** A study of the melting behaviors of $(Th,U)O_2$ and $(Th,Pu)O_2$ MOX using classical molecular dynamics simulations is presented in this chapter
- Chapter 8:** A study of the thermal expansion and thermal conductivity of $(Th,Pu)O_2$ and $(Th,U)O_2$ MOX using classical molecular dynamics simulations is described and compared with experimental data. Moreover, study of the thermal properties of $(Th,Ce)O_2$ MOX which is a surrogate material to $(Th,Pu)O_2$ MOX is also reported along with experimental validation in this chapter
- Chapter 9:** Finally, a summary of results and main conclusions of the work are reported in this chapter. While performing these studies a number of issues arose, which were not addressed in this work. These are also described in this chapter along with future scope of the work.

Chapter 2

Historical Perspective

2.1 Phase Transformations and its Pathways

Solid-solid phase transformations are ubiquitous in nature and are of fundamental interest in the field of materials science. A solid undergoes a phase transition when a particular phase of the solid become unstable under a given set of thermodynamic conditions. Mapping of competing phases and associated phase transformations (with pressure, temperature and impurities) can provide predictive design for improved control of alloy properties. phase transformation can be mechanistically classified as either reconstructive or diffusive and displacive [17, 25]. The former involves atomic movements from the parent to the product lattice sites by random diffusional jumps where the first and/or second-coordination bonds are broken and reformed. The latter involves cooperative movements of large numbers of atoms in a diffusionless process where changes in higher coordination can be effected by distortion in the primary bond. Atomic movements in displacive transformations can be accomplished by a homogeneous distortion, shuffling of lattice planes, static displacement waves or a combination of these.

2.1.1 Displacive Transformation in pure Zr

Two examples of a displacive phase transformations are **(a)** *martensitic transformation*: the transformation of hcp alpha-phase (α) to a hexagonal omega structure (ω) and **(b)** ω *transformation*: the transformation of bcc beta-phase (β) to a omega structures (ω), where, the hcp and bcc lattice is transformed into the hexagonal omega-structure, respectively, by a periodic displacement of lattice planes and are mostly observed in Ti and Zr based alloys.

(a) Martensitic Transformation

A martensitic phase transformation is “first-order, displacive, diffusionless, athermal structural phase transformation.” A first-order transformation has discontinuity in a structural variable, such as volume, along with transformational hysteresis. The displacive nature requires the unit cell of the parent lattice to distort continuously into the unit cell of the daughter lattice. Such a change produces orientation relations between the phases: Certain vectors and planes in the parent phase will be parallel to unique vectors and planes in the daughter phase. This is written as as $[x_1x_2x_3]_{parent} || [y_1y_2y_3]_{daughter}$ and $(h_1h_2h_3)_{parent} || (k_1k_2k_3)_{daughter}$ for the parallel vectors and planes, respectively. The phase transformation happens very quickly, often on the order of the speed of sound in the material [17,25]. At these speeds, the phase transformation is diffusionless, as the atoms do not have time to travel very far, though there may still be small relaxations during the transformation. Finally, the kinetics of the transformation are athermal: the amount of daughter phase in the crystal depends only on the driving force (temperature or applied stress), not the holding time [25,33].

α and ω Crystallography

Figure 2.1 shows the crystal structure for α -Zr: hexagonal closed-packed (hcp). Each basal plane is a hexagonal layer with a lattice constant of $a_\alpha = 3.233$ Å; alternating layers are stacked like hard-spheres in an ABAB pattern. This two-atom unit cell (space group $P6_3/mmc$ [18]) has atoms at Wyckoff positions (c): $(\frac{1}{3}\frac{2}{3}\frac{1}{4})$ and $(\frac{2}{3}\frac{1}{3}\frac{3}{4})$. The ideal c/a ratio of $\sqrt{8/3} = 1.633$ produces twelve nearest neighbors exactly a distance a_α away. In Zr, the c/a ratio is the slightly lower 1.592; thus, each atom has 6 neighbors at 3.20 Å.

Figure 2.1 also shows the crystal structure of ω -Zr. The ω phase is a hexagonal structure (space group $P6/mmm$) with three atoms per unit cell; AlB_2 being the prototype. The geometry is very layered: the first layer (A) is made from atoms at the Wyckoff position (a):(0 0 0), and the next layer (B) from atoms at the Wyckoff positions (d): $(\frac{1}{3}\frac{2}{3}\frac{c}{2a})$ and $(\frac{2}{3}\frac{1}{3}\frac{c}{2a})$ where $\frac{c}{2a} \sim 0.62$. The lattice constant of the hexagonal lattice is very wide ($a_\omega = 5.05$ Å), while the spacing from A to next A layer is small ($c_\omega = 3.15$ Å). Atoms in the honeycomb B layer have a total of 9 neighbors: 3 at 2.92 Å in the same B layer and 6 at 3.32 Å in the A layers above and below. Atoms in the hexagonal A layer have a total of 12 neighbors: 12 at 3.32 Å in the B layers above and below. The volume per atom in ω is 2.5% lower than α ,

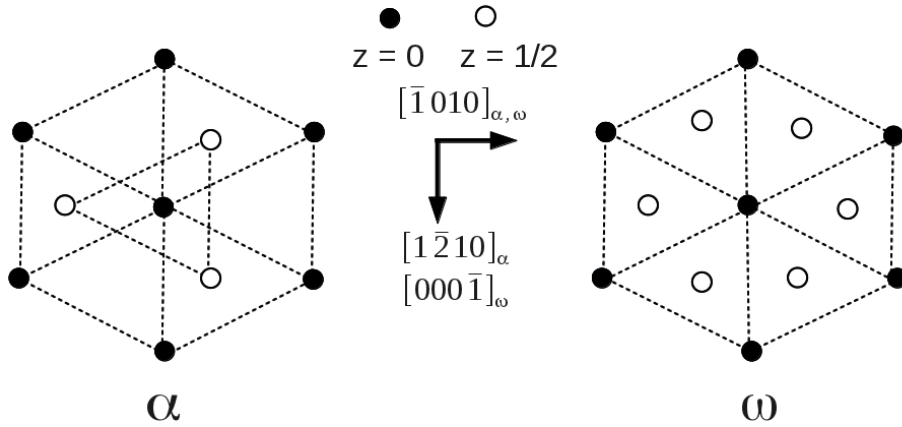


Figure 2.1: A schematic representation of the atoms on the basal plane for α and ω . Two inequivalent lattice sites are shown as solid and open circle.

as it is a high pressure phase. Thus, the symmetry of the crystal is high and there are 24 point-group operations, the same as for a simple hexagonal lattice. The ω phase has a quite open structure and packing ratio (~ 0.57) is larger than that of the simple cubic lattice (~ 0.52), but substantially lower than the bcc (~ 0.68), fcc or hcp structure (~ 0.74).

$\alpha \rightarrow \omega$ Martensitic Transformation in Zr: Experimental Studies

The first study on pure Zr involving high-pressure room temperature resistivity measurements has shown a phase transition at a pressure of about 60 kbar [18]. Jayaraman *et al.* [34] have also detected transformations in Ti and Zr at 80-90 kbar and 50-60 kbar, respectively, using the same technique. In the beginning, these transformations were thought to be the $\alpha \rightarrow \beta$ transformation, as the high temperature β phase was supposed to be the denser phase. Jamieson *et al.* [35, 36], later on, identified the high-pressure phase to be one with a simple hexagonal structure (ω phase). The work of Jamieson also demonstrated the difficulties in determining the equilibrium $\alpha \leftrightarrow \omega$ phase boundary in Ti and Zr as the transformation is associated with a large hysteresis. Due to this large hysteresis, it is possible to retain the high pressure ω phase at ambient pressures. Detailed high-pressure investigations revealed that the transformation pressures are different under continuous loading and step loading [37, 38]. Using the equilibrium transformation data compiled by Kutsar and German [38] for the $\alpha \rightarrow \beta$, $\beta \rightarrow \omega$ and $\alpha \rightarrow \omega$ transformations, Sikka *et al.* [18] have constructed a schematic pressure-temperature phase diagram for the group IV transition metals. Figure 2.2 shows the triple point coordinates (P_t, T_t),

the equilibrium and the hysteresis line superimposed on the pressure-temperature phase diagram of Zr.

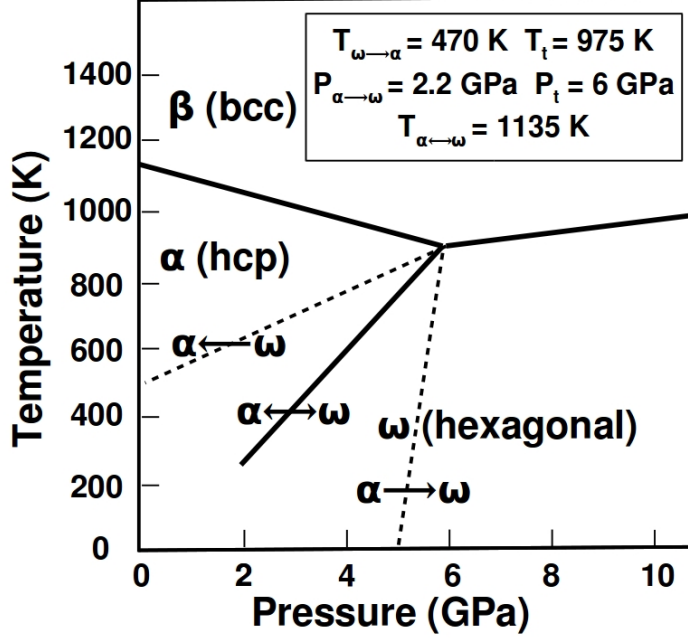


Figure 2.2: A schematic representation of the phase diagram of Zr. Three main phases: the room temperature α (hexagonal-closed packed), the high temperature β (body-centered cubic), and the high pressure ω (hexagonal structure) can be identified. The $\alpha \rightarrow \omega$ transformation and its reverse $\omega \rightarrow \alpha$ are strongly hysteric; the finish transformations are indicated by the dashed lines. At room temperature, when Zr is pressurized to ω and then returned to atmospheric pressure, there is retained ω phase in the α phase. The ω phase is removed by annealing at $T_{\omega \rightarrow \alpha} = 470$ K. The $\omega \leftrightarrow \alpha$ room temperature equilibrium pressure $P_{\alpha \rightarrow \omega}$ of 2.2 GPa is found at the discontinuity in shear strength under pressure (caused by ω particles in α). The dotted line continues the $\omega \leftrightarrow \alpha$ equilibrium line from the triple point (P_t, T_t) down to atmospheric pressure to guide the eye. (reproduced from Sikka *et al.* [18])

The $\alpha \rightarrow \omega$ transformation has also been studied in dynamic (shock) experiments involving pressure pulses of microsecond duration. These phase transformations under shock conditions are usually observed as discontinuities in shock velocity (U_s) versus particle velocity (U_p) plots. McQueen *et al.* [39] have noticed the discontinuities in U_s versus U_p plots for Ti (175 kbar, 370 K), Zr (260 kbar, 540 K) and Hf (400 kbar, 725K). The transition pressures under shock loading conditions have been found to be substantially higher than those reported for static pressure conditions. An extensive hysteresis in the α/ω transition has also been observed in shock pressure experiments.

It has been noticed that the transformation pressure, $P_s^{\alpha \rightarrow \omega}$, determined by different research groups, shows a fairly high scatter for pure Zr (22 kbar to 60 kbar) [18]. This large scatter has been attributed to variations in the pressure exposure time, the starting microstructure, the impurity content and the hydrostatic component of the applied pressure.

Moreover, Zhau *et al.* [40] measured unit-cell parameters of α , β and ω -zirconium metal at pressures up to 17 GPa and temperatures up to 973 K. From these measurements, thermal and elastic properties for the three phases of zirconium have been derived. Compressional and shear wave velocities as well as unit-cell volumes across the $\alpha - \omega$ transition of Zr have been measured up to 10.5 GPa at room temperature by Liu *et al.* [41] using ultrasonic interferometry in conjunction with synchrotron radiation. In the pressure range of 5.0 to 6.2 GPa, a mixture of α and ω phase is clearly identified and the α phase is completely transformed to ω phase at 6.8 GPa. The measured velocity jumps across the $\alpha - \omega$ transition are 9.6% and 13.1% for P and S waves, respectively. Negative pressure dependence for the shear modulus of α -Zr has been found at pressures from 1.4 to 2.9 GPa, which may be ascribed to the shear instability of the α phase prior to transition. According to velocity data, the onset pressure of the $\alpha - \omega$ transition is determined to be 4.0 GPa.

Experimentally, it is only possible to correlate orientation relationships (ORs) between the parent and the product phases [18]. Previous experimental examinations based on electron diffractometry were analyzed leading to three possible suggestions for ORs for the formation of ω from α in pressure treated pure Zr. The first structural model was predicted by Usikov and Zilbershtein (UZ) [42] in which $\alpha \rightarrow \omega$ transformation proceeds via thermodynamically unstable β -phase under static pressure treatment. The OR's were derived by a lattice correspondence matrix which itself was the product of already known $\alpha \rightarrow \beta$ and $\beta \rightarrow \omega$ transformation matrices. Two omega variants (both having the same strains but different shuffles) predicted by this procedure are listed below,

$$\begin{aligned} (0001)_\alpha || (01\bar{1}1)_\omega; [11\bar{2}0]_\alpha || [10\bar{1}1]_\omega & \quad \mathbf{OR\ I} \\ (0001)_\alpha || (11\bar{2}0)_\omega; [11\bar{2}0]_\alpha || [0001]_\omega & \quad \mathbf{OR\ II.} \end{aligned} \quad (2.1)$$

Rabinkin, Talianker and Botstain (RTB) [43] reported another OR where direct $\alpha \rightarrow \omega$ transformation model under static pressure treatment was considered and it was concluded that only three crystallographically equivalent variants corresponding to **OR II** of UZ were possible. The OR of RTB is similar to that

previously reported by Silcock [44] for Ti based alloys. The atomic movements proposed by Silcock and RTB for direct $\alpha \rightarrow \omega$ transformation are generally similar in nature but differ in detail. Later on, Kutsar *et al.* [45] reported the α/ω OR in the shock treated Zr to be the same as the OR II of UZ. Finally, Song and Gray (SG) [26] in shock compressed Zr have reported a new OR, *viz.*,

$$(0001)_\alpha || (10\bar{1}1)_\omega; [10\bar{1}0]_\alpha || [11\bar{2}\bar{3}]_\omega \quad \mathbf{OR\ III} \quad (2.2)$$

which appeared distinct from those previously reported in static high pressure experiments. Later on, by analyzing selected area diffraction patterns of shock loaded Zr samples, G. Joyti *et al.* [46] showed that **OR III** observed by SG is in fact a subset of **OR I** observed by UZ. They also pointed out that $\alpha \rightarrow \omega$ transformation mechanism in Zr remains similar in both conditions.

In literature, there have been attempts to correlate $\alpha \rightarrow \omega$ transformation to phonon softening mechanism. Anomalous behavior of transverse optical phonon mode (E_{2g}) of α -Zr has been observed at Γ -point of the hcp brillouin zone in Raman scattering experiments under pressure [47]. It has also been elaborated that frequencies of E_{2g} phonon mode ($\nu_{E_{2g}}$) is related with C_{44} shear elastic constant by an empirical relation and $\alpha \rightarrow \omega$ transformation is associated with softening of C_{44} as well [48]. In these experiments, the measured $\nu_{E_{2g}}$ are continuously get softened under pressure and coexistence of α and ω -phase was observed even up to 16 GPa confirming the sluggish kinetics of this transformation [47] even though experimentally reported transition pressure is in the range of 2.2-7 GPa. It has also been suggested that $s \rightarrow d$ electron transfer dominates the structural sequence observed under pressure for group IV transition metals [18, 49]. Therefore, theoretical study of C_{44} and E_{2g} phonon mode dynamics as function of pressure is required to understand the role of this phonon in $\alpha \rightarrow \omega$ transformation. Moreover, the study of electronic band structure as function of pressure will help understanding the driving mechanism for this transformation.

$\alpha \rightarrow \omega$ Martensitic Transformation in Zr: Computational Studies

Previous theoretical studies have been aimed to study phase diagram of pure Zr as well as to determine thermal and mechanical properties of α, β and ω phases. Ostanin *et al.* [50] used the full-potential linear muffin-tin orbital (FP-LMTO) method within the local density approximation (LDA) and generalized gradient approximation (GGA) to calculate the total energy and equilibrium lat-

tice properties for the observed phases of Zr. The temperature dependences of the free energy, specific volume, bulk modulus, Debye temperature, and Grüneisen constant were calculated for these structures within the Debye model. The P-T phase diagram constructed from the calculated thermodynamical Gibbs potentials within the GGA fitted well the available room-temperature data on the $\alpha \rightarrow \omega$ and $\omega \rightarrow \beta$ transitions. At ambient pressure, calculated $T_{\beta \rightarrow \alpha} = 1193$ K, which is close to the observed experimental value.

Hao *et al.* [51] calculated the phase diagram of $\alpha \rightarrow \omega$ of Zr by using the density-functional theory and quasiharmonic lattice dynamics. This work is based on the calculation of the Gibbs free energy of α and ω phases, and for each fixed temperature the phase transition pressure is determined by the point at which the two free energies cross. The calculated phase boundary was in better agreement with the available experimental data than other theoretical results. Their calculated results found that the alpha structure as most stable at zero temperature and this conclusion agreed well with that of Schnell and Albers [52]. For the omega structure the phonon dispersions were predicted. The calculated volume thermal expansion coefficients for α -Zr were also predicted and the results were in good agreement with the experimental data at $T > 100$ K.

Hao *et al.* [53] also investigated the effect of hydrostatic pressure on the structures of zirconium metal at zero temperature using the projector augmented wave (PAW) within the Perdew-Burke-Ernzerhof (PBE) form of the GGA. The calculated $\omega \rightarrow \beta$ transition at around 26.8 GPa, which was in excellent agreement with the experimental values. They also found that the ω phase is most stable at 0 K and 0 GPa. This conclusion is supported by first-principles calculations of Schell *et al.* [52] and Jona *et al.* [54]. The elastic constants of ω -Zr under high pressures were calculated and the compressional and shear wave velocities increased monotonically with increasing pressure. The results were in good agreement with the available experimental data and the pressure dependences of three anisotropies of elastic waves were also presented.

Recently, Hu *et al.* [55] investigated the structures, phonon dispersions, phase transitions and thermodynamics of Zr from first-principles calculations. At zero temperature, α -Zr transformed to ω -Zr at 0.98 GPa and then to β -Zr at 31.6 GPa. The axial ratio c/a increased with increasing pressure for α -Zr, but it was nearly invariant under compression for ω -Zr. Within the quasi-harmonic Debye model, the full phase diagram of Zr was obtained. The zero pressure phase transition from α -Zr to β -Zr occurred at 1130 K. The transition pressure from α -Zr to ω -Zr at 300 K was 2.10 GPa and the predicted triple point was at 6.35 GPa, 910 K, which

was close to the experimental data. The thermal properties including the entropy, isotherm, isobar and thermal pressure in a wide range of pressure and temperature were predicted successfully.

In all experimental observations, the $\alpha \rightarrow \omega$ transformation pathways are always inferred from the OR between the parent and the product phases. Also, for a given set of ORs multiple transformation pathways can be inferred and determining energetically favorable one by experimental means is exceedingly difficult. Hence, the actual atomistic pathway for $\alpha \rightarrow \omega$ transformation in pure Zr is still not properly understood, despite several attempts. Previous theoretical studies are mainly emphasized on the determination of phase diagram and $\alpha \rightarrow \omega$ transformation pressure. No previous theoretical study attempts to determine atomistic mechanism of $\alpha \rightarrow \omega$ phase transformation in pure Zr.

(b) $\text{bcc}(\beta) \rightarrow \omega$ transformation

The occurrence of ω -phase was first observed by Frost *et al.* [19] in aged Ti-8%Cr alloys. This phase has also been observed in many other alloy systems where the high temperature bcc phase is stable up to room temperature. In particular, alloys based on group IV B elements (Ti, Zr and Hf) have shown pronounced tendency toward the $\beta \rightarrow \omega$ transformation under pressure and/or thermal treatment. As a metastable phase, it has also been observed in other bcc alloys based on noble metals [56–58] and transition metals [59–63].

The mechanism of the $\text{bcc}(\beta) \rightarrow \omega$ transformation can be represented as the collapse of the $(222)_\beta$ plane due to a propagation of $2/3 \langle 111 \rangle_\beta$ longitudinal displacement wave, causing two neighboring $(222)_\beta$ plane to move toward each other by a displacement in the $[111]$ direction, while each third plane remains unmoved and so on (Figure 2.3). This type of transformation is called displacive because it involves cooperative (military-like) movement of atoms over small distances (a fraction of lattice translation vectors) [17, 18]. If the collapse is complete (Figure 2.3(c), ideal ω), six-fold rotation symmetry is generated around the specific $\langle 111 \rangle$ direction along which collapse of lattice planes occurred; while a trigonal symmetry is attained (resulting structure is associated with a trigonal space group $P\bar{3}m1$) for incomplete collapse (Figure 2.3(b), non-ideal ω , ω'') [17, 18].

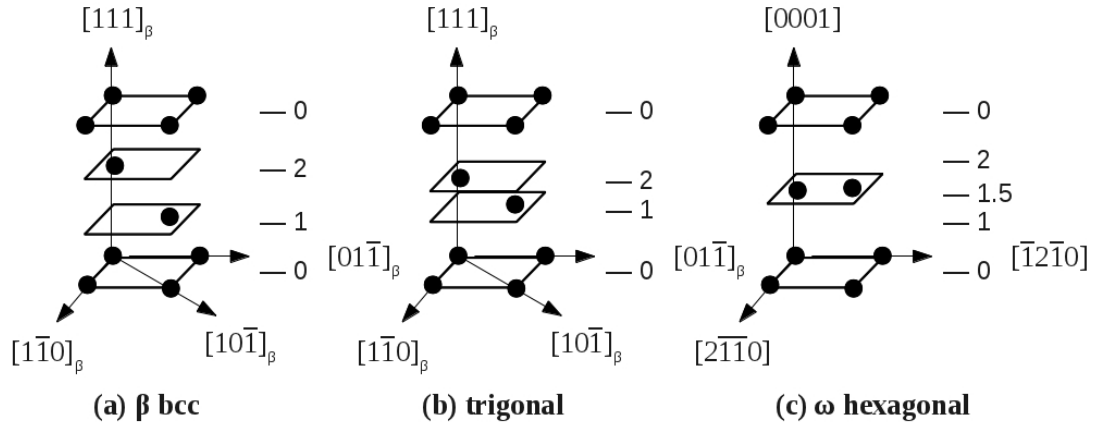


Figure 2.3: Schematic diagram showing stacking of the $(222)_{bcc}$ planes of the bcc (cubic symmetry) (a) ω' structure (partial collapse of the planes, trigonal symmetry) (b) and ω (AlB_2) structure (full collapse of two of the planes, hexagonal symmetry). Systematic collapse of the bcc planes (marked as 1 and 2) into a single plane (-1.5) generates AlB_2 structure. Planes marked as 0 remain stationary. The parameter Z is a measure of the movement of the second and third plane along with their Wyckoff counterparts.

2.1.2 Diffusive-Displacive Transformation in Zr-Al alloys

In general, a phase transformation in a solid results in the creation of one or more new phases within the matrix phase. The operative transformation mechanisms, diffusive and displacive, may interact or compete with each other. There are recognized examples of phase transformations in solids that appear to exhibit the characteristics of both diffusional and displacive transformations. In fact, in most solid-solid phase transformations, the concomitant displacive-diffusional mechanism is the rule rather than an exception [14–17, 20–22].

The formation of ordered derivatives of the ω phases from disordered bcc phases is accomplished by coupled diffusive-displacive phase transformation processes. In these transformations replacive ordering is usually mediated through thermally activated atomic diffusion (resulting in change in composition and chemical ordering) for decorating specific sub-lattice sites by specific atomic species in the disordered parent structure [17, 22, 64]. It is also important to note that chemical ordering which involves only the chemical rearrangement of constituent atomic species leading to an ordered phase without changing the basic lattice framework of the disordered phase is designated as replacive transformation [17, 22].

The best known alloy system where this interplay of diffusive and displacive

process is observed is eutectoid steel. The high temperature austenite phase typically decomposes into pearlite, *i.e.*, ferrite plus cementite (iron carbide, Fe_3C), by a diffusive process. For fast cooling rates, a transformation from austenite (face-centered cubic) to metastable martensite (base-centered tetragonal) may, instead, take place. Such coupled diffusive-displacive transformations have also been observed in other materials, for instance, Ti, Zr and Hf based alloys. Group IV elements exhibit two distinct allotrimorphs - stable low temperature hexagonal close-packed (hcp) α and stable high temperature body centered cubic (bcc) β phases. Alloys of these elements, containing a critical concentration of β -stabilizing elements, form a metastable, non-closed-packed hexagonal ω phase upon rapid cooling from the high temperature single β phase field followed by isothermal/athermal annealing [17, 18, 22].

Importantly, the formation of the ω phase has been actively studied over a decade due to its complex formation mechanism and its deleterious influence on mechanical and superconducting properties [14–17, 20–22]. Especially, the Zr and Zr-rich alloys, a representative of group IV element, have several attractive mechanical properties including high ductility, strength and resistance to corrosion as well as mechanical and irradiation damage. For these reasons, it is an interesting class of materials for multiple applications ranging from structural components in nuclear reactors to a solid solution strengthener in superalloys [14–17, 20–22]. The present study aims to investigate the formation mechanism and basic thermodynamic tendencies in ω phase formation in Zr rich Zr-Al-Nb alloys.

(a) Athermal and Isothermal $\beta \rightarrow \omega$ Transformations

The formation of metastable ω phase in Ti and Zr alloys from the high temperature single β phase field, containing a critical concentration of β stabilizing elements, has been classified as either athermal or isothermal based on kinetics of the transformations [17, 18]. The athermal $\beta \rightarrow \omega$ transformation is purely displacive in nature involving collapse of the $\{111\}$ planes of the bcc phase via a shuffle mechanism, diffusionless and is of first order. The ω phases so obtained has a composition very close to that of the β phase. These transitions do not require any thermal activation and proceed with the velocity of elastic disturbances in the crystals. In contrast, if a solid solution of the alloy of concentration beyond the athermal range is maintained at temperatures for which the diffusion rates are appreciable, favorable concentration fluctuations can occur in the β -matrix creating solute-lean embryos of composition lying within the athermal range. These solute-lean embryos can then transform to ω -phase by the (111) plane collapse mechanism.

Therefore, from the viewpoint of instabilities in the β phase, the athermal ω results from a pure structural instability while the isothermal ω results from concurrent compositional and structural instabilities. These multiple ω phases encountered in Ti and Zr alloys can be attributed to the competing structural and compositional instabilities, inherent within the bcc β phase of these alloys on quenching from high temperatures [17, 18, 22, 64–68]. Eventually, on annealing for long periods of time these metastable ω precipitates are replaced by the equilibrium α phase, the former having a significant influence on the morphology, size-scale and distribution of the latter. As the underlying mechanisms are different, the morphological features are also different for ω phases in the β matrix. The composition range over which athermal ω -phase forms has been shown to depend on the type of solute and, according to some investigators, [64, 65] on the electron-atom ratio of the alloy which is controlled by the solute valence and concentration. For example, athermal ω phase forms in a limited range of concentration of the alloying element which for the Zr-Nb alloys is limited to the range of 5-17% Nb [64–67]. On the other hand, a modulated structure of ω particles in a beta matrix develops when alloys in the composition range 12-25% Nb is aged at appropriate temperatures [68].

(b) Experimental Studies in Zr-Al and Zr-Al-Nb Alloys

Several studies on phase transformation in Zr_2Al based alloys have shown that a number of metastable phases can be produced in these alloys by non equilibrium processing techniques [22]. The metastable phases reported are the disordered bcc (β), hcp (α), B2, DO_{19} , ω and its ordered derivatives, e.g., $B8_2$, $D8_8$, etc. These phases undergo various phase reactions during subsequent thermal treatments, finally leading to the formation of the equilibrium $L1_2$ structure. On the other hand, the formation of the $L1_2$ phase under equilibrium condition occurs through sluggish peritectoid reactions and requires very long aging time for completion. In addition, alloy compositions close to Zr_3Al are amenable to amorphization by mechanical alloying or by irradiation by heavy ions [69]. The formation of metastable phases under non equilibrium condition provides an alternative path for the attainment of equilibrium phase and therefore has significant practical applications. Many of the transformation sequences, involving one or more metastable phases, have been identified and it has been shown that the formation of these metastable phases appears to show a hierarchical sequence [17] expressed in the form of a symmetry tree which is not unique to Zr-Al system but is known to exist in other alloy systems too. The most common feature of these transformations is the formation of ω phase and its ordered derivatives, which provides a path where lattice registry is maintained and

the phase transformation occurs through progressive attainment of a close packed structure from one that is relatively open [17].

The presences of chemically ordered ω -based structures of intermetallic phases such as Zr_2Al ($P6_3/mmc$ symmetry, $B8_2$) and Zr_5Al_3 ($P6_3/mcm$ symmetry, $D8_8$) have already been reported in Zr_3Al and Zr_3Al-Nb alloys. Banerjee and Cahn *et al.* [23] have reported the occurrence of a $\beta \rightarrow B8_2$ transformation in a rapidly solidified Zr_3Al alloy which undergoes spinodal decomposition of β phase prior to the formation of the chemically ordered Zr_2Al phase ($B8_2$ structure) by ‘athermal’ $\beta \rightarrow \omega$ transformation in the Al enriched regions. Tewari *et al.* [24] reported the formation of Zr_5Al_3 phase ($D8_8$ structure) in rapidly solidified (Zr_3Al)-Nb (3 and 10 wt.% Nb) alloys. The evolution of the $D8_8$ phase in β (partially ordered B2) matrix, which could be regarded as one of the ordered derivatives of the ω phase, could be described in terms of a superimposition of the concentration and displacive ordering waves in the β phase. Concentration ordering waves corresponds to ordering of Al atoms as well as vacancy in the β matrix, whereas, displacive ordering waves corresponds to periodic displacement of $\{222\}_\beta$ planes. On further aging, $\beta + Zr_5Al_3$ phase converts to Zr_2Al ($B8_2$) by Zr diffusion in the structural vacancy positions. The formation of ordered ω phase by concomitant replacive-displacive processes is the obscure part of these transformations.

The formation of trigonal (incomplete) ω phase (ω'') in Ti-Al-Nb alloys have also been reported by several experiments [70–76]. Strychor *et al.* [75] have reported the formation of ordered ω structures in Ti-Al-Nb alloys. The high-temperature phase in this case has the B2 structure which, on quenching, transforms into an ordered ω'' structure having the space group $P\bar{3}m1$. Bendersky *et al.* [70] constructed the symmetry tree showing the symmetry changes that occur during the gradual lattice collapse associated with the $\beta \rightarrow \omega$ displacement ordering and the accompanying chemical ordering in a coupled displacive/replacive ordering process in $Ti_3Al_{2.25}Nb_{0.75}$ alloy.

On the contrary, very few experimental studies have been attempted to understand equilibrium phase stability and phase transformation in Zr-rich Zr_2Al-Nb alloy. The binary intermetallic phases Zr_4Al_3 , Zr_5Al_3 and Zr_2Al appearing in the Zr-Al system are considerably extended in the ternary Zr-Al-Nb system [77]. Hansen *et al.* [77] studied isothermal section of Zr-Al-Nb alloys at 925 °C and predicted 19 at% Nb solubility in $(Zr,Nb)_2Al$, where, $(Zr,Nb)_2Al$ forms in a Ni_2In (space group $P6_3/mmc$) prototype structure having composition close to $Zr_{59}Nb_{20}Al_{21}$.

(c) Computational Studies

Earlier, Nguyen-Manh *et al.* [78] employed first principles full-potential linear muffin-tin orbital (FPLMTO) approach within local density approximation (LDA) to calculate the stability of the ordered omega phase in the aluminides of transition metals, viz., Zr, Ti, Nb and V. They investigated only the displacive mode of the transformation leaving replacive part of the transformation unaddressed. In another theoretical investigation by Sanati *et al.* [79] on ordered omega phase formation in Ni₂Al alloy using the FPLMTO method, it was shown that rearrangement of the atoms within a supercell tends to inhibit ω -type transformations. Sanati *et al.* [80] also studied electronic structure, phase stability, and chemical ordering of the omega phase in a Ti₃Al₂X (X = Nb, V) alloy by employing a pseudopotential based first-principles plane wave method. Their study also indicated that the formation of the omega phase in Ti₃Al₂X is a displacive-replacive coupled transformation. In these two studies, it was shown that the replacive transformation involving random jumps of atoms within the unit cell occurred, keeping the chemical composition intact, in a fashion so as to maximize the number of Ni-Al (for Ni₂Al) and Ti-Al (for Ti₃Al₂Nb) bonds present as the 1st nearest neighbor in the unit cell. Sanati *et al.* [81] also examined $B2 \rightarrow \omega'' \rightarrow B8_2$ transformation using first principles calculations in Ti₃Al₂Nb alloy and concluded that configurational entropy plays a major role in the formation of B8₂ phase. Recently, S. Nag *et al.* [82] showed, using a combination of both experimental and theoretical techniques, that in Ti-Mo alloys the displacive component in the product phase changes continuously with changing composition lending credence to mixed mode nature of formation of ordered- ω phase.

Most of the earlier experimental studies in Zr-Al and Zr-Al-Nb alloys explained the formation of ordered ω phase on the basis of symmetry analysis and no relative thermodynamic stability analysis of the phases which appeared in the process of transformation was carried out. Moreover, it is also not clear whether replacive and displacive processes occur in quick succession or they interact and/or compete with each other in these transformations. Whether diffusion is making a suitable chemical environment (chemical composition and/or chemical order) for the displacive process to take place or the vice versa? These questions have not been addressed adequately either experimentally or theoretically. Moreover, no previous computational study attempts to determine phase transformation pathway in Zr-Al and Zr-Al-Nb alloys involving replacive and displacive process.

2.1.3 Superionic Transition in ThO₂

Superionic conductors are those materials that allow the macroscopic movement of ions through their structure, leading to exceptionally high (liquid-like) values of ionic conductivity whilst in the solid state. This behavior typically occurs at elevated temperatures and is characterized by the rapid diffusion of a significant fraction of one of the constituent species within an essentially rigid framework formed by the other species [28–32]. Many compounds, including XF₂ (X = Ca, Ba, Sr, Pb), XSi₂ (X = Mg, Sn, Ge, Pb), and XO₂ (X = Ce, Pr, Th, U, Pu), crystallize in the face-centered cubic fluorite structure (CaF₂ type), where the cation is coordinated to eight anions, and the anion is surrounded by four cations. They show unusually high (“liquid-like”) anionic conductivity (values in the range $10^{-2} - 1 \text{ } \Omega^{-1} \text{cm}^{-1}$) in the solid state far below their melting points [28–32]. Among them, thorium dioxide (ThO₂), a typical superionic conductor, has drawn considerable attention in recent years due to its wide applications as ultra-high temperature material, nuclear fuel material and solid-state electrolyte [29, 83–85]. Moreover, owing to its prominent hardness, ThO₂ has potential applications as a high-k dielectric material and a laser host [85]. Doped thoria, (Th,M)O_{2-x}, where M represents a dopant metal, has superior characteristics in terms of its application as a candidate solid electrolyte. This is because of considerably high O ion conductivity caused by oxygen vacancy formation on doping with lower-valent cations [28, 29, 32, 83, 84]. Thoria is also important for its potential use in nuclear energy applications [28, 29, 32].

The manner in which the superionic state is achieved has been proposed [28–32] as a means to classify superionic materials, namely:

1. **Type I** superionic materials become superionic at temperatures above a first-order structural phase transition. This behavior is typified by the superionic α -phase of AgI. In this material the ionic conductivity increases by around three orders of magnitude, on passing through the $\beta - \alpha$ phase transition at 420 K.
2. **Type II** superionic materials attain high levels of ionic conductivity following a gradual and continuous disordering process within the same phase. Below the superionic transition, T_c , the number of conducting defects increases rapidly before saturating above T_c . The superionic transition is often accompanied by an anomaly in the specific heat and lattice expansion. $\beta - PbF_2$ displays typical type II superionic behavior.

3. **Type III** superionic materials do not have a clear phase transition, but achieve high levels of ionic conduction via increased mobility of a (generally fixed) number of thermally activated defects. An Arrhenius plot of the temperature dependence of the ionic conductivity for a type III superionic conductor would show linear behavior. Sodium β -aluminas are typical type III superionic materials.

(a) Experimental Studies

In the recent past, there have been a few attempts to study structural and anionic diffusion properties of ThO_2 as a superionic conductor. Willis *et al.* [86] measured the Bragg reflections of ThO_2 by neutron diffraction in the temperature range between 293-1373 K and determined mean-square thermal displacements of the atoms in ThO_2 as a function of temperature. They observed that, with the rise of temperature, the oxygen atoms tend to move from fluorite-type positions at (0.25, 0.25, 0.25) towards the large interstitial sites at (0.5, 0.5, 0.5) along $\langle 111 \rangle$ direction. At 1273 K, the mean atomic co-ordinates of the oxygen atoms are (0.25 + δ , 0.25 + δ , 0.25 + δ), where $\delta = 0.014$ for ThO_2 . This relaxation effect indicates that either oxygen sublattice is disordered or they vibrate anharmonically across the ideal lattice sites along the [111] direction. Similarly, Clausen *et al.* [87] and Hutchings *et al.* [88] observed presence of Frankel disorder of the oxygen sublattice in the single crystal of stoichiometric ThO_2 above 2300 K in their coherent diffuse quasi-elastic neutron scattering experiments. Their study on single crystal UO_2 also showed presence of Frankel disorder of the oxygen sublattice above 2000 K. The presence of Frankel disorder was determined by allowing a fraction, n_d , of the oxygen ions to leave their regular lattice sites when fitted to the higher-temperature data. The cations were assumed to remain on their regular sites. The defective oxygen ions were assumed to occupy either or both of the two types of ‘defect’ sites in the ‘empty’ oxygen cubes: the 12 ‘I’, interstitial sites at positions near the mid-point of the regular anion sites, such as $\pm(0.25 + y, 0.25 - y, 0)$, and the 8 ‘R’, relaxed anion sites at $\pm(x, x, x)$ relative to the cation sites. The cations were assumed to remain on their regular lattice sites and the diffuse scattering was assumed to arise primarily from anion-anion correlations.

The relative population of these sites could be given by one of six different possible models as described by Dickens *et al.* [89] and designated as I-VI. The models were fitted to the data at each temperature. The measured intensities were carefully corrected for thermal diffuse scattering, extinction and absorption before being fitted to the models. It should be emphasized that n_d includes both the

true Frankel vacancies and those arising from relaxation. It was found that the value of nd resulting from fits to the data was relatively independent of the model used; however, the fraction of these ‘vacancies’ which form true Frankel pairs was deduced from a model, and the ‘best’ model was taken as that one which gave the best account of both diffraction and diffuse scattering data. The simplest such cluster model was one based on a single Frankel pair, where the interstitial is located at an ‘I’ site and causes its two nearest neighbors to relax towards the center of adjacent empty cubes at ‘R’ sites (model VI). These were labeled as 3 : 1 : 2 clusters, where the v : i : r notation denotes the number of vacancies : Frankel interstitials : relaxed anions. The optimum values of $x = 0.34 \pm 0.01$ and $y = 0.05 \pm 0.03$ were found to be almost independent of temperature for UO_2 . Similar results were also observed for ThO_2 [87, 88]. Moreover, neutron scattering data showed an increase of nd by a factor of 2.5 at temperature ~ 2800 K compared to its value at ~ 2500 K for ThO_2 [88]. The anion disorder is also reflected in the behavior of the acoustic and optic phonon modes where neutron scattering measured lifetimes decrease rapidly. However, well defined long-wavelength acoustic modes were observed upto 2930 K, enabling the elastic constants UO_2 to be measured upto 2930 K, indicating that their contribution to the thermal conductivity would remain significant. The inelastic scattering from lattice modes gave no indication of the nature of the electronic disorder excited in UO_2 . A similar thermally induced oxygen lattice disorder was also observed in ThO_2 [88].

Indirect evidence for superionic behavior within ThO_2 was provided by measurements of its enthalpy by drop calorimetry and differentiation of these data with respect to temperature to obtain specific heat ($C_p(T)$). Fischer *et al.* [90] measured enthalpy increments of ThO_2 using an induction heated drop calorimeter in the 300-3643 K temperature range and found discontinuities in the measured enthalpy-temperature curve. Moreover, the heat capacity value changes discontinuously from a value of $96.97 \text{ J mol}^{-1} \text{ K}^{-1}$ to $142.33 \text{ J mol}^{-1} \text{ K}^{-1}$ at 2950 K and remains constant up to a temperature of 3643 K. They suggested that a diffuse or order-disorder phase transition occurs at approximately 80% of the melting temperature. Therefore, ThO_2 is an type II superionic material which attains high level of ionic conductivity following a gradual and continuous disordering process within the same fluorite structure.

Moreover, Nafe *et al.* [91] analyzed the ionic conductivity of $\text{Th}_{1-x}\text{Y}_x\text{O}_{2-0.5x}$ ($0.05 \leq x \leq 0.29$) compounds over a wide temperature range (between 300-2000 K) and suggested that at low and medium temperature range, the ionic conductivity increases with temperature at a higher rate in compounds having high Y concentra-

tions. As higher Y doping concentrations leads to creation of higher oxygen vacancy concentrations and hence higher anionic conductivity with increase of temperature. But at temperatures above 1500 K, the ionic conductivity reaches a saturated value irrespective of doping concentration. Similarly, Hohnke *et al.* [92] emphasized that an electrical transport occurs by thermally activated hopping of oxygen ions via empty anion sites which reaches a maximum at $x \sim 0.07$ for $(\text{Th},\text{D})\text{O}_{2-x}$ (D=trivalent cation doping) regardless of dopant size and charge (below 1673 K). These results clearly indicate that the mechanism involved for high ionic conductivity above 2000 K is fundamentally different from thermally activated oxygen hopping mechanism purely mediated by vacancies occurring at lower temperatures.

(b) Computational Studies

There are a few theoretical studies describing the electronic structure and superionic behavior of ThO_2 to which we draw attention. For example, Mo *et al.* [93] calculated the electronic structure and frequency dependent dielectric constant of ThO_2 , UO_2 and $(\text{Th},\text{U})\text{O}_2$ utilizing the Heyd-Scuseria-Ernzerhof method (HSE) using a screened hybrid density functional. The HSE calculated structural properties and the electronic band-gap correctly reproduced the experimental band-gap. Martin *et al.* [94] used molecular dynamics simulations to investigate the thermal expansion, oxygen diffusion, and heat capacity of pure thoria and uranium doped (1-10%) thoria between 1500 K and 3600 K. The MD calculated diffusion coefficients of ThO_2 showed increase above 3000 K, due to superionic conductivity. Williams *et al.* [95] calculated the effect of grain boundaries ($\Sigma 3$, $\Sigma 5$, $\Sigma 9$, $\Sigma 11$ and $\Sigma 19$) on oxygen diffusion also using molecular dynamics simulation in UO_2 . They showed higher oxygen diffusion near the grain boundaries compared to that in bulk UO_2 . They also found that oxygen diffusion is enhanced at all boundaries and in the adjacent regions with a strong dependence on temperature and the local structure. Finally, Potashnikov *et al.* [96] performed comprehensive analysis using MD simulations to study anion self diffusion in UO_2 . This study considered 10 interatomic potentials to calculate the diffusion coefficient, superionic transition temperature and defect formation energies within the standard MD simulations framework.

There are no computational study to determine transformation pathway from normal \rightarrow superionic phase in ThO_2 . Moreover, no previous theoretical study describes anion transport mechanism in superionic phase and correlation of phonon modes in the evolution of superionic phase.

2.1.4 Melting Behavior of (Th,U)O₂ and (Th,Pu)O₂ MOX

In the past decade, there has been a renewal of interest in studying the feasibility of thorium-based fuel as a potential advanced fuel for Generation IV nuclear energy systems producing fewer minor actinides than in uranium-based fuel [3–5]. Therefore, considerable attention is being devoted to develop, for example, the thorium molten salt reactor (MSR), (Th,U)O₂ or (Th,Pu)O₂ mixed oxide (MOX) fuel for conventional pressurized water reactors (PWR) and advanced heavy water reactors (AHWR), as well as the thorium fueled accelerator driven sub-critical reactor (ADSR). The AHWR system, fueled by (Th,U)O₂ or (Th,Pu)O₂ MOX, is being actively pursued in India and other countries as a viable route to utilize the vast thorium reserves.

AHWR fuel element cluster consist of three concentric rings around a central rod and each fuel pin contains fuel pellets in Zircaloy-2 clad tubes. The fuel in the two inner rings of an AHWR fuel cluster contains UO₂ in ThO₂ where the UO₂ is mainly ²³³U. The uranium percentage in the UO₂/ThO₂ fuel is 3% UO₂ in ThO₂ in the inner ring and 3.75% UO₂ in ThO₂ in the middle ring. The outer ring contains PuO₂ in ThO₂ in two axial zones, 4.0% PuO₂ in the bottom half of the cluster and 2.5% PuO₂ in the top half of the cluster [5]. The radial and axial variation of fissile loading controls the power/critical heat flux ratio, a standard design parameter that is even more important in this design due to the use of natural circulation cooling of the reactor core at full power. In these reactor fuels, ThO₂ based MOX is considered as ²³²Th is not itself fissile and upon absorbing a neutron in the reactor environment will transmute to ²³³U [5], which is an excellent fissile fuel material. Therefore, ²³²ThO₂ fuels need a fissile material as a ‘driver, such as ²³⁵U or ²³⁹Pu, to initiate the fission required to convert ²³²Th to fissile ²³³U so that a chain reaction can be maintained.

Moreover, AHWR with low enriched uranium (AHWR-LEU) has a significantly lower requirement of mined uranium per unit energy produced as compared to most of the current generation thermal reactors. AHWR-LEU incorporates a number of passive safety features and is associated with a fuel cycle having reduced environmental impact. The advantages of this concept shall be effective utilization of fissile material, no shielding requirement during fabrication, lesser cost of fuel, minimization of waste and reduced safety concerns (proliferation risks). The proposed AHWR-LEU fuel element cluster has the same construction as the AHWR but the fuel composition is entirely different. The composition of the fuel is (Th,U)O₂ with U enriched upto 19.75% of ²³⁵U. The uranium percentage in the UO₂/ThO₂

fuel is different in each of the three rings, upto 18% UO_2 in ThO_2 in the inner ring, up to 22% UO_2 in ThO_2 in the middle ring, and up to 22.5% in the outer ring [97]. Therefore, uranium percentage in $(\text{Th,U})\text{O}_2$ MOX fuel of $< 25\%$ is of practical interest from AHWR and AHWR-LEU fuel.

The melting behavior of actinide oxides and their MOX is a fundamental property of a nuclear material related to its thermodynamical and structural stability. The melting temperature is also an important engineering parameter for nuclear fuel design and safety assessment, as it defines operational limits of nuclear fuel (for both UO_2 and ThO_2 based) in its application environment [3–5]. The onset of melting at the centerline of the fuel rod has been widely accepted as an upper limit to the allowable thermal rating of a nuclear fuel element [3–5]. The melting point (MP) must be taken into account when designing a new fuel, as it limits the power that can be extracted from the fuel element. Knowledge of the melting point is also important for the fabrication of chemically homogeneous fuel pellets of MOX (such as $(\text{Th,U})\text{O}_2$ and $(\text{Th,Pu})\text{O}_2$) since ThO_2 and UO_2 have high melting points of 3663 K and 3100 K, respectively, and relatively low diffusion coefficients at normal sintering temperatures [4]. Thorium dioxide exists up to its melting point as a single cubic fluorite phase, isomorphous, and completely miscible with UO_2 and PuO_2 . Moreover, the melting points of the nuclear fuels are depreciated by factors such as; stoichiometry and composition, irradiation dose, impurities and their concentrations.

(a) Experimental Studies

In order to understand the thermo-physical behavior of thoria based MOX fuels under reactor operation conditions, subject to irradiation, and to predict their performance under accidental conditions, thermodynamic quantities such as, melting temperatures, enthalpy and densities of those solids as well as their liquid phases need to be evaluated. Moreover, determination of these thermodynamic properties for $(\text{Th,Pu})\text{O}_2$ MOX by experiment is very difficult due to the radioactivity and toxicity of PuO_2 based systems, which require extensive and expensive safety precautions [3–5]. As a result, the number of studies addressing these thermodynamic quantities for PuO_2 and $(\text{Th,Pu})\text{O}_2$ MOX is small. During the last four decades, even though melting temperatures and high temperature thermodynamic quantities for ThO_2 and UO_2 have been widely investigated by various experimental techniques, melting behaviors of PuO_2 , $(\text{Th,U})\text{O}_2$ and $(\text{Th,Pu})\text{O}_2$ MOX are much less in evidence [90, 98–123]. Important thermodynamic quantities such as density and enthalpy increment of both solid and liquid phase as well as heat of

fusion are only available for pure UO_2 [116, 118, 119]. For ThO_2 , these thermodynamic quantities for the solid phase are available only over a limited temperature range [90, 113–115, 117] and no data is available for the liquid phase. Recently, Böhler *et al.* [102] and Bruycker *et al.* [112] determined melting temperatures of PuO_2 using a laser heating method and pyrometry. Valu *et al.* [124] determined enthalpy increments of $\text{Th}_{1-x}\text{Pu}_x\text{O}_2$ (for $x = 0, 0.03, 0.08, 0.30, 0.54, 0.85$ and 1) using drop calorimetry in the temperature range 476 K to 1790 K. Still, high temperature enthalpy and density values of solid PuO_2 , $(\text{Th,Pu})\text{O}_2$ and $(\text{Th,U})\text{O}_2$ MOX as well as their respective liquid phases are not available.

(b) Computational Studies

No previous computational study is available to determine melting temperatures of $(\text{Th,Pu})\text{O}_2$ and $(\text{Th,U})\text{O}_2$ MOX across the composition range. Martin *et al.* [94] used molecular dynamics (MD) simulations to investigate the thermal expansion, oxygen diffusion and heat capacity of pure thoria and uranium doped (1-10%) thoria between 1500 K and 3600 K. Using MD simulation, Cooper *et al.* [125] determined thermal expansion coefficient, enthalpy and specific heats of $(\text{U}_x,\text{Th}_{1-x})\text{O}_2$ ($x = 0, 0.25, 0.50, 0.75$ and 1.0) MOX between 300 and 3600 K. These studies have not compared their MD calculated values thoroughly with available experimental values and they have not extended their study for the liquid phase. Moreover, these studies have not considered variation of density for solid and liquid phases of $(\text{Th,Pu})\text{O}_2$ and $(\text{Th,U})\text{O}_2$ MOX across the composition range.

2.2 Thermal Properties of ThO_2 based MOX

2.2.1 Experimental Studies

In view of reactor fuel property evaluation, during the last three decades, thermal properties (thermal expansion and thermal conductivity) of ThO_2 and $(\text{Th,U})\text{O}_2$ MOX have been studied widely [6, 126–136] and a summary of literature information on thermal expansion and thermal conductivity measurements about the compounds investigated, methods of measurement/analysis and the temperature range of investigation are given in Table 2.1.

(a) $(\text{Th,U})\text{O}_2$ MOX

The literature data on thermal expansion shows $\text{Th}_{1-x}\text{U}_x\text{O}_2$ MOX with $x <$

0.06 has been well studied by Tyagi *et al.* [127, 128] and for $0.25 > x > 0.06$ range very few studies have been attempted. Among these, Momin *et al.* [130] reported lower CTE of $7.1 \times 10^{-6} \text{ K}^{-1}$ for $\text{Th}_{0.8}\text{U}_{0.2}\text{O}_2$ compared to $9.5 \times 10^{-6} \text{ K}^{-1}$ for ThO_2 in 298-1600 K temperature range. On the contrary, Rodriguez *et al.* [131] reported CTE of $12.5 \times 10^{-6} \text{ K}^{-1}$ for $\text{Th}_{0.8}\text{U}_{0.2}\text{O}_2$ in 1100-2400 K temperature range. Therefore, considerable scatter in CTE value exists which can be attributed to different methods of preparation of samples which ultimately lead to samples of different stoichiometry and impurity contents. Moreover, the scattering in reported thermal conductivity values of (Th,U) O_2 MOX exists in the same composition and temperature range. In most of the studies, thermal conductivity values are reported for different density of pellets and no impurity content evaluation were performed. So, it is difficult to comprehend the source of discrepancy of thermal expansion and thermal conductivity data for these samples unless the above parameters are known. Hence, it is imperative for fuel designer to measure the thermal expansion of the samples prepared by their own methods. One of the primary goal of this study is to generate thermal expansion data for (Th,U) O_2 MOX in a range which is of interest from AHWR and AHWR-LEU fuel composition.

(b) (Th,Pu) O_2 MOX

Determination of thermal properties of (Th,Pu) O_2 MOX by experimental means is very difficult due to associated radiotoxicity, high specific activity and proliferation risk of PuO_2 based systems and require extensive and expensive safety precautions [4, 6, 137, 138]. As a result, the number of experimental studies addressing the thermal and melting properties of (Th,Pu) O_2 MOX is limited.

However, PuO_2 is emulated by CeO_2 in many laboratory scale experiments on (Th,Pu) O_2 as CeO_2 and PuO_2 have quite similar physico-chemical properties, namely, ionic size in octahedral and cubic coordinations, melting point, standard enthalpy of formation and specific heat [6, 138]. Hubert *et al.* [139] suggested that ThO_2 and PuO_2 form an ideal solid-solution in the entire composition range. Mathews *et al.* [140, 141] and Tyagi *et al.* [127] determined thermal expansion of $\text{Th}_{1-x}\text{Ce}_x\text{O}_2$ ($x=0, 0.04, 0.08, 0.1, 0.2, 0.3, 0.4, 0.5, 0.6, 0.7, 0.8, 0.9, 1.0$) MOX using dilatometry and high temperature X-ray diffraction (HT-XRD) techniques; whereas only Cozzo *et al.* [142] determined thermal diffusivity and conductivity of $\text{Th}_{1-x}\text{Pu}_x\text{O}_2$ MOX ($x = 0.0, 0.03, 0.08, 0.3$ and 1.0) over a temperature range between 500 K and 1600 K. Basak *et al.* [134] determined thermal conductivity of ThO_2 -4wt.% PuO_2 MOX over a temperature range between 923-1773 K.

Table 2.1: Summary of literature data on thermal expansion coefficient and thermal conductivity of ThO₂ and (Th,U)O₂ MOX

UO ₂ composition (in wt.%)	Temperature Range (K)	Thermal Expansion Coefficient (10 ⁻⁶ K ⁻⁶)	Remarks
0, 4, 10, 20	293-1773	-	Dilatometry, Kutty <i>et al.</i> [126] (2008)
0, 2, 4, 6	293-1623	9.67, 9.82, 10.09, 10.37	HT XRD, Tyagi <i>et al.</i> [127] (2004)
0, 2	298-1473	9.58, 9.74	HT XRD, Tyagi <i>et al.</i> [128] (2000)
13, 55, 91	298-1973	10.33, 10.83, 11.45	HT-XRD, Anthonysamy <i>et al.</i> [129] (2000)
0, 20	298-1600	9.5, 7.1	HT-XRD, Momin <i>et al.</i> [130] (1991)
0	293-2273	9.67	Rodriguez <i>et al.</i> [131] (1981) review
20	1100-2400	12.5	Rodriguez <i>et al.</i> [131] (1981) review
UO ₂ composition (in wt.%)	Temperature Range (K)	Thermal Conductivity reported for % of theoretical density	Remarks
4, 10, 20	298-1500	95	Kutty <i>et al.</i> [126] (2008)
12	573-1573	82.2	Ronchi <i>et al.</i> [136] (2003)
2	300-1200	Unknown	Pillai <i>et al.</i> [132] (2000)
<20	273-1073	-	Bakker <i>et al.</i> [6] (1997) review
<30	273-2200	-	Konings <i>et al.</i> [133] (1995) review
2	800-2100	100	Basak <i>et al.</i> [134] (1989)
0, 20, 100	773-1773	-	Rodriguez <i>et al.</i> [131](1981) review

2.2.2 Computational Studies

Theoretical studies on thermal properties of (Th,Pu)O₂ and (Th,Ce)O₂ MOX have been scantily reported. Xiao *et al.* [143] calculated thermodynamics and thermal properties of Th_{1-x}Ce_xO₂ MOX using first principles based calculations with projector augmented wave (PAW) pseudopotential formalism for x = 0.0, 0.25, 0.50, 0.75 and 1.0. The choice of these higher MOX compositions in the first principles based calculations came mainly due to limitation on the maximum supercell size and hence available computational resources.

Over the last few decades there have been continuous effort to determine thermal, thermo-mechanical, diffusion properties and their change due to irradiations for UO₂ based fuels using molecular dynamics (MD) simulations employing classical pair potentials [144–146]. On the other hand, very few studies attempted to study similar properties for ThO₂ based fuels. Initially, Martin *et al.* [94] used molecular dynamics simulations to investigate the thermal expansion, oxygen diffusion, and heat capacity of pure thoria and uranium doped (1-10%) thoria between 1500 K and 3600 K. The MD calculated diffusion coefficients of ThO₂ showed increase

above 3000 K, due to superionic conductivity. Behera *et al.* [147] developed several ThO₂ interatomic potential of the functional form Buckingham and Buckingham-Morse to study cohesive energy, elastic properties and surface energies of ThO₂. Later on, Cooper *et al.* [125, 148] developed an interatomic potentials for AcO₂ (Ac=Am,Ce,Cm,Np,Th,Pu and U) by adopting a Buckingham-Morse-Many-body functional form. This potential is capable of reproducing a range of thermo-physical properties (lattice parameter, bulk modulus, enthalpy and specific heat) between 300 and 3000 K. Cooper *et al.* [125] also developed an interatomic potential for (Th,U)O₂ MOX and using molecular dynamics, the thermo-physical properties of the (U_x,Th_{1-x})O₂ (x= 0, 0.25, 0.50, 0.75 and 1.0) system have been investigated between 300 and 3600 K. The thermal dependence of lattice parameter, linear thermal expansion coefficient, enthalpy and specific heat at constant pressure is explained in terms of defect formation and diffusivity on the oxygen sublattice.

The mechanical and thermal properties at these high concentrations of MOX calculated from ab-initio and/or MD simulations are of little use for the design of AHWR fuel where compositions of $x < 0.08$ are of practical interest. Therefore, additional work is required to determine thermal properties of (Th,Ce)O₂, (Th,Pu)O₂ and (Th,U)O₂ MOX in a composition range of interest and wide temperature range followed by through experimental validation. Under this scenario, the MD simulation technique is a powerful tool to evaluate thermal properties of MOX in the desired composition range as well as in the high temperature regime which is not easily accessible to experimental techniques.

Chapter 3

Theoretical Methodologies

3.1 Introduction

Over the last few decades there has been a significant increase in the usage of computational methods within the scientific community for the basic and advanced research. With rapidly growing computational processing power and continuing development of basic algorithms, atomic scale modeling has become a valuable tool to provide a useful insight into the behavior of atoms on spatial and temporal scales often inaccessible to traditional experimental investigations.

Atomistic simulations can, broadly, be divided into two categories, quantum mechanical calculations and classical mechanical calculations with empirically derived potential set. In quantum mechanical simulations (often referred to as *ab-initio*) many-body Schrödinger equation is solved. Solution of the Schrödinger equation gives a large quantity of the information related to electronic structure of the system. For the simplest cases *ab-initio* calculations are considered to be exact but various approximations needs to be adopted while studying larger systems to make the calculations tractable. Early quantum mechanical calculations were limited to simple system like H_2^+ or He atom. Despite consideration of empirical approximations, significant computational resources are required even for these simple system. The advent of Density Functional Theory (DFT) has expanded the scope of *ab-initio* simulations to include complex molecular systems and condensed matter.

The second category of atomistic simulation may be characterized as a method of “particle tracking”. Operationally, it is a method for generating the trajectories of a system of N particles by direct numerical integration of Newton’s equations of motion, with appropriate specification of an interatomic potential and

suitable initial and boundary conditions. This is an atomistic modeling and simulation method when the particles in question are the atoms that constitute the material of interest. The underlying assumption is that one can treat the ions and electrons as a single, classical entity and they do not yield information about electronic structures. Despite this apparent limitation, classical “particle tracking” simulations can be extremely useful for predicting phase stability, phase transformations, thermo-physical and thermo-mechanical properties. Compared to *ab-initio* calculations, the “particle tracking” method employing pair potentials requires significantly less computational power and can easily be applied to much larger aggregate of atoms (in some cases million of atoms).

In the subsequent sections, theoretical foundations and computational methodologies related to atomistic simulations are described.

3.2 Electronic Structure Theory

The state of any quantum-mechanical system is described by a mathematical object $\Psi(\mathbf{r},\sigma)$ (wave function) in the configurational space of all independent variables that describes the system. The wave function is not an observable itself but $|\Psi(\mathbf{r},\sigma)|^2 d^3\mathbf{r}$ gives the probability of finding the state at position, \mathbf{r} , with spin, σ , in an elementary volume $d^3\mathbf{r}$ in real space. The time evolution of the wave function is given by the Schrödinger equation

$$-i\hbar\frac{\partial\Psi}{\partial t} = \hat{H}\Psi \quad (3.1)$$

where \hat{H} is a mathematical operator called Hamiltonian. For a system of interacting nuclei and electrons, Hamiltonian operator is consisting of sum of kinetic energy operator \hat{K} due to the motion of electrons and nuclei and potential energy operator (\hat{V}) arising from interactions between nuclei-nuclei, nuclei-electron and electron-electron, represented as:

$$\hat{H} = \hat{K}_{electrons} + \hat{K}_{nuclei} + \hat{V}_{electron-electron} + \hat{V}_{nuclei-nuclei} + \hat{V}_{nuclei-electron} \quad (3.2)$$

$$\hat{H} = -\frac{\hbar^2}{2m} \sum_i \nabla_{r_i}^2 - \frac{\hbar^2}{2} \sum_I \frac{1}{M_I} \nabla_{R_I}^2 + \hat{V}(\mathbf{r}, \mathbf{R}), \quad (3.3)$$

where $\mathbf{r} = (\mathbf{r}_1, \mathbf{r}_2, \mathbf{r}_3, \dots)$ and $\mathbf{R} = (\mathbf{R}_1, \mathbf{R}_2, \mathbf{R}_3, \dots)$ are the positions of the electrons and nuclei, respectively.

$$\hat{V}(\mathbf{r}, \mathbf{R}) = \sum_{i < j} \frac{e^2}{|\mathbf{r}_i - \mathbf{r}_j|} + \sum_{I < J} \frac{Z_I Z_J e^2}{|\mathbf{R}_I - \mathbf{R}_J|} - \sum_{i, I} \frac{Z_I e^2}{|\mathbf{r}_i - \mathbf{R}_I|} \quad (3.4)$$

describes the Coulomb interactions between nuclei and electrons. Among the solutions of eq.(3.1) we are mainly interested in the stationary states, in which some observables of the physical system, *e.g.*, total energy, have well defined and constant values. Such solutions are provided by a time independent Hamiltonian like eq.(3.2) and the problem is simplified, consequently, to a time independent Schrödinger equation of the form

$$\hat{H}\Psi = E\Psi \quad (3.5)$$

Solving the above eq.(3.5) for a large number of interacting nuclei-electron system is a daunting task. The aim of the physical theory is to provide us with basic approximations, which are both solvable and accurate. In the first simplification one makes use of the fact that the mass of a nucleus M_I is much larger than the mass of an electron m and as a result, the motion of the nuclei is much slower than that of electrons. Thus, one can consider the positions of the nuclei as fixed and account only for the electron degrees of freedom. This is known as the **Born-Oppenheimer approximation** and the wave function of electrons moving in the external field of fixed nuclei is described by the following equation

$$\left(-\frac{\hbar^2}{2m} \sum_i \nabla_{\mathbf{r}_i}^2 + \hat{V}_{ee} + \hat{V}_{ext}(\mathbf{R})\right)\Psi_{\mathbf{R}}(\mathbf{r}) = E(\mathbf{R})\Psi_{\mathbf{R}}(\mathbf{r}) \quad (3.6)$$

for fixed nuclear positions both the energy and wave functions of electrons depend on, \hat{V}_{ee} , the Coulomb interaction between electrons and \hat{V}_{ext} , the Coulomb interaction between electrons and fixed nuclei. Equation (3.6) is an eigen value problem and solution of this equation gives both $\Psi_{\mathbf{R}}(\mathbf{r})$ and $E(\mathbf{R})$. For the Hamiltonian, $\Psi_{\mathbf{R}}(\mathbf{r})$ is the electronic wave function, which is a function of each of the spatial coordinates of each of the N electrons, so $\Psi_{\mathbf{R}}(\mathbf{r}) = \Psi_{\mathbf{R}}(\mathbf{r}_1, \mathbf{r}_2, \dots, \mathbf{r}_N)$ and E is the ground-state energy of the electrons. In principle, this equation is exactly solvable analytically with desired accuracy using *Configuration Interaction or Quantum Monte-Carlo*. However, in reality, only system with small number of interacting electrons (*e.g.*, small molecules and clusters) can be treated with this method.

Equation (3.6) suggests that the electronic wave-functions belong to a $3N$ dimensional space, *i.e.*, $\Psi \in \mathbb{R}^{3N}$. To get an order of magnitude estimate of this complexity, consider a material system with 100 electrons and consider a discretization of the real line, \mathbb{R} , with just 100 points. Electronic structure calculation of this

system, which involves solving the eigenvalue problem given by eq. (3.6), requires the computation of eigenvalues and eigenfunctions of an astronomical $100^{300} \times 100^{300}$ matrix. This translates into a computational complexity that is so huge, that it makes the computation of materials properties using quantum mechanics infeasible.

The situation looks even worse when we look again at the Hamiltonian, \hat{H} . The term in the Hamiltonian defining electron-electron interactions is the most critical one from the point of view of solving the equation. The form of this contribution means that the individual electron wave function cannot be found without simultaneously considering the individual electron wave functions associated with all the other electrons. In other words, the Schrödinger equation is a many-body problem.

The only plausible way is to somehow replace the many electron problem to an effective one-electron problem by introducing one-electron approximation, which assumes the electrons to move in the mean field of other electrons and ions. Historically, the first such self-consistent field approximation was the Hartree-Fock theory which treats parallel spin electron exchange interaction exactly (via a determinantal wave function), but completely neglects the other (*i.e.*, anti-parallel spin) electrostatic contribution due to Coulomb correlation. The various approximate methods developed over more than 5 decades constitute the theories of electronic structure [149]. The most popular among them is density-functional theory, which is discussed below.

3.2.1 Density Functional Theory (DFT)

The utilization of the electron density as a central quantity and hence the formulation of the many-particle problem within a single-particle framework is the essence of the DFT. Thus, the major statement of the DFT is that the exchange-correlation energy can be expressed solely in terms of the electron density $\rho(r)$. Thus, the many-body physical system is described by a physical object, the electron density in the real 3-dimensional space, instead of an abstract multi-variable mathematical object, the wave function. Hohenberg and Kohn have shown that such a description is exact for the ground state and they developed an exact formal variational principle for the ground-state energy, in which the electron density $\rho(\mathbf{r})$ is the variable function.

According to the postulates of quantum mechanics, the expectation value of

the *energy* E of the many-body system for an arbitrary state is calculated as

$$\begin{aligned}
E &= \langle \Psi | \hat{H} | \Psi \rangle \\
&= \sum_i \int \left(\prod_i dr_i \right) \Psi^*(\mathbf{r}) \left(-\frac{\hbar^2}{2m} \nabla_{r_i}^2 + \frac{1}{2} \sum_{j \neq i} \frac{e^2}{|\mathbf{r}_i - \mathbf{r}_j|} - \sum_I \frac{Z_I e^2}{|\mathbf{r}_i - \mathbf{R}_I|} \right) \Psi(\mathbf{r})
\end{aligned} \tag{3.7}$$

Since the electrons are indistinguishable particles, the summation in eq. (3.7) can be performed and the above expression can be represented by distribution functions

$$\begin{aligned}
E &= E[\rho(\mathbf{r}), \rho_{12}(\mathbf{r}, \mathbf{r}')] \\
&= -\frac{\hbar^2}{2m} \int d\mathbf{r} [\nabla^2 \rho_{12}(\mathbf{r}, \mathbf{r}')]_{r'=r} + \frac{e^2}{2} \int d\mathbf{r} \frac{\rho_{12}(\mathbf{r}, \mathbf{r}')}{|\mathbf{r} - \mathbf{r}'|} d\mathbf{r}' + \int d\mathbf{r} \rho(\mathbf{r}) U(r)
\end{aligned} \tag{3.8}$$

Thus, the total energy of the many-electron system is a functional of one-electron density $\rho(\mathbf{r})$

$$\rho(\mathbf{r}) = N \int \left(\prod_{i=2}^N d\mathbf{r}_i \right) |\Psi(\mathbf{r}, \dots, \mathbf{r}_i, \dots, \mathbf{r}_N)|^2, \tag{3.9}$$

and two-particle density $\rho_{12}(\mathbf{r}, \mathbf{r}')$

$$\rho_{12}(\mathbf{r}, \mathbf{r}') = N(N-1) \int \left(\prod_{i=3}^N d\mathbf{r}_i \right) |\Psi(\mathbf{r}, \mathbf{r}', \dots, \mathbf{r}_i, \dots, \mathbf{r}_N)|^2. \tag{3.10}$$

The two-particle density eq.(3.10) represents interaction between electrons and makes difficult to solve eq.(3.6) exactly. Equation (3.6) can also be represented as

$$\begin{aligned}
\hat{H} &= \sum_i H_i + \frac{1}{2} \sum_{i < j} \frac{e^2}{|\mathbf{r}_i - \mathbf{r}_j|} \\
H_i &= -\frac{\hbar^2}{2m} \nabla_i^2 + V(\mathbf{r}_i)
\end{aligned} \tag{3.11}$$

where H_i is the Hamiltonian of a single electron interacting with all nuclei. If we neglect electron-electron interactions then we are dealing with single electron problem

$$\begin{aligned}
\hat{H} &= \sum_i H_i, & \hat{H}_i \psi_i &= E_i \psi_i, \\
E &= \sum_i E_i, & \Psi(\mathbf{r}) &= \prod_i \psi_i(\mathbf{r}_i),
\end{aligned} \tag{3.12}$$

and the two-particle density would become product of one-electron densities

$$\rho_{12}(\mathbf{r}, \mathbf{r}') = \rho(\mathbf{r})\rho(\mathbf{r}'). \quad (3.13)$$

Totally omitting electron-electron interaction is grossly incorrect, however, electron-electron electrostatic repulsion can be incorporated within one-electron approximation. In this picture, electron-electron interaction is replaced with one-electron effective potential where one given electron is moving in the average field generated by rest of the electrons, *i.e.*,

$$\hat{H} = \sum_i (H_i + V_{eff}(\mathbf{r}_i)) = \sum_i \mathbf{H}'_i. \quad (3.14)$$

This idea essentially leads to the *Hartree* approximation and the energy of a many-body system becomes a functional of only one electron density

$$E_H[\rho(\mathbf{r})] = -\frac{\hbar^2}{2m} \int d\mathbf{r} \left[\nabla^2 \rho_{12}(\mathbf{r}, \mathbf{r}') \right]_{r'=r} + \frac{e^2}{2} \int d\mathbf{r} \frac{\rho(\mathbf{r})\rho(\mathbf{r}')}{|\mathbf{r} - \mathbf{r}'|} d\mathbf{r}' + \int d\mathbf{r} \rho(\mathbf{r})U(\mathbf{r}). \quad (3.15)$$

In this approximation the electron-electron interaction energy would be overestimated for three reasons: **(a)** Owing to the *Pauli exclusion principle* the electrons are kept out of each other's way. This leads to the lowering of electron-electron interaction energy by the so-called exchange energy **(b)** Mutual electrostatic repulsion of electrons also keep the electrons apart. This repulsion, termed as the correlation energy, further lowers the electron-electron interaction energy **(c)** Interaction of an electron with itself is also included in $E_H[\rho(\mathbf{r})]$ which needs to be excluded. The sum of the corrections that need to be added to the Hartree energy to correctly define electron-electron interaction energy is called the “**exchange and correlation energy**” [150]. It is also important to note that electrons are having quantum spin character and as fermions obey *Pauli exclusion principle*. According to this exclusion principle, two electrons can not be in the same quantum state and consequently two electron having same spin can not be found at the same place. Therefore, many-body wave function must satisfy *exchange symmetry*.

The electron correlation means that

$$\rho_{12}(\mathbf{r}, \mathbf{r}') \neq \rho(\mathbf{r})\rho(\mathbf{r}'). \quad (3.16)$$

Further understanding of correlation can be obtained by introduction of correlation

function $h(\mathbf{r}, \mathbf{r}')$ as

$$\rho_{12}(\mathbf{r}, \mathbf{r}') = \rho(\mathbf{r})\rho(\mathbf{r}') [1 + h(\mathbf{r}, \mathbf{r}')]. \quad (3.17)$$

By integration of eq. (3.17) and (3.10) gives

$$\begin{aligned} \int d\mathbf{r}' \rho_{12}(\mathbf{r}, \mathbf{r}') &= \left(N + \int d\mathbf{r}' \rho(\mathbf{r}') h(\mathbf{r}, \mathbf{r}') \right) \rho(\mathbf{r}) = (N - 1) \rho(\mathbf{r}) \\ \text{where} \quad \int d\mathbf{r}' \rho(\mathbf{r}') h(\mathbf{r}, \mathbf{r}') &= -1. \end{aligned} \quad (3.18)$$

By defining *exchange-correlation* hole as

$$\rho_{xc}(\mathbf{r}, \mathbf{r}') = \rho(\mathbf{r}') h(\mathbf{r}, \mathbf{r}') \quad (3.19)$$

the energy of the many-electron system can be written as

$$\begin{aligned} E[\rho(\mathbf{r})] &= -\frac{\hbar^2}{2m} \int d\mathbf{r} \left[\nabla^2 \rho_{12}(\mathbf{r}, \mathbf{r}') \right]_{r'=r} + \frac{e^2}{2} \int d\mathbf{r} \frac{\rho(\mathbf{r})\rho(\mathbf{r}')}{|\mathbf{r} - \mathbf{r}'|} d\mathbf{r}' + \\ &\frac{e^2}{2} \int d\mathbf{r} \frac{\rho(\mathbf{r})\rho_{xc}(\mathbf{r}, \mathbf{r}')}{|\mathbf{r} - \mathbf{r}'|} d\mathbf{r}' + \int d\mathbf{r} \rho(\mathbf{r}) U(\mathbf{r}). \end{aligned} \quad (3.20)$$

It is observed that the electron correlation due to exchange symmetry and instantaneous interactions between the electrons gives rise to a non-local distribution of exchange-correlation holes and lowers the energy of the system by reducing the contribution of Coulomb repulsion.

Let's consider the many-body system described by 3.6, which is a collection of N electrons moving under the influence of an external potential $U(\mathbf{r})$ and the mutual Coulomb repulsion. The DFT of Hohenberg, Kohn, and Sham [151, 152], which represents the ground-state energy of the material system in terms of the ground state electron-density $\rho_0(\mathbf{r})$, described as

$$\rho_0(\mathbf{r}) = N \int \left(\prod_{i=2}^N d\mathbf{r}_i \right) |\Psi_0(\mathbf{r}, \dots, \mathbf{r}_i, \dots, \mathbf{r}_N)|^2. \quad (3.21)$$

The basic theorems which are the pillars of the DFT were formulated by Hohenberg and Kohn can be summarized as follows:

(a) **Theorem 1:** For a non degenerate ground state, Ψ_0 , the external potential $U(\mathbf{r})$ is uniquely determined (to within an additive constant) by the density distribution $\rho_0(\mathbf{r})$.

Let's consider the many-body system described by (3.6), which is a collection of N electrons moving under the influence of an external potential $U(\mathbf{r})$ and the mutual Coulomb repulsion. We denote the electronic density in the ground state Ψ_0 by equation (3.21) which is clearly a functional of $U(\mathbf{r})$. Conversely $U(\mathbf{r})$ is a unique functional of $\rho_0(\mathbf{r})$, apart from a trivial additive constant.

A straightforward corollary of the above statement is that the ground-state energy E_0 is also uniquely determined by the ground-state charge density or, in mathematical terms, E_0 is a functional of $\rho_0(\mathbf{r})$

$$E_0[\rho_0(\mathbf{r})] = \langle \Psi_0 | \hat{H} | \Psi_0 \rangle = F[\rho_0(\mathbf{r})] + \int d\mathbf{r} \rho_0(\mathbf{r}) U(\mathbf{r}), \quad (3.22)$$

where $F[\rho_0(\mathbf{r})] = \langle \Psi_0 | \hat{T} + \hat{V}_{ee} | \Psi_0 \rangle$

is a *universal* functional of the charge density $\rho_0(\mathbf{r})$, valid for any *many-body* system. As $F[\rho_0(\mathbf{r})]$ does not depend on the external potential and therefore it is a universal functional.

(b) **Theorem 2:** For a given $U(\mathbf{r})$, the correct $\rho_0(\mathbf{r})$ minimizes the (nodedegenerate) ground state energy, which is unique functional of $\rho_0(\mathbf{r})$

In other words, the true ground state density is the density that minimizes $E[\rho]$, and that the other ground state properties are also functional of the ground state density, with the constraint

$$\int d\mathbf{r} \rho_0(\mathbf{r}) = N \quad (3.23)$$

It is well known for a system of N particles, the energy functional of Ψ

$$E[\Psi] = \langle \Psi | \hat{U}(\mathbf{r}) | \Psi \rangle + \langle \Psi | \hat{T} + \hat{V}_{ee} | \Psi \rangle \quad (3.24)$$

has a minimum at the correct ground state Ψ_0 , relative to arbitrary variations of Ψ in which the number of particles is kept constant. In particular, let Ψ be the ground state associated with a different external potential $U'(\mathbf{r})$. Then by eq. (3.24) and (3.22)

$$E[\Psi] = F[\rho(\mathbf{r})] + \int d\mathbf{r} \rho(\mathbf{r}) U(\mathbf{r}) > F[\rho_0(\mathbf{r})] + \int d\mathbf{r} \rho_0(\mathbf{r}) U(\mathbf{r}) = E[\Psi_0] \quad (3.25)$$

Thus the minimal property of eq. (3.22) is established relative to all density functions $\rho(\mathbf{r})$ associated with some other external potential $U'(\mathbf{r})$.

The classical Coulomb energy (Hartree term) can be extracted from $F[\rho_0]$

$$F[\rho(\mathbf{r})] = \frac{e^2}{2} \int d\mathbf{r} \frac{\rho(\mathbf{r})\rho(\mathbf{r}')}{|\mathbf{r} - \mathbf{r}'|} d\mathbf{r}' + G[\rho(\mathbf{r})], \quad (3.26)$$

and then the ground-state energy of an interacting inhomogeneous electron gas in a static external potential $U(\mathbf{r})$ can be written as

$$E_0[\rho_0(\mathbf{r})] = \int d\mathbf{r} \rho_0(\mathbf{r}) U(\mathbf{r}) + \frac{e^2}{2} \int d\mathbf{r} \frac{\rho_0(\mathbf{r})\rho_0(\mathbf{r}')}{|\mathbf{r} - \mathbf{r}'|} d\mathbf{r}' + G[\rho_0(\mathbf{r})] \quad (3.27)$$

where $G[\rho(\mathbf{r})]$ is a universal functional of the density. In this way, DFT exactly reduces the N-body problem to the determination of a 3-dimensional function $\rho(\mathbf{r})$, which minimizes the functional $E[\rho(\mathbf{r})]$. However, the functional $G[\rho(\mathbf{r})]$ is not known and an exact expression for $E[\rho(\mathbf{r})]$ is unlikely to be found. At this point we have to make another approximation.

3.2.2 Kohn-Sham equations

Kohn-Sham equations [152] provide an approach for practical implementation of DFT. In this formulation, the system of interacting electrons is mapped on to an auxiliary system of non-interacting electrons having the same ground-state density $\rho_0(\mathbf{r})$. The universal functional can be represented as

$$G[\rho_0(\mathbf{r})] = T_s[\rho_0(\mathbf{r})] + E_{xc}[\rho_0(\mathbf{r})] \quad (3.28)$$

where $T_s[\rho_0(\mathbf{r})]$ and $E_{xc}[\rho_0(\mathbf{r})]$ is the kinetic energy of a system of non-interacting electrons and the exchange-correlation energy of an interacting system with density $\rho_0(\mathbf{r})$, respectively. For a system of non-interacting electrons the ground-state charge density can be represented as a sum over one-electron occupied states, described by wave functions $\psi_{i\sigma}(\mathbf{r})$, called the Kohn-Sham orbitals,

$$\rho_0(\mathbf{r}) = \sum_{i\sigma} |\psi_{i\sigma}(\mathbf{r})|^2. \quad (3.29)$$

Minimizing the total energy under the constraints of orthonormality

$$\int d\mathbf{r} \psi_{i\sigma}^*(\mathbf{r}) \psi_{j\sigma'}(\mathbf{r}) = \delta_{ij} \delta_{\sigma\sigma'} \quad (3.30)$$

for the one-electron orbitals by applying the variational principle to the Kohn-Sham functional, one finds a set of one-electron Schrödinger equation:

$$(H_{KS} - \epsilon_{i\sigma})\psi_{i\sigma}(\mathbf{r}) = 0, \quad (3.31)$$

where *Kohn-Sham Hamiltonian* H_{KS} is defined as

$$H_{KS} = -\frac{\hbar^2}{2m}\nabla^2 + V_{KS}(\mathbf{r}) = -\frac{\hbar^2}{2m}\nabla^2 + V_H(\mathbf{r}) + V_{xc}[\rho_0(\mathbf{r})] + U(\mathbf{r}) \quad (3.32)$$

$$\text{and} \quad V_{xc}[\rho_0(\mathbf{r})] = \frac{\delta E_{xc}[\rho_0(\mathbf{r})]}{\delta \rho_0(\mathbf{r})}$$

The set of the Kohn-Sham equations is a set of self-consistent equations that resemble the conventional Hartree and Hartree-Fock equations, but also include exchange and correlation effects. However, we still do not know the analytical expression for the exchange-correlation functional E_{xc} .

3.2.3 Approximations to Exchange-Correlation functionals

The electron-electron interactions are accounted for by the exchange-correlation functional $E_{xc}[\rho(\mathbf{r})]$. No analytical form of this functional exists and computations rely on approximations, most commonly the local density and generalized gradient density approximations (LDA and GGA, respectively).

In local density approximation (LDA), the material is divided infinitesimally into small volumes, with each volume contributing to the total exchange correlation energy by an amount equal to that of an identical volume filled with a homogeneous electron gas that has the the same density [153]. The exchange-correlation energy functional by this method for the homogeneous electron gas is given by, The exchange-correlation functional can be written in terms of exchange-correlation energy density ($\epsilon_{xc}[\rho(\mathbf{r})]$) as

$$E_{xc}^{LDA}[\rho(\mathbf{r})] = \int d\mathbf{r} \epsilon_{xc}^{LDA}[\rho(\mathbf{r})]\rho(\mathbf{r}) \quad (3.33)$$

where $\epsilon_{xc}^{LDA}(\rho(r))$ is the exchange-correlation energy per electron in a uniform electron gas of density ρ . For a homogeneous gas of electrons the charge density $\rho(\mathbf{r})$ is constant, but even for this simple system the exact analytical form of $\epsilon_{xc}(\rho(\mathbf{r}))$ is unknown. However, numerical results from Monte-Carlo calculations by Ceperley and Alder [154] have been parameterized by Perdew and Zunger [155] with a simple

analytical form

$$\epsilon_{xc}[\rho_0(\mathbf{r})] = \begin{cases} -0.4582/r_s - 0.1423/(1 + 1.0529\sqrt{r_s} + 0.3334r_s), & r_s \geq 1 \\ -0.4582/r_s - 0.0480 + 0.0311\ln r_s - 0.0116r_s + 0.0020r_s \ln r_s, & r_s \leq 1 \end{cases} \quad (3.34)$$

where $r_s = (3/4\pi n)^{1/3}$ in atomic units ($e^2 = \hbar = m = 1$).

In Generalized Gradient Approximation (GGA), the exchange-correlation contribution of every infinitesimal volume not only depends on that volume, but also on the density in neighboring volumes. Thus, the gradient in density between different volumes is also taken into account in this approach:

$$E_{xc}^{GGA}[\rho(\mathbf{r})] = \int d\mathbf{r} \epsilon_{xc}^{GGA}[\rho(\mathbf{r}), \nabla\rho(\mathbf{r})] \rho(\mathbf{r}) \quad (3.35)$$

GGA exists in different flavors. The GGA of Perdew and Wang (PW91) [156, 157] is a non-empirical functional based on fitting to a numerical GGA produced by the real-space cutoff procedure. The GGA of Perdew, Burke, and Ernzerhof (PBE) [158] is a non-empirical functional with parameters derived to satisfy a specific set of exact constraints.

3.2.4 DFT+ U and Hybrid Functionals

Transition metal or rare-earth metal ions with partially filled d or f shells usually contain strongly correlated electrons. Because of the orbital-independent potentials in LDA and GGA, they cannot properly describe such systems. For example, LDA predicts transition metal oxides to be metallic with itinerant d electrons because of the partially filled d shells. Instead, these transition metal oxides are Mott insulators and the d electrons are well localized. In order to properly describe these strongly correlated systems, orbital-dependent potentials should be used for d and f electrons. There are several approaches available nowadays to incorporate the strong electron-electron correlations between d electrons and f electrons. Of these methods including the self-interaction correction (SIC) method [159], Hartree-Fock (HF) method [160], GW approximation [161], LDA+ U method [162] and Hybrid DFT method [163, 164] is the most widely used one. In this thesis LDA+ U and Hybrid DFT method is used. So a short description of LDA+ U and Hybrid DFT method is given below.

In the LDA+ U method, the electrons are divided into two classes: delocalized s , p electrons which are well described by LDA (GGA) and localized d or f

electrons for which an orbital-dependent term $\frac{1}{2}U \sum_{i \neq j} n_i n_j$ should be used to describe Coulomb d - d or f - f interaction, where n_i are d - or f -orbital occupancies. The total energy in LDA+U method is given as [162]:

$$E_{tot}^{LDA+U}[\rho_\sigma(\mathbf{r}), \{n_\sigma\}] = E^{LDA}[\rho_\sigma(\mathbf{r})] + E_U[\{n_\sigma\}] - E_{dc}[\{n_\sigma\}] \quad (3.36)$$

where σ denotes the spin index, $\rho_\sigma(r)$ is the electron density for spin- σ electrons and $\{n_\sigma\}$ is the density matrix of d or f electrons for spin- σ , the first term is the standard LDA energy functional, the second term is the electron-electron Coulomb interaction energy given by [162]:

$$E_U[\{n_\sigma\}] = \frac{1}{2} \sum_{\{m\}, \sigma} \{ \langle m, m'' | V_{ee} | m' m'' \rangle n_{mm', \sigma} n_{m'' m'' - \sigma} - (\langle m, m'' | V_{ee} | m' m'' \rangle - \langle m, m'' | V_{ee} | m''', m' \rangle) n_{mm', \sigma} n_{m'' m'' - \sigma} \} \quad (3.37)$$

where m denotes the magnetic quantum number, and V_{ee} are the screened Coulomb interactions among the d or f electrons. The last term in Eq. (3.97) is the double-counting term which removes an averaged LDA energy contribution of these d or f electrons from the LDA energy. It is given by [162]:

$$E_{dc}[\{n_\sigma\}] = \frac{1}{2}UN(N-1) - \frac{1}{2}J[N_\uparrow(N_\uparrow-1) + N_\downarrow(N_\downarrow-1)] \quad (3.38)$$

where $N_\sigma = Tr(n_{mm', \sigma})$ and $N = N_\uparrow + N_\downarrow$. U and J are screened Coulomb and exchange parameters. As a simple approximation, if the exchange and non-sphericity is neglected, Eq. (3.97) is simplified to [162]:

$$E_{tot}^{LDA+U} = E_{LDA} + \frac{1}{2}U \sum_{i \neq j} n_i n_j - \frac{1}{2}UN(N-1) \quad (3.39)$$

The orbital total energies ϵ_i are derivatives of Eq. 3.98 with respect to orbital occupations n_i :

$$n_i = \frac{\delta E}{\delta n_i} = \epsilon_{LDA} + U\left(\frac{1}{2} - n_i\right) \quad (3.40)$$

In this simple consideration, the LDA orbital energies are shifted by $-\frac{U}{2}$ for occupied orbitals ($n_i = 1$) and by $+\frac{U}{2}$ for unoccupied orbitals ($n_i = 0$), resulting in lower and upper Hubbard bands separated by U , which opens a gap at the Fermi energy in transition metal oxides.

In hybrid functionals approach, a portion of the Hartree-Fock non-local exchange E_X^{HF} is mixed with the exchange term taken from standard PBE (E_X^{PBE}).

This is used to generate the unscreened PBE0 functional:

$$E_{XC}^{PBE0} = \alpha E_X^{HF} + (1 - \alpha) E_X^{PBE} + E_C^{PBE} \quad (3.41)$$

Usually α varies between 0 and 1 but previous work by Perdew et al. [165] has suggested a value of $\alpha = 0.25$ as derived from perturbation theory. Due to the non-local nature of the functional above, the convergence as a function of cutoff energy can be very slow when using a plane-wave basis set. To alleviate this problem, Heyd-Scuseria-Ernzerhof [166, 167] suggested separating the exchange term into short and long range terms and truncating the slow decaying long range term leading to a screened functional:

$$E_{XC}^{HSE06} = \alpha E_X^{HF, sr}(\mu) + (1 - \alpha) E_X^{PBE, sr}(\mu) + E_X^{PBE, lr}(\mu) + E_C^{PBE} \quad (3.42)$$

μ is the screening parameter, it is used to partition the short and long range using complementary error and error functions (erfc and erf respectively) according to [168]

$$\frac{1}{r} = sr(r) + lr(r) = \frac{erfc(\mu r)}{r} + \frac{erf(\mu r)}{r} \quad (3.43)$$

An optimum value for μ was found empirically to be 0.207 \AA^{-1} [166, 167, 169]. Setting $\mu = 0$ restores the PBE0 functional while for $\mu \rightarrow \infty$, HSE06 is reduced to PBE.

3.2.5 The plane-wave basis set

In order to get the desired information about the system of interacting electrons and nuclei we have to solve a set of differential equations for the Kohn-Sham orbitals 3.31 in a self-consistent way. One can expand the Kohn-Sham orbital $|\psi\rangle$ in an infinite set of linearly independent basis vectors $|i\rangle$ of the Hilbert space

$$|\psi\rangle = \sum_i c_i |i\rangle \quad (3.44)$$

In the expansion (3.44) the coefficients c_i are numbers. Within this representation, the Kohn-Sham differential equations become a set of linear equations

$$\sum_j (H_{ij} - \epsilon S_{ij}) = 0 \quad (3.45)$$

where $H_{ij} = \langle i | H_{KS} | j \rangle$ is Kohn-Sham Hamiltonian matrix and $S_{ij} = \langle i | j \rangle$ is overlap matrix. As a result of this transformation, we now deal with lists of numbers c_i , H_{ij} , and S_{ij} , that are appropriate for numerical modeling. Since computers can only deal with finite sets of numbers, the exact expansion of the wave function (3.44) must be approximated by a finite set of coefficients c_i . Therefore, we have to use a truncated basis set of vectors and solve the matrix equation (3.45) for a finite set of coefficients c_i . We can do this truncation in a controllable way and have the desired accuracy in the approximation, which is something that, up to this point, has not been attained with the exchange-correlation functional approximation. Now the task of practical implementation of DFT is reduced to the methods of solving the matrix equation (3.45) and to the choice of a suitable basis set. Different basis sets gave rise to different electronic structure methods.

There are two kinds of basis sets of vectors that are mostly used in modern electronic structure calculations. The first emerged from the idea that the one-electron wave functions $\psi(\mathbf{r})$ of electrons in an assembly of atoms resemble the wave functions $\phi_\alpha(\mathbf{r})$ of electrons in isolated atoms

$$\psi(\mathbf{r}) = \sum_{\alpha} c_{\alpha} \phi_{\alpha}(\mathbf{r}) \quad (3.46)$$

The other choice of basis functions originates from the idea that electrons in condensed matter behave like free particles and consequently, the one-electron orbital can be expanded in a set of plane waves $exp(i\mathbf{k}\mathbf{r})$

$$\psi(\mathbf{r}) = \sum_{\mathbf{k}} c_{\mathbf{k}} \exp(i\mathbf{k}\mathbf{r}) \quad (3.47)$$

These two quite different basis sets, usually called localized and plane wave basis sets, respectively, have produced two large classes of widely used computational methods: (i) the linear augmented-plane-waves [170, 171] and linear maffin-tin orbital [172, 173] methods, and (ii) the *ab-initio* pseudopotential methods [174–176].

The advantages of using plane wave function as basis set are listed below:

1. unbiased and independent of atom positions in the unitcell as well as species
2. for a large number of atoms in condensed matter the plane wave methods have been much more successful as the wave functions can be made as accurate as necessary by simply increasing the number of plane waves, which helps the method to be systematically improvable
3. complete orthonormal set and easy to handle

4. efficient calculation of convolution by using fast Fourier transformation (FFT) to switch between real space mesh and reciprocal mesh
5. for a periodic system like crystals plane wave is natural choice of basis set due to Bloch theorem
6. forces acting on atoms are equal to Hellmann-Feynman forces, no basis set correction to the forces (no pulay forces)
7. no preconception is required regarding the form of the solution and no basis set superposition error.

A perfect crystal represents a periodic arrangement of atoms and is described by a periodically repeated unit cell. In a 3-dimensional space the unit cell is described by a set of three vectors \mathbf{a}_i . The periodicity is described by an infinite set of vectors $\mathbf{R}_m = \sum_i m_i \mathbf{a}_i$, where m_i are integers and it is called a Bravais lattice. Hence, the Kohn-Sham effective potential is periodic due to the translational symmetry

$$V_{KS}(\mathbf{r} + \mathbf{R}_m) = V_{KS}(\mathbf{r}) \quad (3.48)$$

and the solutions of the Kohn-Sham equation (3.31) are the Bloch functions

$$\psi_{i\mathbf{k}}(\mathbf{r}) = u_{i\mathbf{k}}(\mathbf{r}) \exp(i\mathbf{k}\mathbf{r}), \quad u_{i\mathbf{k}}(\mathbf{r} + \mathbf{R}_m) = u_{i\mathbf{k}}(\mathbf{r}), \quad (3.49)$$

where \mathbf{k} is a vector in the reciprocal space. The periodic systems are represented by plane waves in the same way as periodic functions are represented by Fourier series. These are generally easy to deal with on the computer.

3.2.6 The pseudopotential approximation

One can consider a Bravais lattice \mathbf{R} and its reciprocal lattice \mathbf{G} . The Kohn-Sham wave functions are classified by a band index i and a Bloch vector \mathbf{k} in the Brillouin Zone 3.49. A plane wave basis set is defined as

$$\langle \mathbf{r} | \mathbf{k} + \mathbf{G} \rangle = \frac{1}{\sqrt{V}} e^{i(\mathbf{k} + \mathbf{G})\mathbf{r}}, \quad \frac{\hbar^2}{2m} |\mathbf{k} + \mathbf{G}|^2 \leq E_{cut} \quad (3.50)$$

where V is the system volume, and E_{cut} is the cutoff of the kinetic energy of plane waves. Thus, the plane wave basis is defined by the crystal structure and by the cutoff. Unfortunately, the extended character of plane waves makes it difficult to

accurately reproduce the localized functions of the core states. When an electron is near the nucleus, it experiences a strong attractive potential, which gives it a large kinetic energy. This means that the wave vector \mathbf{k} of such an electron is very large and consequently, the basis set must contain a large number of plane waves to correctly describe that electron, which will make the calculations impractical. We can deal with the problem of large plane wave basis set, or large cutoff energy, by replacing the true nucleus potential with a pseudopotential. The interaction between valence electrons and atomic cores is described by a weak effective potential which gives a correct picture of the electron states and the energy of the system. With this idea we assume that the core electrons do not significantly contribute to chemical bonding and solid state properties. Thus, the core electrons are thought to be exactly in the same states as in the isolated atom, or to be “frozen” in their atomic states.

This simplification gives rise to a family of pseudopotential methods in contrast to the “all-electron methods” (*i.e.*, those where all electrons, valence and core electrons, are treated in the same way). Historically, the pseudopotential approach is related to the orthogonalized plane wave method (OPW), in which the basis set consists of plane waves, orthogonalized to lower-lying core states ψ_{core}^α :

$$\psi_{\mathbf{k}+\mathbf{G}}(\mathbf{r}) = e^{i(\mathbf{k}+\mathbf{G})\mathbf{r}} - \sum_{\alpha} \sum_{core} \langle \psi_{core}^\alpha | e^{i(\mathbf{k}+\mathbf{G})\mathbf{r}} \rangle \psi_{core}^\alpha(\mathbf{r}) \quad (3.51)$$

The most straightforward way of screening the “true” potential with a fixed core density is not practically used. The Coulomb field of a not fully compensated bare charge remains singular at the nuclei. Moreover, a true valence wave function must have nodes in the intra-atomic region for ensuring its orthogonality to the core states (see figure 3.1). The description of these nodes by plane waves needs high cutoffs. In reality, one works with smooth node-free pseudofunctions generated in a shallow pseudopotential. The construction of a pseudopotential typically starts with the choice of an appropriate reference configuration and pseudopotential radii r_c , which can be different for different l-channels. As a rule, the following conditions are imposed:

1. The pseudofunction must have no nodes (in order to avoid wiggles that would demand for higher cutoff).
2. The pseudofunction matches the all-electron one beyond the cutoff radius.
3. Norm conservation, meaning that the charge contained within the pseudopotential radius is the same for the pseudofunction and the all-electron one.

Otherwise, deviations from this rule give rise to ultrasoft pseudopotentials.

4. The eigenvalues corresponding to pseudo functions must be equal to those of the all-electron solution - at least for the reference configuration.

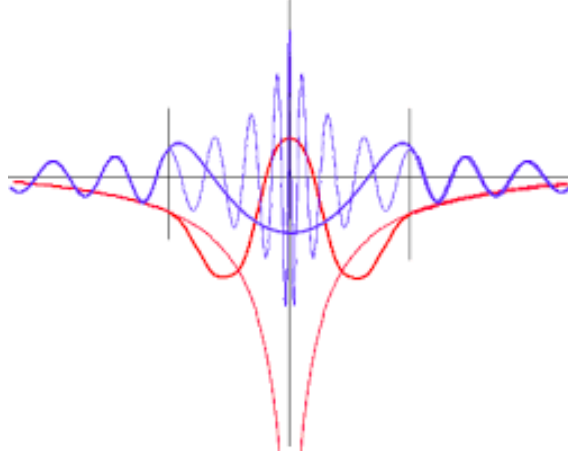


Figure 3.1: A schematic representation of the potentials (red lines) and wave functions (blue lines) for an atom. The real potential and wave function are shown with thin lines, while the pseudopotential and wave function are shown in thick lines. Outside the cutoff region (vertical black lines) the two are identical.

Nowadays, pseudopotentials being in use are usually of ab-initio nature. They are “cooked” (with the use of certain approximations and criteria) from the “true” (all-electron) solutions for free atoms or ions. As it was mentioned above, there can be some deviations from the rule of norm conservation for pseudopotentials. Namely, Vanderbilt (Vanderbilt, 1990) [175] suggested to abandon the norm-conservation condition, that would allow to make the pseudolization radius r_c essentially larger, limited only by the condition that the spheres of this radius centered on different atoms must not overlap in a simulation. A big advantage would be that pseudopotentials generated with larger r_c are much softer and hence a much lower planewave cutoff is needed. The ultrasoft pseudopotentials can be characterized by some important features:

1. The cutoff radius R , beyond which all all-electron and pseudo-properties (wave-functions, potential) coincide, is only limited by next-neighbor distance.
2. The necessary plane wave cutoff for the plane wave basis is drastically reduced.
3. The amount of computational work (in the generation of pseudopotential) is increased. But most of these additional efforts need not to be repeated in the course of iterations.

4. If the local potential in the sphere varies in the course of iterations, it can be considered as part of pseudopotential, so the pseudopotential develops itself as the calculation proceeds (similar to all-electron methods).
5. The main area of application of ultrasoft pseudopotentials is for large systems, where the relative cost of the pseudopotential generation is relatively low, as compared to solving the electronic structure problem. For the latter, a low plane wave cutoff is a major advantage.

3.2.7 Projector Augmented Wave

The Projector-Augmented wave method (PAW) has been developed by Peter Blöchl in 1994 (Blöchl, 1994) [176]. The new method was needed to enhance the accuracy and computational efficiency of the plane wave pseudopotential approach and to provide the correct wave functions, rather than the fictitious wave functions provided by the pseudopotential approach. The PAW method describes the wave functions by a superposition of different terms: There is a plane wave part, the pseudo wave function, and expansions into atomic and pseudo-atomic orbitals at each atom. On one hand, the plane wave part has the flexibility to describe the bonding and tail region of the wave function, but fails to describe correctly all the oscillations of the wave function near the nuclei. On the other hand, the expansions into atomic orbitals are well suited to describe the nodal structure of the wave function near the nuclei, but the local orbitals lack flexibility to describe the bonding and tail regions. The PAW method combines the virtues of both numerical representations in one well-defined basis set. In order to avoid solving two electronic structure calculations, *i.e.*, one with plane waves and one using atomic orbitals, the PAW method does not determine the coefficients of the “atomic orbitals” variationally. Instead, they are unique functions of the plane wave coefficients. The PAW method is in principle able to recover rigorously the density functional total energy, if plane wave and atomic orbital expansions are complete. This provides a systematic way to improve the basis set errors.

A comparison of PAW and ultrasoft pseudopotential (US-PP) are as follows:

1. The radial cutoffs (core radii) are smaller than the radii used for the US-PP
2. PAW potentials construct the exact valence wave function with all nodes in the core region
3. PAW potential contains the numerical advantages of PP calculations while

retaining the physics of all electron calculations, including the correct nodal behavior of the valence electron wave function and the ability to include upper core states in addition to valence states in the self-consistent iterations.

4. PAW potentials are generally of similar hardness across the periodic table. The US-PP become progressively softer when move down in the periodic table. PAW potentials are usually slightly harder than US-PP
5. Most of the PAW potentials were optimized to work at a cutoff of 300-350 eV. For US-PP, the radial cutoff were chose according to the covalent radius
6. For compounds where often species with very different covalent radii are mixed, the PAW potentials are clearly superior. FOr one component system the US-PP might be slightly faster (at the price of a somewhat reduced precision)
7. Less parameters involved in the construction of PAW potentials and it has improved accuracy for magnetic materials, alkali and alkali earth elements, early 3d elements to left of periodic table, lanthanide's and actinides etc.
8. PAW avoids transferability problems of PP by calculation of true density

3.2.8 Hellmann-Feynman Forces

Within the framework of the Born-Oppenheimer approximation (3.6) we solve the many-body problem of interacting electrons in the potential of fixed nuclei. In crystals with simple structure the positions of the atoms are fixed by the symmetry, but for more complex systems the equilibrium atomic positions are not known and we need to calculate them. The nuclei are considered as classical objects and at zero temperature the equilibrium atomic positions $\bar{\mathbf{R}}_0$, are determined by the minimum of the total energy E_{tot} of the system, which is the sum of the electronic energy E (the minimum of the Kohn-Sham energy functional) and the electrostatic energy E_{II} of the ion-ion interaction.

If we consider the electrons in their ground state for any given configuration of ions \mathbf{R} , the total energy will be a function of the atomic positions

$$E_{tot}(\mathbf{R}) = E(\mathbf{R}) + E_{II}(\mathbf{R}) \quad (3.52)$$

The procedure to find the atomic configuration that yields the minimum total energy is called structural optimization or relaxation. For infinite periodic structure there

is a distinction between atomic displacements that change the shape and volume of the unit cell (elastic modes) and atomic displacements internal to the unit cell (phonon modes). Usually, the optimization of the lattice and of the atomic positions is done using different procedures.

If the unit cell is fixed, then the problem of finding the minimum of the total energy as a function of atomic positions can be solved by calculating the gradients of the energy (forces) with respect to the variables (the positions of nuclei in the unit cell). There is one thing we must account for when finding the equilibrium configuration by minimizing forces: gradient algorithms are very likely to bring the system to the closest local minimum (a zero gradient point), rather than to the global minimum (the lowest energy minimum).

The derivatives of the total energy E_{tot} with respect to the atomic positions R_i are called Hellmann-Feynman forces. The Hellmann-Feynman theorem states that for the many body Hamiltonian and wave function, only terms containing explicit derivatives in the Hamiltonian contribute, while the terms containing implicit derivatives through the wave functions must vanish:

$$\begin{aligned}
 F_i &= -\frac{dE}{d\mathbf{R}_i} = -\frac{d}{d\mathbf{R}_i}\langle\Psi|H|\Psi\rangle = -\langle\Psi|\frac{\delta H}{\delta\mathbf{R}_i}|\Psi\rangle - \tilde{F}_i \\
 \text{where} \quad \tilde{F}_i &= \langle\frac{d\Psi}{d\mathbf{R}_i}|H|\Psi\rangle + \langle\Psi|H|\frac{d\Psi}{d\mathbf{R}_i}\rangle \\
 &= E\left(\frac{d\Psi}{d\mathbf{R}_i}|\Psi\rangle + \langle\Psi|\frac{d\Psi}{d\mathbf{R}_i}\right) = E\langle\Psi|\Psi\rangle = 0.
 \end{aligned} \tag{3.53}$$

The Hellman-Feynman theorem must also apply to the DFT approximation of a many-body problem. By using the expression (3.52), we can write the force as

$$F_i = -\int d\mathbf{r}\rho(\mathbf{r})\frac{\delta U(\mathbf{r})}{\delta\mathbf{R}_i} - \frac{\delta E_{II}}{\delta\mathbf{R}_i} = \tilde{F}_i \tag{3.54}$$

where the first two terms explicitly depend on ionic positions (the first is due to Coulomb interaction between the electrons and the nuclei and is the external potential term in the Kohn-Sham energy functional) and the last term \tilde{F}_i contains implicit derivatives through the Kohn-Sham orbitals:

$$\tilde{F}_i = \sum_k \int d\mathbf{r} \left(\frac{\delta\psi_k^*(\mathbf{r})}{\delta\mathbf{R}_i} \frac{\delta E}{\delta\psi_k^*(\mathbf{r})} + \frac{\delta\psi_k(\mathbf{r})}{\delta\mathbf{R}_i} \frac{\delta E}{\delta\psi_k(\mathbf{r})} \right). \tag{3.55}$$

The functional derivative yields the Kohn-Sham Hamiltonian

$$\frac{\delta E}{\delta \psi_k^*(\mathbf{r})} = H_{KS} \psi_k(\mathbf{r}), \quad (3.56)$$

and we can write \tilde{F}_i as

$$\tilde{F}_i = \sum_k \int d\mathbf{r} \left(\frac{\delta \psi_k^*(\mathbf{r})}{\delta \mathbf{R}_i} H_{KS} \psi_k(\mathbf{r}) + \frac{\delta \psi_k(\mathbf{r})}{\delta \mathbf{R}_i} H_{KS} \psi_k^*(\mathbf{r}) \right). \quad (3.57)$$

Furthermore, using the fact that the total number of electrons in the system is conserved, we obtain the following identity

$$\frac{d}{d\mathbf{R}_i} \int d\mathbf{r} \rho(\mathbf{r}) = \sum_k \int d\mathbf{r} \left(\frac{\delta \psi_k^*(\mathbf{r})}{\delta \mathbf{R}_i} \psi_k(\mathbf{r}) + \frac{\delta \psi_k(\mathbf{r})}{\delta \mathbf{R}_i} \psi_k^*(\mathbf{r}) \right) = 0. \quad (3.58)$$

and we can also rewrite the expression for \tilde{F}_i as

$$\tilde{F}_i = \sum_k \int d\mathbf{r} \left(\frac{\delta \psi_k^*(\mathbf{r})}{\delta \mathbf{R}_i} (H_{KS} - \epsilon_k) \psi_k(\mathbf{r}) + \frac{\delta \psi_k(\mathbf{r})}{\delta \mathbf{R}_i} (H_{KS} - \epsilon_k) \psi_k^*(\mathbf{r}) \right). \quad (3.59)$$

which becomes zero in the ground state. Consequently, as in the exact many-body case, the forces acting on the atoms are expressed through the ground state matrix elements of the gradient of the external potential $U(\mathbf{r}, \bar{\mathbf{R}})$, plus the gradient of the electrostatic potential due to interactions between nuclei, $E_{II}(\bar{\mathbf{R}})$:

$$F_i = - \int d\mathbf{r} \rho(\mathbf{r}) \frac{\delta U(\mathbf{r})}{\delta \mathbf{R}_i} - \frac{\delta E_{II}}{\delta \mathbf{R}_i}. \quad (3.60)$$

3.3 Self-consistent Iterative Optimization

The Hohenberg-Kohn theorems assure us that the ground state electronic density uniquely determines the Hamiltonian, so the Kohn-Sham Hamiltonian is expressed in terms of ρ . This leads to a circular problem, in which the equations we must use to calculate ρ themselves depend on ρ . We address this conundrum by guessing an initial charge density and then iterating to self consistency. A typical DFT code will follow a simplistic path as shown in Fig. 3.2. The initial charge density guess is derived from a superposition of atomic charge densities. At the beginning of the calculation the wave function arrays are populated with random numbers. The initial charge density is used to construct the Kohn-Sham Hamiltonian. An initial charge density is guessed based upon an initial structure that is fed into the code.

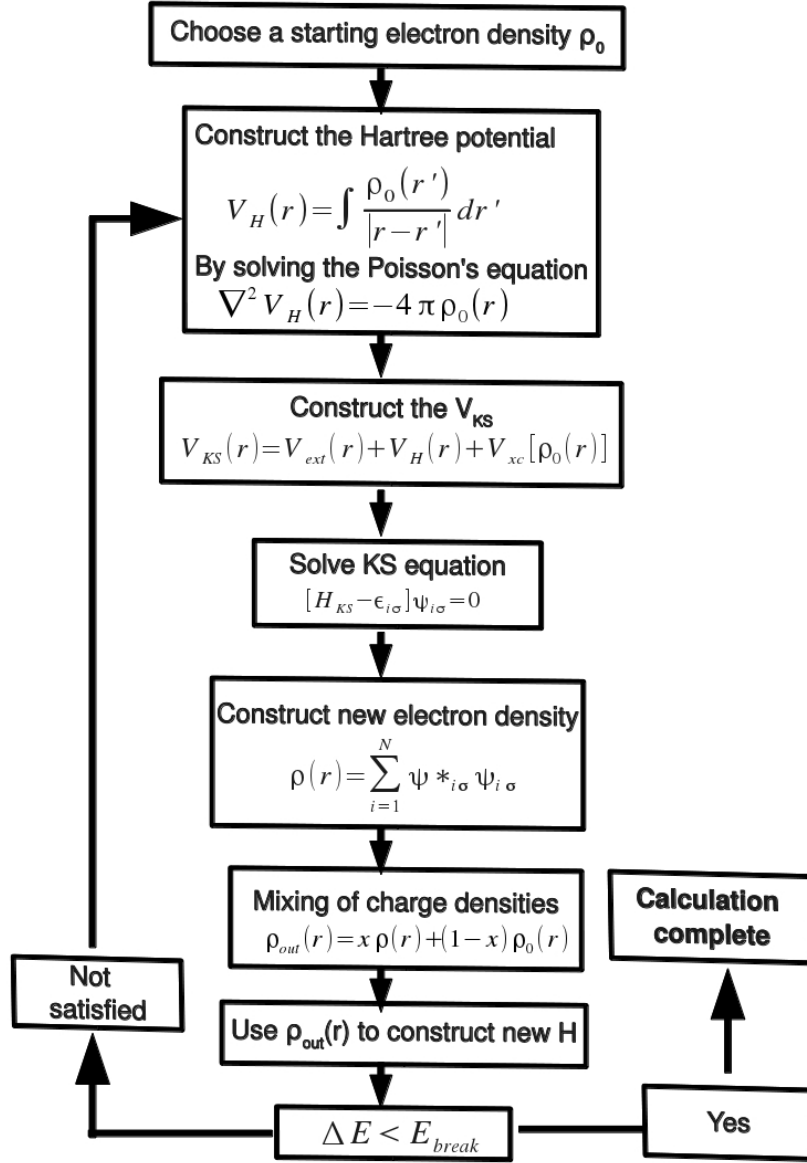


Figure 3.2: Flowchart illustrating the iterative scheme for the calculation of ground state electron density using Kohn-Sham approximation.

That generates an effective potential which is used to solve the one particle Kohn-Sham equations whose wave functions are used in turn to generate a new charge density. The process is repeated iteratively until the new density gives an energy that is consistent with the old density. Once this self-consistency is achieved forces on the atoms can be calculated by invoking the the Hellman-Feynmann equations.

To get a feel for how this process works it is helpful to look at the inner workings of an actual software package that solves the Kohn-Sham equations. Throughout the thesis Vienna Ab-initio Simulation Package (VASP) [177] has been used for the first-principles calculations. Computational details for each of the system are provided in the individual chapters.

3.4 First-principles Lattice Dynamics Theory

We solve the Schrödinger equation Eq.(3.1) for an interacting many-particle system via the Born-Oppenheimer approximation Eq.(3.6) which decouples degrees of freedom of electrons and ions. Within this approximation, we freeze the motion of ions and solve the quantum equation of motion for the ground state of the electronic subsystem. For a given structure we can optimize the unit cell parameters and the position of atoms in this cell via Hellmann-Feynman forces and bring the structure to equilibrium at $T = 0$ K. Within the framework of the static lattice model, which neglect the thermal motion of atoms and consider them fixed at some average positions, we can still explain a large number of material properties, such as the electronic structure and chemical properties, shapes and symmetry of crystals, material hardness, low temperature structural phase transformations, x-ray, electron and ion beams Bragg scattering, etc [178]. We know, however, that atoms actually move around inside the crystal and this motion gives rise to the concept of temperature. And even at $T = 0$ K, atoms are not frozen in fixed positions due to the uncertainty principle [179]. There are a number of properties of matter that cannot be explained by a static model, such as thermal expansion, structural phase transition at finite-temperature, including melting, sound propagation and thermal conductivity, the phenomenon of superconductivity and interaction of radiation with matter, etc [178]. Thus, we need to find an accurate description for the dynamics of the crystal lattice to account for the thermal motions of ions. In many cases such a description is possible due to a classical nature of the ionic motion.

The motion of a classical object such as an atom as a whole is determined accurately by the second Newton's law of mechanics:

$$M \frac{\partial^2 \mathbf{R}}{\partial t^2} = -\nabla U(\mathbf{R}(t), t) \quad (3.61)$$

where M is the atomic mass and $U(\mathbf{R}, t)$ is the instantaneous potential energy of the atom at a position $\mathbf{R}(t)$. Equation 3.61 is a key equation to describe the lattice dynamics, and to solve this equation the knowledge of the interatomic interactions or forces in a crystal is needed. Therefore, the concept Hellmann-Feynman forces plays an important role in the description of matter at finite temperature and accurate values of these forces are provided by DFT based ab initio calculations.

In the following, we assume that at finite temperatures ions oscillate about the equilibrium positions of a static lattice at $T = 0$ K, and the atomic displacements are small compared to the interatomic distances. Hence, we can unambiguously

label each ion with a Bravais lattice site $R_{\sigma l}^0$ about which it oscillates, and the instantaneous position of this ion can be written as:

$$R_{\sigma l}(t) = R_{\sigma l}^0 + u_{\sigma l}(t), \quad (3.62)$$

where $u_{\sigma l}$ is the displacement of an atom σ in a unit cell l . The total energy E_{tot}^0 of the system of interacting electrons and nuclei at $T = 0$ K, with nuclei fixed at equilibrium positions $\bar{\mathbf{R}}_0 = (\mathbf{R}_1^0, \dots, \mathbf{R}_1^0, \dots, \mathbf{R}_N^0)$ is given by:

$$E_{tot}^0(t) = E_{KS}(\bar{\mathbf{R}}_0) + E_{II}(\bar{\mathbf{R}}_0), \quad (3.63)$$

where E_{KS} is the Kohn-Sham ground state energy of the electronic system in the external potential of fixed nuclei, and E_{II} is the energy due to the electrostatic interaction between ions. The total energy of the system with atoms displaced from their mean equilibrium positions due to thermal agitation can be expanded for small displacements $\bar{\mathbf{u}}$ as [180]

$$\begin{aligned} E_{tot}(\bar{\mathbf{R}}_0 + \bar{\mathbf{u}}) = & E_{tot}^0 + \frac{1}{2} \sum_{\sigma l \alpha, \sigma' l' \beta} \Phi_{\sigma l, \sigma' l'}^{\alpha \beta} u_{\sigma l}^{\alpha} u_{\sigma' l'}^{\beta} + \\ & \frac{1}{3!} \sum_{\sigma l \alpha, \sigma' l' \beta, \sigma'' l'' \gamma} \Phi_{\sigma l, \sigma' l', \sigma'' l''}^{\alpha \beta \gamma} u_{\sigma l}^{\alpha} u_{\sigma' l'}^{\beta} u_{\sigma'' l''}^{\gamma} + \dots \end{aligned} \quad (3.64)$$

where, in particular, $\Phi_{\sigma l, \sigma' l'}^{\alpha \beta}$ is the force-constant matrix, given by $\frac{\delta^2 E_{tot}}{\delta u_{\sigma l}^{\alpha} \delta u_{\sigma' l'}^{\beta}}$ evaluated at $\bar{\mathbf{R}}_0$. Thus, for a distorted lattice, the total energy of the system (with frozen ions) differs from that of an ideal lattice by the potential energy of the displaced atoms, which is exactly the quantity required to solve the Newton's equations of motion. If we consider only small displacements, such that we can neglect higher order anharmonic terms in the expansion (3.64), then the problem of the lattice dynamics is reduced to the problem of a system of independent harmonic oscillators, which has an exact solution.

The equations of motion describing the lattice dynamics within the approximation of harmonic motion are:

$$M_{\sigma} \ddot{u}_{\sigma l}^{\alpha} = - \frac{\partial E_{tot}(\bar{\mathbf{R}})}{\partial \mathbf{u}_{\sigma l}^{\alpha}} = \sum_{\sigma' h, \beta} \Phi_{\sigma l, \sigma' l+h}^{\alpha \beta} u_{\sigma' l+h}^{\beta} \quad (3.65)$$

where $h = l - l'$ and $\Phi_{\sigma l, \sigma' l+h}^{\alpha \beta} = \Phi_{\sigma l, \sigma' l'}^{\alpha \beta}$, which expresses the fact that the force matrix depends on relative positions of atoms only. One can see that Eqs.(3.65) are invariant under the lattice translations within the quasi-harmonic approximation,

thus the displacements of atoms should satisfy the Bloch theorem:

$$\mathbf{u}_{\sigma l}(t) = e^{i\mathbf{q}\mathbf{R}_{\sigma 1}^0} \mathbf{u}_{\sigma}(\mathbf{q}, t) \quad (3.66)$$

where \mathbf{q} is a wave vector defined in the same reciprocal space of wave vectors \mathbf{k} that describes the electronic states, and the problem of the lattice dynamics reduces to the following eigenvalue problem:

$$\sum_{s'\beta} \left(D_{\sigma\sigma'}^{\alpha\beta}(\mathbf{q}) - (\omega_{s\mathbf{q}}^0)^2 \delta_{\sigma\sigma'} \delta_{\alpha\beta} \right) u_{\sigma'}^{\beta}(\mathbf{q}) = 0 \quad (3.67)$$

where $D_{\sigma\sigma'}^{\alpha\beta}(\mathbf{q})$ is the Fourier transform of the force constant matrix known as the dynamical matrix. $\omega_{s\mathbf{q}}^0$ are the frequencies of the lattice vibrations about the equilibrium positions at $T = 0$ K. The approximation is called quasi-harmonic since the phonon frequencies might depend on volume through the dynamical matrix.

For a crystal structure with n atoms in the unit cell, the system of equations (3.67) has $3n$ solutions, labeled s for each reciprocal vector \mathbf{q} . Thus, the displacement of an atom in a crystal can be written as:

$$u_{\sigma l}(t) = \sum_{s\mathbf{q}} u_{\sigma s}(\mathbf{q}) e^{i(\mathbf{q}\mathbf{R}_{\sigma 1}^0 - \omega_{s\mathbf{q}}^0 t)}, \quad (3.68)$$

where $u_{\sigma s}(\mathbf{q})$ is the amplitude vector that tells us how the atom σ moves under the influence of the wave with frequency $\omega_{s\mathbf{q}}^0$. It is usual to define a set of new quantities $Q_{s\mathbf{q}}^0$, referred to as normal mode coordinates, by rewriting Eq.(3.68) as

$$u_{\sigma l}(t) = \frac{1}{\sqrt{M_{\sigma} N}} \sum_{s\mathbf{q}} e_{\sigma s}(\mathbf{q}) e^{i\mathbf{q}\mathbf{R}_{\sigma 1}^0} Q_{s\mathbf{q}}(t), \quad (3.69)$$

Since an atomic displacement is always a real quantity, $Q_{s\mathbf{q}}(t)$ are subject to the following constraint $Q_{s\mathbf{q}}^* = Q_{s-\mathbf{q}}$. Vectors $e_{\sigma s}(\mathbf{q})$ give the direction in which each atom σ moves and is called the *displacement vectors* or the *polarization vectors*. On the other hand, these vectors are the eigenvectors of the eigenvalue equations (3.67) and, in order that the normal modes $Q_{s\mathbf{q}}$ to be orthogonal, these eigenvectors satisfy the following orthogonality conditions:

$$\sum_{\sigma} e_{\sigma s}(\mathbf{q}) e_{\sigma s'}(-\mathbf{q}) = \delta_{ss'} \quad (3.70)$$

There are basically two elegant approaches to calculate phonons in a crystal

by means of ab-initio electronic structure calculations. One strategy, called linear response method, calculates the dynamical matrix in the framework of the Density Functional Perturbation Theory (DFPT) [181, 182]. The small displacement method [183] is based on the fact that for small displacements of atoms from equilibrium positions, the relation between forces and displacements is linear (Eq.(3.72)).

(a) Calculating Phonons using Small Displacement Method

Within the quasi-harmonic approximation, the relation between the Hellmann-Feynman forces, $F_{\sigma l}$, acting on atom σ in a unit cell l , and the displacements $u_{\sigma' l}$ is given by the force-constant matrix $\Phi_{\sigma l \alpha, \sigma' l' \beta}$:

$$F_{\sigma l}^{\alpha} = -\frac{\partial E_{tot}(\bar{\mathbf{u}})}{\partial \mathbf{u}_{\sigma l}^{\alpha}} = \sum_{\sigma' l' \beta} \Phi_{\sigma l \alpha, \sigma' l' \beta}^{\alpha \beta} u_{\sigma' l'}^{\beta} \quad (3.71)$$

and the vibrational frequencies $\omega_{s\mathbf{q}}^0$ are the eigenvalues of the dynamical matrix $D_{\sigma\sigma'}(\mathbf{q})$, defined as:

$$D_{\sigma\sigma'}^{\alpha\beta}(\mathbf{q}) = \frac{1}{\sqrt{M_{\sigma}M_{\sigma'}}} \sum_l \Phi_{\sigma l \alpha, \sigma' l' \beta}^{\alpha \beta} \exp[i(\mathbf{q}(\mathbf{R}_{\sigma' l'}^0 - \mathbf{R}_{\sigma l}^0))]. \quad (3.72)$$

If the complete force-constant matrix is known, then the dynamical matrix $D_{\sigma\sigma'}(\mathbf{q})$, and the phonon frequencies $\omega_{s\mathbf{q}}^0$ can be obtained at any \mathbf{q} .

All that has to be done is to displace a single atom σ' from the equilibrium position $\mathbf{R}_{\sigma' l'}^0$ in the unit cell l' in the Cartesian direction β by a small displacement $u_{\sigma' l'}^{\beta}$, providing that all other atoms are held fixed at their equilibrium positions $\mathbf{R}_{\sigma l}^0$. Then, the forces $F_{\sigma l}^{\alpha}$ acting on all other atoms give directly the elements of the force-constant matrix $\Phi_{\sigma l, \sigma' l'}^{\alpha \beta}$ for the given $(\sigma' l' \beta)$. In a general case, we have to repeat this procedure $3n$ times, where n is the number of atoms in the unit cell, however the 3D space group symmetry of the lattice reduces this number substantially. The small displacement method gives the exact force-constant matrix in the limit of infinite crystal. In practical calculations, a crystal is replaced by a super-cell, and in order to get accurate results, the super-cell must be large enough so that the elements $\Phi_{\sigma l, \sigma' l'}^{\alpha \beta}$ vanish at the boundaries. Because of the periodic boundary conditions, the dynamical matrix is exactly calculated at reciprocal wave vectors commensurate with the supercell lattice vectors. The reason is that moving one atom in the supercell also means moving all its periodic images, and consequently,

the relation between the force is not linear any more:

$$\begin{aligned}
F_{\sigma l}^{\alpha} &= -\frac{\partial E_{tot}(\bar{\mathbf{u}})}{\partial \mathbf{u}_{\sigma l}^{\alpha}} = \sum_L \sum_{\sigma' l' \beta} \Phi_{\sigma, l+L; \sigma' l'}^{\alpha\beta} u_{\sigma', l'+L'}^{\beta} \\
&= \sum_L \sum_{\sigma' l' \beta} \Phi_{\sigma, l+L; \sigma' l'}^{\alpha\beta} u_{\sigma', l'}^{\beta},
\end{aligned} \tag{3.73}$$

where l labels the unit cell position in the supercell, L labels all possible images of the supercell. The corresponding dynamical matrix is given by

$$\begin{aligned}
D_{\sigma\sigma'}^{\alpha\beta}(\mathbf{q}) &= \frac{1}{\sqrt{M_{\sigma}M_{\sigma'}}} \sum_L \sum_l \Phi_{\sigma, l+L; \sigma' l'}^{\alpha\beta} \exp[i(\mathbf{q}(\mathbf{R}_{\sigma' l'}^0 - \mathbf{R}_{\sigma l}^0))] \\
&= \frac{1}{\sqrt{M_{\sigma}M_{\sigma'}}} \sum_{l+L} \exp[i\mathbf{q}\mathbf{R}_{\mathbf{L}}] \Phi_{\sigma, l+L; \sigma' l'}^{\alpha\beta} \exp[i(\mathbf{q}(\mathbf{R}_{\sigma' l'}^0 - \mathbf{R}_{\sigma, l+L}^0))]
\end{aligned} \tag{3.74}$$

where R_L is a vector connecting two supercells. One can see, that for reciprocal vectors \mathbf{q} such that $\mathbf{q}\mathbf{R}_{\mathbf{L}} = 2n\pi$ the above expression gives the exact dynamical matrix (3.73).

In this thesis we employ the lattice dynamics software package PHON [184] in conjunction with the density functional package VASP [177] to obtain lattice dynamical behavior from first-principles. PHON finds the optimal (in the least-squares sense) force constant elements using the singular value decomposition method [184, 185]. Each symmetry inequivalent atom is displaced in each symmetry inequivalent direction. A supercell is created for each atomic displacement and the Hellmann-Feynman forces are computed for each atom in the distorted supercell. To avoid error due to the periodic nature of the boundary conditions, the supercell must be large enough so that the force constants fall off by at least three orders of magnitude at the edge of the supercell compared to the center of the supercell centered on an atom [184].

After their extraction through the fitting process to the Hellmann-Feynman forces, the force constant matrix is used to construct the dynamical matrix (Eq. 3.74). The diagonalization of the dynamical matrix at a series of wave vectors (\mathbf{k}) along straight lines in reciprocal space gives the phonon dispersion curves for the crystal. The diagonalization of the dynamical matrix at a set of randomly distributed (selected by Monte Carlo sampling) \mathbf{k} vectors distributed homogeneously over the first Brillouin zone yields the phonon density of states.

The relation between polarization vectors ($\epsilon(\mathbf{k})$) and the direction of wave propagation (\mathbf{k}) divide phonon modes into those of longitudinal and transverse na-

ture. In an isotropic medium, for a given \mathbf{k} , it is always possible to choose solutions such that one of the modes is polarized along the direction of wave propagation ($\epsilon \parallel k$), while two are polarized perpendicular to the direction of wave propagation ($\epsilon \perp k$). We call the branch with $\epsilon \parallel k$ the longitudinal branch. The branches with $\epsilon \perp k$ are the transverse branches. An additional classification of phonon modes derives from the behavior of a phonon branch as k vanishes at the origin of the Brillouin Zone. Acoustic branches are those that show a vanishing frequency as k goes to the origin. There are always exactly 3 acoustic branches to match the 3 dimensions of space we experience. 3r-3 of the branches are optical branches, which maintain finite frequencies of vibration as k goes to 0. These optic branches tend to be flatter due to the fact that in these modes the intracellular interactions are stronger than the interactions between cells.

(b) Calculating Phonons using Linear Response Method

The main idea to calculate the phonon dispersion in DFPT is based on the fact that the linear order variation in the electron charge density upon the application of a perturbation to the crystal induces a variation in energy up to a third order of the perturbation [182]. Thus, using the standard perturbation theory, the linear order variation of the electronic charge density can be calculated using only the ground state wave-functions of the crystal, which are provided by DFT calculations. If the perturbation is a vibrational wave with wave-vector \mathbf{q} , then the dynamical matrix at that wave-vector $D_{\sigma\sigma'}(\mathbf{q})$ can be obtained by calculating the change of the charge density to linear order in the perturbation theory.

The advantage of the small displacement method is that it works as an add-on to any DFT code that provides forces. However, the need to use large supercells makes it computationally less efficient. The advantage of the linear response method is that it is capable to give the exact phonon frequencies at requested points, which is suitable for systems with anomalies in the phonon dispersion.

3.5 Empirical Pair Potential based Classical Molecular Dynamics Calculations

In this category of atomistic simulation, Newton's law's of motion are solved as a function of time for a simulation cell containing a collection of atoms acting under the influence of forces due to other atoms in the system. Using this method the time evolution of the atoms in the system can be observed as a function of variables

such as temperature and pressure.

Molecular dynamics proceeds by solving Newton's equations of motion to predict the behavior of atoms within a given supercell. Using a set of forces defined by an interatomic potential (section 3.5.1), the temporal evolution of the atomic accelerations, velocities and positions can be determined according to Newton's laws of motion [186]. By assigning kinetic energy to the system, molecular dynamics (MD) allows the atomic trajectories to be sampled. The gradient of the potential energy of an atom, $\phi_i(r(t))$, with respect to position is used to determine the direction and magnitude of the atomic acceleration:

$$\ddot{\mathbf{r}}(t) = \frac{\mathbf{F}_i(\mathbf{r}(t))}{m_i} = \frac{-\nabla\phi_i(\mathbf{r}(t))}{m_i} \quad (3.75)$$

where in Cartesian coordinates the force on an atom, F_i , is given by the gradient of the potential energy, $\nabla\phi_i$, where the mass of the atom is m_i and \ddot{r} is the acceleration.

The atomic configuration is used in conjunction with the interatomic potential, to determine the acceleration of the atoms at a given time t (equation 3.75). Using the velocity Verlet integration method [187, 188] it is possible to determine the atomic position and velocity at time $t + \delta t$ as follows. A second order differential equation can be split into two first order differential equations, *i.e.*, $a(t) = \dot{v}(t) = \ddot{r}(t)$ and $v(t) = \dot{r}(t)$. By Taylor expanding $r(t + \delta t)$ about $r(t)$ and $v(t + \delta t)$ about $v(t)$ one gets:

$$\begin{aligned} \mathbf{r}(t + \delta t) &= \mathbf{r}(t) + \delta t\dot{\mathbf{r}}(t) + \frac{\delta t^2}{2}\ddot{\mathbf{r}}(t) + O(\delta t^3) \\ \mathbf{v}(t + \delta t) &= \mathbf{v}(t) + \delta t\dot{\mathbf{v}}(t) + \frac{\delta t^2}{2}\ddot{\mathbf{v}}(t) + O(\delta t^3) \end{aligned} \quad (3.76)$$

All of the above terms can be defined in terms of known quantities except for \ddot{v} . However, Taylor expansion of \ddot{v} remedies this:

$$\dot{\mathbf{v}}(t + \delta t) = \dot{\mathbf{v}}(t) + \delta t\ddot{\mathbf{v}}(t) + O(\delta t^2) \quad (3.77)$$

All terms in the equation 3.76 can be written in terms of $\mathbf{r}(t)$, $\mathbf{v}(t)$ and $\mathbf{a}(t)$

$$\mathbf{r}(t + \delta t) = \mathbf{r}(t) + \delta t\mathbf{v}(t) + \frac{\delta t^2}{2}\mathbf{a}(t) + O(\delta t^3) \quad (3.78)$$

$$\mathbf{v}(t + \delta t) = \mathbf{v}(t) + \frac{\delta t}{2}[\mathbf{a}(t) + \mathbf{a}(t + \delta t)] \quad (3.79)$$

where the acceleration of an atom, $a(t)$ is defined by the gradient of its potential

energy, $\mathbf{a}(t) = -\frac{\nabla\phi_i(\mathbf{r}(t))}{m_i}$. This approach of solving Newton's equations of motion means that information about the position, $r(t)$, and velocity, $v(t)$, of atoms at time t is sufficient to determine the atomic trajectories for subsequent steps, that is,

1. Calculate new positions, $r(t + \delta t)$, using equation 3.78
2. Determine $a(t + \delta t)$ using equation 3.75 and the updated positions
3. Calculate new velocities, $v(t + \delta t)$, using equation 3.79 and start again.

By repeatedly solving the velocity Verlet equations the evolution of the system with time can be examined. Despite significant improvements in the computational power available system sizes are still very small ($10^3 - 10^6$ atoms) compared to Avogadro's number and simulations times are limited to the order of 10^{-9} second [189]. As such, the MD simulations presented here are limited to nanometer-sized systems and nanosecond timescales. Underlying these system constraints is the need to keep the timestep to only 1 or 2 femto seconds (fs).

Comparing the results of a simulation containing several thousand atoms with those obtained from a macroscopic sample poses several challenges. For example, a volume element in a material is constrained by the surrounding bulk. At a surface these constraints break down and sometimes quite extensive atomic relaxation can occur. In macroscopic systems, only a small percentage of the atoms are at the surface and therefore contribute little to bulk properties. This is not the case for the small number of atoms constituting a molecular-dynamics simulation. Here the surface area to volume ratio is considerable and surface effects can hinder attempts to obtain bulk properties from such a system. To counteract this, periodic boundary conditions are introduced.

According to this condition, each atom in the primary simulation cell is repeated identically in each of the periodic cells. This has the effect of creating a system that imitates a bulk crystal but, because the atomic positions and velocities in the periodic cells are identical to those in the primary cell, the information must only be recorded once for the atoms in the primary cell. The atoms in the periodic cells are essentially only there to ensure the correct atomic forces in the primary cell. This is particularly important for ionic systems where the superposition of Coulomb forces due to a periodic arrangement of charged species creates a long range electrostatic field. Note that if the trajectory of an atom takes it over the periodic boundary it appears at the opposite side of the cell. As the primary cell size is increased the system becomes closer to a true representation of the crystal.

It is important to select the correct supercell size according to the feature that one is attempting to study.

Molecular-dynamics calculates the position and velocity of atoms in a model. A measurable quantity such as temperature is a macroscopic property: somehow the atomic quantities probed by simulation must be reconciled with bulk properties. Statistical mechanics provides the bridge between the atomic scale and macroscopic properties and at its center is the concept of the thermodynamic ensemble. A thermodynamic ensemble represents all the different ways in which the positions and momenta of atoms in a system can arrange themselves, where each state has one or more extensive quantities in common. Extensive quantities are the independent thermodynamic variables of a system, from which all other quantities can be obtained. For instance, it is implicit in the description of molecular-dynamics given above that, as time develops, the total energy of the system remains constant. In addition the volume and the number of atoms in the system also remain constant. In other words the state of the molecular-dynamics system at each time-step is a member of an ensemble where the number of atoms (N), volume (V) and energy (E) are the extensive variables. This gives rise to what is known as the NVE of micro canonical ensemble.

Bulk properties are calculated by ensemble averages, where an observable value is averaged over all states of a system with a weighting in favor of low energy states (in NVE this corresponds to high entropy states). Weighting towards low energy states essentially ensures the bulk properties are averaged according to the time spent in a given state. In molecular dynamics this is achieved by taking an average of states sampled over a number of time-steps. However, the simulation must be in equilibrium to ensure the MD time average corresponds to the ensemble average and, thus, the true thermodynamic quantity.

3.5.1 The Born Interpretation of Interatomic Forces

The empirical simulations conducted in this thesis assume that it is possible to treat an ionic lattice using a classical Born like model [190, 191], whereby the constituent ions are represented by a periodic array of point charges. To calculate the total energy, $\Phi(r_1, \dots, r_n)$, of the system requires the summation of the interactions experienced by each atom as a result of the other atoms in the system. This can be expressed formally using equation 3.80.

$$\Phi(r_1, \dots, r_n) = \sum_{i,j=1}^n \Phi_2(r_{ij}) + \sum_{i,j,k=1}^n \Phi_3(r_{ijk}) + \sum_{i,j,k,l=1}^n \Phi_4(r_{ijkl}) + \dots \quad (3.80)$$

In above equation, the $\sum_{i,j=1}^n \Phi_2(r_{ij})$ term refers to the interactions between pair of ions i and j at a given separation r_{ij} . The $\sum_{i,j,k=1}^n \Phi_3(r_{ijk})$ and $\sum_{i,j,k,l=1}^n \Phi_4(r_{ijkl})$ terms describe the interactions of ion triplets and quartets respectively: these terms as well as interactions between higher numbers of ions are generally truncated owing to the dominance of the pairwise interaction. Equation 3.80 then becomes equation 3.81,

$$\Phi(r_1, \dots, r_n) = \sum_{i,j=1}^n \Phi_2(r_{ij}). \quad (3.81)$$

From this point onwards, $\Phi_2(r_{ij})$ will be written as $E_{ij}(r_{ij})$. The form this pair potential function takes is a important factor in determining the success of the model.

Coulomb Potential

It is a fundamental concept in science that the potential energy of a charged body will be affected by the presence of another charged body (or more accurately, by its electric field). If two ions i and j , with charges q_i and q_j respectively are separated by a distance, r_{ij} , then their potential energy can be expressed using the Coulomb potential:

$$E_{ij}^{coulomb} = \frac{q_i q_j}{4\pi\epsilon_0 r_{ij}} \quad (3.82)$$

$E_{ij}^{coulomb}$ represents the potential resulting from the interaction of charges on ions i and j and ϵ_0 is the permittivity of free space. Partial charges can be used such that $q = Z_{eff}|e|$, however they must be proportional to their formal charges ensuring the system remains charge neutral.

As the magnitude of the Coulombic potential energy decreases as a function of $\frac{1}{r_{ij}}$, it converges slowly, *i.e.*, the Coulombic interaction is long range. Whilst this term may seem very simple to calculate, the slow rate of convergence means it is necessary to consider the influence of a great number of ions for each ion in the system, thus placing large demands on computational resources. The number of operations required scales with $O(N^2)$, where N denotes the number of atoms

in the system, making very large systems without a more efficient computational mechanism unfeasible.

In order to allow rapid and guaranteed convergence of above equation, the Ewald summation [178] can be employed. The Ewald technique [192] is able to incorporate periodic boundary conditions and will increase the computational efficiency to $O(N)$, by decomposing interactions into real space and reciprocal space parts, each of which sum quickly and with guaranteed convergence [193]. The use of periodic boundary conditions employed in the simulations leads to long-range periodicity of the simulation cell. This periodicity, can be accurately described in reciprocal space by a Fourier transform. This avoids the use of a simple and less accurate truncation of the long-range interactions. For a detailed explanation of the Ewald technique, see the introductory text by Rapaport [194].

The form of equation 3.82 ensures that the interaction between two like charged atoms will be repulsive while the interaction between atoms with opposite charges will be attractive. In fact, considering the Coulombic potential alone, for two oppositely charged ions, as $r \rightarrow 0 \text{ \AA}$, $E_{ij}(r_{ij}) \rightarrow -\infty \text{ eV}$. This implies that the lowest energy configuration for this system would be for the ions to be sitting atop one another, which is clearly unphysical. Therefore, there must be some other force coming into play, at shorter separations, to ensure that the ions do not collapse onto each other.

Short Range Potential

At small separations, the charge distributions of two adjacent ions will begin to overlap, resulting in a repulsive force. As the separation, r_{ij} , decreases, the extent of this overlap is increased further, to a point at which it becomes the dominant force, thus preventing the ions moving to occupy the same space. This repulsive force arises as a result of the Coulombic interactions between the nuclei as well as, indirectly, from the Pauli exclusion principle. The Pauli exclusion principle states that no two fermions may occupy the same quantum state [193]. When electron clouds overlap the Pauli exclusion principle dictates that the ground state charge distribution will be of a higher energy, thus increasing the electronic energy.

The short range interactions of ions are approximated by using empirical potentials. Different short range potential forms have been developed depending on the bonding of the system studied. For example, the covalency is often described using the Morse potential [195] and, alternatively, the Buckingham potential [196] has been developed to describe short range repulsion and attractive van der Waals

interactions [197]. All such potentials have parameters that underpin their ability to describe the properties of a material. In particular, the lattice parameter, elastic constants and specific heat have been key experimental properties used in the selection of candidate parameter sets. Potential forms are described below:

Buckingham Potential

$$\phi^{short}(r_{ij}) = A_{\alpha\beta} \exp\left(-\frac{r_{ij}}{\rho_{\alpha\beta}}\right) - \frac{C_{\alpha\beta}}{r_{ij}} \quad (3.83)$$

Buckingham-Morse Potential

$$\begin{aligned} \phi^{short}(r_{ij}) = & A_{\alpha\beta} \exp\left(-\frac{r_{ij}}{\rho_{\alpha\beta}}\right) - \frac{C_{\alpha\beta}}{r_{ij}} \\ & + D_{\alpha\beta} [\exp(-2\gamma_{\alpha\beta}(r_{ij} - r_0)) - 2\exp(-\gamma_{\alpha\beta}(r_{ij} - r_0))] \end{aligned} \quad (3.84)$$

Embedded Atom Method Potential

Splitting the energy of the system into a set of independent pair interactions is a simplification of the atomic interactions of a real system. This is most clearly identified by the Cauchy violation ($C_{12} \neq C_{44}$) observed experimentally in a wide range of oxide elastic constants, including UO_2 [198]. If the system energy was truly the sum independent pair interactions then there would be no Cauchy violation [199]. Dawes and Basak [200] developed the embedded atom method (EAM) as a many-body addition to the pairwise description in order to describe metallic systems, so that the energy of the system can be written as:

$$U_{ij} = \frac{1}{2} \sum_i \sum_{i \neq j} \phi_{\alpha\beta}(r_{ij}) + \sum_i F_{\alpha}(\rho_T) \quad (3.85)$$

where the first term is attributed to the highly repulsive pairwise interactions and the second term is the embedded atom method. ρ_T represents the total electron density at atom i due to all surrounding atoms j and is closely approximated by the sum of the individual atomic densities (*i.e.*, $\rho_T = \sum_{i \neq j} \rho_{\beta}(r_{ij})$). The embedding function, F_{α} , determines the embedding energy of atom i due to the total electron density of the surrounding atoms, ρ_T . The selection of a non linear embedding function, F_{α} , ensures the pairwise density functions, $\rho_{\beta}(r_{ij})$, cannot be separated when describing the total energy of the system, thus making the potential many-bodied. In other words the bonding between two atoms cannot be described without knowledge of the surrounding atomic positions. Due to the strong analogy between this

potential description and the electronic structure of metals, the EAM has primarily been used for modeling metals. Therefore, previous EAM models are beyond the scope of this thesis, as here only oxides are considered. However, in a later chapter the EAM is used as a perturbation to a more conventional Buckingham-Morse potential, in order to extend the modeling of actinide oxides beyond a pairwise description without needing to use shells.

3.5.2 Ensembles

Evans [201] defines an ensemble as “an essentially infinite number of systems characterized by identical dynamics and identical state variables (N , V , E , or T etc.) but different initial conditions.” The intensive and extensive quantities of the system do not change between the individual ensemble members sampled by MD timesteps.

If one assumes that in real systems, the atomic kinetic energies follow a Maxwell-Boltzmann distribution, then by the summation of the velocities of all the atoms in a system, the macroscopic temperature may be derived. Temperature, for example, can be calculated by using ensemble averages provided by the MD simulation instantaneously at every timestep of the simulation. Thus, the temperature of the system is kept in line with the ensemble by controlling the velocities of the atoms directly. A MD simulation tends to sample energy minimum (some of which may be metastable) for a given set of ensemble variables. By letting the system evolve over a period of time, a great number of thermodynamically likely configurations can be obtained. Assuming a long enough sampling time, the statistical average of positions with time is approximately equal to the average bulk properties of all possible structure variations to a point where they can be assumed to be indistinguishable. This is also known as the ergodic hypothesis [201]. From these sets of positions, certain properties of the system can then be extracted.

The most fundamental of the three ensembles used, is the micro-canonical ensemble. It is often referred to as NVE, as it fixes the number of particles in the system (N), the volume of the system (V), and the energy of the system (E). In a simulation this means that throughout the simulation, these three factors will not alter on average. It is the most fundamental, because unlike some of the other ensembles, it treats energy extensively, allowing the kinetic and potential energies to vary without constraints. It allows energy changes, provided that the total energy remains constant between ensemble members. It was used for equilibrium data collection where temperature control was not required.

In the canonical ensemble (NVT), the number of particles (N), volume (V)

and temperature (T) of the system are fixed. It was used mainly in cases where the system is very unstable and would otherwise undergo large and highly unphysical temperature and volume changes, such as during the melt-quench of a glass composition.

The isothermal-isobaric ensemble (NPT) fixes the number of particles (N), the system pressure (P) and the system temperature (T). As volume is not fixed within the NPT ensemble, volume relaxation of the simulation cell can occur. This allows, for example, predictions of volume change due to radiation damage to be considered.

3.5.3 Temperature and Pressure Control

In order to calculate thermodynamic properties of the solid materials it is necessary to control the temperature of the MD simulation using a thermostat. The equivalent mechanism for pressure is called a barostat and works along the same principles. A thermostat scales the atomic velocities, which affects the instantaneous temperature derived from the sum of all atomic momenta (equation 3.86):

$$\sum_{i=1}^N \frac{|\vec{p}_i|^2}{2m_i} = \frac{K_b T}{2} (3N - N_c) \quad (3.86)$$

where \vec{p}_i is the momentum of atom i , k_b is the Boltzmann constant, N is the number of degrees of freedom and N_c the number of constraints. The simplest form of a thermostat is to scale the velocities of all atoms in the system by a fixed factor to attain the target temperature. By simply scaling the velocities, energy is not conserved and thus the generated velocities are not part of the ensemble [202]. In addition, the lack of temperature oscillations can lead to locally metastable states to be sampled rather than a wider distribution of possible states, as these fluctuations may lead to a new, more stable minimum of the potential energy surface.

To produce true members of the isothermal ensembles (NPT, NVT), the concept of a time delayed energy flux to and from an external energy buffer is required. The most common analogy for these kind of thermostats is that of a system coupled to a “heat bath” of the desired system temperature. This heat bath is used to gradually remove excess kinetic energy from the system, which is moved into an external energy buffer akin to a hot (or cold) object in a much larger bath of water, which slowly assumes the same temperature. This allows for the rescaling of atomic energies, whilst keeping either the total momentum or the total energy (of the combination of simulation box and heat bath) constant. Equilibration occurs

for a set period of time, allowing some of the energy to be transferred to or from the heat bath. In radiation damage simulations, the heat bath is only applied to atoms crossing the bounding box, as otherwise the energy introduced by a radiation event is removed too quickly from the system for damage to be adequately modeled.

Unless otherwise stated, a system-wide Berendsen thermostat [203] was used in NVT calculations. It allows more rapid convergence of the system when compared to other thermostats (such as Nosé-Hoover), making it more suitable for use during the early stages of a simulation. The Berendsen thermostat features a heat bath of a fixed temperature, but does not generate trajectories within the micro-canonical ensemble, as whilst it does conserve total momentum, it does not conserve energy [202]. For each atom, a friction term κ_{Ber} is applied to the unscaled velocity vector $\vec{v}(t + \Delta t)$ to produce the new velocity vector $\vec{v}_{scaled}(t + \Delta t)$ as follows:

$$\kappa_{Ber}(t + \Delta t) = \left[1 + \frac{\Delta t}{\tau_T} \left(\frac{\sigma_{Ber}}{E_{kin}(t + \Delta t)} - 1 \right) \right]^{1/2} \quad (3.87)$$

where $\sigma = \frac{N}{2} k_B T_{ext}$

is the energy of the Berendsen thermostat [203], which depends on the degrees of freedom N of the system, the external temperature T_{ext} , which corresponds to the temperature of the heat bath and τ_T , which called the relaxation parameter and is related to the frequency of temperature fluctuations (kept fixed at 1 ps in all simulations here). Thus,

$$\vec{v}_{scaled}(t + \Delta t) = \vec{v}(t + \Delta t) \kappa_{Ber} \quad (3.88)$$

Nosé-Hoover thermo- and barostats [204] were used in NPT simulations. The Nosé-Hoover algorithm does not adjust the velocities of the next time step directly, but rather changes the rate at which the velocity changes. This ensures that all trajectories are in line with the canonical (NVT) ensemble in the real system and the micro-canonical ensemble in the extended system. However, unlike Berendsen [203], the lack of direct scaling retards the thermostat effect, and will lead to stronger oscillations [202]. This is not a serious problem in a system close to its thermal equilibrium. The velocity change is given by

$$\frac{d\vec{v}(t)}{dt} = \frac{\vec{a}(t)}{m} - \kappa_{NH}(t) \vec{v}(t) \quad (3.89)$$

A first order differential equation controls the friction coefficient κ_{NH}

$$\frac{\kappa_{NH}(t)}{dt} = \frac{2E_{kin}(t) - 2\sigma}{q_{mass}} \quad (3.90)$$

where σ is the thermostat energy as given in equation 3.87, and q_{mass} is the Nosé-Hoover thermostat mass given by

$$q_{mass} = 2\sigma\tau_T^2 \quad (3.91)$$

which depends on the relaxation parameter τ_T .

The pressure can be maintained at a constant value in a simulation by scaling the volume or an alternative is to couple the system to a “pressure bath” analogous to a temperature bath. The rate of change of pressure is given by

$$\frac{dP(t)}{dt} = \frac{1}{\tau_p} (P_{bath} - P(t)) \quad (3.92)$$

τ_p is the coupling constant, P_{bath} is the pressure of the ‘bath’ and $P(t)$ is the actual pressure at time t . The volume of the simulation box is scaled by a factor λ , which is equivalent to scaling the atomic coordinates by a factor $\lambda^{1/3}$. Thus

$$\lambda = 1 - \kappa \frac{\delta t}{\tau_p} (P - P_{bath}) \quad (3.93)$$

The new positions are given by:

$$r'_i = \lambda^{1/3} r_i \quad (3.94)$$

The constant κ can be combined with the relaxation constant τ_p as a single constant. This expression can be applied isotropically (such that the scaling constant is equal for all three directions) or anisotropically (where the scaling factor is calculated independently for each of the three axes). In general, it is best to use the anisotropic approach as this enables the box dimensions to change independently.

In the pressure bath-coupling methods as introduced by Anderson, an extra degree of freedom corresponding to the volume of the box is introduced in the system. The kinetic energy associated with this degree of freedom is $\frac{1}{2}Q(\frac{dV}{dt})^2$, where Q is the mass of the piston. This can also be considered to be equivalent to a piston acting on the system. The potential energy of the piston is PV where V is the volume of the system and P is the desired pressure. The piston of small mass gives rise to rapid oscillations in the box where as infinite mass gives normal molecular dynamics behavior. The volume can vary during simulation, with the

average volume being determined by the balance between the internal pressure of the system and the desired external pressure. In the Nosé approach a scaled time is used and the coordinates of the extended system are related to the ‘real’ coordinates by:

$$r'_i = V^{-1/3}r_i \quad (3.95)$$

3.6 Thermal Properties from MD Simulations

3.6.1 Thermal Expansion

At high temperatures, the anharmonic nature of the atomic interaction becomes significant and leads to thermal expansion in solids. When analyzing the system at various temperatures the usual experimental conditions are generated by the NPT method (with constant number of particle, pressure and temperature). Initial atomic velocities are generated by using a Monte-Carlo method according to the Maxwellian distribution. With this initial conditions, the system is allowed to evolve for several thousand time steps to reach thermal equilibrium. The criterion of establishing thermal equilibrium for the system at low temperatures is to monitor equipartition of the kinetic and potential energy. A series of MD simulations are conducted for several temperatures to calculate lattice parameters and volumes of the simulation cell at each temperature and hence the thermal expansion coefficient is determined.

3.6.2 Thermal Conductivity by Green-Kubo method

In Green-Kubo (GK) formalism [205, 206], an estimate of a transport coefficient relies on the integral of an accurate time-correlation of the equilibrium fluctuations of the corresponding heat flux in the system. Mathematically, GK theorem relates the lattice thermal conductivity tensor κ_{ij} to the integral of the ensemble average of the time correlation function of the heat current $J_i(t)$:

$$\kappa_{ij} = \frac{V}{k_B T^2} \int_0^\infty \langle \mathbf{J}_i(0) \mathbf{J}_j(t) \rangle \quad (3.96)$$

where $i, j = x, y, z$, V = simulated cell volume, k_B = Boltzman’s constant and T = temperature. $\mathbf{J}_i(0)$ and $\mathbf{J}_j(t)$ are the instantaneous heat flux in the i direction at time zero and instantaneous heat flux in the j direction at time t , respectively. Though the upper limit on the integral is infinite the duration of the simulation

must only exceed the relaxation time beyond which the integrand vanishes. In molecular dynamics simulations time is discretized into time-steps, and thus in practice equation 3.96 becomes a summation

$$\kappa_{ij} = \frac{V\Delta t}{k_B T^2} \sum_1^M (N-m) \sum_{n=1}^{N-m} \mathbf{J}_i(m+n) \mathbf{J}_j(n) \quad (3.97)$$

where N is the total number of time-steps, each of length Δt , $J_i(m+n)$ the instantaneous heat flux in the i direction at time-step $m+n$ and $J_j(n)$ the instantaneous heat flux in the j direction at time-step n . The instantaneous heat flux, in a given direction, is evaluated from the energy associated with each atom in the simulation

$$\mathbf{J} = \frac{d}{dt} \frac{1}{V} \sum_{i=1}^N \mathbf{r}_i e_i \quad (3.98)$$

where \mathbf{J} is the heat flux vector, r_i the position vector of atom i and e_i the energy associated with atom i , and the sum is over all N atoms. The energy associated with each atom is the sum of its kinetic energy and potential energy

$$e_i = \frac{1}{2} m_i \mathbf{v}_i^2 + \frac{1}{2} \sum_j^N u_{ij}(r_{ij}) \quad (3.99)$$

where m_i is the mass of atom i , \mathbf{v}_i the velocity vector of atom i , and $u_{ij}(r_{ij})$ the pair-wise interaction between atoms i and j when separated by a distance r_{ij} . Substituting equation 3.99 into equation 3.98 we obtain

$$\mathbf{J}(\mathbf{t}) = \frac{1}{V} \left[\sum_i^N e_i \mathbf{v}_i + \sum_i^N \sum_{j \neq i}^N (\mathbf{f}_{ij} \cdot \mathbf{v}_j) \cdot \mathbf{r}_{ij} \right] \quad (3.100)$$

where e_i = energy per atom of i th atom, \mathbf{f}_{ij} = force on atom i due to neighbor j , \mathbf{v}_i = velocity of atom i and $\mathbf{r}_{ij} = \mathbf{r}_i - \mathbf{r}_j$, where \mathbf{r}_i is the position vector of atom i .

It important to note that in the Green-Kubo calculations, finite-size effect are important and the calculated values converge towards experimental values with increasing system size. Such convergence must be checked for in order to ensure that calculated values are accurate.

Chapter 4

Finding Lowest Energy Barrier Pathway for $\alpha \rightarrow \omega$ Martensitic Transformation in Zr

4.1 Introduction

This chapter presents a systematic theoretical investigation of atomistic pathways for $\alpha \rightarrow \omega$ transformation adopting two approaches. In the first approach, we model transformation pathways by examining the experimentally proposed Usikov and Zilbershtein (UZ) [42], Rabinkin, Talianker and Botstain (RTB) [43] and Song and Gray (SG) [26] pathways (see section 2.1.1 (a) for details). We calculate transformation energy barrier for these three pathways by first-principles calculations employing Nudged Elastic Band (NEB) method and by comparison we suggest the lowest barrier pathway. In the second approach, initially, we generate transformation pathways by applying a symmetry analysis program based on search for an intermediate unstable common structure with definite space group symmetry G between parent G_1 (α , space group: P6₃/mmc) and product G_2 (ω , space group: P6/mmm) structures having no group-subgroup relation. Then, we calculate their energy barriers by first-principles calculations. Finally, we correlate pathways obtained from these two approaches to decide the most energetically favorable one. The second approach also ensures to generate all possible pathways that exist (with a given range of lattice strains and atomic shuffles) other than experimentally reported pathways.

The second approach deals with the problem of finding the most likely pathway for a $G_1 \rightarrow G \rightarrow G_2$ transformation which eventually reduces to produce a

relevant subset of possible pathways and sorting them by their energy barriers. There are infinitely many unique pathways to transform one crystal continuously into another; however, only a few of them do not involve movement of individual atoms by an appreciable distance. We produce the set of pathways (G 's) with minimum total shape change (strain) and minimum atomic motion (shuffle) from its parent structure (G_1). The symmetry analysis program generated pathways are sorted by using the first-principles calculated energy barrier of each transformation pathway. We further determine the change in transformation barrier height due to application of pressure for the lowest energy barrier pathway. Finally, we calculate transverse optical phonon mode ($\nu_{E_{2g}}$), C_{44} and electronic band structures of α -phase as a function of pressure to identify actual driving force for this transformation.

In the next section (section 4.2) a description of methodology for the first-principles calculations, elastic and phonon frequency calculations are described. Then, the details of the experimentally proposed UZ, RTB and SG pathways are described followed by their enthalpy barrier calculations in section 4.3. After that, symmetry analysis based program generated pathways are described followed by their enthalpy barrier calculations in section 4.4. In this section experimentally proposed and symmetry based program generated pathways are correlated to identify the most energetically favored pathway and its pressure variations. Finally, in section 4.5 pressure variation of transverse optical phonon mode ($\nu_{E_{2g}}$), C_{44} and electronic band structure of α phase are presented for finding driving force for this transformation.

4.2 Computational Details

Our theoretical investigation includes examination of TPs, elastic stability, dynamical stability and electronic band structure of α Zr under hydrostatic compression. All the calculations have been performed employing plane wave based ab-initio simulator Vienna Ab-initio Simulation Package (VASP) [177] with generalized gradient approximation (GGA) for the exchange and correlation potentials as parameterized by Perdew, Burke and Ernzerhof (PBE) [158]. The frozen core all electron projector-augmented wave (PAW) potentials [176] were used for the ion-electron interactions with $4s$ $4p$ $5s$ $4d$ states as valence states for Zr. The expansion of electronic wave functions in plane waves was set to a kinetic energy cut-off of 400 eV for all the structures and Brillouin zone integration was done using the k-point mesh of $18 \times 18 \times 14$, $10 \times 10 \times 10$ and $22 \times 16 \times 6$ Monkhorst-Pack [208] grid in the full Brillouin zone for

our 4, 6 and 12 atoms supercell calculations, respectively, to ensure energy convergence to within 0.1 meV/atom. The Methfessel-Paxton technique [209] was used for free energy calculations with a modest smearing of 0.1 eV, which resulted in a very small entropy term (<0.1 meV/atom) in all the cases. The relaxation of the atomic positions, the unit cell shape and size were performed using the conjugate gradient algorithm until the atomic forces are less than 5 meV/Å and the stresses are smaller than 0.01 GPa.

In order to determine elastic moduli, the total energy at a given volume is calculated as a function of appropriate strain (e). The energy of the strained lattice is expressed as follows [210]:

$$E_c(e, V) = E_c(0, V) + \frac{1}{2}V \sum_{i=1}^6 \sum_{j=1}^6 C_{ij} e_i e_j \quad (4.1)$$

The second order derivative of this energy with respect to strain provided the elastic moduli. The hcp Zr single crystal has 5 independent elastic constants, C_{11} , C_{12} , C_{33} , C_{13} and C_{44} . To determine shear modulus C_{44} , we used following volume conserving strain:

$$\begin{pmatrix} 1 & 0 & \alpha \\ 0 & \frac{\alpha^2}{1-\alpha^2} & 0 \\ \alpha & 0 & 0 \end{pmatrix} \quad (4.2)$$

Phonon calculations were performed using the small displacement method based code PHON [184]. The interatomic forces were obtained using first-principles calculations with 54 atom ($3 \times 3 \times 3$ supercell of hcp unitcell) supercell. To obtain the force constants for the phonon calculations, atomic displacements of 0.03 Å were employed.

4.3 Atomistic Details and Enthalpy Barriers of Experimentally Proposed Pathways

4.3.1 UZ Pathway [42]

In order to study UZ pathway, it is useful to visualize the $\alpha \rightarrow \omega$ transformation in two steps, $\alpha \rightarrow \beta$ and $\beta \rightarrow \omega$. In the first step, $\alpha \rightarrow \beta$ transformation was studied at constant volume via inverse Burgers pathway [211] and considering a

base centered orthorhombic cell having lattice parameters:

$$a_0(\lambda_1) = \frac{a_\beta}{\delta(\lambda_1)}; \quad b_0(\lambda_1) = \delta(\lambda_1)a_\beta\sqrt{2}; \quad c_0 = a_\beta\sqrt{2} \quad (4.3)$$

$$\delta(\lambda_1) = 1 + \left(\left(\frac{3}{2}\right)^{\frac{1}{4}} - 1\right)\lambda_1$$

and with 4 atom basis at:

$$\begin{aligned} &0, \frac{3 + \lambda_2}{12}b_0(\lambda_1), \frac{1}{4}c_0; \quad 0, \frac{9 + \lambda_2}{12}b_0(\lambda_1), \frac{1}{4}c_0 \\ &0, \frac{9 - \lambda_2}{12}b_0(\lambda_1), \frac{3}{4}c_0; \quad 0, \frac{3 - \lambda_2}{12}b_0(\lambda_1), \frac{3}{4}c_0 \end{aligned} \quad (4.4)$$

where $\lambda_1=\lambda_2=1$ and $\lambda_1=\lambda_2=0$ correspond to hcp and β lattice, respectively. λ_1 represents the shear deformation and λ_2 represents the shuffle displacement. The calculated equilibrium lattice parameter for β Zr (a_β) was 3.5818 Å. This transformation causes atomic movement of 0.42 Å accompanied by 3.6% contraction along the $[11\bar{2}0]$ direction and 6.2% expansion along the $[1\bar{1}00]$ direction [44].

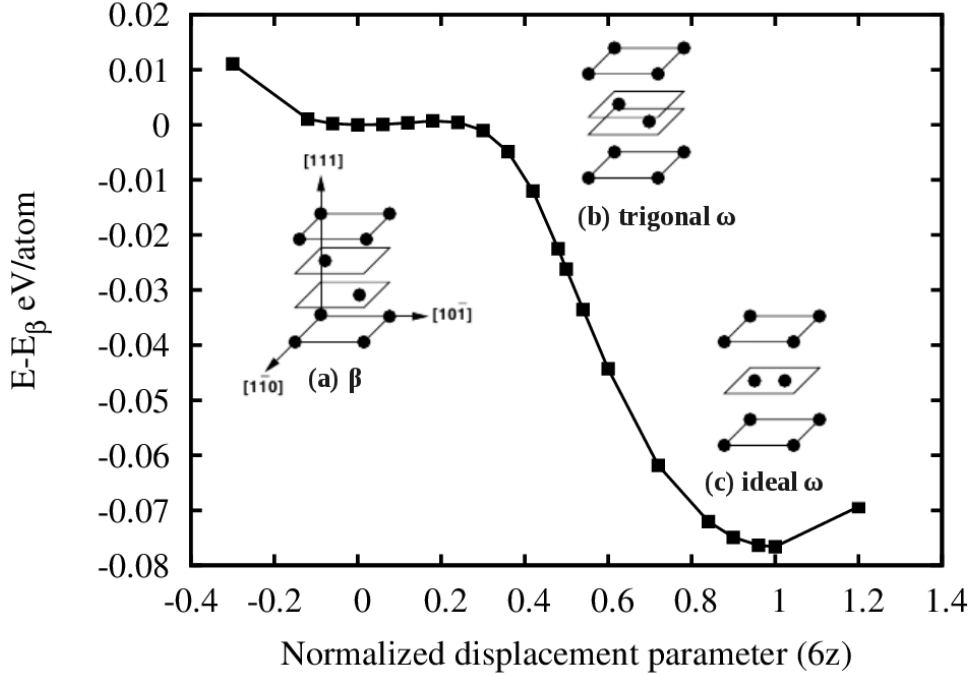


Figure 4.1: Energy barrier of $\beta \rightarrow \omega$ transformation for possible range of atomic shuffles. Normalized atomic shuffle parameter $6z = 0$ and 1 correspond to β and ω structure, respectively.

In the second step, $\beta \rightarrow \omega$ transformation requires only a shuffle of $\lambda_3 = a_\beta \frac{\sqrt{3}}{12} \sim 0.52$ Å. Details of the atomic movements of this transformation is described

in Figure 4.1. The trigonal C6 incomplete ω -phase (shown in Figure 4.1 is based on the $P\bar{3}m1$ space group (International Table No. 164). This is a prototype structure of CdI_2 and has 3 atoms per unitcell: (1a) 0 0 0, (2d) $1/3$ $2/3$ $2/3-z$ and $2/3$ $1/3$ $1/3+z$. In CdI_2 structure Cd atom occupy the (1a) Wyckoff position and the I atoms occupy the (2d) positions. When $z = 0$, this structure transforms into the hexagonal C32 complete ω -structure. When $z = 1/6$, it is equivalent to the β structure for $c/a = \sqrt{3/8}$. The hexagonal C32 complete ω -phase is based on the $P6/mmm$ space group (International Table No. 191). This is a prototype structure of AlB_2 and has 3 atoms per unitcell: (1a) 0 0 0, (2d) $1/3$ $2/3$ $1/2$ and $2/3$ $1/3$ $1/2$. In AlB_2 structure Al atom occupy the (1a) Wyckoff position and the B atoms occupy the (2d) Wyckoff positions. Figure 4.1 also depicts GGA-PBE calculated energy barrier for the $\beta \rightarrow \omega$ transformation and transformation barrier for this pathway is 80.8 meV/atom.

4.3.2 RTB Pathway [43]

Figure 4.2 describes the direct transformation RTB pathway which involves significant atomic shuffles and relatively small strains. The energy barrier calculations of RTB pathway were performed considering a 12 atom hcp supercell using calculated equilibrium lattice parameters a_α (3.2314 Å) and c_α (5.1748 Å) with atomic positions as described in Table 4.1.

In RTB pathway, each atom shuffles by 0.87 Å on the $(0001)_\alpha$ plane. The accompanying strains required to produce the ω lattice with correct c/a ratio was determined by performing a lattice shape relaxation using DFT-GGA at constant volume of a supercell having hcp lattice vectors but atomic positions corresponding to the ω lattice. The lattice strains (ϵ 's) obtained by this procedure is listed in Table 4.1 and it can be noted that $\epsilon_x\epsilon_y\epsilon_z \sim 1$, as we performed our calculations at constant volume. It can be noted that for the hcp supercell $\epsilon_x=\epsilon_y=\epsilon_z=1$. Moreover, the PAW-PBE calculated strains of -2.22% along $[1\bar{2}10]_\alpha$ direction, -2.09% along $[0001]_\alpha$ direction and 4.46% along $[\bar{1}010]_\alpha$ direction are in good agreement with experimentally determined strains of -2.97%, -2.14% and 3.94% along the respective directions [43].

4.3.3 SG Pathway [26]

Figure 4.3 illustrates another direct transformation pathway described by SG which involves small atomic shuffles and strains. The details of the PAW-PBE calculated

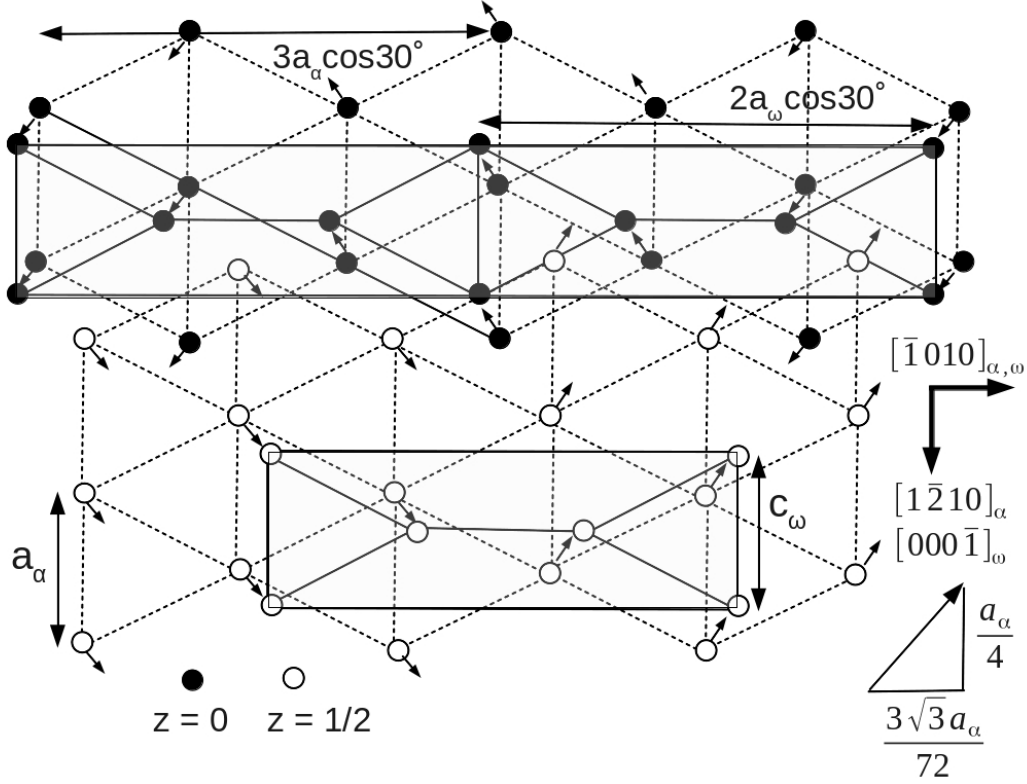


Figure 4.2: **The RTB pathway:** in each $(0001)_\alpha$ stacking plane three neighboring closed-pack $[\bar{1}\bar{2}10]_\alpha$ atomic rows are displaced by a distance $\frac{a_\alpha}{4}$ along $[\bar{1}\bar{2}10]_\alpha$ direction and the next three parallel atomic rows are displaced by the same distance along the opposite direction $[\bar{1}2\bar{1}0]_\alpha$ produces atomic arrangement corresponds to that of $[\bar{1}\bar{2}10]_\omega$ plane of distorted ω structure. An additional small atomic shuffle of $\frac{a_\alpha\sqrt{3}}{24}$ along $[\bar{1}010]_\alpha$ direction is also required to produce ideal ω structure. This shuffle is accompanied by strain components of -2.97% along $[\bar{1}\bar{2}10]_\alpha$ direction, -2.14% along $[0001]_\alpha$ direction and 3.94% along $[\bar{1}010]_\alpha$ direction to produce a hexagonal ω structure with correct c/a ratio. The orientation relations connecting the α and ω supercells are $(0001)_\alpha \parallel (1\bar{2}10)_\omega$; $[\bar{1}\bar{2}10]_\alpha \parallel [0001]_\omega$.

atomic positions and strains are described in Table 4.1. In SG pathway all 6 atoms in the supercell shuffles by 0.47 \AA on the $(0001)_\alpha$ plane and 4 atoms out of 6 additionally shuffles by 0.51 \AA out of the $(0001)_\alpha$ plane accompanied by strains of $\epsilon_x = 0.906$, $\epsilon_y = 1.113$ and $\epsilon_z = 0.997$ produces ω supercell from α as also given in Table 4.1. For this pathway, strains were determined as described for the RTB pathway. It is also crucial to note that orientation relationships between ω supercell and α : $(0001)_\alpha \parallel (1\bar{1}\bar{1}1)_\omega$; $[11\bar{2}0]_\alpha \parallel [01\bar{1}1]_\omega$ as described in Figure 4.3 which is a subset of **(OR I)**: $(0001)_\alpha \parallel (01\bar{1}1)_\omega$; $[11\bar{2}0]_\alpha \parallel [01\bar{1}1]_\omega$.

The NEB calculations were performed by taking 9 images to determine enthalpy barrier for RTB and SG direct transformation pathways. The NEB method

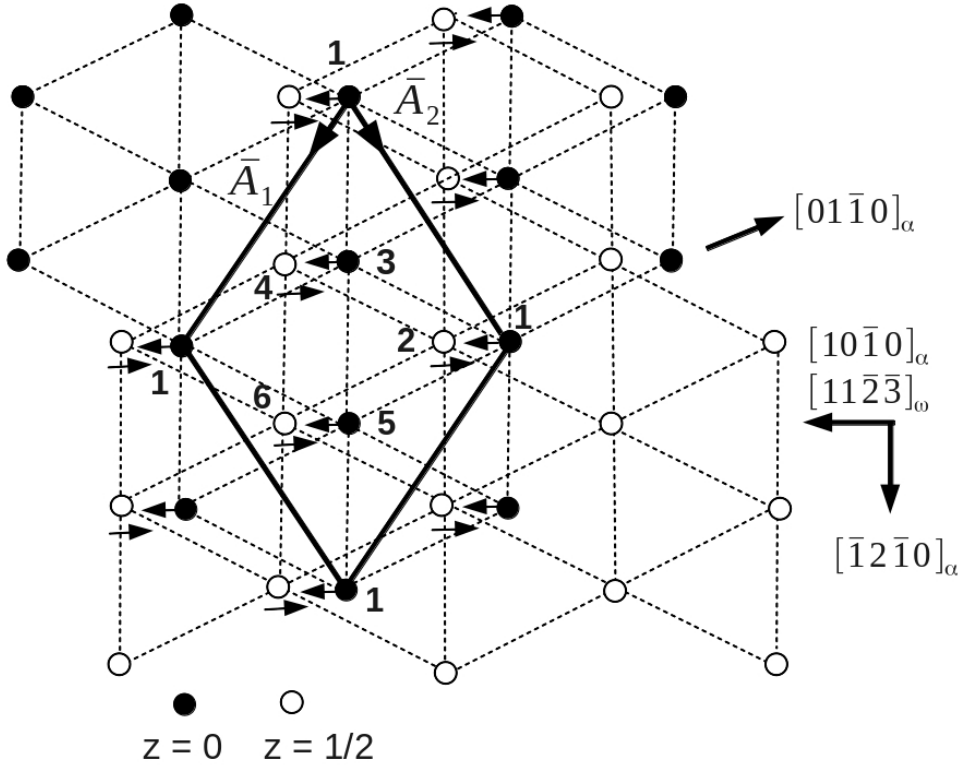


Figure 4.3: **The SG pathway:** in each stacking $(0001)_\alpha$ plane atoms of label 1, 3, 5 and atoms of label 2, 4, 6 are moved by $\frac{a_\alpha\sqrt{3}}{12}$ along $[10\bar{1}0]_\alpha$ and $[\bar{1}010]_\alpha$ directions, respectively. This shearing movement can be decomposed into two equal movements by a fraction $\pm\frac{1}{12}$ along A_1 and A_2 (as described in Table 1). Additionally, atoms of level 2, 3 and 3, 4 are shifted by a fraction $-\frac{1}{12}$ and $\frac{1}{12}$ of A_3 lattice vector along A_3 , respectively. In this process $(0001)_\alpha$ plane transforms into $(10\bar{1}1)_\omega$ plane. The arrows indicate atom movements along the $(0001)_\alpha$ plane only. This shuffle is accompanied by lattice strain ϵ such that $A'(\omega) = \epsilon A(\alpha)$ to produce a hexagonal ω structure with correct c/a ratio. The supercell lattice vectors are also shown (as described in Table 1) in this figure. The atomic arrangements in this figure are depicted according to our choice of supercell. The orientation relations connecting the α and ω supercells are $(0001)_\alpha \parallel (0\bar{1}11)_\omega$; $[11\bar{2}0]_\alpha \parallel [01\bar{1}1]_\omega$.

generates a discrete pathway (by generating a chain of images) connecting initial and final states. By relaxing atomic positions and lattice shape at constant volume, it passes through the transition state to guarantee that the final pathway lies along the minimum energy pathway to produce true energy barrier. Figure 4.4 shows the change in enthalpy along $\alpha \rightarrow \omega$ transition path for the RTB and SG pathway. The SG pathway has the lowest barrier height of 22 meV/atom compared to 58 meV/atom and 73.7 meV/atom for the RTB and UZ pathway, respectively.

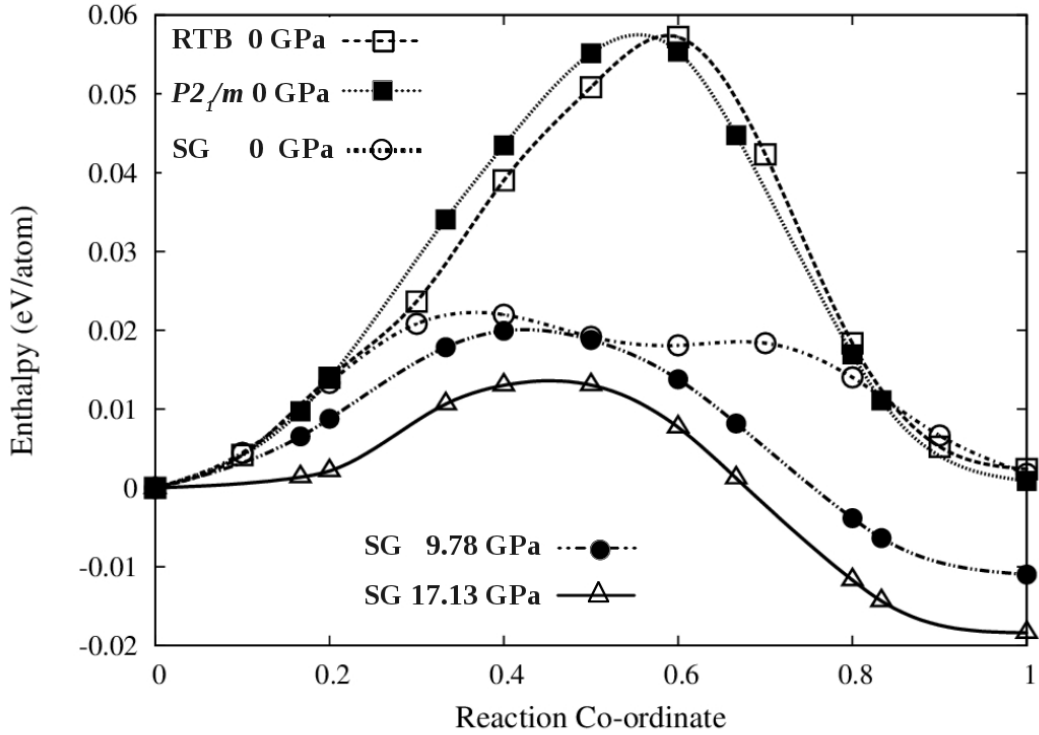


Figure 4.4: GGA-PBE Calculated enthalpy barrier versus reaction co-ordinate as a function of pressure for the RTB and SG pathway using ab-initio NEB method with 9 intermediate images. At 0 GPa enthalpy barrier for the SG pathway is almost 3 times lower than the RTB pathway. With increasing pressure barrier for the SG pathway also decreases and even at 17.13 GPa barrier is not zero.

4.4 COMSUBS Generated Pathways

We applied a space-group symmetry based method employing group-subgroup relations for characterizing martensitic transformation, called COMSUBS [212] package, to generate possible TPs (or mapping $G_1 \rightarrow G \rightarrow G_2$) via G from G_1 (with our PAW-PBE calculated lattice parameters $a_\alpha = 3.2314 \text{ \AA}$, $c_\alpha = 5.1748 \text{ \AA}$) to G_2 (with $a_\omega = 5.0575 \text{ \AA}$, $c_\omega = 3.1572 \text{ \AA}$) by considering both strains and atomic displacements. The mapping is restricted by the constraint that the symmetry G must be maintained along the entire path G_1 to G_2 . This program finds possible paths taken by atoms in a martensitic phase transition which is accomplished by finding maximal common subgroups of the two phases. This methodology has already been successfully implemented to determine TP for pressure induced NaCl \rightarrow CsCl transformation in the past [213].

This methodology includes user defined input of allowed strain tolerance,

Table 4.1: Details of the α and ω supercell generated to study RTB and SG pathway. The strains required to produce the ω lattice with correct c/a ratio from α shown in the table are our PAW-PBE calculated values.

Pathway	Supercell and Strains	Atomic Positions for α	Atomic Positions for ω
RTB	$A_1 = a_0 \epsilon_x \hat{x}$ $A_2 = -c_0 \epsilon_y \hat{y}$ $A_3 = -3\sqrt{3} a_0 \epsilon_z \hat{z}$ strains $\epsilon_x = 0.978$ $\epsilon_y = 0.979$ $\epsilon_z = 1.044$	0 1/4 2/9	-1/4 1/4 5/24
		0 1/4 5/9	1/4 1/4 13/24
		0 1/4 8/9	-1/4 1/4 21/24
		0 3/4 1/9	-1/4 3/4 3/24
		0 3/4 4/9	-1/4 3/4 11/24
		0 3/4 7/9	1/4 3/4 19/24
		1/2 1/4 1/18	1/4 1/4 1/24
		1/2 1/4 7/18	3/4 1/4 9/24
		1/2 1/4 13/18	3/4 1/4 17/24
		1/2 3/4 5/18	1/4 3/4 7/24
1/2 3/4 11/18	3/4 3/4 15/24		
1/2 3/4 17/18	3/4 3/4 23/24		
SG	$A_1 = a_0 \frac{\sqrt{3}}{2} \epsilon_x \hat{x} + a_0 \frac{3}{2} \epsilon_y \hat{y}$ $A_2 = -a_0 \frac{\sqrt{3}}{2} \epsilon_x \hat{x} + a_0 \frac{3}{2} \epsilon_y \hat{y}$ $A_3 = a_0 \epsilon_y \hat{y} + c_0 \epsilon_z \hat{z}$ strains $\epsilon_x = 0.906$ $\epsilon_x = 1.113$ $\epsilon_x = 0.997$	0 0 0	1/12 -1/12 0
		1/6 5/6 1/2	1/12 11/12 1/2
		1/3 1/3 0	5/12 1/4 -1/12
		1/2 1/6 1/2	5/12 1/4 5/12
		2/3 2/3 0	3/4 7/12 1/12
		5/6 1/2 1/2	3/4 7/12 7/12

nearest neighbor (NN) distances and unit-cell size change. We used the following criteria:

- (a) only 6 and 12 atom supercells with principal elements of the strain tensor being less than 1.2 and greater than 0.8 is considered
- (b) relative to the center of mass, no atom shuffles more than 1.3 Å and
- (c) considering only subgroups where the NN distance in the structure is halfway between G_1 and G_2 is greater than 2.85 Å.

The basis for setting up these criteria is the displacive-diffusionless nature

Table 4.2: Maximal common subgroup (G) of the two phases $G_1 = P6_3/mmc$ and $G_2 = P6/mmm$ of Zr. G provides a possible path for the transition from G_1 to G_2 as $G_1 \rightarrow G \rightarrow G_2$. We give the atomic positions and supercell lattice vectors of G_1 and G_2 in terms of the conventional lattice vectors $a_1 = a_0(\frac{1}{2}\hat{x} - \frac{\sqrt{3}}{2}\hat{y})$, $a_2 = a_0(\frac{1}{2}\hat{x} + \frac{\sqrt{3}}{2}\hat{y})$, $a_3 = c_0\hat{z}$ of G_i (a_0 and c_0 are the respective equilibrium lattice parameters of G_i). In the last column an estimate of the approximate barrier height is given.

Common Subgroups	Supercell Lattices	α Wyckoff Positions	ω Wyckoff Positions	Barrier Height (meV/atom)
C2/c (15)	α : origin (1/2 1/2 1/2) (1,0,-2),(1,2,0),(1,0,1) ω : origin (0 0 -1/2) (1,-1,2),(-1,-1,0),(0,0,-2)	2(e) 0, 11/12, 1/4 4(f) 1/6, 5/12, 7/12	2(e) 0, 1, 1/4 4(f) 1/6, 1/2, 2/3	66.3
Pbcm (57)	α : origin (1 3/2 0) (1,0,0),(3,6,0),(0,0,1) ω : origin (-1/2 0 0) (0,0,-1),(-2,2,0),(1,1,0)	4(d) 3/4, 31/36, 1/4 4(d) 3/4, 7/36, 1/4 4(d) 3/4, 19/36, 1/4	4(d) 1, 7/8, 1/4 4(d) 1/2, 5/24, 1/4 4(d) 1/2, 13/24, 1/4	67.7
P2 ₁ /m (11)	α : origin (0 0 0) (-1,0,0),(0,0,1),(0,3,0) ω : origin (0 -1/2 0) (0,0,1),(1,1,0),(-1,1,1)	2(e) 2/3, 1/4, 2/9 2(e) 2/3, 1/4, 8/9 2(e) 2/3, 1/4, 5/9	2(e) 3/4, 1/4, 1/4 2(e) 7/12, 1/4, 11/12 2(e) 11/12, 1/4, 7/12	89.1
Pnma (62)	α : origin (0 0 0) (2,1,0),(0,0,-1),(0,3,0) ω : origin (0 1/2 0) (0,0,-2),(1,1,0),(1,-1,0)	4(c) 5/6, 1/4, 5/6 4(c) 5/6, 1/4, 1/6 4(c) 5/6, 1/4, 1/2	4(c) 1, 1/4, 3/4 4(c) 3/4, 1/4, 1/12 4(c) 3/4, 1/4, 5/12	115.0
P $\bar{1}$ (2)	α : origin (0 0 0) (0,0,2),(1,2,0),(-1,1,0) ω : origin (1/2 1/2 1/2) (0,-1,-3),(-1,-1,0),(-1,0,-1)	2(i) 1/8 1/3 0 2(i) 3/8 0 1/3 2(i) 1/8 2/3 1/3 2(i) 3/8 1/3 2/3 2(i) 1/8 0 2/3 2(i) 3/8 2/3 0	2(i) 1/8 3/8 1/8 2(i) 3/8 1/8 3/8 2(i) 1/6 2/3 1/2 2(i) 5/12 5/12 3/4 2(i) 1/12 1/12 3/4 2(i) 1/3 5/6 0	304.6
P $\bar{1}$ (2)	α : origin (-1/2 1/2 1) (1,0,1),(-1,2,1),(-1,-1,1) ω : origin (1/2 1 -1/2) (0,0,-2),(0,2,-1),(1,1,-1)	2(i) 1/24 19/24 5/12 2(i) 23/24 7/8 11/12 2(i) 1/24, 11/24, 3/4 2(i) 13/24, 23/24, 3/4 2(i) 13/24, 7/24, 5/12 2(i) 11/24, 3/8, 11/12	2(i) 1/8 3/4 1/2 2(i) 1/8 11/12 5/6 2(i) -1/8, 5/12, 5/6 2(i) 5/8, 11/12, 5/6 2(i) 3/8, 1/4, 1/2 2(i) 3/8, 5/12, 5/6	355.7

of this transformation. A displacive transformation distorts the lattice and changes the shape of the crystal, while diffusionless character restricts movement of atoms small compared to the nearest neighbor distances [17, 33]. Therefore, we consider only strain components within range of $\pm 20\%$ compared to G_1 structure and NN distance at the halfway is 93.5% of the average of 3.19 Å and 2.92 Å. It can be noted that the NN distance is 3.19 Å in G_1 and 2.92 Å in G_2 . With these criteria,

we obtained 6 subgroups, which we list in Table 4.2. We also give our PAW-PBE calculated enthalpy barriers for the halfway structures (G) in table 4.2 by calculating energies of the G_1 , G_2 and G structures for each pathway.

From Table 4.2, four lowest energy barrier pathways can easily be noticed out of possible 6 pathways. We then analyzed these four lowest energy barrier pathways using a symmetry analysis program FINDSYM [212] and found out that pathway with Pnma, Pbcm and C2/c subgroups are identical with the experimentally proposed UZ, RTB and SG pathways, respectively. Another pathway with subgroup P2₁/m follows the **OR II** and was studied using NEB calculations and the barrier height of this pathway is same as that of RTB pathway (shown in Figure 4.2). Therefore, symmetry based pathway generation program and model pathways given from experimental inputs essentially outline the same subset of possible pathways. It can also be noted that during the transformation the closest nearest-neighbor distance is 3.01 Å for SG pathway which is larger than 2.93 Å and 2.91 Å for the RTB and UZ pathway, respectively. Therefore, the SG pathway is a suitable combination of small strains, small relative atomic shuffle - which are the essential criterion for diffusionless displacive transformation. It can also be noted that the calculated barrier height for C2/c TP (generated using COMSUBS) is higher than that for SG, as the structure we used (as written by COMSUBS output) to calculate the enthalpy barrier for C2/c TP lies exactly halfway between G_1 and G_2 , assuming atomic displacement and lattice strain parameters are varying linearly from G_1 to G_2 [212, 213]. Enthalpy barrier calculated with this halfway structure is approximate and estimates only the upper bound on the barrier height. The path from G_1 to G_2 , which passes over the lowest barrier, will most likely not follow this linear variation in atomic displacement and lattice strain parameters. Figure 4.4 also shows the change in enthalpy along $\alpha \rightarrow \omega$ transition path for the SG pathway as a function of pressure. As pressure increases the enthalpy of ω decreases compared to α and even at 17.13 GPa the transformation is not complete. This result is also in agreement with the experimental fact that even at 16 GPa, the Raman frequencies corresponding to both α and ω were observed [47].

4.5 Precursor to $\alpha \rightarrow \omega$ transformation

The hcp structure allows one Raman active phonon mode which is transverse optical phonon mode (E_{2g}) at Γ point of the hcp brillouin zone. Figure 4.5 illustrates the energy variation (compared to undistorted supercell of hcp) of zone centre E_{2g} mode as function of different compressed volume V (with respect to the equilibrium

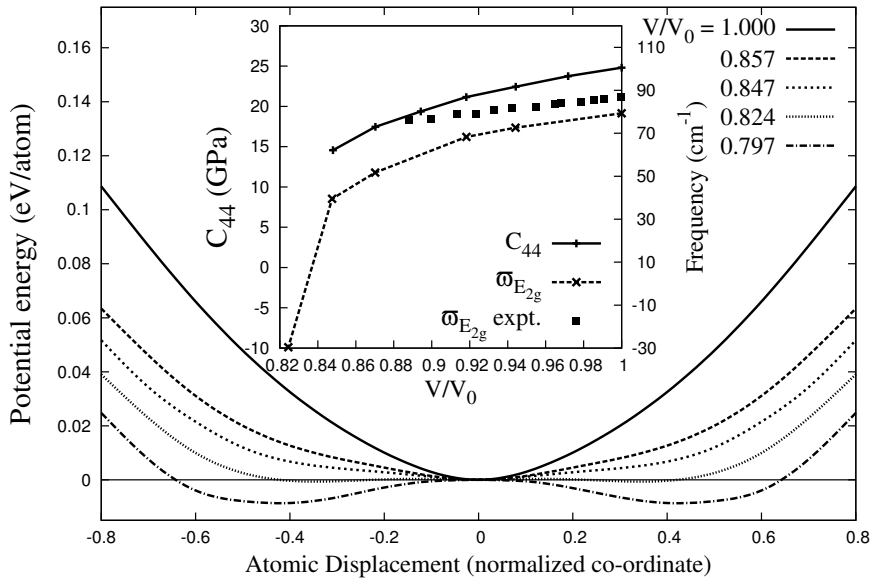


Figure 4.5: Variation of calculated potential energy versus zone center phonon mode (E_{2g}) in terms of normalized atomic displacement as a function of volume compression. The inset figure shows variation of the calculated zone center phonon frequencies and calculated values of C_{44} as a function of volume compression. The calculated values of $\nu_{E_{2g}} = 79.3 \text{ cm}^{-1}$ and $C_{44} = 24.8 \text{ GPa}$ at ambient pressure are in good agreement with respective experimental values of 87 cm^{-1} [47] and 33 GPa [215] (room temperature). Solid boxes show experimental values of $\nu_{E_{2g}}$ as a function of pressure [47].

volume V_0) using frozen phonon method [214]. For $V/V_0 = 1$, the effective potential has a minimum at zero atomic displacement. With increasing pressure, the effective potential transforms into double well from a single well having maxima at equilibrium atomic position between V/V_0 values of 0.847 and 0.824, corresponding to the pressure range of 20.47 - 24.83 GPa, which is much higher than the experimentally observed $\alpha \rightarrow \omega$ transformation pressure. Additionally, we calculated phonon dispersion curves using small displacement method and C_{44} elastic constant for different pressure and the calculated results are also plotted in Figure 4.5. Even though the calculated $\nu_{E_{2g}}$ values as a function of pressure from phonon dispersion curve show similar behavior compared to experimental values, the calculated $\nu_{E_{2g}}$ underestimates the experimental values over the whole pressure range and can be attributed to the thermal entropy effects as experimental values were obtained at 300 K. Moreover, the calculated $\nu_{E_{2g}}$ at $V/V_0 = 0.824$ is negative and is consistent with the fact that the calculated potential landscape for the E_{2g} mode became double well nature at this compression.

We also calculated band structure of hcp Zr along different symmetry di-

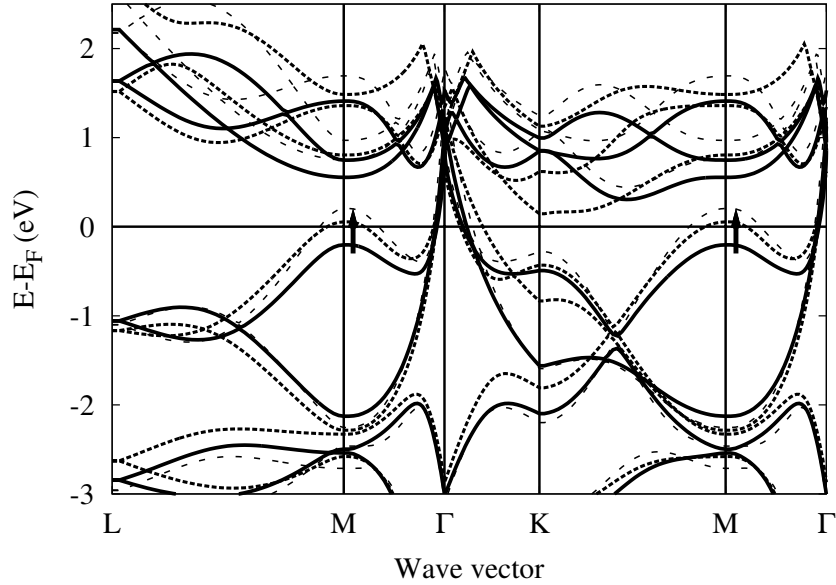


Figure 4.6: Band structure of α Zr along high symmetry directions at ambient pressure (solid line), at 9.363 GPa (large dotted line) and distorted hcp lattice to simulate a zone center TO E_{2g} mode (small dotted line) at ambient pressure.

rections at ambient pressure and at 9.36 GPa along with distorted hcp lattice to generate E_{2g} phonon mode at ambient pressure (illustrated in Figure 4.6). With increasing pressure around special k-point ‘M’ a d -like band moves up continuously leaving the Fermi level behind (indicted by arrows in Figure 4.6). This same feature is observed with E_{2g} phonon mode distorted hcp lattice indicating that this transformation is, in fact, driven by change in the topology of band structure, which leads to softening of E_{2g} phonon mode and C_{44} under compression.

4.6 Summary

Our systematic theoretical study of finding basic atomistic mechanism leads to the direct SG pathway being the energetically most preferred one for pressure induced $\alpha \rightarrow \omega$ transformation in pure Zr. This pathway is a suitable combination of small strains and small relative atomic shuffle compared to the NN distances, which are the essential criterion for diffusionless displacive transformation. The most favorable TP has a $C2/c$ common space group along the TP and has an enthalpy barrier of 22 meV/atom at 0 K. Our calculations show, the pressure induced softening of shear elastic constant (C_{44}) and transverse optical phonon frequency at Γ point is a precursor to this transformation. We also find the topological change in the band structure around special k-point ‘M’ is associated with this transformation.

Chapter 5

$\beta \rightarrow$ ordered- ω Phase

Transformation Pathways in Zr-Al Alloys

5.1 Introduction

In chapter 4, a modeling strategy is presented to determine the phase transformation pathway on the free energy landscape of a displacive transformation where a maximal common-subgroup (G) is determined in a diffusionless-displacive transformation of α (G_1 , P6₃/mmc) \rightarrow ω (G_2 , P6/mmm) in pure Zr. In this chapter, we present results of theoretical studies to determine phase transformation pathway in a diffusive-displacive transformation. One example of a mixed-mode phase transformation is the transformation of disordered β -phase to a variety of ordered ω structures in Zr rich Zr₂Al and Zr₂Al-Nb alloys. Here, the bcc lattice is transformed into the hexagonal ω -structure by a periodic displacement of lattice planes (described in section 2.1.1) while the decoration of the ω -lattice by different atomic species occurs through diffusional atomic movements. This study presents results of the quantitative determination of thermodynamic tendencies for diffusive *vis-a-vis* displacive processes at different stages of the transformation to delineate the actual pathway on the free energy landscape.

In the present work, we attempt to understand the mechanism of formation (or transformation pathway) of ordered- ω (Zr₂Al phase having B8₂ structure, space grp. P6₃/mmc) by replacive-displacive processes in an alloy of Zr₂Al (having disordered bcc (β) structure) by employing purely a first-principles computational methodology. The essential idea behind selecting this particular configuration (com-

position and structure) is that experimentally, at this composition, the sequence of formation of various ordered ω phase have already been reported [23]. We also determine relative stability of ordered ω and several disordered configurations of ω and β structures. We also correlate instability with respect to ω -type atomic displacements in Zr_2Al alloy and the number of Zr-Al bonds present in the unit cell.

To extend this study, formation of chemically ordered athermal ω phases having compositions Zr_3Al_2Nb and Zr_4AlNb from respective disordered β phase of same composition through coupled replacive-displacive processes is also investigated. In order to represent a structure which is compositionally close to $Zr_{59}Nb_{20}Al_{21}$ alloy, we consider 16.67 atom% Nb substitutions in Zr_2Al binary phase (see section 2.1.2). We select two compositions, *viz.*, Zr_3Al_2Nb and Zr_4AlNb for our calculations because this compositions arise naturally as a ternary extension of Zr_2Al phase (Ni_2In prototype structure) if one Zr atom is replaced by Nb atom leading to Zr_3Al_2Nb and if one Al atom is replaced by Nb atom leading to Zr_4AlNb in a 6 atom unitcell. For Zr_2Al -Nb systems, only “athermal ω ” (no change in composition during the transformation) has been studied. To the best of our knowledge, no other theoretical study has been attempted to study the formation of Zr_3Al_2Nb and Zr_4AlNb ternary alloys. The present study is concerned with the electronic origin of disordered $\beta \rightarrow$ chemically ordered athermal ω transformations in Zr_3Al_2Nb and Zr_4AlNb alloy employing purely a first-principles based approach. In this transformation replacive ordering is mediated through random atomic jumps (keeping composition intact to parent phase) for decorating specific sublattice sites by specific atomic species in the disordered parent structure. First principles calculations are used to calculate crystal structure parameters, structural stabilities and electronic properties for β and ω structures. We also compare mechanical stability and ductility of Zr_2Al and Zr_3Al_2Nb as well as Zr_4AlNb phases.

5.2 Disordered $\beta \rightarrow$ ordered- ω Athermal Transformation Pathway in Zr_2Al alloy

The equilibrium Zr_2Al ($B8_2$) structures can be viewed as chemically ordered derivatives of the ω structure. The $\beta \rightarrow B8_2$ transition can be accomplished by decorating the β (bcc) lattice with ordered arrangements of different atomic species and introducing a lattice collapse akin to the $\beta \rightarrow \omega$ transition [17, 22, 23].

Banerjee *et al.* [23] studied the phase evolution process during rapid solidifi-

cation of an alloy close to Zr_3Al composition and the quenched-in structure shows a supersaturated β phase with composition modulation resulting from spinodal decomposition. On subsequent ageing, the amplitude of composition modulation along the $\langle 100 \rangle_\beta$ directions increases and finally the aluminium enriched regions of cuboidal shape undergo the $\beta \rightarrow B8_2$ transition. Each single cuboidal block is seen to transform into a single $B8_2$ particle. The absence of multiple variants of $B8_2$ crystals within a cuboidal block, unlike that observed in the $\beta \rightarrow \omega$ transformation on quenching, suggests that the transformation is driven by an instability towards the development of concentration and displacement waves.

5.2.1 Description of Crystal Structures

The $B8_2$ structure of the Zr_2Al phase belongs to space group $P6_3/mmc$ (194) and its prototype is Ni_2In with 6 atoms per unit cell:

$$Ni : (2a) 0 0 0 \text{ and } 0 0 1/2,$$

$$In : (2c) 1/3 2/3 1/4 \text{ and } 2/3 1/3 3/4,$$

$$Ni : (2d) 1/3 2/3 3/4 \text{ and } 2/3 1/3 1/4.$$

As discussed by Bendersky *et al.* [70], all the relevant structures related to the omega phase formation can be indexed by $P\bar{3}m1$ space group which is a subgroup of both the parent and daughter structures. Therefore, all the relevant structures (bcc, ω' and ω ($B8_2$)) can be represented by a general lattice with Wyckoff positions as:

$$(1a) 0 0 0$$

$$(1b) 0 0 1/2$$

$$(2d1) 1/3 2/3 1/6+Z \text{ and } 2/3 1/3 5/6-Z$$

$$(2d2) 2/3 1/3 1/3-Z \text{ and } 1/3 2/3 2/3+Z.$$

The bcc and $B8_2$ lattices can be realized for $Z = 0$ (Figure 5.1(a) with $c/a = \sqrt{6}/2$ (ideal value)) and $Z = 1/12$ (Figure 5.1(c)), respectively. Similarly, the ω' structure is realized for $0 < Z < 1/12$ (Figure 5.1(b)).

5.2.2 Computational Methodology

The ground-state energy calculations were performed using a plane wave based code, viz., the Vienna Ab-initio Simulation Package (VASP) [177]. The VASP is based on the density functional theory (DFT) and we used generalized gradient approximation (GGA) for the exchange and correlation potentials as parameterized

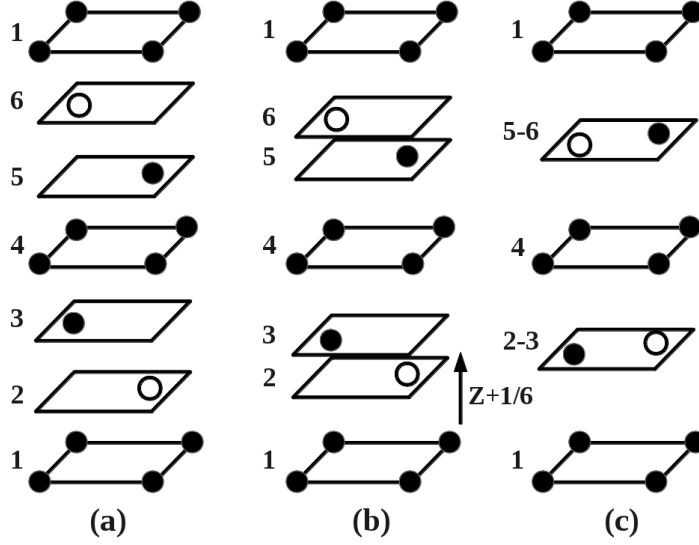


Figure 5.1: (a) Stacking of the $(222)_\beta$ planes of the bcc Zr_2Al phase, (b) ω'' structure (partial collapse of the planes), (c) ω structure (full collapse of two of the planes). The parameter Z is a measure of the movement of the second and third plane along with their Wyckoff counterparts. When all planes are equidistant, $Z = 0$, and the first plane is at a distance $1/6$ of c/a above the lowest plane. As the shuffle progresses to completion, this plane moves up by $1/12$ of c/a (the plane above it simultaneously moves down by $1/12$ of c/a).

by Perdew, Burke and Ernzerhof (PBE) [158]. The frozen core all electron projector augmented wave (PAW) potentials [176] were used for the ion-electron interactions. For Zr: $4s\ 4p\ 5s\ 4d$ and for Al: $3s\ 3p$ states were used as valence states. The expansion of electronic wave functions in plane waves was set to kinetic energy cutoff (E_{cut}) of 350 eV for all the structures. The Brillouin-zone integration was done using the Monkhorst-Pack [208] k-point mesh. The Methfessel-Paxton technique [209] was used for free energy calculations with a modest smearing of 0.1 eV, which resulted in a very small entropy term (<0.1 meV/atom) in all the cases. For each structure, optimization was carried out with respect to E_{cut} and k-point meshes to ensure convergence of total energy to within a precision better than 1 meV/atom.

In order to calculate the ground state energy of the ordered Zr_2Al configuration, we studied all possible distinct arrangements of the Zr and Al atoms in the six-atom bcc unit cells as shown in 5.1. We optimized the lattice constant ‘ a ’ of all these bcc configurations (taken in the hexagonal symmetry as described in previous section). Then, we calculated their energies as a function of displacement parameter (Z) along the $(111)_{bcc}$ direction. The lattice parameters (a , c/a) of the intermediate structures (with different Z value) that arise in the transformation

$\beta \rightarrow \omega$ were optimized for each configuration.

5.2.3 Relative Stability of the Phases

Table 5.1 enlists our results for equilibrium lattice parameters (a and c/a), bulk moduli (B_0) and energies of formation (E_{form}) for pure Zr (hcp), Al (fcc) and ordered B8₂ (Zr₂Al) along with available experimental [216–223] and other theoretical results [224, 225]. The ground state cohesive energy ($E_c(V)$) was fitted to the Birch-Murnaghan equation of state [226] state as a function of volume to determine the cell parameters, equilibrium volume (V_0) and bulk modulus using equation:

$$E_c(V) = \frac{B_0 V}{B'_0(B'_0 - 1)} \left[B'_0 \left(1 - \frac{V_0}{V} \right) + \left(\frac{V_0}{V} \right)^{B'_0} \right] + E_0 \quad (5.1)$$

where B_0 is bulk modulus, B'_0 is the pressure derivative of B_0 and E_0 is a constant. The energy of formation (E_{form}) is the quantity of interest to determine stability of these phases. The energy of formation (E_{form}) is calculated as:

$$E_{form}(Zr_x Al_y) = \frac{1}{N_{Zr} + N_{Al}} \left[E_C(Zr_x Al_y) - x E_C(Zr) - y E_C(Al) \right] \quad (5.2)$$

where $E_C(Zr_x Al_y)$ is the cohesive energy of Zr_xAl_y phase, and $E_c(Zr)$, $E_C(Al)$ are the cohesive energies per atom of Zr (hcp) and Al (fcc) phases, respectively. N_{Zr} and N_{Al} refer to the number of Zr and Al atoms in the unit cell of Zr_xAl_y.

As seen in Table 5.1, our DFT-GGA results of equilibrium lattice parameters (a and c/a) are in good agreement (within $\sim 1-4\%$ with the experimental values, wherever available) and other theoretical results for the Zr, Al and B8₂ phases. Our GGA results for B_0 of pure Zr and Al phases are within 3-6% of respective experimental values; while that for the B8₂ phase, the calculated value is in good agreement (within 2%) with the other theoretical results.

The calculated ground state cohesive energies of all ordered configurations of the bcc-Zr₂Al structure are listed in Table 5.2. It can be seen that the configurations marked {a}, {b} and {c} in Figure 5.2 are the most stable configurations for their energies are the lowest and degenerate. The following relations hold for the energies of configurations (Figure 5.2): $E\{a\}=E\{b\}=E\{c\}$, $E\{d\}=E\{e\}$, $E\{f\}=E\{g\}=E\{h\}$ and $E\{a\}<E\{d\}<E\{f\}$. In Table 5.2, the energy difference of each configuration is compared to $E\{a\}(=E\{b\}=E\{c\})$. Also listed are the number of Zr-Al, Zr-Zr and Al-Al bonds present in the first and second nearest neighborhood for each configuration. We designate the configuration (Figure 5.2 {a}) as Γ -Zr₂Al. As can

be seen from Table 5.1, the energy of formation of this ordered configuration was calculated to be -0.241 eV/atom.

Table 5.1: DFT-GGA ground-state properties of Zr-Al system along with pure Zr (hcp) and Al (fcc) phases. Experimental (in parenthesis) and other calculated ab-initio values in braces are also given.

Structures	a (Å)	c/a	B_0 (GPa)	E_{form} (eV/atom)
fcc Al $Fm\bar{3}m$ (225)	4.042 (4.032) [216] {4.044} [224]	-	75.9 (88.2 [217], 79.4 [218], 82.0 [219]) {74.2} [224]	0.000
hcp Zr $P6_3/mmc$ (194)	3.265 (3.229) [220] 3.208 [224]	1.5920 (1.5921) [220] (1.59987) [224]	93.6 (97.2) [221] 95.9 [224]	0.000
Γ -Zr ₂ Al ordered bcc	3.465	-	-	-0.241
B8 ₂ -Zr ₂ Al $P6_3/mmc$ (194)	4.923 (4.894 [222], 4.882 [223]) {4.882} [224]	1.2066 (1.2114 [222], 1.2122 [223]) {1.2020} [224]	100.6 {105.2} [224]	-0.364 {-0.389 [224], -0.370 [225]}

5.2.4 Ordered ω Phase Formation: Replacive *versus* displacive process

In order to examine how the cohesive energy of ordered bcc Zr₂Al configuration (Γ -Zr₂Al) changes as a function of magnitude of plane collapse (Z), we calculated its energy as a function of Z and the result is shown in Figure 5.3. We calculated energies of all other configurations ({b} - {h} of Figure 5.2) also as a function of extent of plane collapse (parameterized by Z) and the results are also given in Figure 5.3. In the figure 5.3, the energies of all configurations as function of normalized displacement parameter are plotted with respect to that of the most stable configuration (depicted as Γ in Table 5.1 and configuration {a} of Figure 5.2). It is clear from Figure 5.3 that only the Γ -Zr₂Al configuration of bcc-Zr₂Al phase can reduce its energy significantly through the displacive process. This was the reason we designated this particular configuration as Γ -Zr₂Al in the first place. The energies of all other configurations increase or decrease slightly with the extent of plane collapse. In other words, the displacive process in the bcc-Zr₂Al structure

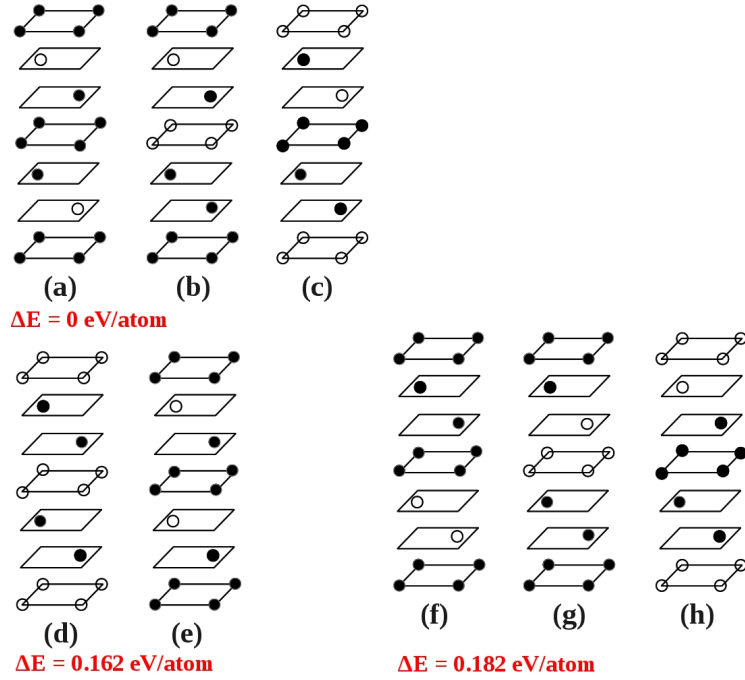


Figure 5.2: All possible arrangements ($\{a\}$ - $\{h\}$) of Zr and Al atoms on the bcc lattice corresponding to bcc Zr_2Al alloy. Dark gray and light gray circles represent Zr and Al atoms, respectively.

Table 5.2: Difference between cohesive energies of possible configurations of the bcc- Zr_2Al composition compared to the Γ - Zr_2Al configuration ($E-E_{\Gamma-Zr_2Al}$) and number of first and second nearest neighbour (nn) Zr-Al, Zr-Zr and Al-Al bonds. Bond lengths (in brackets (\AA)) of these 1st and 2nd nn bonds of configurations $\{a\}$, $\{b\}$ and $\{c\}$ in their bcc and ω' (24% plane collapse) structures are also enlisted.

Config- urations	Z	$E-E_{\Gamma-Zr_2Al}$ (meV/atom)	Number of Al-Zr bonds in 1 st and 2 nd nn	Number of Zr-Zr bonds in 1 st and 2 nd nn	Number of Al-Al bonds in 1 st and 2 nd nn
{a}	0.00 (bcc)	0.00	16 (3.00), 6 (3.47)	8 (3.00), 9 (3.47)	-
	0.02	-36.3	6 (2.93), 4 (3.00)	2 (3.00), 6 (3.04)	-
{b}	0.00 (bcc)	0.00	16(3.00),6(3.47)	8(3.00),9(3.47)	-
	0.02	34.4	3(2.93),4(3.00)	3(3.00),2(3.04)	-
{c}	0.00 (bcc)	0.00	16(3.00),6(3.47)	8(3.00),9(3.47)	-
	0.02	34.4	3(2.93),4(3.00)	3(3.00),2(3.04)	-
{d}	0 (bcc)	161.7	12, 12	10, 6	2
{e}	0 (bcc)	161.7	12, 12	10, 6	2
{f}	0 (bcc)	181.6	10, 12	11, 6	3
{g}	0 (bcc)	181.6	10, 12	11, 6	3
{h}	0 (bcc)	181.6	10, 12	11, 6	3

prefers an arrangement where every Al atom is surrounded by Zr atoms (see Table 5.2) because of stronger Zr-Al bonds supporting the ordering tendency in this alloy. In overall, the present calculations suggest that the configuration with maximum number of Zr-Al bonds has greater tendency for ω -type atomic displacements.

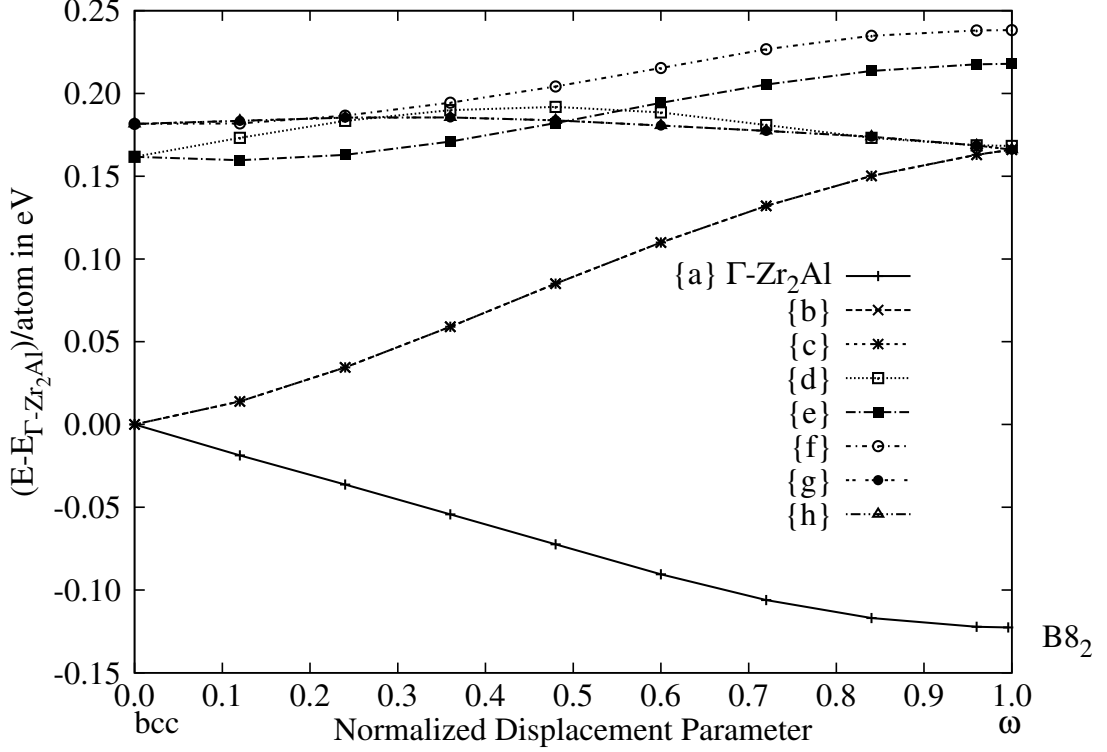


Figure 5.3: The variation of energy difference ($E-E_{\Gamma} - Zr_2Al$) as a function of magnitude of ω -type collapse of atomic planes for all configurations corresponding to bcc-Zr₂Al phase (see Figure 5.2), where $E_{\Gamma} - Zr_2Al$ is cohesive energy of the most stable configuration Γ . Here, the ω and bcc structures correspond to normalized displacement parameter equals to 1.0 and 0.0, respectively.

Table 5.2 also enlists the cohesive energy differences (compared to ground state cohesive energy of Γ -Zr₂Al structure) of the intermediate ω' structures ($Z=0.02$, 24% plane collapsed compared to their respective bcc configurations) of configurations {a}, {b} and {c} along with number of Zr-Al, Zr-Zr and Al-Al bonds present as first and second nearest neighbors as well as their bond lengths. The number of Zr-Al and Zr-Zr bonds present in configuration {a}, {b} and {c} are same in their bcc structures. The number of these bonds as well as bond lengths start changing due to ω type displacements. Configuration {a} in its ω' structure, is having more number of Zr-Al bonds as 1st nearest neighbor as compared to ω' structures of configurations {b} and {c}. From this observation it can be deduced that the presence of more number of Zr-Al bonds as first nearest neighbor makes the configuration

more favorable energetically in the bcc structure as well as helps the configuration to achieve ordered ω structure through displacive transformation by reducing the Zr-Al bond lengths.

The electronic origin of the correlation between the number of Zr-Al bonds and the stability of the structure can be understood by analyzing its electronic structure. In Figure 5.4, we show total as well as partial density of states (DOS) of configuration {b} of Zr_2Al structure (for both $Z=0$ and $Z=1/12$), the most stable configuration Γ ($Z=0$) and the corresponding $B8_2$ ($Z=1/12$) structure. The total DOS of both the bcc configurations, *viz.*, {b} at $Z=0$ and Γ (see Figure 5.4 (i) and (iii)) are almost identical with strong mixing between Zr- d and Al- p states near the Fermi energy (E_F) and the presence of a pseudo gap near the E_F between the bonding and antibonding states; though the degree of interaction is more in configuration Γ than in configuration {b} for $Z=0$. On the other hand, the partial DOS of $B8_2$ (Figure 5.4(iv)) shows the strongest d - p interactions and more pronounced pseudo gap between the bonding and antibonding states compared to all other configurations. Also, the number of states at E_F ($N(E_F)$) for $B8_2$ is 0.89 states/atom which is the lowest compared to that of other configurations, *viz.*, $N(E_F)=1.11$ states/atom for both configurations Γ and {b} with $Z=0$ and $N(E_F)=1.30$ states/atom for configuration {b} with $Z=1/12$. These observations clearly confirm the high stability of $B8_2$ structure as compared to configurations {b} (for both $Z=0$ and $Z=1/12$) and Γ .

5.3 Disordered $\beta \rightarrow$ ordered- ω Athermal Transformation Pathways in Zr_2Al -Nb Alloys

5.3.1 Phase Stability and bcc $\rightarrow \omega$ Transformation

In order to decide which lattice position Nb atom is going to occupy in bcc lattice of Zr_2Al , we examined several atomic configurations by performing simple translational and/or rotational symmetry operations and found out 6 and 10 distinct configurations of bcc- Zr_3Al_2Nb (Figure 5.5) and bcc- Zr_4AlNb (Figure 5.6), respectively. The unit cells of both bcc- Zr_3Al_2Nb and bcc- Zr_4AlNb have six atoms as shown in Figure 5.5 and 5.6. We constrained the c/a ratio to $\sqrt{6}/2$ (ideal value) and optimized the lattice constant (a) for all bcc structures having distinct atomic configurations (shown in Figure 5.5 and 5.6). The calculated ground state cohesive energies of all configurations of the bcc- Zr_3Al_2Nb and bcc- Zr_4AlNb are listed in

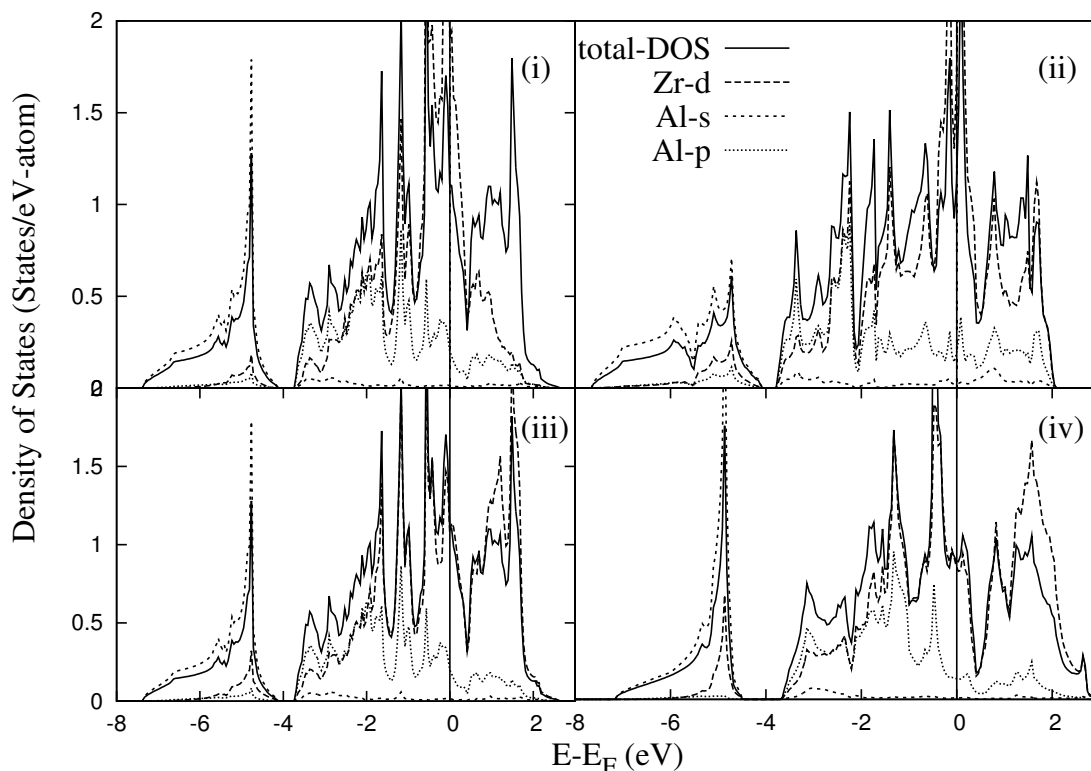


Figure 5.4: Total and partial density of states (DOS) of Zr_2Al structure for (i) configuration $\{b\}$ with $Z=0$ (ii) configuration b with $Z=1/12$ (iii) configuration Γ and (iv) $B8_2$ showing strong interaction between Zr-d and Al-p states.

Table 5.3. The configuration shown in figure 5.5(a) is the most stable configuration and we designate this configuration as $\Gamma-Zr_3Al_2Nb$ for convenience. In Table 5.3, the energy difference of each configuration compared to $\Gamma-Zr_3Al_2Nb$ and number of Zr-Al and Zr-Nb bonds present in the first nearest neighborhood (NN) for each configuration are also listed. Based on the general description of the crystal structure given in section 2, Zr atoms occupy the Wyckoff sites (1a) and (2d2), the Al atoms the site (2d1), and the Nb atoms the site (1b) in $\Gamma-Zr_3Al_2Nb$.

There is a striking similarity between $\Gamma-Zr_3Al_2Nb$ configuration and most stable bcc structure in $\Gamma-Ti_3Al_2Nb$ in the previous study of Sanati *et al.* [227]. The experimentally measured site occupancies of the ω'' -phase in Ti_4Al_3Nb alloy indicate that the phase transformation first involves a change in chemical order with a transfer of Nb atoms out of collapsing planes (Figure 5.1) into stationary ones [70]. It is suggested that the absence of the Nb atoms from the collapsing planes is because of the strong interaction between Ti and Al atoms (due to considerably large negative heat of mixing between them). Therefore, transition-metal-Al interactions are the origin of the both the chemical ordering and the ω -phase formation in the

B2 phase of TiAl-X (X = Nb, V) system [70, 228, 229]. A similar argument can be extended to understand stability of bcc Zr_3Al_2Nb alloy. In bcc Zr_4AlNb , configurations (a), (g) and (i) are having same cohesive energies and these configurations are more stable compared to other configurations. Though energetically degenerate configurations, *viz.*, (a), (g) and (i) of Zr_4AlNb structure are symmetrically equivalent in the bcc structure, but these configurations become distinct during ω -type collapse (See Figure 5.8). There is an order of magnitude differences in the energies ($E_{bcc} - E_{most\ stable}$) between different configurations corresponding to Zr_3Al_2Nb and Zr_4AlNb alloys. In other words, chemical ordering effects are predominant in Zr_3Al_2Nb alloy as compared to those in Zr_4AlNb alloy.

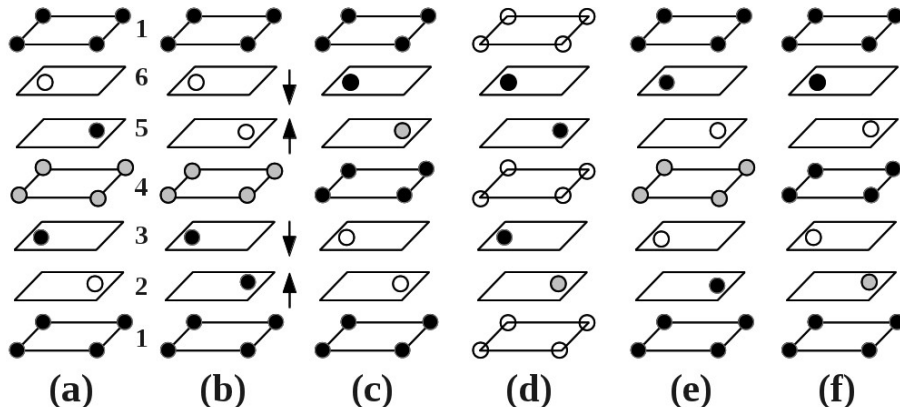


Figure 5.5: Different arrangements of the atoms for Zr_3Al_2Nb alloy with an underlying bcc structure. Black, white and gray atoms show Zr, Al and Nb, respectively. Systematic collapse of the bcc planes (marked as 2, 3 and 5, 6) into a single plane (2-3 and 5-6) generates ω structure while keeping planes marked as 1 and 4 stationary. This is true for all the configuration.

Then, starting from the Γ - Zr_3Al_2Nb , we varied the positions of the $(222)_{bcc}$ planes in small steps along $[111]_{bcc}$ direction as shown in Figure 5.5 and optimized the lattice parameters (a, c/a) for each new structure that arises in the transformation path. We calculated total energy as a function of atomic plane displacement Z (where Z is a dimensionless parameter varying between 0 and 1/12 in units of c/a) and our results are shown in Figure 5.7. The lattice corresponds to Z=0 is the Γ - Zr_3Al_2Nb structure and Z=1/12 corresponds to the complete ω structure. The incomplete ω structure is realized for $1/12 > Z > 0$. From Figure 5.7 it is evident that minimum in energy vs atomic plane displacement curve occur at a structure with 77% collapse of atomic planes - designate this structure as ω' with space group $P\bar{3}m1$. Finally, the ground state structural parameters (a, c/a) and Bulk moduli (B_0) for the Γ , ω' (at the energy minima) and ω - Zr_3Al_2Nb along with pure Nb (bcc) are listed in Table 5.4. We have calculated structural and cohesive parameters of

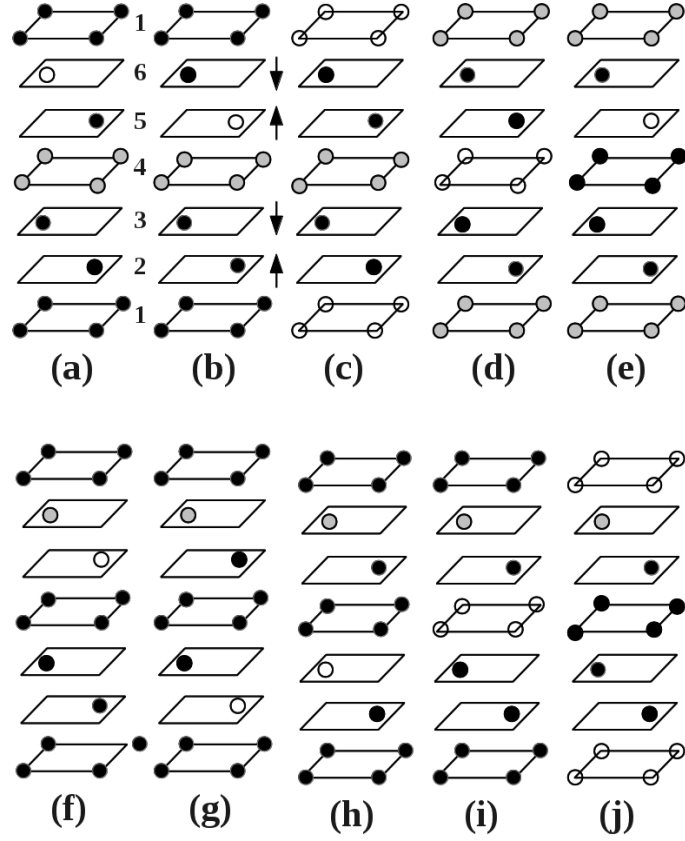


Figure 5.6: Different arrangements of the atoms for Zr_4AlNb alloy with an underlying bcc structure. Black, white and gray atoms show Zr, Al and Nb, respectively. Systematic collapse of the bcc planes (marked as 2, 3 and 5, 6) into a single plane (2-3 and 5-6) generates ω structure while keeping planes marked as 1 and 4 stationary. This is true for all the configuration.

$B8_2-Zr_2Al$ and incorporated in Table 5.4 for the sake of comparison.

Moreover, adopting the same methodology as described above (section 5.2.2), we calculated total energy as a function of atomic plane displacement (Z) for Zr_4AlNb (Figure 5.5) and the results are shown in Figure 5.8. It is evident from Figure 5.8 that the minimum in energy versus atomic plane displacement curve occurs for configuration (i) and (j) with full collapse of atomic planes ($Z = 1/12$, ideal ω , space group $P3m1$). The calculated ground state structural parameters (a , c/a) and Bulk moduli (B_0) for the ω - Zr_4AlNb is also listed in Table 5.4. A comparison of Figures 5.7 and 5.8 clearly shows that a prominent structural instability exists in Zr_3Al_2Nb alloy as compared to that in Zr_4AlNb alloy. Moreover, atomic arrangements corresponding to configurations (i) and (j) of Zr_4AlNb show an energy barrier of ~ 8 meV/atom in the energy versus displacement (Z) curve. On the other hand, no energy barrier exists in the energy versus displacement (Z) curve for (a), (e) and (f) configurations of Zr_3Al_2Nb alloy.

Table 5.3: Difference between energy of possible distinct configurations and the most stable configuration and number of first nearest neighbor Zr-Al and Zr-Nb bonds. Though energetically degenerate configurations, *viz.*, (a), (g) and (i) of Zr_4AlNb structure are symmetrically equivalent in the bcc structure, but these configurations behave differently during ω -type collapse.

Zr_3Al_2Nb			
Configurations	$E-E_{\Gamma}(meV/atom)$	No. of Al-Zr bonds	No. of Zr-Nb bonds
(a), Γ	0	16	8
(b)	266	7	5
(c)	248	8	6
(d)	223	7	5
(e)	138	10	2
(f)	102	11	3
Zr_4AlNb			
Configurations	$E-E_{bcc}(meV/atom)$	No. of Al-Zr bonds	No. of Zr-Nb bonds
(a)	0	8	8
(b)	45	5	5
(c)	19	6	6
(d)	39	6	6
(e)	26	6	6
(f)	45	5	5
(g)	0	8	8
(h)	19	6	6
(i)	0	8	8
(j)	45	5	5

The bulk modulus (B_0) and equilibrium volume (V_0) were obtained by fitting the ground state cohesive energy (E_C) versus volume data to the Birch-Murnaghan equation of state [226]. As seen in Table 5.4, our VASP-GGA results of equilibrium lattice parameters (a and c/a) are in good agreement (within 1-4% with the experimental values and other theoretical results for the Zr, Al, Nb and $B8_2$ -Zr₂Al. Our GGA calculated results of a and c/a for ω -Zr₃Al₂Nb and ω -Zr₄AlNb overestimates experimentally determined a (within 5%) and underestimates experimentally determined c/a (within 4%), respectively [77]. It is also crucial to note that the experimentally reported (Zr,Nb)₂Al is compositionally close to Zr₅₉Al₂₀Nb₂₁ in contrast to our chosen compositions Zr₅₀Al_{33.33}Nb_{16.67} (Zr₃Al₂Nb) and Zr_{66.67}Al_{16.67}Nb_{16.67} (Zr₄AlNb). Our GGA results for B_0 of pure Zr, Al and Nb phases are within 3-6%

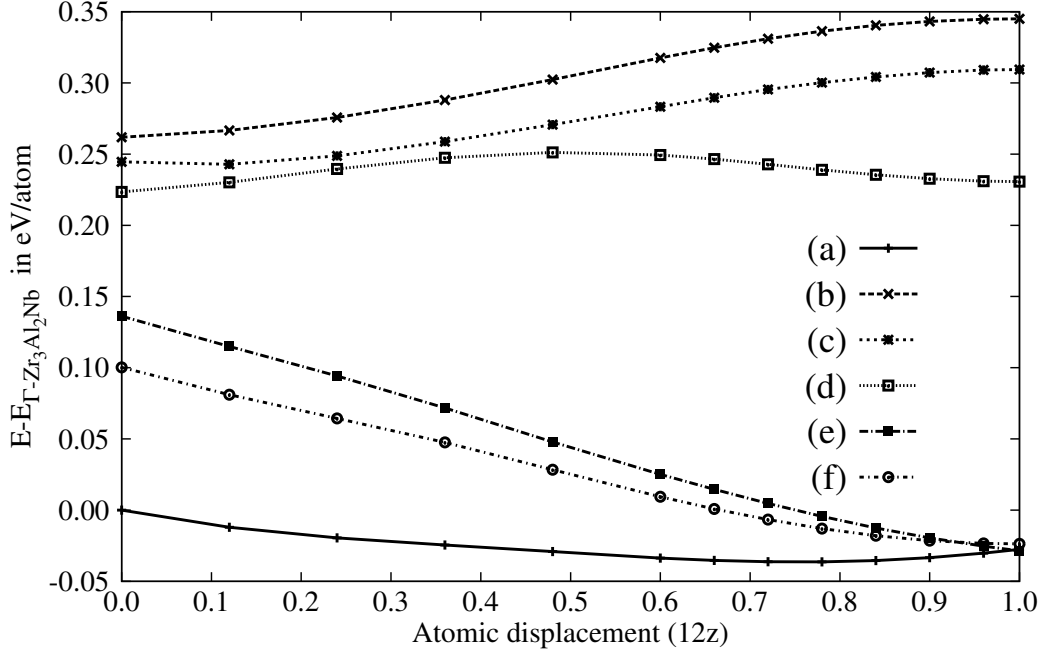


Figure 5.7: Calculated total energy as a function of atomic displacement for 6 distinct Zr_3Al_2Nb configuration.

of respective experimental values; while that for the $B8_2-Zr_2Al$, the calculated value is in good agreement (within 2%) with the other theoretical results. For Zr_3Al_2Nb and Zr_4AlNb phases, there are no previous theoretical predictions available in the literature.

The heat of formation (E_{form}) is the quantity of interest for the determination of the stability of the phases and to assess strength of interatomic bonding. In view of this, we calculated the heat of formation of binary Zr_2Al , ternary Zr_3Al_2Nb (Γ , ω' and ω) and $\omega-Zr_4AlNb$. The heat of formation (E_{form}) can be described as:

$$E_{form}(Zr_xAl_yNb_z) = \frac{1}{N_{Zr} + N_{Al} + N_{Nb}} [E_C(Zr_xAl_yNb_z) - xE_C(Zr) - yE_C(Al) - zE_C(Nb)] \quad (5.3)$$

where $E_C(Zr_xAl_yNb_z)$ is the cohesive energy of $Zr_xAl_yNb_z$ phase, and $E_C(Zr)$, $E_C(Al)$ and $E_C(Nb)$ are the cohesive energies per atom of Zr (hcp), Al (fcc) and Nb (bcc) phases, respectively. N_{Zr} , N_{Al} and N_{Nb} refer to the number of Zr, Al and Nb atoms in the unit cell of $Zr_xAl_yNb_z$. Table 5.4 shows that E_{form} value of the $\omega'-Zr_3Al_2Nb$ is more negative than the Γ and ω structures which confirms higher stability of ω' compared with Γ and ω structures. $\omega-Zr_4AlNb$ is less stable than

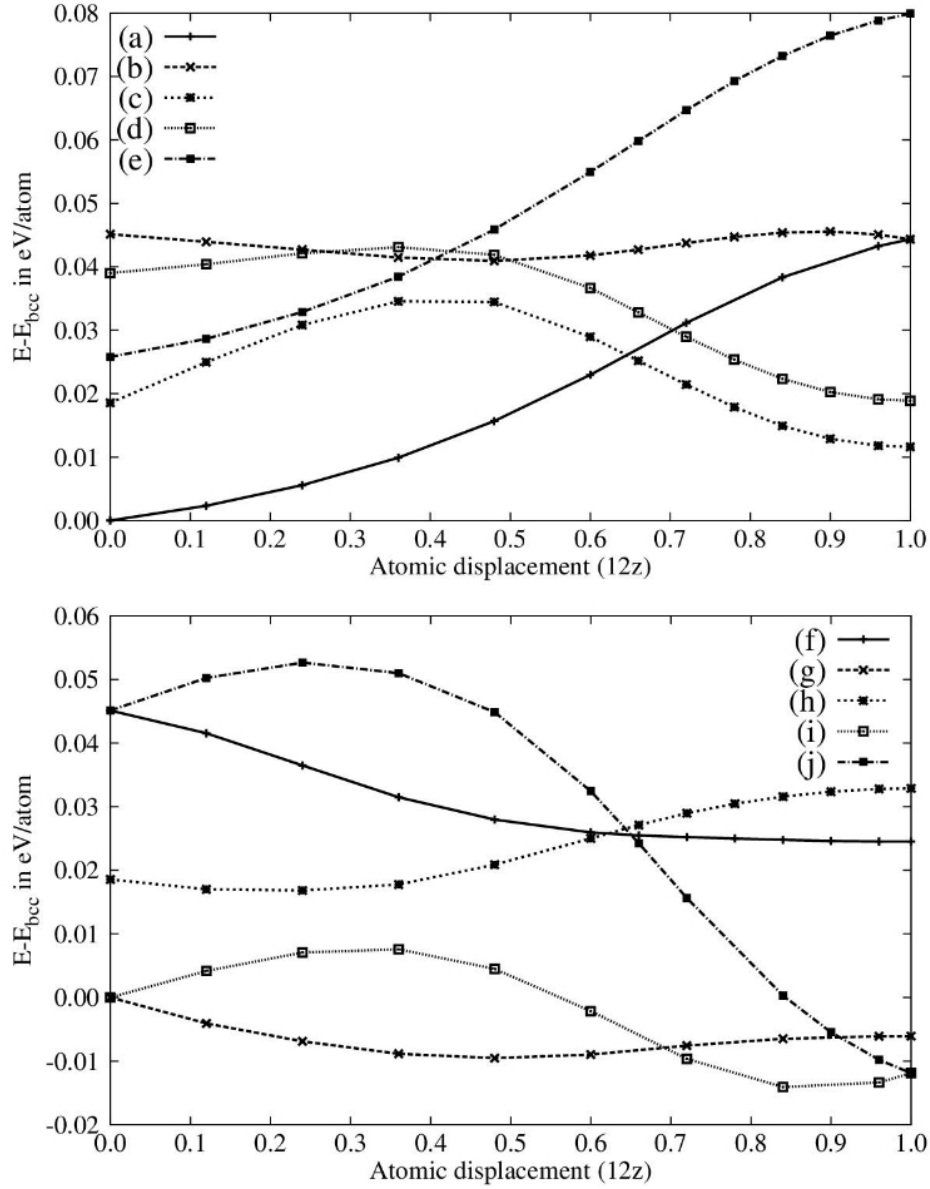


Figure 5.8: Calculated total energy as a function of atomic displacement for 10 distinct Zr_4AlNb configuration. Energy values in the y axis are given with respect to configuration (i).

ω' - Zr_3Al_2Nb and E_{form} value of ω - Zr_4AlNb is almost four times lower compared to that of ω' - Zr_3Al_2Nb . Moreover, chemically ordered ω - Zr_2Al ($B8_2$) is more stable than both ω' - Zr_3Al_2Nb and ω - Zr_4AlNb ternary derivatives.

In order to further reveal the change in nature of bonding due to ω -type atomic displacements in Zr_3Al_2Nb , we compare total and angular momenta-decomposed

Table 5.4: DFT-GGA ground-state properties of Zr_3Al_2Nb (Γ, ω' and $B8_2$), ω - Zr_4AlNb along with pure Nb (bcc) phase. Experimental (in parentheses) and other calculated ab-initio values in braces are also given. References [77] enlist experimental values of a and c/a for $Zr_{59}Al_{20}Nb_{21}$ alloy.

Structures	a (Å)	c/a	B_0 (GPa)	E_{form} (eV/atom)
bcc Nb	3.3227	1.0000	171.0	-
$Im\bar{3}m$ (229)	(3.3024) [219] 3.2929 [231]		(173.0) [230] 175.2 [231]	- -
Γ - Zr_3Al_2Nb $P\bar{3}m1$ (164)	3.4144	-	113.5	-0.312
ω' - Zr_3Al_2Nb $P\bar{3}m1$ (164)	4.8196 (4.6100) [77]	1.2370 (1.2826) [77]	114.0	-0.350
ω - Zr_3Al_2Nb $P\bar{3}m1$ (164)	4.8184	1.2367	114.7	-0.332
ω - Zr_4AlNb $P3m1$ (154)	4.8964	1.2248	105.2	-0.078
$B8_2$ - Zr_2Al $P6_3/mmc$ (194)	4.9230	1.2066	100.6	-0.364

density of states (DOS) for Γ and ω' - Zr_3Al_2Nb structures in Figure 5.9 (a) and (b), respectively. As seen in both the figures, a low lying band in the energy range -7.5 to -4.5 eV is dominated by Al s electrons and is separated by a narrow forbidden gap from other densities. This is the result of strong hybridization between s band of Zr and Al. In the valence band region the bonding and antibonding states are separated by a pseudo gap and the Fermi level (E_F) lies in the bonding region. In this region Al-p, Zr-d and Nb-d states are bonded strongly by hybridization. In the conduction band region (region mostly above E_F) the non-bonding d states are present and total DOS resembles the Zr-d DOS. These features are similar in both Γ and ω' - Zr_3Al_2Nb DOS but there are some differences. The width of the forbidden gap (which separates low lying bands and valence bands) and depth of the pseudo gap is higher in ω' than in Γ - Zr_3Al_2Nb . This signifies the degree of covalent bonding is higher in ω' than Γ - Zr_3Al_2Nb . Similar higher degree of covalent bonding can also be observed in the bonding states of ω' - Zr_3Al_2Nb as Zr-Al bond distances are smaller in ω' than in Γ - Zr_3Al_2Nb .

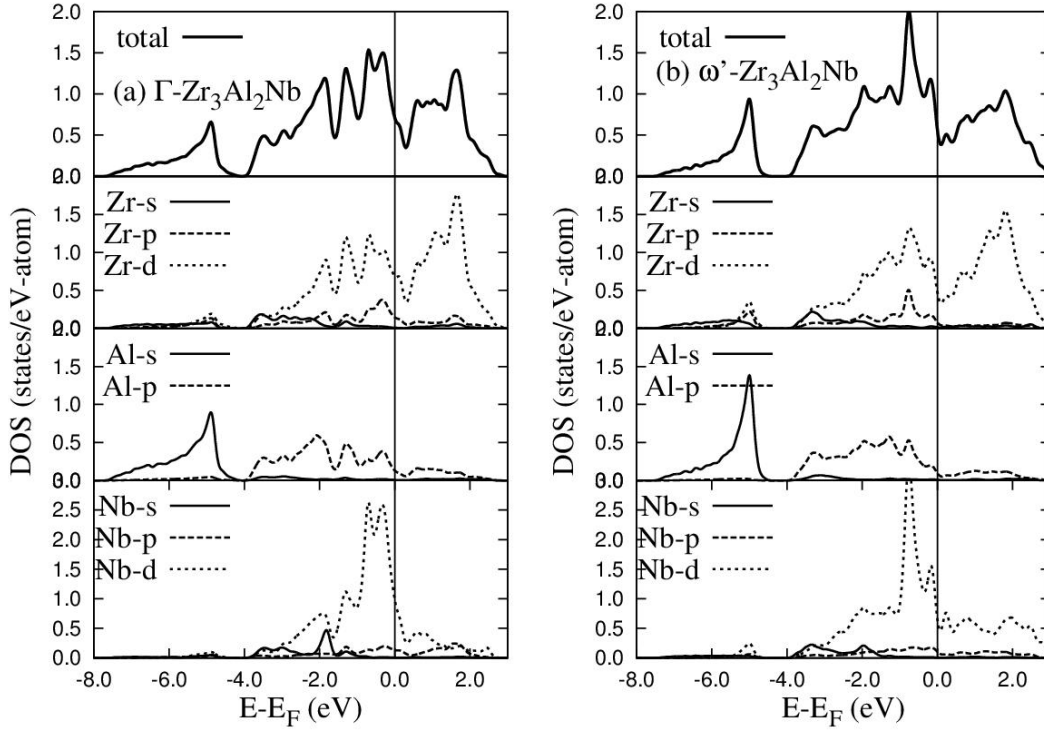


Figure 5.9: Total and partial DOS of (a) Γ and (b) ω' - $\text{Zr}_3\text{Al}_2\text{Nb}$. Fermi energy (E_F) is represented by vertical line.

5.3.2 Mechanical Stability of ω' - $\text{Zr}_3\text{Al}_2\text{Nb}$, ω - Zr_4AlNb and $\text{B8}_2\text{-Zr}_2\text{Al}$ alloys

Elastic constants are the measure of the resistance of a crystal to an externally applied stress. Generally, the single-crystal elastic constants can be obtained by calculating the total energy as a function of appropriate lattice deformation. Depending on the crystal symmetry and the type of lattice deformation imposed, the curvature of the total energy versus strain curves can define either a particular elastic constant or a combination of elastic constants. The internal energy ($E(V, \{e_i\})$) of a crystal under an infinitesimal strain e_i , with respect to the energy $E(V_0, 0)$ of the unstrained geometry, can be written as

$$E(V, \{e_i\}) = E(V_0, 0) + \frac{V_0}{2} \sum_{i,j=1}^6 C_{ij} e_i e_j + O(e^3) \quad (5.4)$$

where V_0 is the volume of the unstrained system with $E(V_0, 0)$ being the corresponding energy, C_{ij} 's are the single-crystal elastic constants and the strain tensor $\epsilon = e_i, e_j, \dots$ is given in Voigt notation. These elastic constants can be determined by a polynomial fitting of the calculated deformation energy $\Delta E = E(V, e_i) - E(V_0, 0)$

as a function of the strains as given in Table 3 for the hexagonal and trigonal crystals [232, 233]. For a hexagonal system, there are 5 independent elastic constants, viz., $C_{11}, C_{12}, C_{13}, C_{33}$ and C_{44} [180]. Similarly for trigonal system, there are 6 independent elastic constants, viz., $C_{11}, C_{12}, C_{13}, C_{33}, C_{44}$ and C_{14} [234]. The maximum strains used for total energy fitting to derive elastic moduli were kept within 2% of the undeformed lattice vectors in these calculations.

Table 5.5: The listing of strains (e_i) used for the calculation of elastic constants at 0 K for the ω' -Zr₃Al₂Nb, ω -Zr₄AlNb and B8₂-Zr₂Al (the unlisted e_i 's = 0).

Crystal	Strain	Δ/V_0
Hexagonal/ Trigonal	$e_1 = e_2 = \delta$	$C_{11} + C_{12}\delta^2$
	$e_1 = -e_2 = \delta$	$C_{11} - C_{12}\delta^2$
	$e_3 = \delta$	$\frac{1}{2}C_{33}\delta^2$
	$e_5 = \delta$	$2C_{44}\delta^2$
	$e_1 = e_2 = e_3 = \delta$	$\frac{1}{2}(2C_{11} + 2C_{12} + 4C_{13} + C_{33})\delta^2$
only for Trigonal	$e_1 = e_4 = \delta$	$\frac{1}{2}(2C_{11} + 4C_{13} + 4C_{14})\delta^2$

Mechanical stability of a crystalline structure is manifested by positive strain energy against any homogeneous elastic deformation. For hexagonal and trigonal crystals, the requirement of mechanical stability leads to the following restrictions on its elastic constants [180, 234]:

$$C_{12} > 0; C_{33} > 0; C_{44} > 0; C_{11} > C_{12} \text{ and } (C_{11} + C_{12})C_{33} > 2C_{13}^2 \text{ (hexagonal)}$$

$$C_{11} > C_{12}; (C_{11} + C_{12})C_{33} > 2C_{13}^2 \text{ and } (C_{11} - C_{12})C_{44} > 2C_{14}^2 \text{ (trigonal)}.$$

Table 5.6 enlists PAW-PBE calculated single crystal elastic constants of ω' -Zr₃Al₂Nb, ω -Zr₄AlNb and B8₂-Zr₂Al along with previous theoretically calculated values for B8₂-Zr₂Al [235]. PAW-PBE calculated single crystal elastic constant values are in agreement with previously calculated values. The calculated elastic constants of ω' -Zr₃Al₂Nb, ω -Zr₄AlNb and B8₂-Zr₂Al obey the mechanical stability criteria and hence all these structures are mechanically stable. The present calculations showed that the value of C_{11} for ω' -Zr₃Al₂Nb is the largest among these three structures and value of C_{11} for B8₂-Zr₂Al is close to that for ω' -Zr₃Al₂Nb, whereas for ω -Zr₄AlNb it has the smallest value. It is noteworthy that ω -Zr₄AlNb has the largest C_{12} value followed by that of B8₂-Zr₂Al and ω' -Zr₃Al₂Nb. From Table 5.6, it can be seen that the value of C_{33} become eventually larger going from B8₂-Zr₂Al, ω -Zr₄AlNb to ω' -Zr₃Al₂Nb, which means B8₂-Zr₂Al is easily deformed along [0001] direction compared to other two structures. The calculated value of C_{44} is lowest

in ω -Zr₄AlNb and this value is less than the half of C_{44} values in ω' -Zr₃Al₂Nb and B8₂-Zr₂Al.

The ductility behavior of this alloy can be assessed by evaluating polycrystalline elastic properties. The elastic parameters were usually obtained from first-principle calculations for single crystals but the majority of synthesized and experimentally examined alloys are prepared and investigated as polycrystalline, i.e., in the form of aggregated mixtures of microcrystallites with a random orientation. Thus, it is necessary to calculate the elastic parameters for polycrystalline materials and the Voigt-Reuss-Hill (VRH) approximation [236–238] is widely used. Voigt's and Reuss's schemes represent the upper and lower bound for the structural parameters, respectively, and the final values of the polycrystalline bulk modulus (B_{VRH}) and the shear modulus (G_{VRH}) are obtained by the averages of the two:

$$B_{VRH} = \frac{B_R + B_V}{2}; \quad G_{VRH} = \frac{G_R + G_V}{2} \quad (5.5)$$

For hexagonal phases the Voigt (B_V) and Reuss (B_R) bulk moduli are given by

$$B_V = \frac{1}{9}[2(C_{11} + C_{12}) + C_{33} + 4C_{13}] \quad (5.6)$$

$$B_R = \frac{(C_{11} + C_{12})C_{33} - 2C_{13}^2}{C_{11} + C_{12} + 2C_{33} - 4C_{13}}$$

Similarly, the upper and lower bounds for the shear modulus of hexagonal phase according to the Voigt (G_V) and Reuss (G_R) can be represented as

$$G_V = \frac{1}{30}[C_{11} + C_{12} + 2C_{33} - 4C_{13} + 12C_{44} + 12C_{66}]$$

$$G_R = \frac{5}{2} \frac{((C_{11} + C_{12})C_{33} - 2C_{13}^2)^2 C_{44} C_{66}}{3B_V C_{44} C_{66} + ((C_{11} + C_{12})C_{33} - 2C_{13}^2)^2 (C_{44} + C_{66})} \quad (5.7)$$

where $C_{66} = \frac{1}{2}(C_{11} - C_{12})$

The isotropic bulk modulus and shear modulus values for polycrystalline ω' -Zr₃Al₂Nb and ω -Zr₄AlNb were first calculated using the above relations. Table 5.6 enlists single-crystal elastic constants as well as isotropic bulk, shear and Young modulus of these phases and B8₂-Zr₂Al. We were not able to compare our calculated values of Young and Shear modulus for Zr₃Al₂Nb and Zr₄AlNb due to unavailability of any experimental values. The calculated bulk moduli of these structures are in agreement with that obtained through the fit to Birch-Murnaghan equation of state.

In general, the large values of shear modulus are indicative of pronounced directional bonding between atoms. The value of shear modulus for B8₂-Zr₂Al is the largest, followed by that for ω'-Zr₃Al₂Nb and ω-Zr₄AlNb. As indicated in DOS analysis, there is a strong directional bonding between Zr and Al atoms in ω'-Zr₃Al₂Nb which results in larger values of shear modulus. In contrast, ω-Zr₄AlNb is having less pronounced directional bonding compared to Zr₃Al₂Nb and Zr₂Al in accordance with calculated shear modulus values. The polycrystalline Young modulus (E) were then computed from these values using the following relationship:

$$E = \frac{9B_{VRH}G_{VRH}}{3B_{VRH} + G_{VRH}} \quad (5.8)$$

Young's modulus is used to provide a measure of the stiffness of the solid, i.e., the larger the value of E, the stiffer the material. Our calculated E values indicate ω'-Zr₃Al₂Nb and B8₂-Zr₂Al are of comparable stiffness but ω-Zr₄AlNb is having smaller E value compared to these two structures.

Brittle/ductile behavior, an important mechanical characteristics of materials, is closely related to their reversible compressive deformation and fracture ability. The ductile materials can be bent greatly and reshaped without breaking as they accommodate local stress concentrations. In contrast, brittle materials have only a small amount of elongation at fracture. In simplest ways, the most widely used malleability measures are the Pugh's criterion (G/B ratio) [239] and the Cauchy pressure (CP) [240]. As it is known empirically, if $G/B < 0.5$, a material behaves in a ductile manner, and if $G/B > 0.5$, a material demonstrates brittleness. As regards the Cauchy pressure (for example, for cubic crystals $C_P = (C_{12} - C_{44})$), it is often used to explore the geometry of chemical bonding since it yields negative values for directionally bonded (covalent) solids and positive ones for ductile metals [241–243]. One may consider two types of Cauchy pressure in an hexagonal crystal, $C_{12} - C_{66}$ and $C_{13} - C_{44}$. We have enlisted these two values of CP for the ω'-Zr₃Al₂Nb, ω-Zr₄AlNb and B8₂-Zr₂Al hexagonal crystal. According to our calculated values for G/B and CP it is evident that the ductility property of both ω'-Zr₃Al₂Nb and B8₂-Zr₂Al is very poor and as expected from the general notion that the chemically ordered ω phases often shows brittle behavior [1,2,6]. In contrast, G/B is less than 0.5 and $C_{13} - C_{44}$ value is highest for ω-Zr₄AlNb. Therefore, the directional bonding nature in B8₂-Zr₂Al is higher (negative $C_{13} - C_{44}$ value) and it reduces with the addition of Nb in ω'-Zr₃Al₂Nb. In contrast, less pronounced directional binding in ω-Zr₄AlNb manifests this structure to be ductile.

Table 5.6: Calculated values of elastic constants for the ω' -Zr₃Al₂Nb, ω -Zr₄AlNb and B8₂-Zr₂Al.

Elastic Property	ω' -Zr ₃ Al ₂ Nb	ω -Zr ₄ AlNb	B8 ₂ -Zr ₂ Al
C_{11} (GPa)	202.0	167.5	195.0 {178.3}
C_{12} (GPa)	77.1	84.8	80.2 {85.4}
C_{13} (GPa)	58.6	59.3	54.5 {51.2}
C_{33} (GPa)	226.3	199.7	190.6 {189.2}
C_{44} (GPa)	57.9	25.0	67.02 {57.7}
C_{14} (GPa)	-10.8	-1.46	-
Bulk Modulus B_{HVR} (GPa)	113.1	104.6	106.4
Shear modulus G_{HVR} (GPa)	69.9	39.7	70.8
Young's modulus E (GPa)	173.9	105.7	173.6
G/B	0.613	0.379	0.665
$C_{12} - C_{66}$ (GPa)	14.7	43.4	22.8
$C_{13} - C_{44}$ (GPa)	0.7	34.3	-12.5

5.3.3 Bond Stability and Bond Strength

Since the number of nearest and second nearest neighbors is changing in ω -type atomic displacements, we chose a structure in which Zr-Al bonds can exist as the first and second nearest neighbors. This type of configuration can be visualized from Figure 5.1(a). Then we calculated E_{form} for underlying bcc Zr₂Al structure which is -0.240 eV/atom. Comparing this Eform value with that of B8₂-Zr₂Al (-0.364 eV/atom) indicates that Zr-Al bonds are stronger at shorter distances. Similar kind of bcc structures can also be made with composition Nb₂Al and Zr₂Nb if Zr atoms are replaced with Nb in Figure 5.1(a) which corresponds to Nb₂Al and Al atoms are replaced with Nb in Figure 5.1(a) which corresponds to Zr₂Nb. Also, B8₂ structures can be generated if similar atomic replacements are followed in Figure 5.1(c) structure. We calculated Eform value of these structures to determine bond strength of Nb-Al and Zr-Nb as a function of distance. From these calculations, it is evident that B8₂-Nb₂Al (-0.286 eV/atom) is more stable than bcc-Nb₂Al (-0.220 eV/atom). In other words, Nb-Al bonds are also stronger at shorter distances and Nb-Al bonds are weaker compared to Zr-Al bonds. But stability of B8₂-Zr₂Nb (-0.071 eV/atom) and bcc-Zr₂Nb (-0.072 eV/atom) is almost similar. In this case, the stability sequence is reversed compared to previous two situations. So the Zr-Nb bonds are weak at shorter distances. These parameters indicate that the most

stable bond is Zr-Al followed by the Nb-Al, and the Zr-Nb bond is the least stable. Moreover, the Zr-Al bonds are more stable than the Nb-Al at shorter distances.

It can be noted that the Γ -Zr₃Al₂Nb phase is metastable due to presence of weak Zr-Nb bonds between the 3rd, 4th and 5th atomic planes. Even though the strong Zr-Al bonds are present as 1st NN and Nb-Al bonds are present as 2nd NN in this structure. The Zr-Al bonds can increase their strength by reducing distances between them and Zr-Nb bonds prefer to expand. So, inherently, Γ -Zr₃Al₂Nb structure is destabilized with respect to ω -type atomic displacements. A similar argument can also be given for the most stable bcc Zr₄AlNb configurations. Therefore, the displacive process in the Γ -Zr₃Al₂Nb and most stable bcc Zr₄AlNb structure prefers an atomic arrangement where every Al atom is surrounded by Zr atoms owing to stronger Zr-Al bonds supporting the ordering tendency in this alloy. Overall, the present calculations suggest that the configuration with maximum number of Zr-Al bonds has a greater tendency for omega-type atomic displacements. Therefore, the ω phase is formed due to the competition between Zr-Al and Zr-Nb bonding arrangements.

5.3.4 Chemical Ordering *versus* Displacive Tendencies

To understand the effect of the chemical ordering on the stability of the Γ -Zr₃Al₂Nb phase with respect to ω -type atomic displacement, several different structures were investigated (Figure 5.5). The lattice parameters of each rearranged structure were optimized. If the calculated energy for the Γ -Zr₃Al₂Nb structure is represented as E_{Γ} , the following sequence holds for the structures shown in Figure 5.5: $E_{\Gamma} < E_f < E_e < E_d < E_c < E_b$. In Table 5.3 we enlist the energy difference of each structure compared to E_{Γ} along with number of Zr-Al and Zr-Nb bonds as the first NN for different configurations. We found that there is a direct relation between number of Zr-Al bonds present in the structure and energy of the underlying bcc structures. The structure with higher number of Zr-Al bond is energetically more stable. Figure 5.7 shows variation of total energy as a function of ω -type atomic displacement for different atomic configurations (as shown in Figure 5.5). Using the results of bond strength sequence from the last section we can explain the energy sequence of different structures. It is evident that the Zr-Al bond is stronger than the Zr-Nb and Zr-Al bonds are stronger at shorter distances, relative to their positions in the underlying bcc structure. So it is expected to observe relative instability towards ω -type atomic displacement for a bcc structure with more number of Zr-Al bonds. According to our results, the structures in Figure 5.5(e), 5.5(f) and 5.5(a) are

showing instability towards an ω -type structure formation. Therefore, our results are in agreement with the previous structural stability analysis.

The calculated ground-state cohesive energies of all ordered configurations of the bcc-Zr₄AlNb structure are listed in Table 5.4. It can be seen that the configurations marked (a), (g) and (i) in Figure 5.6 are the most stable configurations, as their energies are the lowest and degenerate. The following relations hold for the energies of configurations (Figure 5.8): $E_{(a)} = E_{(g)} = E_{(i)}$, $E_{(c)} = E_{(h)}$, $E_{(f)} = E_{(b)} = E_{(j)}$ and $E_{(a)} < E_{(c)} < E_{(e)} < E_{(d)} < E_{(b)}$. In Table 5.3, the energy difference of each configuration is compared to $E_{(a)} (= E_{(g)} = E_{(i)})$ along with number of Zr-Al and Zr-Nb bond present in 1st NN for each configurations. As discussed in the previous section, the results of bond strength sequence can explain the energy sequence of different bcc structures. Accordingly, configurations (a), (g) and (i) are more stable compared to other configurations because of more number of Zr-Al bonds present in 1st NN. Figure 5.8 shows variation of total energy as a function of ω -type atomic displacement for different atomic configurations (as shown in Figure 5.6).

Based on the first principles calculations the Figure 5.7 shows the possible way that structures (b)-(d) can reduce their energies by rearranging atoms to another low energy configuration. On the other hand, for structures (e) and (f), the energy could be reduced by undergoing a (nondiffusive) structural transformation to a complete ω structure. However energies of the complete ω structures are higher than the energy of the ω' -Zr₃Al₂Nb structure. Thus, after ω -type transformation, the energy of these systems can be further reduced by diffusion and displacement of atoms. Similarly, Figure 5.8 shows the possible pathways that structures (a), (e) and (h) of Zr₄AlNb can reduce their energies by rearranging atoms (diffusive jumps) to another low energy configurations. On the other hand, for structures (g), (i) and (j), the energy could be reduced by undergoing a (nondiffusive) structural transformation to a complete ω structure and final ω structure is degenerate for configurations (i) and (j). Our calculations shown in Fig. 5.7 and Fig. 5.8 reveal the possible coupled paths (diffusive and displacive) for the Zr₃Al₂Nb and Zr₄AlNb system for chemical ordering. These kind of transformation paths have also been observed in different experiments for Ti based alloys [70,228,229]. Therefore, chemical orderings of the atoms play a crucial rule in the stability of the bcc structures with respect to the ω -type displacive transformation in both Zr₃Al₂Nb and Zr₄AlNb alloys. Moreover, the driving energies for this solid-solid transformations can easily be quantified from Figure 5.7 and 5.8 by comparing potential barriers of different configurations which give ~ 270 meV/atom and ~ 70 meV/atom for Zr₃Al₂Nb and Zr₄AlNb alloy, respectively.

5.4 Summary

We performed first principles calculations to understand possible mechanism of ordered ω -Zr₂Al, ω Zr₃Al₂Nb and Zr₄AlNb phase formation from disordered counterpart by a coupled replacive-displacive transformation mechanism. For the binary alloy, our ab-initio calculations showed that at any intermediate stage of the transformation, the extent of plane collapse (displacive process) directly depends upon the degree of replacive ordering achieved by the system. Our calculations also showed that the displacive process prefers an atomic arrangement where every ‘Al’ atom is surrounded by ‘Zr’ atoms as 1st nearest neighbors in the unit cell. The interpretation in terms of higher number of Zr-Al bonds present as 1st nearest neighbor in the unit cell clearly shows inherently strong tendency of chemical ordering in this alloy.

For ternary alloys, our study predicts formation of chemically ordered ω phase with the trigonal symmetry (space group $P\bar{3}m1$, non-ideal ω) in Zr₃Al₂Nb and chemically ordered ω phase with the trigonal symmetry (space group $P3m1$, ideal ω) in Zr₄AlNb alloy. In order to decide position of Al and Nb atoms in the bcc lattice several symmetrically inequivalent atomic configurations were examined. Moreover, based on the number of Zr-Al and Zr-Nb bonds present as first nearest neighbor in the unit cell of each configuration, one can predict the stability of each rearranged structure.

This study delineates the most probable pathway on the free energy surface of diffusive *vis-a-vis* displacive transformation by quantitative determination of thermodynamic tendencies at different stages of the transformation. We believe that this mechanism is broadly relevant to other coupled replacive-displacive phase transformations in many alloys.

Chapter 6

Superionic Transition in ThO₂

6.1 Introduction

In this chapter, we present results of our computational work done to study superionic phase transformation pathway in ThO₂. It is now well established that cubic fluorite structured materials undergo a transition to the “superionic” regime at temperatures close to, but below, their melting points. This transition is associated with (i) a dramatic increase in ionic conductivity [88, 244, 245] although electronic conductivity remains low (ii) a dynamic disorder in the anion sublattice. But the details of anion transport mechanisms are still not completely understood [88, 143, 245–249]. Moreover, it is essential to understand microscopic mechanism responsible for macroscopic superionic conduction.

Within the literature, the study of high temperature superionic transition in UO₂, has remained the subject of interest motivated by its use as a fuel for nuclear fission reactors [6, 28, 87, 88, 250]. But very little attention has been paid to other fluorite group members, e.g., ThO₂. With renewed interest in studying the feasibility of thorium-based materials as a potential fuel for various reactor systems, it is essential to study structural stability at extreme thermodynamic conditions. In the halide compounds, superionic transition temperature (T_c) is typically $\sim 0.8T_m$ (T_m being the melting temperature). For ThO₂, which has a $T_m = 3600$ K, a superionic transition might then be expected to occur at $T \sim 2900$ K. Although this is well above normal reactor operating temperatures, a detailed knowledge of the anion diffusion properties of ThO₂ is essential for fuel design, performance modeling and safety analysis. Furthermore, the presence of an additional component in the heat capacity C_p (due to the onset of any thermally induced Frenkel disorder) has important consequences when assessing the outcomes of possible reactor accident

scenarios.

The main objectives of this chapter are: (i) to study lattice dynamical and mechanical stability of thoria as a function of isotropic lattice strain (dilation) using first-principles calculations and (ii) to determine the probable directions of diffusion and actual diffusion paths of the oxygen atoms in the superionic regime using classical molecular dynamic simulations. In these calculations isotropic dilation in lattice parameter (ϵ), defines as

$$\epsilon = \frac{a - a_0}{a_0} \quad (6.1)$$

(a_0 = equilibrium lattice constant and a = strained lattice constant), is a manifestation of high temperature environment in pure ThO_2 . Using the density function theory (DFT), the phonon dispersion curves have been calculated as a function of ϵ to study dynamical stability of ThO_2 as a function of temperature. Classical molecular dynamics simulations have been performed to determine easy direction of movement, actual migration pathway of oxygen atoms, and mechanical stability of the structure which is important to understand the diffusion mechanism in the superionic region.

6.2 Computation Methodology

The actinide oxides are the members of a class of strongly correlated materials, the Mott insulators. Their complex physical and chemical properties make them challenging systems to characterize, both experimentally and theoretically. Chiefly, this is because actinide oxides can exhibit both electronic localization and delocalization and have partially occupied f orbitals, which can lead to multiple possibilities for the ground state. Of particular concern for theoretical work is that the large number of competing states display strong correlations which are difficult to capture with computationally tractable methods [251]. Therefore, in this study DFT+ U and Hybrid functional methods have been employed to account for the partially occupied f orbitals.

The Vienna ab initio simulation package (VASP) was employed to perform DFT based electronic structure calculations where the Kohn-Sham equations are solved using a plane wave expansion for the valence electron density and wave functions [177]. The interactions between the ions and electrons are described by ‘Projector Augmented Wave’ (PAW) potentials, which use smaller radial cutoffs (core radii) and reconstruct the exact valence wave function with all nodes in the

core region [176]. The PAW potentials used in this study are those provided in the VASP database which treats thorium $6s^2 7s^2 6p^6 6d^1 5f^4$ and the oxygen $2s^2 2p^4$ electrons as valence electrons. Exchange-correlation effects were treated using the local-density approximation (LDA) in the Ceperley-Alder parametrization and generalized gradient approximation (GGA) in the Perdew-Burke-Ernzerhof parametrization [165] within VASP. The Hubbard U correction was introduced with LDA using the method as proposed by Dudarev *et al.* [252], in which the U parameter (reflecting the strength of on-site Coulomb interaction) and J parameter (adjusting the strength of exchange interaction) are combined into a single parameter $U_{eff} = U - J$ to take care of the Coulomb repulsions between the localized f-electrons. To decide upon a suitable value of U_{eff} , available experimental data for ground state properties (e.g., lattice constant, bulk modulus and electronic band-gap) were compared with LDA+ U calculated values. All the calculations were performed with plane wave cutoff energy of 600 eV. The total energy of ThO₂ was optimized with respect to volume (or lattice parameter) and atomic positions. The conjugate gradient algorithm was used for the unit-cell relaxations until the residual forces and stress in the equilibrium geometry were of the order of 0.005 eV/Å and 0.01 GPa, respectively. A $16 \times 16 \times 16$ k-point mesh was constructed using the Monkhorst-Pack scheme to sample the Brillouin zone [208], which provided convergence in the total energy up to 0.0001 meV/atom.

We further used the screened hybrid functional of Heyd, Scuseria, and Ernzerhof (HSE06) functional [253] which takes into account the effects of nonlocal exchange with 25% Hartree-Fock contribution and a 0.2/Å screening length. As hybrid functional calculations are computationally expensive compared to standard LDA+ U and GGA, we restricted their application to calculate lattice dynamical properties for limited values of isotropic strain.

To calculate phonon frequencies of ThO₂, the small displacement method as implemented in the PHONOPY [254] program was employed. In this methodology, the dynamical matrix is derived by giving small displacements to the atoms in the supercell from their equilibrium positions and calculating the resulting forces within the DFT framework. The phonon dispersion of ThO₂ at different lattice parameters was calculated using the GGA and LDA+ U by giving appropriate atomic displacements in a $3 \times 3 \times 3$ (81 atoms) supercell. For the supercell force calculations a k-point mesh of $8 \times 8 \times 8$ was used. The splitting between the longitudinal optical (LO) and transverse optical (TO) phonon modes was corrected using a non-analytical correction term [255–257]. For the calculation of Born effective charges and high frequency dielectric constants at different values of lattice strain, a linear

response method was employed as implemented in VASP. For the ab-initio part of this study, the temperature effects are considered indirectly by considering isotropic dilation of the lattice parameter.

The MD simulations to study thermal, mechanical and anion transport properties were carried out using the LAMMPS [258] code. Long range coulombic interactions were calculated using the Ewald method [192] with the particle-particle particle-mesh (PPPM) implementation of the method within the MD calculations to improve computational efficiency [258]. The interatomic potential of ThO₂ used, combines the Buckingham-Morse functional form with many-body interactions [148]. The MD supercell had 4000 cations and 8000 anions and was constructed as an array of 10×10×10 unit cells of ThO₂. These structures were equilibrated with 1 fs time steps in the temperature range 300 K to 3000 K (100 K interval) with the NPT ensemble (constant number of particles, pressure and temperature) at zero external pressure using the Berendsen barostat with a time constant of 0.5 ps and the Nosé-Hoover thermostat with a time constant of 0.1 ps. Each simulation of thermal expansion, mean-square displacements, radial distribution functions was carried out initially for 400 ps for equilibration at the desired temperature and then for another 100 ps to get an average value of the thermodynamic quantity.

To calculate the temperature dependent elastic constants, C_{11} , C_{12} and C_{44} , a stress-strain method was applied just after the system was equilibrated within the NPT ensemble at zero external pressure for 200 ps at the desired temperature. In the stress-strain method, positive and negative box displacements (deformation) were applied in all the symmetry directions and the resultant changes in stress were computed to determine elements of the elastic stiffness tensor. The deformation magnitude in the stress-strain calculations were varied from 10^{-6} to 10^{-3} in six equal steps to ensure converged values of single crystal elastic constants (C_{11} , C_{12} and C_{44}). From the calculated values of C_{11} , C_{12} and C_{44} poly-crystalline Young and shear moduli were calculated using the Voigt-Reuss-Hill approximations [236–238].

6.3 Ground State Properties of ThO₂

Table 6.1 compares our GGA and LDA+ U calculated values of equilibrium lattice constant (a_0), bulk modulus (B_0), pressure derivative of bulk modulus (B'_0), single crystal elastic constants (C_{11} , C_{12} and C_{44}), high frequency dielectric constants (ϵ_∞) and Born effective charges (Z^*) of ThO₂, with previously reported theoretical and experimental values in the literature [84, 259–264]. Figure 6.1 shows the variation

of equilibrium lattice constant (a_0), bulk modulus (B_0) and electronic energy-gap (E_g) as a function of U_{eff} calculated for LDA+ U where experimental values are presented as horizontal solid lines. Analysis of this figure shows that the Hubbard-type on-site electronic interaction with value $U_{eff} = 5$ eV yields a better prediction of experimental data (shown in Table 6.1) which is also consistent with a previous theoretical study [264]. Our LDA+ U calculated a_0 is in excellent agreement ($<0.01\%$) with experimentally reported values at room temperature, but our GGA-PBE calculated value is an overestimate (by 0.3%). Our GGA and LDA+ U calculated values of B_0 underestimate (4-6%) and overestimate (5.5-7%) experimentally reported values [84, 259], respectively. Our GGA and LDA+ U calculated values of B'_0 match well with the experimentally reported value by Idiri *et al.* [259] (high pressure synchrotron X-ray diffraction data) but underestimate (by 20%) the value reported by Olsen *et al.* [84] (high pressure XRD). Our GGA calculated elastic constants match well ($<4\%$) with single crystal ThO₂ elastic constant data measured by Mecedo *et al.* [260], but are underestimated compared to those calculated from the inelastic neutron scattering data of Clausen *et al.* [261]. Our GGA and LDA+ U calculated values of ϵ_∞ (4.83 and 4.74, respectively) are in good agreement with the experimental value (4.86) determined by Axe *et al.* [262]. Our GGA and LDA+ U calculated Z^* for Th and O ($Z_{Th}^*=5.41$, $Z_O^*=-2.71$ and $Z_{Th}^*=5.38$, $Z_O^*=-2.69$, respectively) are in good agreement with previous theoretical calculations [263, 264]. Moreover, our theoretically calculated values of a_0 , B_0 , B'_0 , C_{11} , C_{12} , C_{44} and ϵ_∞ are in good agreement with GGA and LDA+ U calculated values by Lu *et al.* [263] and Sevik *et al.* [264], respectively. Therefore, both GGA and LDA+ U provide comparable descriptions of the ground state properties of ThO₂ and therefore both these approximations were considered for the determination of lattice dynamical properties of ThO₂ as a function of isotropic dilation in lattice parameter.

6.4 Lattice Dynamical Properties of ThO₂

Our GGA and LDA+ U calculated phonon dispersion curves (shown in Figure 6.2) are compared with the inelastic neutron scattering measurements of Clausen *et al.* [261] at 293 K and Raman scattering measurements of Jayaraman *et al.* [265] at 295 K. These experimental measurements were performed at room temperature and more accurate comparison of calculated phonon frequencies at special symmetry k-points can be made by performing an LDA+ U calculation of phonon dispersion with an expanded lattice taking into account the thermal expansion of ThO₂ to room temperature ($9.5-10.0 \times 10^{-6} \text{ K}^{-1}$) [6]. A comparison of LDA+ U calculated

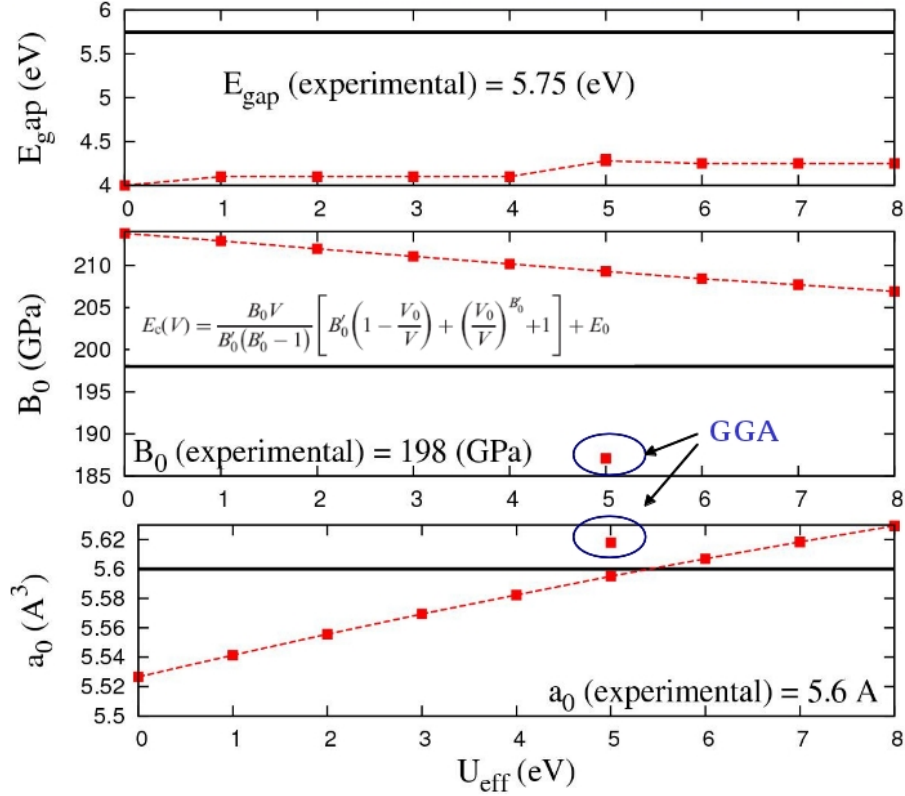


Figure 6.1: Variation of equilibrium lattice constant (a_0), bulk modulus (B_0) and electronic energy-gap (E_g) as a function of U_{eff} calculated for LDA+ U . Experimental values are presented as horizontal solid lines in the graph. In this graph we also show pure GGA calculated values of a_0 and B_0 for comparison with LDA+ U calculated values. For the calculation of bulk modulus Birch-Murnaghan equation of state was employed as shown in B_0 vs. U_{eff} plot.

phonon frequencies across the high symmetry paths with neutron scattering data shows that our LDA+ U results agree well with experimental data in reproducing acoustic phonon frequencies. In almost all symmetry directions of the phonon dispersion curve, GGA calculated phonon frequencies are lower compared to LDA+ U calculated values. In this study, the calculations for phonon dispersion curves were performed on a $3 \times 3 \times 3$ supercell with 81 atoms. We checked convergence of LDA+ U calculated phonon frequencies by performing a similar calculation (small displacement method) with a $4 \times 4 \times 4$ supercell of 192 atoms and results are shown in supplementary information (Figure 6.3). A comparison of the phonon dispersion curves calculated with 81 atoms and 192 atoms supercells show frequency values calculated with smaller the supercell match within 5% of frequency values calculated with the larger supercell. Therefore, further calculations of the phonon dispersion curve as a function of isotropic dilation in lattice parameter were performed with the $3 \times 3 \times 3$ supercell.

Table 6.1: Calculated structural, elastic and dielectric properties of ThO₂ are compared with previous experimental and theoretical results in the literature. (* = our HT-XRD study)

Properties	This work			Previous Experimental Work	Previous Theoretical Work	
	GGA	LDA+ <i>U</i>	MD		GGA	LDA+ <i>U</i>
a_0 (Å)	5.618	5.595	5.596	5.598(4) [84], 5.6001(3) [259], 5.597 *	5.619 [263]	5.60 [264]
B_0 (GPa)	187.4	209.3	192.9	195.3±2.0 [84], 198(2) [259]	190 [263]	216 [264]
B'_0	4.23	4.28	-	5.4±0.2 [84], 4.6(3) [259]	4.3 [263]	
C_{11} (GPa)	352.2	375.4	351.9	367 [260], 377 [261]	351.2 [263]	381 [264]
C_{12} (GPa)	107.8	129.8	113.6	106 [260], 146 [261]	106.9 [263]	134 [264]
C_{44} (GPa)	74.6	105.8	71.7	79 [260], 89 [261]	74.1 [263]	106 [264]
ϵ_∞	4.83	4.74	-	4.86 [262]	4.83 [263]	
Z_{Th}^*	5.41	5.38	-	-	5.41 [263]	5.327 [264]
Z_O^*	-2.71	-2.69	-	-	-2.71 [263]	-2.663 [264]

In Table 6.2, we enlist out GGA and LDA+*U* calculated phonon frequencies as well as experimentally measured phonon frequencies at high symmetry points of the Brillouin zone, *viz.*, Γ , X and L. Our LDA+*U* calculated phonon frequencies of F_{1u} (LO) and F_{2g} modes match well, within $\sim 1\%$ of the neutron scattering and Raman scattering data. However, the LDA+*U* calculated F_{1u} (TO) mode is overestimated by 7% compared to the experimental results and the GGA calculated value is underestimated by 7% compared to the experimental results. At the X point, our LDA+*U* calculated phonon frequencies of E_u (acoustical mode) and E_u (optical mode) match well with inelastic neutron scattering measured frequencies but for the E_g mode, the LDA+*U* calculated value is overestimated by $\sim 23\%$. Overall, optical phonon frequencies are lower for GGA calculations compared to those of LDA+*U*. The experimentally measured E_u mode [261, 265] matches well with calculated values. At the L point, our LDA+*U* calculated phonon frequencies for E_u (acoustical mode), A_{1u} and E_g match very well with inelastic neutron scattering measured frequencies [261]. Conversely, LDA+*U* calculated E_u (optical) and A_{1g} mode frequencies are overestimated. Moreover, our GGA calculated values are always underestimated compared to experimental vales [261, 265].

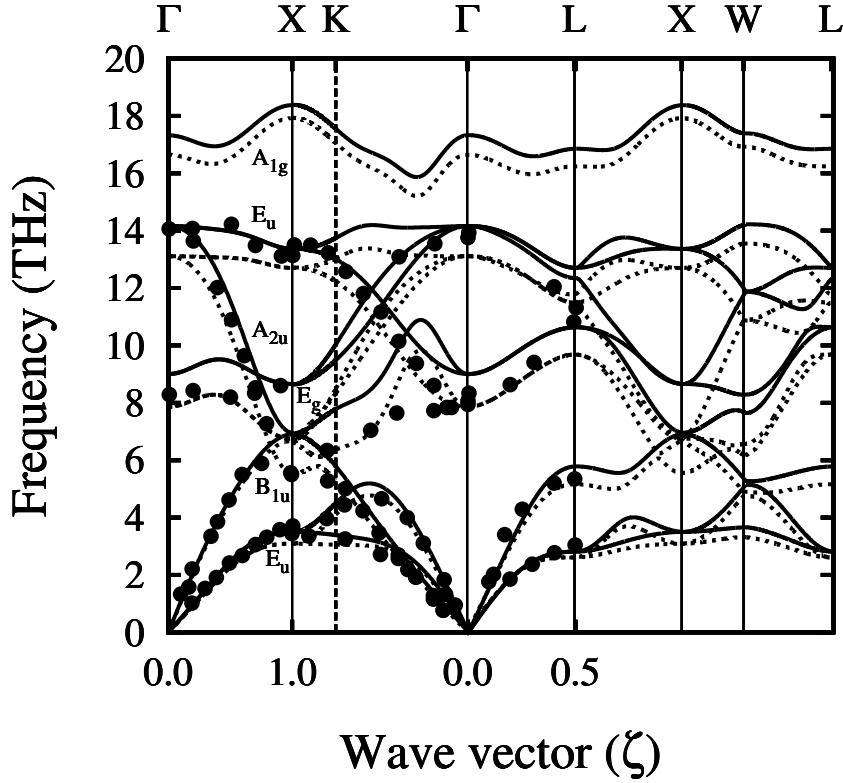


Figure 6.2: Phonon dispersion curve of ThO₂ calculated using GGA and LDA+*U* compared with inelastic neutron scattering data [261] and Raman scattering measured data [265] at room temperature. Solid and dotted line represents LDA+*U* and GGA calculated phonon frequencies, respectively. Solid circles present experimentally measured data. The notation of the special points is Γ (0,0,0), X (0,0,1), W (1,1,0) and L (1,1,1).

6.5 Lattice Dynamical Properties as a function of isotropic strain

Figure 6.4 shows our GGA and LDA+*U* calculated phonon dispersion curves and density of states (DOS) for ThO₂ at different lattice strains (dilation). It is important to note that overall as ϵ increases, the phonon frequencies decrease, as the material itself becomes softer. The singlet B_{1u} mode softens considerably as a function of ϵ at the X point compared to other modes. The E_u doublet mode also softens but the rate of softening of E_u is small compared to the B_{1u} mode. The singlet B_{1u} mode crosses the E_u doublet in the range $0.04 < \epsilon < 0.045$ and $0.045 < \epsilon < 0.05$ for GGA and LDA+*U* calculated phonon frequencies, respectively. A maxima in the phonon DOS in the low frequency region can also be observed at $\epsilon = 0.04$ and $\epsilon = 0.05$ for the GGA and LDA+*U* calculated DOS. A sharp increase in the phonon DOS is observed at the frequency where the B_{1u} mode intersects the

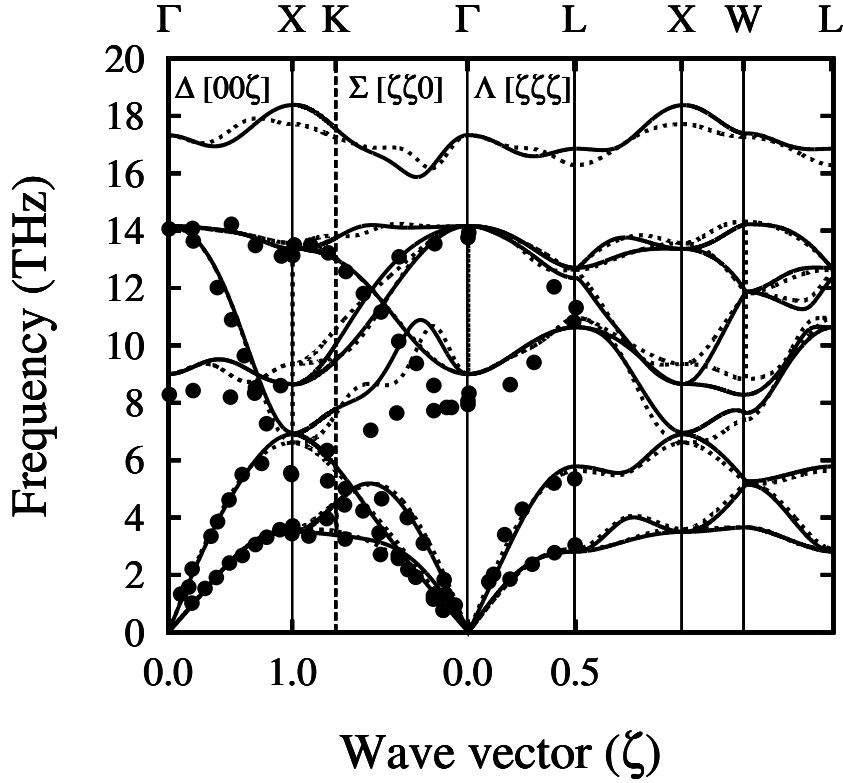


Figure 6.3: Phonon dispersion curve of ThO₂ calculated using LDA+ U and $3\times 3\times 3$ (81 atoms) as well as $4\times 4\times 4$ (192 atoms) supercell compared with inelastic neutron scattering data at room temperature. Solid and dotted line represents calculated phonon frequencies for $3\times 3\times 3$ and $4\times 4\times 4$ supercell, respectively. Solid points are neutron scattering data as reported by Clausen *et al.* [261].

E_u mode (or close to it) at the X point. The crossover of the B_{1u} and E_u modes can be observed clearly in Figure 6.5, where the variation of the B_{1u} and E_u modes is plotted a function of isotropic lattice strain.

Experimentally determined temperature variation of lattice parameters data for ThO₂ shows 3.8% and 4% lattice strain at ~ 3500 K and ~ 4000 K, respectively [122]. Our GGA calculated B_{1u} mode gets softer with increasing ϵ and becomes imaginary in the range $0.04 < \epsilon < 0.045$. Therefore, our GGA calculated results predict an overestimated lattice parameter (or corresponding temperature) to achieve the superionic state compared to those reported experimentally. This can be attributed to the following: (i) the small displacement method (or harmonic approximation) to calculate phonon dispersion curve is not valid as temperature approaches the melting temperature (since anharmonic effects are expected to become important), (ii) while the GGA approximation is reasonably good for predicting ground state structural and mechanical properties of ThO₂ and its efficacy at elevated temperatures is not proven.

Table 6.2: GGA, LDA+ U and HSE06 calculated phonon mode frequencies of ThO₂ at high symmetry points of the Brillouin zone (Γ , X and L) are compared with inelastic neutron scattering and Raman scattering measured phonon frequencies. The results are shown for isotropic lattice strain (ϵ) of 0.00.

Symmetry	Mode	GGA	LDA+ U	HSE06	Experiment
Γ	F_{1u} (LO)	16.6	17.3	16.8	16.9 [261], 17.0 [265]
	F_{2g}	13.1	14.2	12.1	14.1 [261], 13.9 [265]
	F_{1u} (TO)	7.9	9.0	8.2	8.3 [261], 8.4 [265]
X	A_{1u}	17.9	18.4	18.2	-
	E_u	12.7	13.4	13.4	13.3 [261]
	A_{2u}	6.7	8.6	8.1	-
	E_g	6.7	7.0	6.7	5.7 [261]
	B_{1u}	5.6	6.9	5.5	-
	E_u	3.1	3.5	3.4	3.6 [261]
L	A_{1u}	16.2	16.9	16.5	-
	A_{1g}	11.8	12.7	12.6	12.2 [261]
	E_u	11.5	12.4	12.0	11.2 [261]
	E_g	9.7	10.6	10.5	10.7 [261]
	A_{1u}	5.2	5.8	5.3	5.3 [261]
	E_u	2.6	2.8	2.9	2.9 [261]

Figure 6.5 also shows hybrid-functional DFT calculated phonon frequencies of B_{1u} and E_u modes for $\epsilon = 0.0, 0.03, 0.035$ and 0.04 . Hybrid functional (HSE06) provides a significant improvement in the electronic structure description and calculated structural properties of ThO₂ [251]. It is expected that this functional would give accurate phonon dispersion compared to GGA and LDA+ U . As hybrid functional DFT calculations are computationally more demanding than the standard GGA and LDA+ U calculations. We limited the force calculations, using small displacement method to a 2x2x2 supercell of primitive ThO₂. For the calculation of LO-TO splitting at Γ point, experimentally determined value of $\epsilon_\infty = 4.83$ [263] was used. The HSE06 calculated equilibrium lattice parameter (a_0) of 5.5862 Å is matching well previous experiments [84, 259]. Table 6.2 compares hybrid DFT calculated phonon frequencies with GGA and LDA+ U calculated values as well as neutron scattering and Raman scattering data. The hybrid DFT calculated phonon frequencies gives higher frequencies of F_{1u} mode at the Γ point, A_{1g} , E_u , A_{2u} modes at the X point and A_{1u} , A_{1g} , E_u , E_g modes at the L point compared to their GGA calculated values.

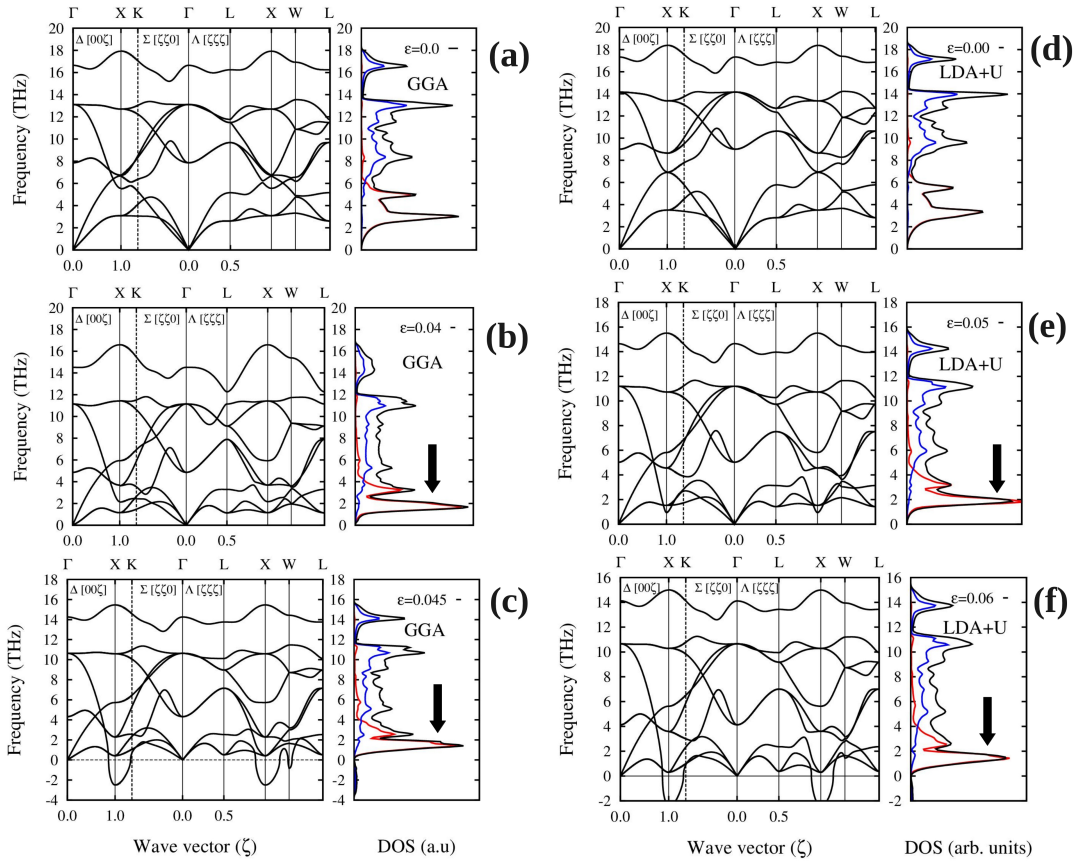


Figure 6.4: Phonon dispersion curve and density of states for ThO_2 calculated using GGA at lattice strain (a) $\epsilon = 0.0$, (b) $\epsilon = 0.04$, (c) $\epsilon = 0.045$ and using LDA+U at lattice strain (d) $\epsilon = 0.0$, (e) $\epsilon = 0.05$, (f) $\epsilon = 0.06$. Red, blue and black lines in DOS plot shows partial DOS of Th, O and total DOS, respectively.

6.6 B_{1u} and E_u phonon mode softening at the X point

Figure 6.5 suggests an almost linear decrease in frequency with increasing lattice strain for GGA and LDA+U calculated B_{1u} and E_u modes from $\epsilon = 0.0$ to 0.04. After $\epsilon > 0.04$, these mode frequencies decrease abruptly and the B_{1u} mode frequencies becomes smaller compared to E_u mode frequencies in the range $0.05 > \epsilon > 0.04$. It was mentioned earlier that there is an increase in the narrow peak in the PDOS when the B_{1u} and E_u modes cross (or are about to cross) at the X point. In other words, the occupations of these modes are higher at high temperatures and possibility of the coupling of these two modes is also high. With further increase of lattice strain B_{1u} mode becomes imaginary at $\epsilon = 0.042$ and 0.052, for GGA and LDA+U, respectively. Using hybrid DFT calculations, we find that the B_{1u} and

E_u modes cross at $\epsilon = 0.03$ (corresponding to $T = 3000$ K [122]) and B_{1u} mode becomes imaginary at $\epsilon = 0.036$ (corresponding to $T = 3430$ K [122]). Therefore, B_{1u} mode becomes imaginary at a temperature below the melting temperature of ThO_2 (≈ 3600 K) [122].

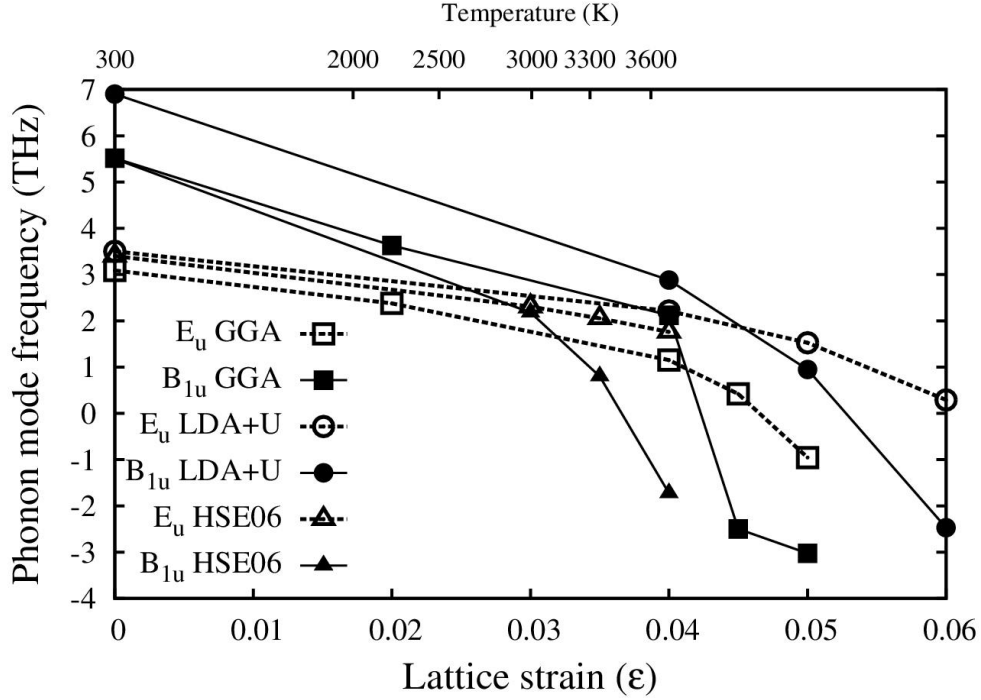


Figure 6.5: GGA, LDA+ U and HSE06 calculated E_u (empty points) and B_{1u} (solid points) mode frequencies at the X point as a function of linear lattice strain. Solid lines are drawn only for visual guidance

The singlet B_{1u} mode consists of O ions motion in the [001] direction as shown in Figure 6.6. If we consider O atoms in the ThO_2 unit cell as a row of atoms along [001], then atomic rows along [110] (and equivalent directions) move in phase and adjacent atomic rows move in the opposite phase. On the other hand, the doubly degenerate E_u mode consists of simultaneous Th and O movement perpendicular to [001]. Figure 6.6 also shows GGA and LDA+ U calculated variation of the potential energy versus zone center phonon mode B_{1u} in terms of the normalized atomic displacement of O atoms as a function of isotropic dilational lattice strains. For $\epsilon = 0$, the effective potential has a minimum at zero atomic displacement. With increasing ϵ (or temperature, $\epsilon = 0.045$), the effective potential transforms into a double well (from a single well) having maxima at equilibrium atomic position. The application of isotropic strain (dilation) modifies the potential energy landscape for the B_{1u} phonon mode in such a fashion that the oxygen atom movement along the [001] direction towards a nearby tetrahedral oxygen site becomes easier compared

to other modes of phonon vibrations corresponding to the volume of the superionic region. Hence, temperature increase could lead to migration of oxygen atoms from one tetrahedral site to a nearby vacant tetrahedral site along a $[001]$ direction. It is also important to note that, the effect of ϵ on the GGA calculated potential energy is greater than the LDA+ U calculated potential energy. This can also be understood from the calculated phonon frequencies as a function of ϵ (Figure 6.5), which shows less softening of the B_{1u} mode for LDA+ U values compared to GGA.

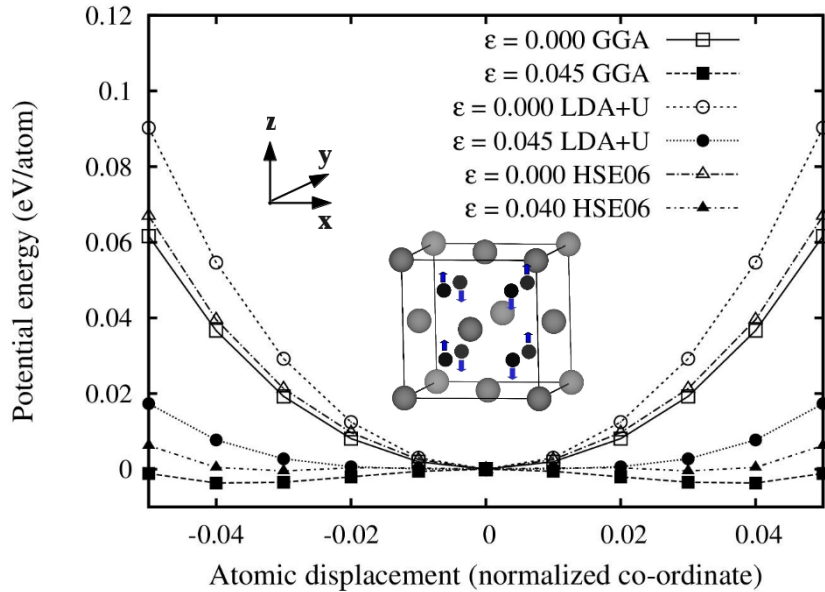


Figure 6.6: GGA, LDA+ U and HSE06 calculated variation of potential energy versus zone center phonon mode B_{1u} in terms of normalized atomic displacement of O atoms as a function of isotropic dilational lattice strains. Actual motion of the O atoms in the ThO₂ unit cell is also shown.

6.7 Transition to Superionic State: The Pathway

6.7.1 Anion Conduction Mechanism

Systematic vibration of oxygen atomic rows along $\langle 001 \rangle$ directions leads to a singlet B_{1u} phonon mode. Similarly, a systematic vibration of Th and O atoms perpendicular to $\langle 001 \rangle$ directions (i.e., in the (110) planes) leads to the E_u phonon mode. At lower values of ϵ (< 0.04), these two modes remain uncoupled and mode frequencies decrease almost linearly with ϵ . Moreover, the amplitude of vibration

of the O atoms along $\langle 001 \rangle$ is higher compared to its amplitude of vibration perpendicular to $\langle 001 \rangle$. With increasing ϵ ($0.04 < \epsilon < 0.05$), the amplitude of vibration perpendicular to $\langle 001 \rangle$ increases and the dynamics of O atoms corresponding to B_{1u} and E_u phonon modes become coupled, which is also manifested by a sharp increase of the narrow peak in the PDOS when the B_{1u} mode frequency become smaller than the E_u mode in the phonon dispersion curve. In other words, coupling of the B_{1u} and E_u phonon modes increases the possibility that the interstitial site is occupied at temperatures close to T_c . The transformation of the potential energy landscape from single well to double well ($|\epsilon| > 0.04$) emphasizes how anions preferentially migrate to interstitial sites along $\langle 001 \rangle$, which leads to Frankel-like positional disorder. With further increase of ϵ , the B_{1u} phonon mode frequencies become imaginary which leads to thermally activated complete disorder of the anion sublattice. Coupling of the B_{1u} and E_u phonon modes changes the superionic conductivity regime, where anionic conductivity is mediated by random anion hopping to interstitial sites along $\langle 001 \rangle$ from correlated anionic motion at interstitial sites F1 (48 g Wyckoff positions) and F2 (32 f Wyckoff positions).

Gavartin *et al.* [266] calculated the phonon dispersion curve and PDOS of Li_2O at 10 K and 1000 K using the quasi-harmonic approximation and MD simulations and found a crossover of the transverse Raman mode (TR) and the LO mode as temperature reached the fast-ionic phase transition point. They attributed this to a change in cationic conductivity mechanism. Mode softening leads to the loss of the relative phase of Li^+ ions moving along the $[100]$ crystal direction (as the TR mode disappears), so that the ionic motion can be considered as a set of coupled oscillators. As soon as a few neighboring ions get in phase, a large amplitude coherent motion rapidly develops along $\langle 100 \rangle$. Such fluctuations propagate a caterpillar-like mechanism, whereby a Li^+ ion moves into the cube-interstitial position, while the rest of the chain of ions moves simultaneously along $\langle 100 \rangle$, each ion filling the site vacated by its nearest-neighbour. Thus, an interstitial ion and a cation vacancy, separated by a few unit cells, can be created within the same elementary event. With further increase of temperature, cation transport is mediated through a hopping mechanism. We believe an equivalent anionic conduction mechanism is followed in ThO_2 .

6.7.2 Migration Barrier for Oxygen Movement

In order to gain further insight into the anion conduction mechanism near the superionic transition point we performed MD simulations to calculate migration

barriers along different symmetry directions and traced the actual oxygen trajectory as a function of time in the superionic state. The migration barrier for oxygen movement was calculated by creating an oxygen vacancy at a regular lattice site and moving another neighbouring oxygen atom from its initial lattice site towards the vacant lattice site along [001], [110], and [111] high-symmetry directions. In **appendix A** a sketch showing vacancy position and direction of migration of oxygen atom toward that vacancy site is given (Figure A.1). An oxygen vacancy was created at a point in 10x10x10 supercell by intentionally removing one oxygen atom from that point and putting that O atom at an octahedral position of fcc lattice far away (nearly five unitcells away) from the defect site to maintain the charge neutrality of the simulation box. Initially, this configuration was optimized and nudged-elastic-band calculations were performed on the optimized structure by moving another neighboring oxygen atom from its initial lattice site towards the vacant site. For this purpose the nudged-elastic-band (NEB) method [267–269] was employed as embedded in LAMMPS. In this calculation 6 intermediate states were inserted and diffusion barriers were calculated. This enabled us to identify the easy direction for oxygen motion towards the vacant site in normal and superionic states. Figure 6.7 shows the NEB calculated oxygen migration barrier along [001], [110] and [111] the three high symmetry directions for lattice parameter $a = 5.6 \text{ \AA}$ (corresponding to the normal state) and $a = 5.8 \text{ \AA}$ (corresponding to the superionic state). The MD NEB calculated oxygen migration barriers along [001], [110] and [111] directions are 0.78 (0.17), 4.77 (4.47) and 5.24 (5.02) eV, respectively, for lattice parameter $a = 5.6 \text{ \AA}$ (and $a = 5.8 \text{ \AA}$). From this analysis it is evident that the $\langle 001 \rangle$ directions are most favorable for oxygen atom movement in normal and superionic states.

6.7.3 Position-Time plot for oxygen migration

In order to identify the superionic transition temperature (T_c) for ThO_2 (corresponding to the potential used in our MD simulations), we initially determined the mean square displacements (MSD), diffusion coefficients of oxygen atoms and radial distribution functions (RDF) of oxygen atoms in the temperature range 2500-3500 K (in 100 K intervals). The MD calculated values of MSD and the RDF of oxygen atoms as a function of temperature were determined and the results are given in **Appendix A** (Figure A.2, A.3 and A.4, respectively). The analysis of MD calculated MSD, diffusion coefficients and RDF of oxygen atoms shows that the superionic transition occurred at 3000 K.

The snapshot of migration for oxygen atoms at 3000 K is shown in Figure

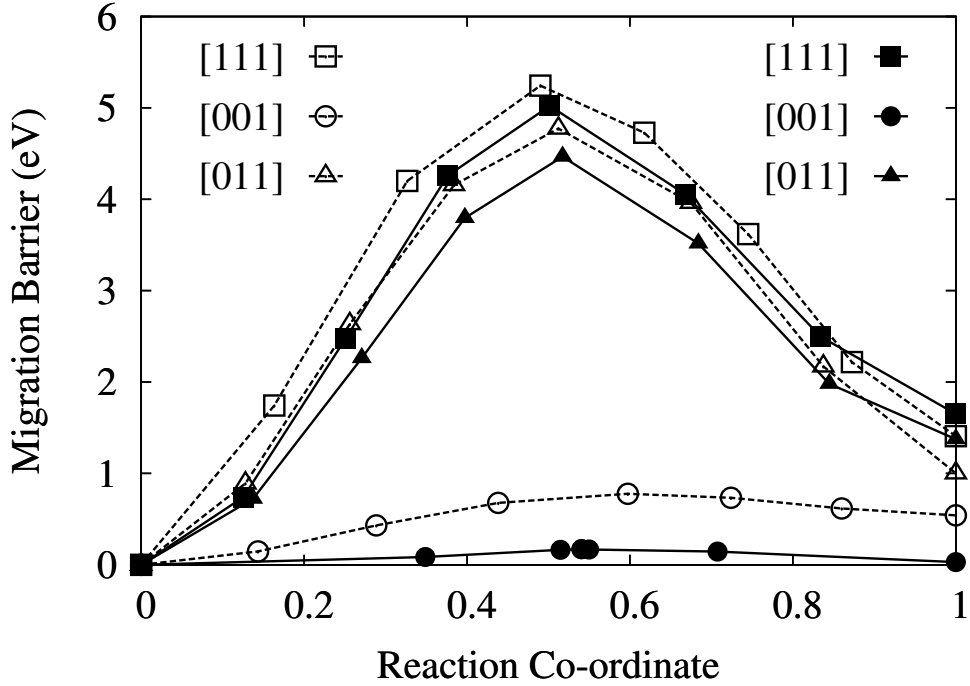


Figure 6.7: MD calculated migration barrier along [001], [110] and [111] high symmetry directions. Solid lines and fill points present MD NEB calculated migration path for $a = 5.6 \text{ \AA}$ (correspond to normal state). Similarly, dotted lines and open points present MD NEB calculated migration path for $a = 5.8 \text{ \AA}$ (corresponds to superionic state).

6.8 as a position-time plot for 20 ps duration in the XY and YZ plane. For these calculations, a $10 \times 10 \times 10$ ThO_2 supercell was initially equilibrated as an NPT ensemble at 3000 K for 500 ps at this temperature the MD calculated equilibrium lattice parameter is 5.803 \AA . This previously equilibrated system was then subjected to a 20 ps run as an NVE ensemble and the trajectories of several oxygen atoms were traced for 20 ps. Among them, the trajectories of two oxygen atoms A and B are shown in Figure 6.8. It is also important to note that at this temperature the atoms are not occupying ideal lattice sites but remain in the tetrahedral region surrounding their ideal lattice sites. Oxygen atom A, initially occupying a position (0.75, 0.75, 1.75), migrates to a position (0.75, 1.25, 1.75) with a jump time of ~ 0.19 ps. The actual atomic position of the atom A can be obtained by multiplying these atomic positions by the equilibrium lattice parameter as shown in Figure 6.8. Atom A resides in the initial position (0.75, 0.75, 1.75) for 11.2 ps and then migrates to position (0.75, 1.25, 1.75) through a octahedral interstitial position (0.50, 0.50, 1.50). On the other hand, atom B, which initially occupies position (5.25, 3.25, 1.75), migrates to position (5.25, 2.75, 1.75) with a jump time of ~ 0.33 ps. Then it moves to position (4.75, 2.75, 1.75) with a jump time of ~ 0.6

ps. Atom B resides in its initial and intermediate positions for 6.00 ps and 9.77 ps, respectively.

The residence time and jump time is determined by calculating a four component vector quantity per atom. The first three components of the vector are the displacements of a atom from its starting position along x, y and z direction (dx , dy and dz). The fourth component is the total displacement, i.e., $\sqrt{(dx^2 + dy^2 + dz^2)}$. We plot $\sqrt{(dx^2 + dy^2 + dz^2)}$ as a function of simulation time for atoms A and B (in **Appendix A**, Figure A.5). From Figure A.5 the residence time and jump time can easily be determined. Similar calculations are performed at 2900 K and no diffusive jumps of oxygen atoms are observed (in **Appendix A**, Figure A.6). Analysis of these results indicates that the oxygen atoms jump from one tetrahedral position to another which is between 1st nearest neighborhood to the initial jump site via a curved diffusion path. Analysis of these results indicates that the oxygen atoms jump from one tetrahedral position to another. At any given instant the probability of an atom sitting in the octahedral position is rather small, which is in accordance with the MD calculated migration barrier values along [001], [110] and [111] directions. A very low migration barrier along $\langle 001 \rangle$ provides oxygen atoms with an easy migration path for random diffusive jumps in the superionic state. Similar result have been reported for UO_2 [89, 90], $\beta\text{-PbF}_2$ [91] and CuI [270, 271].

Neutron diffraction studies using single crystal $\beta\text{-PbF}_2$ showed that the octahedral sites are not significantly occupied at $T > T_c$ [89]. Instead, an appreciable fraction of the anion lattice sites are vacant and located at the F1 and F2 sites. The former was considered to be the location of ‘true’ Frenkel interstitials, situated between the midpoint of the two nearest neighbour anion sites and the centre of an anion cube in $\langle 110 \rangle$ directions, whilst the latter was attributed to nearest neighbour lattice anions relaxed away from their regular sites in $\langle 111 \rangle$ directions towards the centers of adjacent empty anion cubes [89]. This leads to the construction of the two defect cluster models labelled 3:1:2 and 4:2:2 (where the $v : i : r$ notation is number of vacancies : Frenkel interstitials : relaxed anions) [89]. For UO_2 [87, 88] a detailed description of a similar model is given in section 1. Similar results have also been reported for $\gamma\text{-CuI}$ [270, 271] where the ionic density distribution shows no or very little occupation of the octahedral sites with increasing temperature. The MD calculated average potential energy curves obtained for $\gamma\text{-CuI}$ [270] depict that the energy is a minimum for Cu^+ migration at the tetrahedral sites and rises rapidly at the position of the octahedral site.

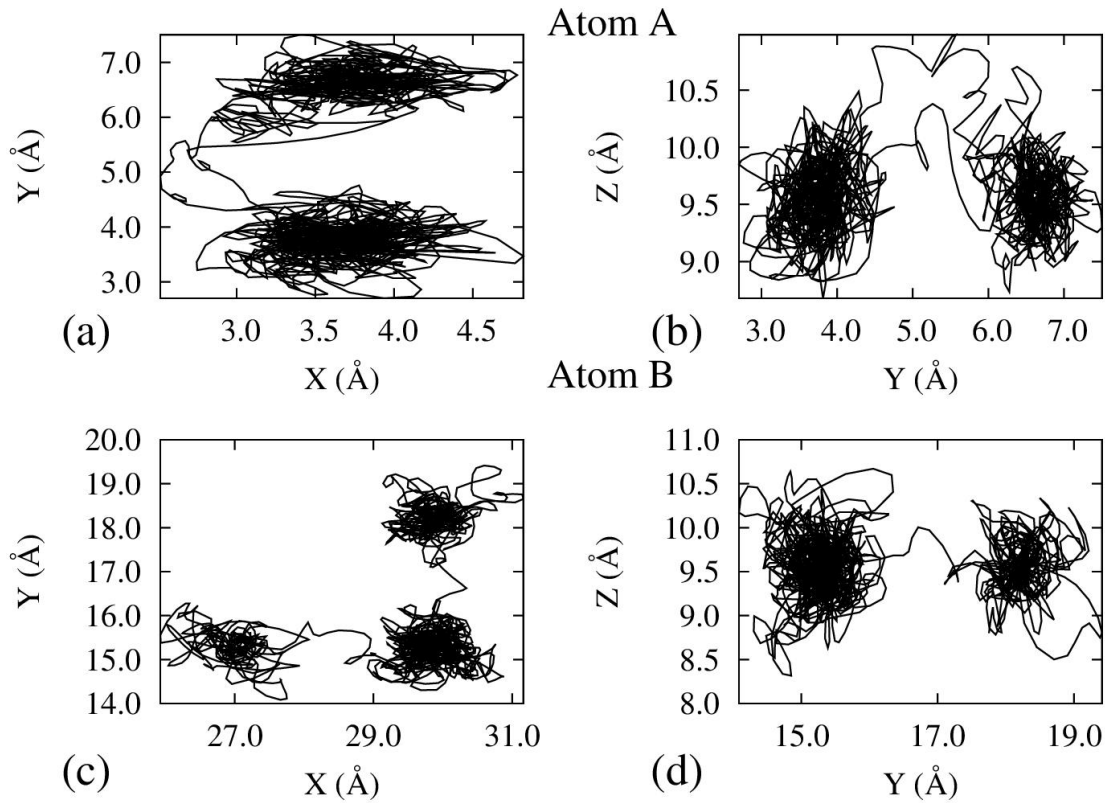


Figure 6.8: Snapshot of the movement of given oxygen atoms (atom A and atom B) for 20 ps time duration in the XY and YZ plane calculated using molecular dynamic simulations at 3000 K. Oxygen atoms preferentially occupy and migrate through tetrahedral positions.

6.8 Temperature variation of single crystal elastic constants

In order to calculate the mechanical stability of ThO_2 elastic constant values were calculated as a function of temperature using LDA+ U , GGA and MD simulations. Figure 6.9 presents single crystal elastic constants (C_{11} , C_{12} and C_{44}) over the strain range 0.00 to 0.05 and also the room temperature single crystal elastic constant values measured by Macedo *et al.* [260]. Our MD calculated elastic constant values at 300 K are also listed in Table 6.1 for comparison with GGA and LDA+ U calculated values (at 0 K) and room temperature experimentally reported values. The MD calculated C_{12} value matches well with experiment, but C_{11} and C_{44} are underestimated (by $< 6\%$). We have plotted MD calculated elastic constant data only upto 2900 K, as the transition of the oxygen sublattice to the superionic states above this temperature did not allow us to employ this methodology.

In our previous discussion it was said that increasing temperature (repre-

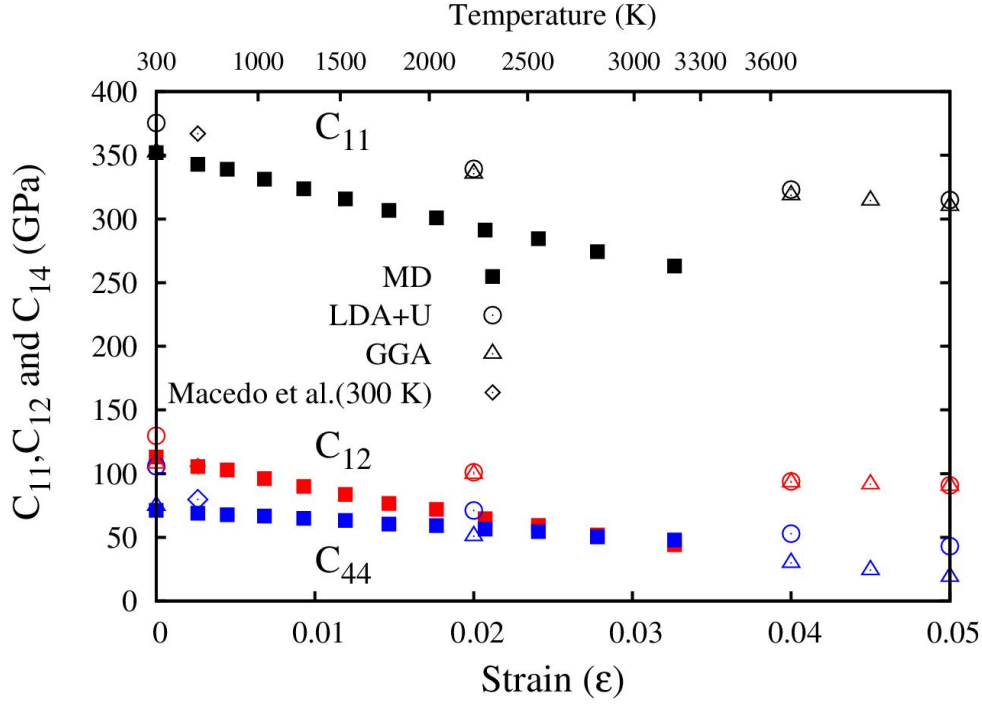


Figure 6.9: LDA+ U , GGA and MD calculated single crystal elastic constants (C_{11} , C_{12} and C_{44}) are shown as a function of lattice strains (temperatures) and experimentally measured room temperature values are also shown (measured by Macedo *et al.* [260] from single crystal ThO_2). Similar symbol with color black, red and blue represents C_{11} , C_{12} and C_{44} , respectively.

sented by isotropic strain) resulted in a significant change in B_{1u} and E_u phonon modes, which in turn changed the elastic properties of single crystal ThO_2 (see section 6.6). From our MD calculated results it was found that C_{11} shows the most softening, which is one of the pertinent characteristics of the superionic transition. C_{12} and C_{44} also get softened but the rate of decrease of C_{11} is higher compared to other elastic constants, as temperature increases. At this point, it is also important to note that the value of C_{12} becomes less than C_{44} around 2750 K. Our results show that the phase stability criteria: $C_{11}+2C_{12} > 0$, $C_{11}-C_{12} > 0$ and $C_{44} > 0$ are satisfied at all temperatures (i.e here values of dilational lattice strain) including the temperature corresponding to the superionic regime where the B_{1u} phonon mode is imaginary. Thus, the fluorite phase of ThO_2 remains elastically stable upto the superionic regime. Further, calculations of bulk, shear and Young modulus were performed and MD calculated values were compared to previous experimentally reported values shown in Figure 6.9.

Finally, the oxygen atom displacement pattern corresponding to B_{1u} mode (in ThO_2), beyond harmonic region, leads to a phase change to a tetragonal struc-

ture in ZrO_2 and HfO_2 . However, experimental phase diagram data for ThO_2 shows that the cubic structure is the only stable phase upto melting temperature. ThO_2 satisfies mechanical stability criterion ($C_{11}+2C_{12} > 0$, $C_{11}-C_{12} > 0$ and $C_{44} > 0$) for lattice parameters corresponding to the superionic state. Therefore, the imaginary phonon mode with $\epsilon = 0.045$ (for GGA, as shown in Figure 6.3) is indicative of oxygen sublattice melting or Frankel like disordering of oxygen sublattice.

6.9 Summary

This study reports the density functional theory (DFT) and classical molecular dynamics (MD) study of the lattice dynamical, mechanical and anionic transport behaviours of ThO_2 in the superionic state. DFT calculations of phonon frequencies were performed at different levels of approximation as a function of isotropic dilation (ϵ) in the lattice parameter. With the expansion of the lattice parameter, there is a softening of B_{1u} and E_u phonon modes at the X symmetry point of the Brillouin zone. As a result of the nonlinear decrease at the X point, the B_{1u} and E_u phonon modes cross each other at $\epsilon=0.03$, which is associated with a sharp increase in the narrow peak of the phonon density of states, signifying a higher occupation and hence a higher coupling of these modes at high temperatures. The mode crossing also indicates anionic conductivity in the $\langle 001 \rangle$ direction leading to occupation of interstitial sites.

Moreover, MD and nudged elastic band calculated diffusion barriers indicate that $\langle 001 \rangle$ is the easy direction for anion migration in the normal and superionic states. With a further increase in the lattice parameter, the B_{1u} mode continues to soften and becomes imaginary at a strain (ϵ) of 0.036 corresponding to a temperature of 3430 K. The calculated temperature variation of single crystal elastic constants shows that the fluorite phase of ThO_2 remains elastically stable up to the superionic regime, though the B_{1u} phonon mode is imaginary in that state. This leads to anionic disorder at elevated temperatures. Tracking of anion positions in the superionic state as a function of time in MD simulations suggests a hopping model in which the oxygen ions migrate from one tetrahedral site to another via octahedral interstitial sites.

Chapter 7

Melting Behavior of (Th,U)O₂ and (Th,Pu)O₂ MOX

7.1 Introduction

In this chapter, we employ classical molecular dynamics (MD) simulations to calculate melting temperature, enthalpy and density as a function of temperature for solid and liquid ThO₂, UO₂ and PuO₂. These MD calculated results are compared with available experimental results to assess the simulation methodology and reliability of the interatomic potentials. Finally, the melting temperatures and thermodynamic properties of both solid and liquid phases of Th rich (Th,U)O₂ and (Th,Pu)O₂ MOX are determined, which are important for AHWR fuel applications [3–5].

7.2 Computational Methodology

7.2.1 Modeling of random solid solutions

A general tactic to generate MOX supercell of (Th,U)O₂ consists of randomly replacing Th atoms by U atoms in the original supercell of ThO₂, conserving the intended average composition of the MOX. The random distribution of substituted ions depends on the configurational space available to the input structure and thus on the size of the simulation supercell. For a given set of potential field parameters, any calculated thermo-physical quantity is dependent on the accessible configurational space of the system [272]. Therefore, the reliability of these studies become questionable as different strategies for random distribution of impurity atoms on supercells, keeping the composition intact, may give different outcomes. In other

words, there is no guarantee that such random distributions will access the whole configurational space and hence may not reproduce the bulk behavior of the actual random solid solution. To overcome this problem, special quasirandom structures (SQS) were employed to establish solid solution configurations. In the SQS method, different random configurations are generated which mimics the correlation functions of an infinite random system within a finite supercell. In the present study, the determination of melting temperatures, enthalpy and density of $\text{Th}_{1-x}\text{U}_x\text{O}_2$ MOX was performed using a 96 atom SQS supercell generated from face centered cubic SQS [272]. In Table 7.1 all the pair and multisite correlation function ($\Pi_{k,m}$) values are compared with those of ideal solid solutions. It is also important to note that for the compositions (x) $> 8/16$ nearest neighbor pair and multisite correlation functions are similar to their $x < 8/16$ counterparts.

In our study, thermo-physical quantities of $\text{Th}_{1-x}\text{Pu}_x\text{O}_2$ MOX are calculated over several randomly generated solid-solution configurations and averages of calculated thermo-physical quantity over those individual configurations are reported. Specifically ten distinct, random distributions were generated for each composition and the thermo-physical properties were obtained by averaging over these configurations. The standard deviation of the calculated thermo-physical properties was found to be negligible. Prior to the final set of calculations a test case was conducted, where the melting temperatures for the ThO_2 - PuO_2 MOX system at a specific composition were found using both the randomized and SQS structures. Both methods produced the same melting temperatures, providing confidence to continue with either method of creating structures.

7.2.2 (Th,U)O₂ and (Th,Pu)O₂ MOX interatomic potentials

The most recent empirical potential for ThO_2 , UO_2 [148], PuO_2 [273] and their MOX [125] which is employed in this study, combines a pair-wise with a many body interaction term. The potential energy, E_i , of an atom i with respect to all other atoms can be represented as:

$$E_i(r_{ij}) = \frac{1}{2} \sum_i \phi_{\alpha\beta}(r_{ij}) - G_\alpha \left(\sum_j \sigma_\beta(r_{ij}) \right)^{\frac{1}{2}} \quad (7.1)$$

The pair interaction potential of two particles i and j of species α and β , separated by r_{ij} consists of a long-range Coulomb interaction ($\phi_C(r_{ij})$) and a short range interaction. The short range interactions are given by combining Morse and Buckingham

Table 7.1: Pair and multisite correlation functions ($\Pi_{k,m}$) of SQS-96 structures for mimicking ideal random $\text{Th}_{1-x}\text{U}_x\text{O}_2$ solid-solution ($x = 1/6, 2/16, 3/16, 4/16, 5/16$ and $6/16$).

$\Pi_{k,m}$	$x = 1/16$ (0.0625)	$x = 2/16$ (0.1250)	$x = 3/16$ (0.1875)	$x = 4/16$ (0.2500)	$x = 5/16$ (0.3125)	$x = 6/16$ (0.3750)
$\Pi_{2,1}$	0.77083	0.56250	0.39583	0.25000	0.14583	0.08333
$\Pi_{2,2}$	0.75000	0.58333	0.41667	0.25000	0.08333	0.00000
$\Pi_{2,3}$	0.75000	0.54167	0.35417	0.22917	0.12500	0.04167
$\Pi_{2,3}$	0.75000	0.50000	0.33333	0.16667	0.08333	0.00000
$\Pi_{2,3}$	0.77083	0.56250	0.39583	0.25000	0.14583	0.08333
$\Pi_{2,3}$	0.75000	0.50000	0.25000	0.00000	0.25000	0.50000
ideal random	0.76562	0.56250	0.39062	0.25000	0.14062	0.06250
$\Pi_{3,1}$	0.68750	0.43750	0.25000	0.12500	0.06250	0.03125
$\Pi_{3,2}$	0.66667	0.43750	0.27083	0.10417	0.02083	0.02083
$\Pi_{3,3}$	0.66667	0.40625	0.23958	0.12500	0.06250	0.02083
$\Pi_{3,3}$	0.64583	0.38542	0.18750	0.09375	0.03125	0.01042
$\Pi_{3,3}$	0.64583	0.41667	0.25000	0.12500	0.04167	0.00000
$\Pi_{3,3}$	0.62500	0.41667	0.22917	0.12500	0.04167	0.02083
$\Pi_{3,3}$	0.62500	0.37500	0.15625	0.09375	0.03125	0.00000
ideal random	0.66992	0.42188	0.24414	0.12500	0.05273	0.01562
$\Pi_{4,1}$	0.62500	0.37500	0.12500	0.00000	0.12500	0.12500
$\Pi_{4,2}$	0.60417	0.35417	0.18750	0.04167	0.02083	0.02083
$\Pi_{4,3}$	0.58333	0.33333	0.16667	0.08333	0.00000	0.08333
ideal random	0.58618	0.31641	0.15259	0.06250	0.01978	0.00391

forms ($\phi_M(r_{ij})$ and $\phi_B(r_{ij})$, respectively). Therefore,

$$\phi_{\alpha\beta}(r_{ij}) = \phi_C(r_{ij}) + \phi_B(r_{ij}) + \phi_M(r_{ij}) \quad (7.2)$$

$$\phi_C(r_{ij}) = \frac{q_i q_j}{4\pi\epsilon_0 r_{ij}} \quad (7.3)$$

$$\phi_B(r_{ij}) = A_{\alpha\beta} \exp\left(-\frac{r_{ij}}{\rho_{\alpha\beta}}\right) - \frac{C_{\alpha\beta}}{r_{ij}} \quad (7.4)$$

$$\phi_M(r_{ij}) = D_{\alpha\beta} \left[\exp(-2\gamma_{\alpha\beta}(r_{ij} - r_{\alpha\beta}^0)) - 2\exp(-\gamma_{\alpha\beta}(r_{ij} - r_{\alpha\beta}^0)) \right] \quad (7.5)$$

where $A_{\alpha\beta}$, $\rho_{\alpha\beta}$, $D_{\alpha\beta}$, $\gamma_{\alpha\beta}$ and $r_{\alpha\beta}^0$ are empirical parameters to describe Buckingham and Morse interactions between atoms i and j . For the Coulombic contribution, an effective ionicity, Z_{α}^{eff} is introduced to replace the formal charges of the ions with charges, $q_{\alpha} = Z_{\alpha}^{eff} e$; $Z_{\alpha}^{eff} = 2.2208$ for tetravalent cations and $Z_{\alpha}^{eff} = -1.1104$ for oxygen anions.

$$\sigma_{\beta}(r_{ij}) = \frac{n_{\beta}}{r_{ij}^8} \quad (7.6)$$

The many body part of Equation 7.1 is achieved by a combination of a set of pairwise interactions ($\left(\sum_j \sigma_{\beta}(r_{ij})\right)$) between atom i and its nearest atoms and then passing it through a non-linear embedding function. Equation 7.2 gives the functional form of $\sigma_{\beta}(r_{ij})$ (n_{β} is the constant of proportionality) and the many-body energy term is proportional to with G_{α} being the constant of proportionality in Equation 7.1.

An error function with a 1.5 Å cut-off distance is also added to Equation 7.6 in order to prevent dominance of non-physical forces arising from the many-body term over the short-range repulsive terms in the MD simulations. The upper limit cut-off distance for the interactions described in equations 7.4, 7.5 and 7.6 was set at 11.0 Å. Further details of the potential parameters have been published previously [125, 148].

7.2.3 MD simulations of thermodynamic properties

MD simulations for thermodynamic quantities were carried out using the MD code LAMMPS [258]. The most recent empirical potential for ThO₂, UO₂ [148] and PuO₂ [273] as well as their MOX [125] which is employed in this study, combines a pair-wise with a many body interaction term. The Coulombic interactions were calculated using the Ewald method [192]. In the present study, the MD supercell was constructed having 4000 cations and 8000 anions by an array of 10×10×10 unit cells for (Th,U)O₂, (Th,Pu)O₂ MOX and their end members. To employ SQS methodology, a 96 atom SQS unitcell was constructed for (Th,U)O₂ MOX over the composition range and a 5×5×5 supercell of the SQS unitcell (4000 cations and 8000 anions) was used for MD simulations. MD runs were performed with a 2 fs time step in suitable temperature intervals over the temperature range 300 K to 6000 K with the NPT ensemble at zero external pressure using the Berendsen barostat with a time constant of 0.5 ps and Nosé-Hoover thermostat with a time constant of 0.1 ps. Each simulation of thermodynamical quantities was carried out initially for 40 ps for equilibration (at the desired temperature) and then for another 10 ps to

get average values of the thermodynamic quantities while heating the system.

To determine thermodynamic quantities for the liquid phase, a supercell containing 12000 atoms was first heated to 6000 K to melt the system mechanically. Then the melted system was quenched to 2000 K from 6000 K in intervals of 100 K. At each temperature the system was equilibrated for 40 ps in the NPT ensemble at zero external pressure using the Berendsen barostat with a time constant of 0.5 ps and Nosé-Hoover thermostat with a time constant of 0.1 ps. The thermodynamical quantities were obtained from the average over the 10 ps run at each temperature.

7.2.4 Two-phase simulations of melting temperatures

We performed two-phase simulations in the isothermal-isobaric (NPT) ensemble to determine the melting temperatures of ThO_2 , UO_2 , PuO_2 and $(\text{Th,U})\text{O}_2$, $(\text{Th,Pu})\text{O}_2$ MOX. A supercell of $36 \times 6 \times 6$ unitcells containing 15552 atoms of pure solid ThO_2 was thermalized at $T_1 = 3000$ K and $P = 0$ GPa via MD runs in the NPT ensemble. Next, atoms in one half of the simulation box ($18 \times 6 \times 6$ supercell) were kept fixed in their positions and MD runs were performed for the other half of the simulation box in the NPT ensemble at a sufficiently high temperature ($T_2 = 5000$ K and $P = 0$ GPa) to create a liquid phase. The resulting supercell was then subjected to MD runs in the NPT ensemble at $T_3 = 4000$ K (which is higher than the expected melting temperature) and $P = 0$ GPa, keeping the same half of the atoms fixed. The result of this process was a supercell containing solid ThO_2 at 3000 K in one half, and liquid ThO_2 at 4000 K in the other half. This ensures a minimum difference of stress between atoms in liquid and solid phases of the supercell [274]. This supercell was then used in the simulations of solidification and melting of ThO_2 . The same methodology was adopted for UO_2 and PuO_2 but with $T_1 = 2500$ K, $T_2 = 5000$ K and $T_3 = 3500$ K. In order to determine the melting temperature of $(\text{Th,U})\text{O}_2$ MOX, SQS generated structures were employed with $T_1 = 2500$ K, $T_2 = 5000$ K and $T_3 = 4000$ K. Similarly, for $(\text{Th,Pu})\text{O}_2$ MOX, random solid-solution structures were employed with $T_1 = 2500$ K, $T_2 = 5000$ K and $T_3 = 4000$ K.

For the two-phase calculations a timestep of 2 fs and a Nos-Hoover thermostat and barostat were applied in the constant pressure temperature (NPT) ensemble, using relaxation times of 0.1 ps and 0.5 ps, respectively. Thus, in this study, the MOX solid and liquid compositions are identical and thus differ from the slightly different composition that would exist in thermodynamic equilibrium.

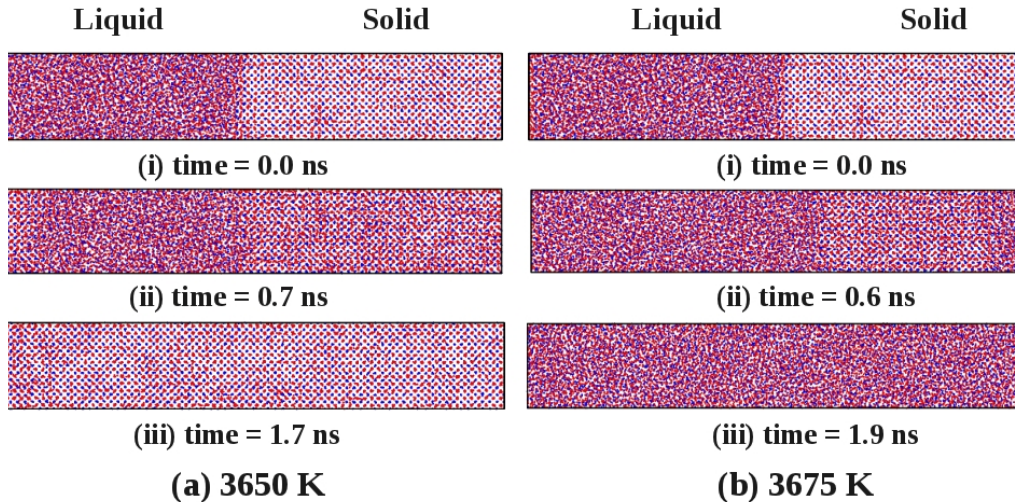


Figure 7.1: Snapshots of the two-phase MD simulation in the NPT ensemble with (a) $T=3650$ K (left panel) and (b) 3675 K (right panel). The red spheres represent O atoms and the blue spheres represent Th atoms. (a) Initial state of the simulation box, which contains both liquid and solid phases. (b) Intermediate state of the simulation box (at 0.6-0.7 ns), where the solid phase propagates to the liquid (at 3650 K) and liquid phase propagates to the solid phase (at 3675 K). (c) Final state of the simulation box (at 1.7-1.9 ns), when the entire system has turned into a solid phase (at 3650 K) and vice-verse (at 3675 K).

7.3 Melting Temperatures of pure oxides

7.3.1 ThO_2

The two-phase supercell (as described in section 8.1) was heated in the NPT ensemble, where the temperature was increased from T_1 to T_3 in 100 K intervals. Each system ran for 1.6 ns of simulation time at a time step of 2 fs. For pure ThO_2 , at 3600 K the solid phase of the simulation box progressed to occupy the entire box. In comparison, at 3700 K the liquid phase of the simulation box progressed to occupy the entire box. Next, the initial two-phase simulation box was heated from 3600 K to 3700 K in 25 K intervals. Each system was equilibrated for at least 2 ns. If the final state appeared to have both liquid and solid phases, more MD runs were performed until the final state of the supercell contained only one phase. The transformation of the two-phase simulation box to a one-phase simulation box near the predicted melting temperature is presented in Figure 7.1. A similar methodology was adopted for melting temperature calculations of pure UO_2 and PuO_2 . The MD calculated range of temperatures where the phase change occurs for ThO_2 , UO_2 and PuO_2 are 3650-3675 K, 3050-3075 K and 2800-2825 K, respectively.

Table 7.2 reports the experimental melting point values for ThO₂, which vary from 3573 K to 3660 K [98–102]. Initially, Lambertson *et al.* [100] predicted the melting point of 3623 K by extrapolating the melting point data of (Th,U)O₂ compositions corresponding to zero UO₂ content. Further refinement was carried out by introducing corrections for the liquidus/solidus curve to incorporate a curvature correction for the pure ThO₂ end to that of the pure UO₂ end of the temperature-composition diagram. Their final recommended value was 3573 K. However, Rand *et al.* [99] argued that the curvature corrections made by other researchers on the ThO₂ or UO₂ rich side of the temperature composition curve need not be the same at both terminal compositions, because the loss of ‘O’ from UO₂ in the UO₂-rich side might be different from that of the ThO₂ rich side and hence recommended a value of 3643 ± 30 K. Ronchi *et al.* [101] recently measured the melting temperature of ThO₂ (under both stoichiometric and hypostoichiometric conditions) experimentally by heating a spherical sample with four symmetrically spaced pulsed Nd YAG lasers and observing the cooling/heating curve with time. For stoichiometric ThO₂, the measured melting point was 3651 ± 17 K [101] and their data is consistent with the data generated by Benz *et al.* [98] (3660 ± 100 K) which is also close to the value of Rand *et al.* [99]. All these values are markedly different from those of Lambertson *et al.* [99]. It is also important to note that the curvature differences at the uranium- and thorium-rich side of the temperature versus composition diagram can be attributed to the loss of oxygen. Furthermore, measurements of the cooling curves of molten ThO₂ and ThO_{1.98} by Ronchi *et al.* [101] reveal that the stoichiometric compound melts congruently at 3651 K, while the hypostoichiometric oxide displays a liquidus at 3628 K and a solidus transition at 3450 K. Recently, Böhler *et al.* [102] revisited the high temperature phase diagram of ThO₂-UO₂ using a laser heating approach combined with fast pyrometry via a thermal arrest method and recommended a melting temperature of 3624 ± 108 K. Finally, our MD calculated value which lies between 3650 K and 3675 K is consistent with the data of Rand *et al.*, Ronchi *et al.*, Benz *et al.*, Böhler *et al.* and even the upper value of Lambertson *et al.*.

7.3.2 UO₂

Experimentally reported melting temperatures of UO₂ vary from 3050 K to 3138 K (Table 7.2) [103–110]. The melting point of UO₂ given in MATPRO [107] is 3113.15 K and this temperature is given based on the equations for the solids and liquids boundaries of the UO₂-PuO₂ phase diagram given by Lyon *et al.* [103]. The

recommended value by ORNL [109] for $\text{UO}_{2.00}$ is 3120 ± 30 K and for $\text{PuO}_{2.00}$ is 2701 ± 35 K. In recent experimental measurements of the heat capacity of liquid UO_2 , using laser heating of a UO_2 sphere, Ronchi *et al.* [105] made several measurements of the freezing temperature of UO_2 on different samples. For specimens in an inert gas atmosphere with up to 0.1 bar of oxygen, they obtained melting points in the interval 3070 ± 20 K. Higher melting temperatures (3140 ± 20 K) were obtained for samples in an inert gas atmosphere without oxygen. The variation in melting temperature is in accordance with the expected lower oxygen-to-uranium (O/U) ratio in the latter samples. The melting point of UO_2 drops on variation of the O/M ratio away from stoichiometry: for example, if the melting point of stoichiometric UO_2 is 3138 K, its value drops to 2698 K at an O/U ratio of 1.68 and to 2773 K at an O/U ratio of 2.25 [105]. Thus the MD calculated melting temperature, which lies between 3050 K and 3075 K, is in fairly consistent with experimental data available in the literature for stoichiometric UO_2 .

7.3.3 PuO_2

The melting point of PuO_2 has not been studied as extensively as those of UO_2 and ThO_2 . Previously, a series of measurements were performed by Lyon *et al.* [103] using the thermal arrest technique and induction heating of tungsten-encapsulated samples. Also, some other researchers [103, 106–109] studied melting of PuO_2 and reported values in the range 2663–2718 K (Table 7.2), using combined visual detection of melting with a variety of experimental setups, including flame melting under a controlled atmosphere. Kato *et al.* [111] reported the melting temperature of $\text{PuO}_{2.00}$ as 2843 K. The recommended value by ORNL [109] for $\text{PuO}_{2.00}$ is 2701 ± 35 K. Recently; Bruycker *et al.* [112] studied the melting temperature of stoichiometric PuO_2 by fast laser heating and multi-wavelength pyrometry. The transition temperatures obtained by this technique (3017 ± 28 K) are in disagreement with those previously proposed on the basis of more traditional measurements. Our MD calculated melting temperature, which lies between 2800 K and 2825 K, is lower than the melting point reported by Bruycker *et al.* [112] and higher than the recommended value by ORNL [109] but matches well with the value reported by Kato *et al.* [111].

It must be emphasized here that raising temperature close to the melting point may cause loss or gain of oxygen, especially in U- and Pu-based systems, thereby disturbing the equilibrium between the solid-gas and solid-liquid phases. The extent of the shift in the melting point due to shift in the equilibrium can be

Table 7.2: MD calculated melting temperatures of pure ThO₂, UO₂ and PuO₂ are compared with experimentally measured values available in the literature.

System	MD calculated temperature range (K)	Experimental values (K)
ThO ₂	3650-3675	3663 ± 100 Benz <i>et al.</i> [98] 3643 ± 30 Rand <i>et al.</i> [99] 3573 ± 100 Lambertson <i>et al.</i> [100] 3651 ± 17 Ronchi <i>et al.</i> [101] 3624 ± 108 Bohler <i>et al.</i> [102]
UO ₂	3050-3075	3113 ± 20 Lyon <i>et al.</i> [103] 3138 ± 15 Latta <i>et al.</i> [104] 3075 ± 30 Ronchi <i>et al.</i> [105] 3120 ± 30 Adamson <i>et al.</i> [106] 3113.15 MATPRO [107] 3138 ± 15 Komatsu <i>et al.</i> [108] 3120 ± 30 ORNL [109] 3050 ± 55 Böhler <i>et al.</i> [110]
PuO ₂	2800-2825	2663 ± 20 Lyon <i>et al.</i> [103] 2701 ± 35 Adamson <i>et al.</i> [106] 2647 MATPRO [107] 2718 Komatsu <i>et al.</i> [108] 2701 ± 35 ORNL [109] 2843 Kato <i>et al.</i> [111] 3017 ± 28 Bruycker <i>et al.</i> [112]

estimated from experimental results [275], showing melting temperature (of UO₂) of 3147 ± 20 K and 2410 ± 25 K for O/U ratio 2.00 and 2.21, respectively. Unfortunately, this shift in equilibrium due to non-stoichiometry has not been taken into account in our calculations due to lack of suitable consistent potential parameters for U and Pu-based systems having mixed valency. In future, such potentials may be developed to observe the effect of non-stoichiometry on the solid-liquid equilibrium and hence on the melting point.

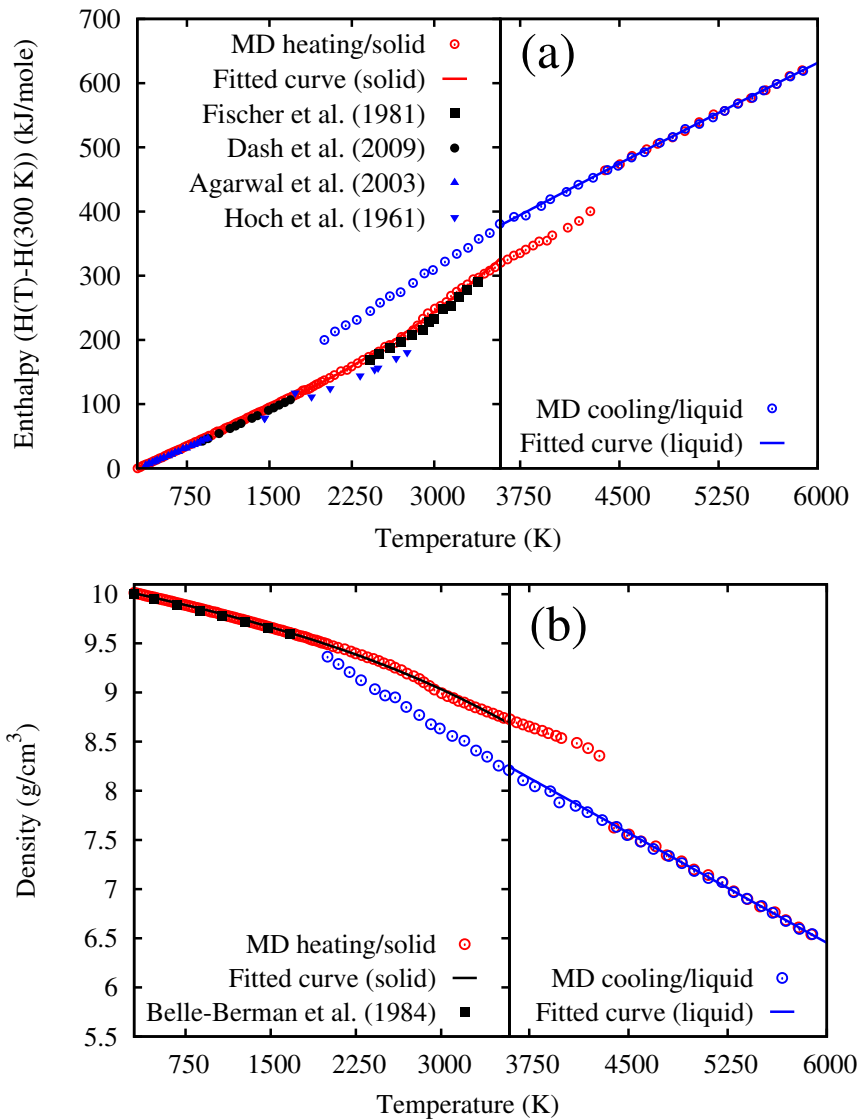


Figure 7.2: MD calculated enthalpy increments (a) and density variation (b) as a function of temperature in the 300-6000 K range for ThO₂ are compared with experimental values.

7.4 Enthalpies and densities of pure oxides

7.4.1 ThO₂

Figure 7.2(a) compares the MD calculated change in enthalpy ($H(T) - H(300\text{ K})$) of ideal ThO₂ upon heating in the 300-6000 K range (i.e. for both solid and liquid phases) and cooling in the 6000-2000 K range, with experimentally available data [90,113–115]. Throughout the 300-3500 K temperature range the change in enthalpy matches well with experimental values, except those of Hoch *et al.* [113]. Figure 2(b) shows our MD calculated density of ThO₂ in the 300-6000 K temperature

Table 7.3: MD calculated enthalpy of fusion of pure ThO₂, UO₂ and PuO₂ are compared with experimentally measured values available in the literature.

System	MD calculated Enthalpy of Fusion (kJ/mol.)	Experimental values (kJ/mol.)
ThO ₂	63.85	88 ± 6, Fink <i>et al.</i> [116] 90.8, IAEA-TECDOC 1496 (2006) [3]
UO ₂	58.94	74.8, Fink <i>et al.</i> [118] 70.0 ± 4, Fink <i>et al.</i> [119] 70.0, MATPRO [107]
PuO ₂	43.21	64 ± 6 [120]

range. The MD calculated values agree well with the experimental values reported by Momin *et al.* [117] in the 298-2273 K range. No experimental data are available for liquid thorium dioxide. Fink *et al.* [116] estimated the specific heat C_p (liquid) to be 61.76 J K⁻¹ mol⁻¹ for liquid ThO₂, which is adopted here. Then if the entropy of fusion is assumed to be identical to that of UO₂ (24 J K⁻¹ mol⁻¹), it yields an enthalpy of fusion for ThO₂ = 88±6 kJ mol⁻¹. From our MD calculated $H(T) - H(300)$ versus temperature data, the enthalpy of fusion is calculated from the width of the discontinuity in the enthalpy axis and it is compared with other values in Table 7.3. This MD calculated the change in enthalpy ($H(T) - H(300)$) data is fitted to a functional form:

$$H(T) - H(300) = C_1\theta[(e^{\theta/T} - 1)^{-1} - (e^{\theta/300} - 1)^{-1}] + C_2[T^2 - 300^2] + C_3e^{\beta/T} \quad (7.7)$$

in the 300-3600 K temperature range, where $C_1 = 99.391$, $\theta = 637.205$, $C_2 = -8.129 \times 10^{-3}$, $C_3 = 3.35847 \times 10^6$, $\beta = 12228.3$, T is the temperature in K, the enthalpy increment, $H(T) - H(300)$, is in J mol⁻¹ and $R^2 < 0.99$. Similarly, for the temperature range 3675-6000 K, MD calculated data of $H(l, T) - H(s, 300)$ for liquid ThO₂, in J mol⁻¹, is fitted to equation:

$$H(l, T) - H(s, 300) = C_1 + C_2T + \frac{C_3}{T} \quad (7.8)$$

where $C_1 = 4.24348 \times 10^4$, $C_2 = 100.961$ and $C_3 = 9.8998 \times 10^7$. A similar set of equations were previously used to represent enthalpy increments of UO₂ for solid and liquid phases by Fink *et al.* [119]. The MD calculated density data for solid ThO₂ is fitted to a 3rd order polynomial equation in the 300-3600 K temperature

range:

$$\rho(T) = C_1 + C_2T + C_3T^2 + C_4T^3 \quad (7.9)$$

to yield parameters $C_1 = 10.084$, $C_2 = -2.4687 \times 10^{-4}$, $C_3 = -9.10318 \times 10^{-9}$ and $C_4 = -8.4684 \times 10^{-12}$, where T is the temperature in K, the density is in g/cm^3 and $R^2 < 0.99$. Similarly, the MD calculated density of liquid for ThO_2 is fitted to a linear equation of the form in the temperature range 3675-6000 K:

$$\rho(T) = C_1 + C_2(T - 3675) \quad (7.10)$$

where $C_1 = 7.72082$ and $C_2 = -7.45616 \times 10^{-4}$.

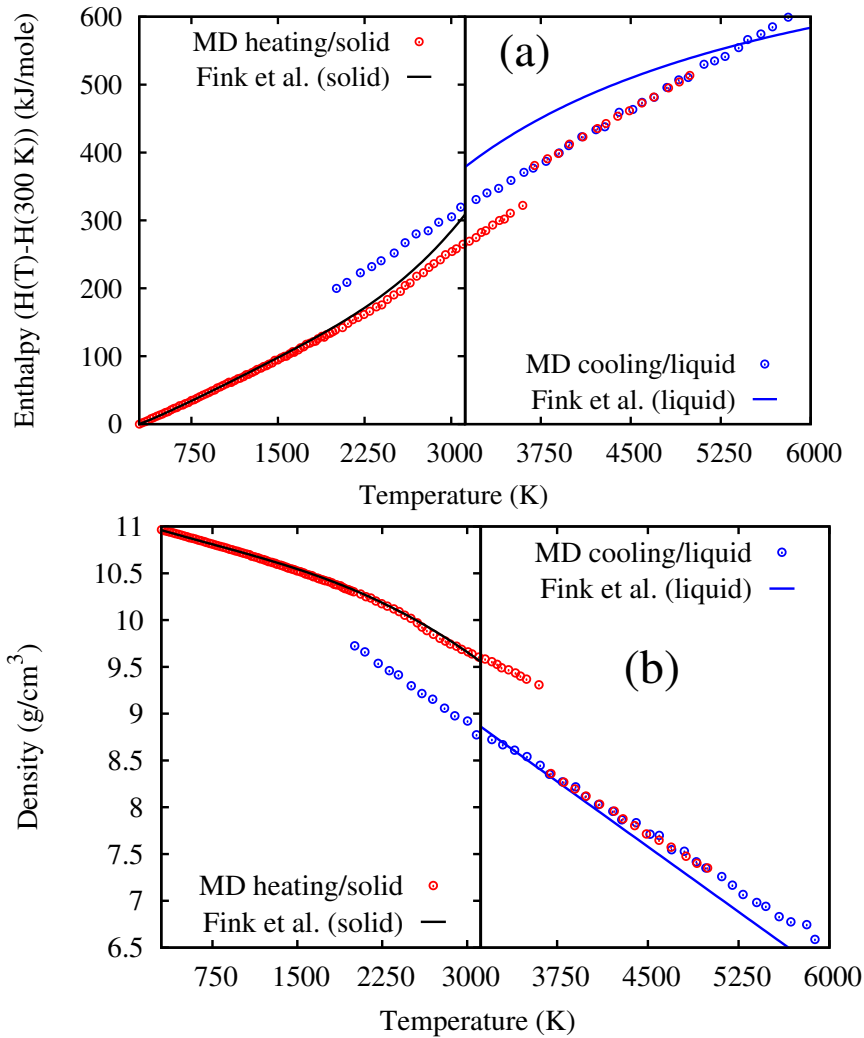


Figure 7.3: MD calculated enthalpy increments (a) and density variation (b) as a function of temperature in the 300-6000 K range for UO_2 are compared with experimental values reported by Fink *et al.* [119].

7.4.2 UO₂

Figure 7.3(a) shows the MD calculated change in enthalpy ($H(T) - H(300\text{K})$) of defect-free UO₂ upon heating in the 300-4500 K range, with the reported experimental data by Fink *et al.* [118, 119] for both the solid and liquid phases. MD calculated density values for solid and liquid UO₂ are compared with experimental values in Figure 7.3(b). MD calculated values for both solid and liquid phases are in good agreement with experimental values reported by Fink *et al.* [119]. From our MD calculated values the enthalpy of fusion is calculated and compared with other experimental values in Table 7.3. Previously, Qin *et al.* [276] also calculated enthalpy increment and density as a function of temperature (300-5000 K range) for UO₂ and our MD calculated values are in good agreement with their MD calculated results.

The MD calculated change in enthalpy ($H(T)-H(300\text{ K})$) values of defect-free UO₂ upon heating match very well upto 2000 K. The underestimation of values from 2000 K to melting can be attributed to the Schottky defects and contribution from the electronic defects, which is not taken into account explicitly in these MD simulations using one-phase approach. Previously, Harding *et al.* [277] reporting on the anomalous specific heat of UO₂ at high temperatures suggested that there is a source of entropy, of the order of 10 cal/mol. K. The calculations in their study show that it is highly unlikely that Frenkel defects on the anion sub-lattice can provide more than a small proportion of this. However, the contribution from electronic defects is large and could account for most of this volume. In their study Harding *et al.* [277], considered only one small polaron reaction: $2\text{U}^4 \rightarrow \text{U}^3 + \text{U}^5$. It is apparent that there are others, which, although having a higher activation energy may make significant contributions close to the melting point. Ronchi *et al.* [278] calculated the contributions from each physical process to the heat capacity to compare with available experimental data and provided an excellent description of the theoretical understanding. They found that from room temperature to 1000 K, the increase in heat capacity is governed by the harmonic lattice vibrations, which may be approximated by a Debye model. Between 1000 and 1500 K, the heat capacity increase arises from the anharmonicity of the lattice vibrations as evidenced in thermal expansion. The increased heat capacity from 1500 to 2670 K is due to the formation of lattice and electronic defects with the main contribution from Frenkel defects. Above the λ -phase transition, the Frenkel defect concentration becomes saturated and Schottky defects become important. Moreover, spin-phonon scattering plays a pivotal role in the low temperature thermal properties of UO₂

but not in ThO_2 [279].

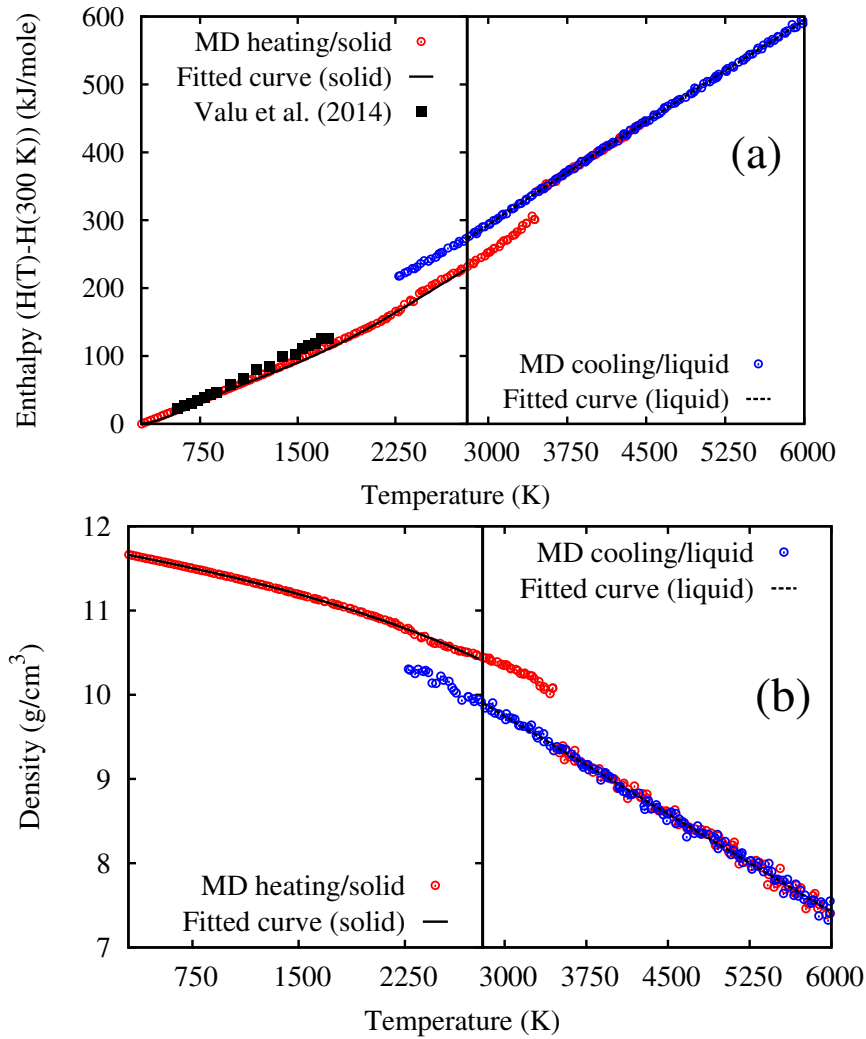


Figure 7.4: MD calculated enthalpy increments (a) and density variation (b) as a function of temperature in the 300-6000 K range for PuO_2 are compared with experimental values.

7.4.3 PuO_2

Figure 7.4(a) compares the MD calculated change in enthalpy ($H(T) - H(300 \text{ K})$) of ideal PuO_2 upon heating in the 300-6000 K range (i.e. for both solid and liquid phases) and cooling in the 6000-2000 K range, with experimentally reported values by Valu *et al.* [124]. Below 1000 K, MD calculated values of the change in enthalpy match well with experimental values but underestimate experimental values above 1000 K. Figure 7.4(b) shows our MD calculated density of PuO_2 in the 300-6000 K temperature range during heating and cooling though no experimental data are available for solid and liquid PuO_2 . No data for the heat capacity or enthalpy of

liquid PuO₂ are known, except a single enthalpy measurement by Ogard *et al.* [120]. The enthalpy of fusion is thus estimated, assuming that the entropy of fusion is identical to that of UO₂ (22.4 J K⁻¹ mol⁻¹), yielding an enthalpy of fusion = 64 ± 6 kJ mol⁻¹.

This MD calculated change in enthalpy ($H(T) - H(300)$) data is fitted to a functional form (equation 7) in the 300-2800 K temperature range, where $C_1 = 238.77$, $\theta = 1269.05$, $C_2 = -68.9664 \times 10^{-3}$, $C_3 = 5.42283 \times 10^6$, $\beta = 8740.69$, T is the temperature in K, the enthalpy increment, $H(T) - H(300)$, is in J mol⁻¹ and $R^2 < 0.99$. Similarly, for the temperature range 2825-6000 K, MD calculated data of $H(l, T) - H(s, 300)$ for liquid PuO₂, in J mol⁻¹, is fitted to equation (8) where $C_1 = 3.08813 \times 10^4$, $C_2 = 96.033$, $C_3 = 7.6837 \times 10^7$. The MD calculated density data for solid PuO₂ is fitted to a 3rd order polynomial (equation 9) in the 300-2800 K temperature range with $C_1 = 11.7581$, $C_2 = -3.229 \times 10^{-4}$, $C_3 = -1.0469 \times 10^{-8}$, $C_4 = -1.6744 \times 10^{-11}$, T is the temperature in K, the density is in g/cm³ and $R^2 < 0.99$. Similarly, the MD calculated density of liquid ThO₂ is fitted to a linear equation (10) in the temperature range 2825-6000 K where $C_1 = 8.4241$ and $C_2 = -7.2256 \times 10^{-4}$.

MD calculated enthalpy of fusion values are consistently lower than experimental values. It has been established in this kind of solid dioxides that the formation of oxygen defects, and in particular of Schottky defects and hypo/hyper stoichiometry, leads to an abrupt increase of the heat capacity as temperature approaches the melting point [101, 280–284]. One-phase approach to calculate enthalpy increments and density does not take into account these effects, resulting in overall underestimation of MD calculated enthalpy of fusion values compared to experimental values. Ideally, discontinuous jump in the enthalpy vs temperature plot signifies melting and/or solidification of the solid-liquid transformation. The temperature at which the discontinuous jump appears should be melting and/or solidification temperature. Figs. 7.2, 7.3, 7.4 shows high melting/solidification temperature by several hundred kelvin compared to equilibrium melting points predicted by two-phase simulations. At this point it is important to note that, the one phase approach is employed in the calculation of enthalpy increments and density as one phase approach is computationally less expensive and easy to implement in the simulations compared to two-phase approach. In one phase method, the supercell is subjected to incremental heating under the NPT ensemble until melted. Similarly, the liquid phase is subjected to the same incremental cooling until recrystallization. The solid-liquid phase transformation is a first order reaction and associated with hysteresis. Based on classical nucleation theory, there is a sudden jump in volume

(or density) upon melting at T_+ (superheating temperature) in a heating simulation of a solid, and there is a drop in volume (or density) at T_- (supercooling temperature) due to fusion in a cooling simulation of a liquid. The density-temperature curve (Figs. 7.2, 7.3, 7.4) reveals the hysteresis effects for the MD simulations of a solid and a liquid. Compared to the hysteresis approach, the two-phase approach is more meaningful and models a first order transformation where two-phases co-exist with an interface between them. The hysteresis approach lacks this feature. The melting temperature T_m is obtained from the solid-liquid coexistence, where the free energies of solid and liquid states becomes equal. So we adopted the two-phase simulation method to calculate the high temperature phase diagram of (Th,U)O₂ and (Th,Pu)O₂ MOX. Superheating and supercooling phenomena are common in MD simulations of solid-liquid phase transformation [284–286].

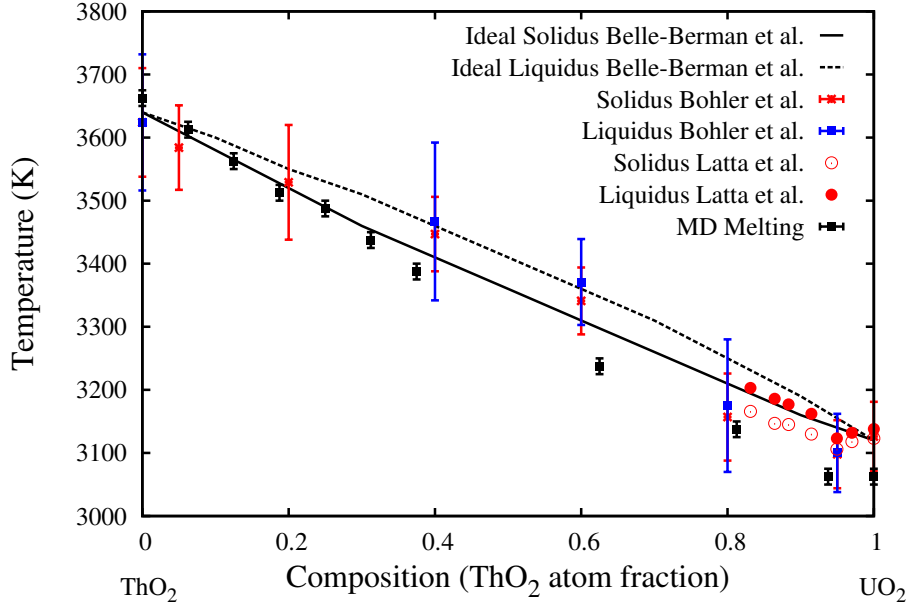


Figure 7.5: MD calculated melting temperatures of (Th,U)O₂ MOX are compared with ideal solidus and liquidus line as well as experimentally reported values.

7.5 Melting Temperatures of (Th,U)O₂ MOX

High temperature phase diagram studies of the ThO₂-UO₂ MOX system have previously been reported by Lambertson *et al.* [100] using a quench technique, whereas Latta *et al.* [121] applied a thermal arrest method to determine the liquidus and solidus of MOX. The measurements of Latta *et al.* [121] in the 0-17 mole % ThO₂ also show deviation from ideal liquidus-solidus curve and this behavior would be

consistent with a shallow minimum at 5 mol% ThO₂. Moreover, the high temperature phase diagram of ThO₂-UO₂ MOX can be constructed with the help of the melting points and enthalpies of fusion of the end members, assuming these complete solution binaries are ideal solid solutions, (i.e. no change in volume or enthalpy on mixing [122]). Assuming an ideal mixing for both the solid and the liquid (ThO₂+UO₂) solutions, the solidus and liquidus line can be obtained by solving the following system of equations:

$$\Delta H_m(ThO_2) \left(\frac{1}{T_m(ThO_2)} - \frac{1}{T} \right) = R \ln \left(\frac{1 - x_l}{1 - x_s} \right) \quad (7.11)$$

$$\Delta H_m(UO_2) \left(\frac{1}{T_m(UO_2)} - \frac{1}{T} \right) = R \ln \left(\frac{x_l}{x_s} \right) \quad (7.12)$$

R is the ideal gas constant (8.314462 kJ. K⁻¹ Mol⁻¹), x_s and x_l are the UO₂ mole fractions on the, respective, solidus and liquidus curves at a given absolute temperature T ($T_m(UO_2) < T < T_m(ThO_2)$). T_m and ΔH_m are the melting temperatures and enthalpies of fusion of the two end members, respectively. As there is no direct experimental measurement of the heats of fusion for ThO₂ or ThO₂-UO₂ solid solutions, the most probable value is that of Fink *et al.* [118] for UO₂ (i.e. 74.8 ± 1 kJ/mol) and the recommended value for ThO₂ is 90.8 kJ/mol [3]. Recently, Böhler *et al.* [110] revisited the high-temperature phase diagram of ThO₂-UO₂ using a laser heating approach combined with fast pyrometry in a thermal arrest method. According to their study, low additions of ThO₂ to UO₂ result in a slight decrease of the solidification temperature and this behaviour would be consistent with a minimum at 3098 K around a composition of 5 mol% ThO₂. The solid/liquid transition temperature was then observed to increase with increasing ThO₂ fraction.

Figure 7.5 shows the solidus and liquidus lines over the full composition range of ThO₂-UO₂ MOX calculated using Equation 7.11. Our MD calculated melting temperatures are also compared with previous experimental investigations by Latta *et al.* [121] and Böhler *et al.* [110]. These calculated melting temperatures are in very good agreement for the ThO₂ rich part of the phase diagram compared to the ideal solidus line calculated using Equation 15 and experimentally determined values by Böhler *et al.* [110]. In UO₂ rich part, the MD calculated values slightly underestimate the ideal solidus line but the estimated values are within the error bars of experimental measurements by Böhler *et al.* [110] (except at the 60 % composition). Our calculations suggest that the melting temperatures of UO₂ and UO₂-6.25 atom% ThO₂ are the same, which lie between 3050 K and 3075 K. This

result is in agreement with the previous experimentally determined melting temperature where a minimum in the phase diagram was found at ~ 5 mol% of ThO₂ by Latta *et al.* [121] and Böhler *et al.* [110].

The solidus-liquidus curve in the uranium rich side is expected to influence by the following facts:

a) The derivation of ideal solidus-liquidus line (from Equation 7.11 and 7.12) assumes that the heat capacity of the end members is independent of temperature and composition in the vicinity of the melting transition. On the contrary, previous experimental studies reported abrupt increase of specific heat due to formation of Frenkel pairs and order-disorder pre-melting transitions [101, 280–283].

b) The creation of oxygen defects is actually likely to occur in uranium-rich samples, because U has a partially filled 5-f electron shell and can therefore easily assume the valences +3, +4, +5 and +6 even in the condensed oxide phases [288].

c) Since at high temperatures uranium dioxide can accommodate in the fcc lattice both oxygen interstitials and vacancies over a wide stoichiometry range (at least, $1.5 \leq O/U \leq 2.25$), important variations of the melting point with stoichiometry are expected in conjunction with the appearance of an oxygen solubility gap when solid solutions UO_{2±x} are melted [275].

The minimum in the uranium rich side of ThO₂-UO₂ phase diagram is an outcome of above mentioned effects. Incorporation of all these effects in the current state of the MD simulation methodologies is difficult. Two-phase simulations employed in this study to calculate melting temperature of ThO₂, UO₂ and MOX indirectly incorporate the effect of lattice defects (mostly Frenkel defects). Non-stoichiometry effect requires U⁺³ - O and U⁺⁵ - O interactions to be incorporated in the potential data set efficiently.

7.6 Melting Temperatures of (Th,Pu)O₂ MOX

In an ideal case of no interaction between the solution end members, the ideal solution solidus and liquidus lines of the binary high-temperature phase diagram are solely defined by the enthalpies of fusion and the melting temperatures of the two end members, as shown in Figure 7.6 for ThO₂-PuO₂ MOX. Figure 7.6 shows two ideal solidus-liquidus curves, generated by taking into account two different melting points of PuO₂ as reported by Bakker *et al.* [6] and Bruycker *et al.* [112]. In this definition it is assumed that the heat capacity is same for solid and liquid phases in the vicinity of melting and only configurational entropy is contributing

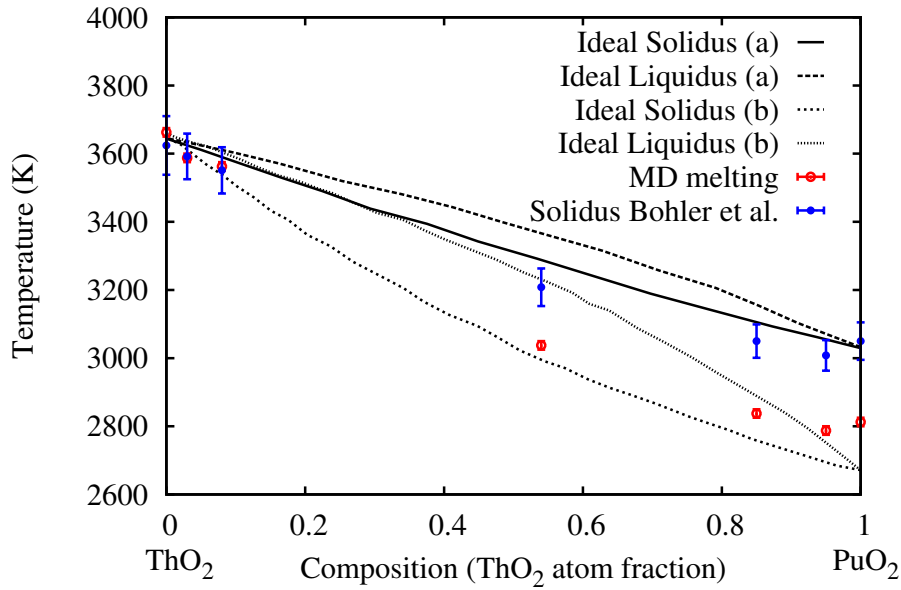


Figure 7.6: MD calculated melting temperatures of $(\text{Th,Pu})\text{O}_2$ MOX are compared with ideal solidus and liquidus line as well as experimentally reported values by Böhler *et al.* [123]. Ideal behavior represented by (a) and (b) is after Bruycker *et al.* [112] and Bakker *et al.* [6], respectively.

to the Gibbs free energy. Figure 7.6 also compares our MD calculated melting temperatures with the solidification temperatures measured by Böhler *et al.* [123] using a laser heating approach combined with fast pyrometry in a thermal arrest method, to determine the melting/solidification phase transition in mixed $(\text{PuO}_2 + \text{ThO}_2)$ at high temperature. Our melting temperatures are in good agreement for the ThO_2 rich part of the phase diagram compared to the ideal solidus line and experimentally determined values by Böhler *et al.* [123]. In the PuO_2 rich part, MD values underestimate (by 200-300 K) the ideal solidus line as our MD calculated melting temperature value of pure PuO_2 is underestimated by 200 K, compared to the experimentally determined value by Bruycker *et al.* [112]. On the other hand, MD values overestimate (by 50-100 K) the ideal solidus behavior as reported by Bakker *et al.* [6]. The MD calculations suggest that the melting temperature of PuO_2 -5 atom% ThO_2 is lower than pure PuO_2 and PuO_2 -15 atom% ThO_2 . This result is in agreement with a previous set of experimental melting temperatures, which are consistent with a minima in the phase diagram at ~ 5 mol% of ThO_2 by Böhler *et al.* [123].

Table 7.4: MD calculated enthalpy increments (in J/mole) of solid and liquid phases of (Th,U)O₂ and (Th,Pu)O₂ MOX are fitted to equation 7.7 and 7.8, respectively and coefficients are enlisted.

MOX	Solid phase enthalpy (300 K-melting point) $H(T) - H(300) = C_1\theta\left[\frac{1}{(e^{\theta/T}-1)} - \frac{1}{(e^{\theta/300}-1)}\right]$ $+C_2[T^2 - 300^2] + C_3e^{\beta/T}$	Liquid phase enthalpy (melting point-6500 K) $H(l, T) - H(s, 300) = C_1 + C_2T + \frac{C_3}{T}$
ThO ₂	$C_1=99.391, \theta=637.205, C_2=-8.129\times 10^{-3},$ $C_3=3.35847\times 10^6, \beta=12228.3$	$C_1 = 4.24348\times 10^4, C_2 = 100.961,$ $C_3 = 9.8998\times 10^7$
Th _{0.9375} U _{0.0625} O ₂	$C_1=110.222, \theta=731.487, C_2=-12.804\times 10^{-3},$ $C_3=3.27702\times 10^6, \beta=11344.4$	$C_1 = 3.4106\times 10^4, C_2 = 102.162,$ $C_3 = 9.8998\times 10^7$
Th _{0.875} U _{0.125} O ₂	$C_1=115.830, \theta=795.683, C_2=-15.229\times 10^{-3},$ $C_3=3.07690\times 10^6, \beta=10780.7$	$C_1 = 3.53084\times 10^4, C_2 = 101.469,$ $C_3 = 9.8996\times 10^7$
Th _{0.8125} U _{0.1875} O ₂	$C_1=117.105, \theta=803.765, C_2=-15.779\times 10^{-3},$ $C_3=3.13532\times 10^6, \beta=10737.2$	$C_1 = 2.98641\times 10^4, C_2 = 102.254,$ $C_3 = 9.8997\times 10^7$
Th _{0.75} U _{0.25} O ₂	$C_1=117.565, \theta=810.081, C_2=-16.092\times 10^{-3},$ $C_3=2.97057\times 10^6, \beta=10487.7$	$C_1 = 3.17325\times 10^4, C_2 = 101.673,$ $C_3 = 9.9000\times 10^7$
Th _{0.6875} U _{0.3125} O ₂	$C_1=132.225, \theta=865.31, C_2=-23.5569\times 10^{-3},$ $C_3=3.03601\times 10^6, \beta=9637.35$	$C_1 = 4.2448\times 10^4, C_2 = 99.1047,$ $C_3 = 9.9007\times 10^7$
Th _{0.97} Pu _{0.03} O ₂	$C_1=103.303, \theta=715.159, C_2=-9.50969\times 10^{-3},$ $C_3=3.97188\times 10^6, \beta=12543.8$	$C_1 = 3.32842\times 10^4, C_2 = 101.59,$ $C_3 = 9.89886\times 10^7$
Th _{0.95} Pu _{0.05} O ₂	$C_1=114.168, \theta=798.406, C_2=-14.1746\times 10^{-3},$ $C_3=3.79121\times 10^6, \beta=11672.6$	$C_1 = 3.17318\times 10^4, C_2 = 101.363,$ $C_3 = 9.90000\times 10^7$
Th _{0.92} Pu _{0.08} O ₂	$C_1=117.924, \theta=805.625, C_2=-16.1121\times 10^{-3},$ $C_3=3.52877\times 10^6, \beta=11122.1$	$C_1 = 3.17322\times 10^4, C_2 = 101.415,$ $C_3 = 9.90000\times 10^7$
Th _{0.80} Pu _{0.20} O ₂	$C_1=118.129, \theta=798.347, C_2=-16.9268\times 10^{-3},$ $C_3=3.03574\times 10^6, \beta=10356.2$	$C_1 = 2.97335\times 10^4, C_2 = 100.395,$ $C_3 = 9.89900\times 10^7$
Th _{0.70} Pu _{0.30} O ₂	$C_1=101.116, \theta=647.798, C_2=-9.52912\times 10^{-3},$ $C_3=2.95858\times 10^6, \beta=11116.8$	$C_1 = 2.99031\times 10^4, C_2 = 99.4849,$ $C_3 = 9.89999\times 10^7$
PuO ₂	$C_1=238.770, \theta=1269.05, C_2=-68.9664\times 10^{-3},$ $C_3=5.42283\times 10^6, \beta=8740.69$	$C_1 = 3.08813\times 10^4, C_2 = 96.033,$ $C_3 = 7.6837\times 10^7$

Table 7.5: MD calculated density (in g/cm³) of solid and liquid phases of (Th,U)O₂ and (Th,Pu)O₂ MOX are fitted to equation 7.9 and 7.10, respectively and coefficients are enlisted.

MOX	Solid phase density (300 K-melting point) $\rho(T) = C_1 + C_2T + C_3T^2 + C_4T^3$	Liquid phase density (melting point-6500 K) $\rho(T) = C_1 + C_2(T - T_m)$
ThO ₂	$C_1 = 10.0912, C_2 = -2.66141 \times 10^{-4},$ $C_3 = -0.456978 \times 10^{-8}, C_4 = 1.12 \times 10^{-11}$	$C_1 = 8.22764, C_2 = -7.35261 \times 10^{-4}$
Th _{0.9375} U _{0.0625} O ₂	$C_1 = 10.1478, C_2 = -2.582 \times 10^{-4},$ $C_3 = -0.52999 \times 10^{-8}, C_4 = 0.94666 \times 10^{-11}$	$C_1 = 8.37026, C_2 = -7.2469 \times 10^{-4}$
Th _{0.875} U _{0.125} O ₂	$C_1 = 10.2002, C_2 = -2.4073 \times 10^{-4},$ $C_3 = -2.1128 \times 10^{-8}, C_4 = 0.66745 \times 10^{-11}$	$C_1 = 8.23388, C_2 = -7.18225 \times 10^{-4}$
Th _{0.8125} U _{0.1875} O ₂	$C_1 = 10.2482, C_2 = -2.09567 \times 10^{-4},$ $C_3 = -4.77534 \times 10^{-8}, C_4 = -1.6402 \times 10^{-12}$	$C_1 = 8.27608, C_2 = -7.41197 \times 10^{-4}$
Th _{0.75} U _{0.25} O ₂	$C_1 = 10.3102, C_2 = -2.1423 \times 10^{-4},$ $C_3 = -4.9352 \times 10^{-8}, C_4 = -1.4689 \times 10^{-12}$	$C_1 = 8.29257, C_2 = -7.47047 \times 10^{-4}$
Th _{0.6875} U _{0.3125} O ₂	$C_1 = 10.357, C_2 = -1.85017 \times 10^{-4},$ $C_3 = -7.20112 \times 10^{-8}, C_4 = -2.5823 \times 10^{-12}$	$C_1 = 8.28532, C_2 = -7.27682 \times 10^{-4}$
Th _{0.97} Pu _{0.03} O ₂	$C_1 = 10.1003, C_2 = -2.2928 \times 10^{-4},$ $C_3 = -2.2473 \times 10^{-8}, C_4 = 0.6232 \times 10^{-11}$	$C_1 = 8.3892, C_2 = -7.3762 \times 10^{-4}$
Th _{0.95} Pu _{0.05} O ₂	$C_1 = 10.1777, C_2 = -2.5411 \times 10^{-4},$ $C_3 = -7.7185 \times 10^{-8}, C_4 = 0.9219 \times 10^{-11}$	$C_1 = 8.4166, C_2 = -7.2388 \times 10^{-4}$
Th _{0.92} Pu _{0.08} O ₂	$C_1 = 10.2065, C_2 = -2.4231 \times 10^{-4},$ $C_3 = -1.9516 \times 10^{-8}, C_4 = 0.6956 \times 10^{-11}$	$C_1 = 8.4241, C_2 = -7.2256 \times 10^{-4}$
Th _{0.80} Pu _{0.20} O ₂	$C_1 = 10.3781, C_2 = -2.0886 \times 10^{-4},$ $C_3 = -5.822 \times 10^{-8}, C_4 = 0.0459 \times 10^{-11}$	$C_1 = 8.66711, C_2 = -7.3751 \times 10^{-4}$
Th _{0.70} Pu _{0.30} O ₂	$C_1 = 10.5298, C_2 = -1.8369 \times 10^{-4},$ $C_3 = -8.9812 \times 10^{-8}, C_4 = 0.7064 \times 10^{-11}$	$C_1 = 8.5617, C_2 = -7.3224 \times 10^{-4}$
PuO ₂	$C_1 = 11.7581, C_2 = -3.229 \times 10^{-4},$ $C_3 = -1.0469 \times 10^{-8}, C_4 = -1.6744 \times 10^{-11}$	$C_1 = 9.9014, C_2 = -7.7439 \times 10^{-4}$

7.7 Enthalpies and Densities of Th rich (Th,U)O₂ and (Th,Pu)O₂ MOX

The MD calculated changes in enthalpy ($H(T) - H(300)$) and density of Th_{0.9375}U_{0.0625}O₂, Th_{0.875}U_{0.125}O₂, Th_{0.8125}U_{0.1875}O₂, Th_{0.75}U_{0.25}O₂ and Th_{0.6875}U_{0.3125}O₂ for both solid and liquid phases were fitted to equations 7.7-7.8 as well as 7.9-7.10 and fitting coefficients are listed in Tables 7.4 and 7.5. Figure 7.7 compares the MD calculated change in enthalpy ($H(T) - H(300)$) values of (a) Th_{0.9375}U_{0.0625}O₂, (b) Th_{0.875}U_{0.125}O₂, (c) Th_{0.8125}U_{0.1875}O₂ and (d) Th_{0.6875}U_{0.3125}O₂ MOX upon heating in the 300-6000 K range, (i.e. for both solid and liquid phases) and cooling in the 6000-2000 K range with experimentally available data for Th_{0.98}U_{0.06}O₂, Th_{0.92}U_{0.08}O₂, Th_{0.90}U_{0.10}O₂, Th_{0.85}U_{0.15}O₂, Th_{0.80}U_{0.20}O₂ and Th_{0.70}U_{0.30}O₂ [114, 115, 287]. MD calculated values of enthalpy increments are in good agreement with experimental values at nearby compositions. Figure 7.7 also shows the variation of fitting equations obtained from our MD calculated data set. No experimental data are available for liquid (Th,U)O₂ MOX.

Similarly, MD calculated changes in enthalpy ($H(T) - H(300)$) and density of Th_{0.97}Pu_{0.03}O₂, Th_{0.95}Pu_{0.05}O₂, Th_{0.92}Pu_{0.08}O₂, Th_{0.80}Pu_{0.20}O₂ and Th_{0.70}Pu_{0.30}O₂ for both solid and liquid phase were fitted to equations 7.7-7.8 as well as 7.9-7.10 and fitting coefficients are listed in Tables 7.4 and 7.5. Figure 7.8 compares the MD calculated change in enthalpy ($H(T) - H(300)$) values of (a) Th_{0.97}Pu_{0.03}O₂ (b) Th_{0.92}Pu_{0.08}O₂ (c) Th_{0.80}Pu_{0.20}O₂ and (d) Th_{0.70}Pu_{0.30}O₂ Th_{0.9375}U_{0.0625}O₂, (b) Th_{0.875}U_{0.125}O₂, (c) Th_{0.8125}U_{0.1875}O₂ and (d) Th_{0.6875}U_{0.3125}O₂ MOX upon heating in the 300-6000 K range (i.e. for both solid and liquid phases) and cooling in the 6000-2000 K range, with experimentally available data [124]. MD calculated values of enthalpy increments are in good agreement with experimental values.

7.8 Summary

The melting behavior of pure ThO₂, UO₂ and PuO₂ as well as (Th,U)O₂ and (Th,Pu)O₂ MOX has been studied using MD simulations at ambient pressure employing newly developed interatomic potentials that combine Coulomb, Buckingham, Morse and many-body functional forms. It was found that:

- 1) The MD calculated MT of ThO₂ and UO₂ lie between 3650-3675 K and 3050-3075 K, respectively, which match well with experiment. For PuO₂, the MD calculated MT value, which lie between 2800-2825 K, falls between previously de-

terminated older experimental values and a recently determined value by Bruycker *et al.* [112]. Moreover, MD calculated values of enthalpy increment for the solid phase of UO_2 match well with experimental values but overestimate (by $\sim 50 \text{ kJ mol}^{-1}$) the value for the liquid phase. Nevertheless the calculated density variation as a function of temperature for both the solid and liquid phases is in good agreement with experiment. Our study reports enthalpy increment values of ThO_2 and PuO_2 for solid as well as liquid phases, which were not reported earlier.

2) Enthalpy of fusion values for ThO_2 , UO_2 and PuO_2 are calculated from the width of the enthalpy discontinuity and calculated values are lower than experimental values as the lattice and electronic defect contribution to the enthalpy is not taken into account in our one-phase simulations.

3) The MD calculated MT of $(\text{Th,U})\text{O}_2$ and $(\text{Th,Pu})\text{O}_2$ MOX show good agreement with the ideal solidus line in the Th rich part of the phase diagram. The ideal solidus line is, however, underestimated by $\sim 50 \text{ K}$ for $(\text{Th,U})\text{O}_2$ in the UO_2 rich parts of the phase diagram. Importantly, our study would be consistent with a minima around 5 atom% of ThO_2 in the high temperature phase diagram of $(\text{Th,Pu})\text{O}_2$ MOX.

4) MD calculated enthalpy increments as a function of temperature for ThO_2 rich $(\text{Th,U})\text{O}_2$ and $(\text{Th,Pu})\text{O}_2$ MOX are in good agreement with experiment. Our MD calculated enthalpy and density values for solid and liquid phases of $(\text{Th,U})\text{O}_2$ and $(\text{Th,Pu})\text{O}_2$ MOX are fitted to a set of equations to generate a consistent set of thermodynamic parameters for those quantities.

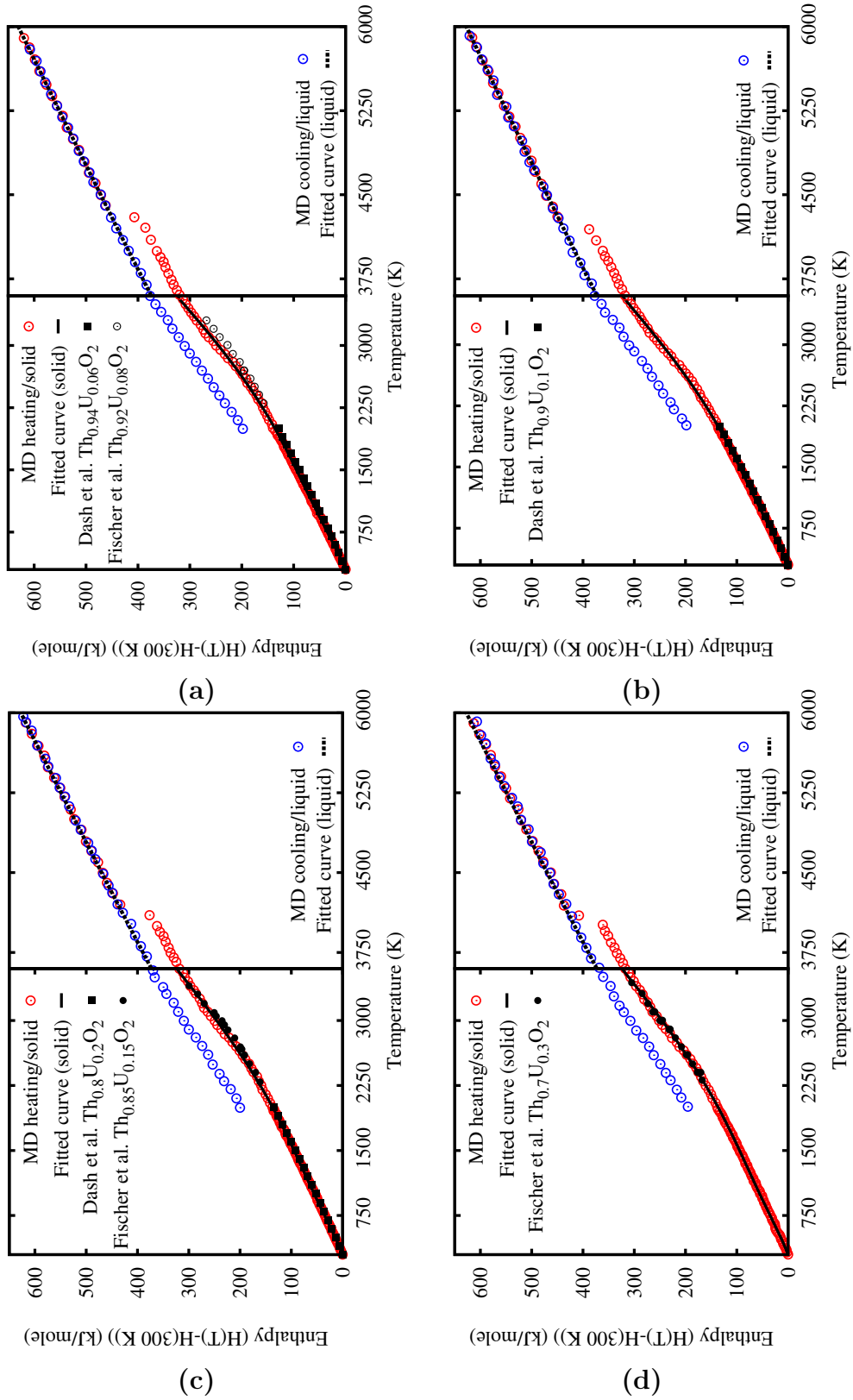


Figure 7.7: MD calculated enthalpy increments of (a) $\text{Th}_{0.9375}\text{U}_{0.0625}\text{O}_2$ (b) $\text{Th}_{0.875}\text{U}_{0.125}\text{O}_2$ (c) $\text{Th}_{0.8125}\text{U}_{0.1875}\text{O}_2$ and (d) $\text{Th}_{0.6875}\text{U}_{0.3125}\text{O}_2$ MOX are compared with experimental values reported by Dash *et al.* [115] and Fischer *et al.* [287].

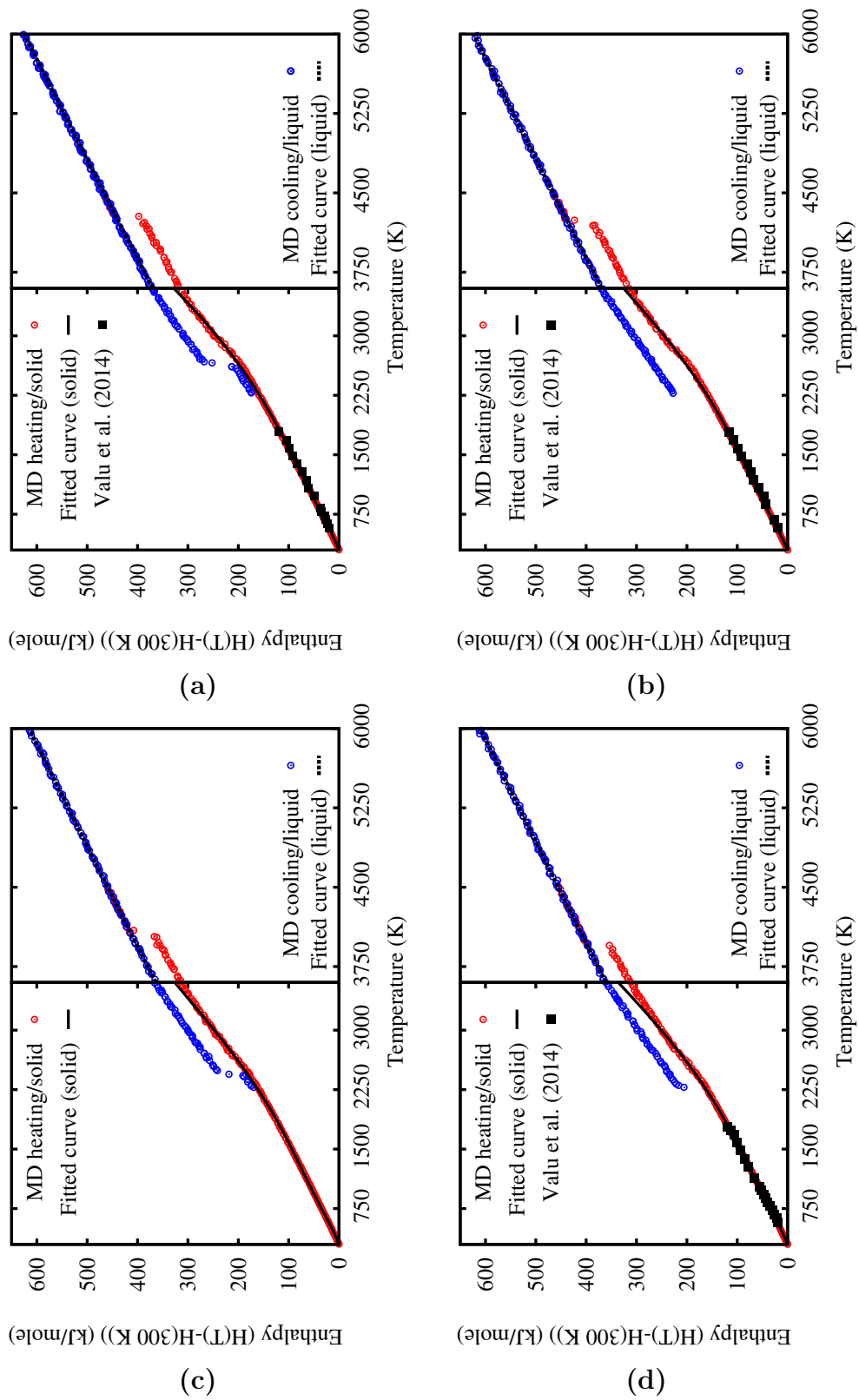


Figure 7.8: MD calculated enthalpy increments of (a) $\text{Th}_{0.97}\text{Pu}_{0.03}\text{O}_2$ (b) $\text{Th}_{0.92}\text{Pu}_{0.08}\text{O}_2$ (c) $\text{Th}_{0.80}\text{Pu}_{0.20}\text{O}_2$ (d) $\text{Th}_{0.70}\text{Pu}_{0.30}\text{O}_2$ MOX are compared with experimental values reported by Valu *et al.* [124] at the same compositions.

Chapter 8

Thermal Properties of (Th,Pu)O₂ and (Th,U)O₂ MOX

8.1 Introduction

This chapter presents a systematic study of thermal expansion and thermal conductivity of (Th,Ce)O₂, (Th,Pu)O₂ and (Th,U)O₂ MOX as a function of temperature. In this study, classical molecular dynamics (MD) simulation is employed to calculate the thermal properties and MD calculated values are thoroughly compared with experimental data.

Measurement of thermal properties of nuclear fuels under high temperature conditions is difficult to perform because of the cost of expensive appliances as well as extensive safety precautions, although the evaluation of the thermal properties of (Th,Pu)O₂ and (Th,U)O₂ MOX fuels is of utmost importance. Classical MD simulation is an efficient technique to obtain the information regarding thermal properties of MOX over a wide temperature range. In recent years, the thermo-physical properties of UO₂ [289–291], PuO₂ [292] and (U,Pu)O₂ [291, 293] as well as ThO₂ [125, 148] have been calculated over a wide temperature range (starting from room temperature) and the calculated results are in good agreement with the experimental results.

The present work adopts a two pronged theoretical and experimental approach to study thermal properties (thermal expansion and thermal conductivity) of (Th,Ce)O₂, (Th,Pu)O₂ and (Th,U)O₂ MOX. The considered compositions of MOX in this study is based upon its applicability in AHWR (ThO₂-1 to 6 wt.% PuO₂ and UO₂ MOX) and AHWR-LEU (ThO₂-6 to 30 wt.% UO₂ MOX). The thermal expansion of Th_{1-x}Ce_xO₂ (x = 0, 0.0625, 0.125), Th_{1-x}Pu_xO₂ (x = 0, 0.0625

and 0.125) and $\text{Th}_{1-x}\text{U}_x\text{O}_2$ ($x = 0, 0.0625, 0.125, 0.1875, 0.25$ and 0.3125) have been calculated using the MD simulations. MD calculated thermal conductivity values of $\text{Th}_{1-x}\text{Ce}_x\text{O}_2$ ($x = 0, 0.0625, 0.125$), $\text{Th}_{0.9375}\text{Pu}_{0.0625}\text{O}_2$ and $\text{Th}_{0.9375}\text{U}_{0.0625}\text{O}_2$ ($x = 0, 0.0625$) MOX using Green-Kubo formalism have been compared with those determined experimentally providing a gateway to more such studies for design of nuclear fuels. Thermal expansion of ThO_2 , ThO_2 -5 wt.% CeO_2 , ThO_2 -8 wt.% CeO_2 , ThO_2 -6 wt.% PuO_2 and ThO_2 -6 wt.% UO_2 have been measured using dilatometry. Moreover, thermal expansion of ThO_2 - x wt.% UO_2 MOX ($x = 0, 6, 13, 25$ and 30) have been measured using high temperature X-ray diffraction. Thermal diffusivity of ThO_2 , ThO_2 -5 wt.% CeO_2 , ThO_2 -6 wt.% PuO_2 and ThO_2 -6 wt.% UO_2 have also been measured using laser flash technique.

All the results related to the (Th,Ce) O_2 MOX are discussed in **Appendix B**. A brief description of the sample preparation, sample characterization techniques and thermal property measurements techniques are given in **Appendix C**.

8.2 MD simulation methodology

The MD calculations of thermal expansion and thermal conductivity of (Th,Pu) O_2 and (Th,U) O_2 MOX were performed using Buckingham-Morse-manybody (BMM) potential model (see section 7.2.2) and the LAMMPS MD Simulator [258] in which Newtonian equations of motion are numerically integrated to predict atom positions and velocities as a function of time using the forces obtained from the potential model described before. The long range Coulomb terms were solved using Ewald summations [192] as implemented within LAMMPS and the cut-off radius for short range interactions was fixed at 12 Å. In the present study, the MD supercell was constructed using an array of $10 \times 10 \times 10$ unit cells in three mutually orthogonal directions with 4000 cations and 8000 anions for both ThO_2 and CeO_2 . For (Th,Ce) O_2 MOX, a $5 \times 5 \times 5$ supercell of 96 atom SQS (described in section 7.2.1) was employed for thermal expansion calculations. These structures were equilibrated with 1 fs time step in the temperature range between 300 K and 3000 K (100 K interval) with the NPT ensemble (constant number of particles, pressure and temperature) at zero external pressure using the with the Berendsen barostat with a time constant of 5 ps and Nosé-Hoover thermostat with a time constant of 1 ps. Each simulation of thermal expansion and isothermal compression was carried out initially for 200 ps for equilibration (at desired temperature and pressure) and then for another 100 ps to get average values of the thermodynamic quantities.

To calculate thermal conductivity of ThO₂ and MOX, initially, supercells were equilibrated by performing a NPT run (with the Nosé-Hoover thermostat and the Berendsen barostat) to allow the volume to expand for 500 ps, followed by a NVE run to equilibrate the system at the desired temperature for 200 ps. After equilibration, the time series data for the heat current was collected under NVE for 2000 ps. The integral of the heat current auto correlation function (HCACF) $C_{ij} = \langle \mathbf{J}_i(0)\mathbf{J}_i(t) \rangle$ was evaluated using the trapezoid rule and thermal conductivity was determined as the average value in the stable regime of the integral (described in section 3.6).

8.3 (Th,Pu)O₂ MOX

8.3.1 Thermal Expansion

The MD calculated average lattice parameters ($a(T)$) of ThO₂, Th_{1-x}Pu_xO₂ ($x = 0.0625$ and 0.125) are plotted as a function of temperature (300-3000 K range) in Figure 8.1. The HT-XRD studies of ThO₂ and Th_{1-x}Ce_xO₂ MOX are also shown in the same figure as no other HT-XRD studies of (Th,Pu)O₂ MOX are available in the literature. The calculated $a(T)$ for ThO₂ and Th_{0.9375}Pu_{0.0625}O₂ matches well with experimentally measured polycrystalline $a(T)$ for ThO₂, Th_{0.96}Ce_{0.04}O₂ and Th_{0.92}Ce_{0.08}O₂ MOX in the temperature range 300-1500 K. MD calculated $a(T)$ for Th_{0.875}Pu_{0.125}O₂ MOX slightly underestimates (<2%) HT-XRD values of Th_{0.92}Ce_{0.08}O₂ MOX. The calculated decrease in lattice parameter as a function of Pu⁴⁺ concentration can be attributed to small ionic radius of Pu⁴⁺ compared to Th⁴⁺ in eight-fold coordination. Therefore, the interatomic potential as well as the SQS models are not only capable of predicting exact behavior of $a(T)$ for ThO₂, but also efficiently estimate $a(T)$ for small PuO₂ doping in ThO₂ matrix. We extended our study by estimating also the $a(T)$ in the temperature range of 300-3000 K. This allowed useful predictions to be made, both at operating temperatures and at extreme temperatures approaching the melting point in view of reactor fuel applications.

In order to further analyze the thermal expansion behavior of Th_{1-x}Pu_xO₂ MOX, the MD calculated and experimentally measured coefficient of thermal expansion (CTE, α) are listed in Table 8.1 along with other literature data. The numerical value of MD calculated α is always greater than the HT-XRD measured α value. This can be attributed to the fact that our MD calculations are performed on a model system with homogeneous distribution of PuO₂ in ThO₂ matrix and

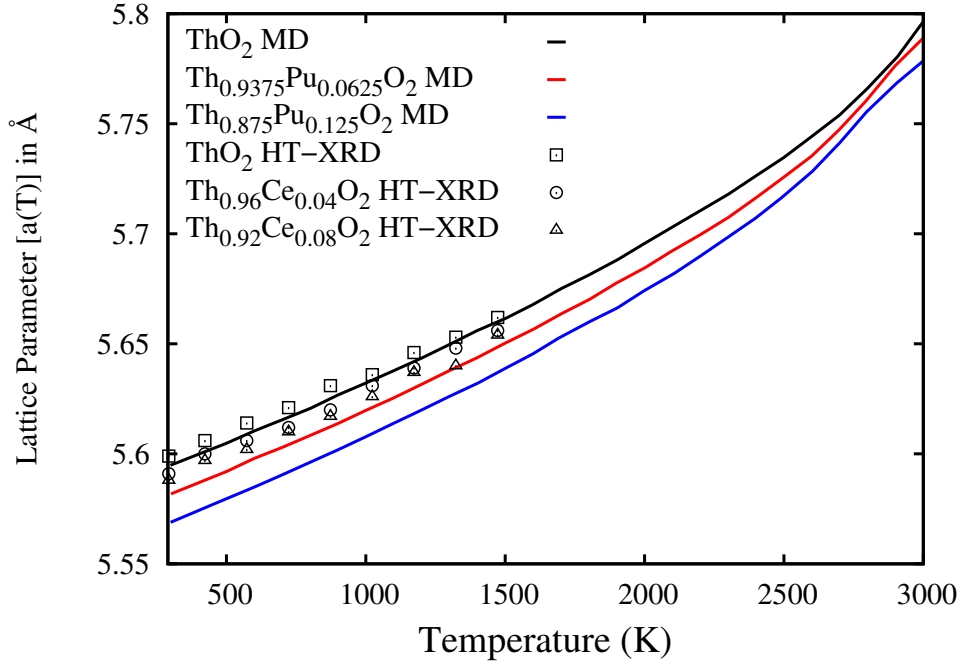


Figure 8.1: MD calculated lattice parameter variation as a function of temperature ($a(T)$) of ThO_2 , $\text{Th}_{0.9375}\text{Pu}_{0.0625}\text{O}_2$ and $\text{Th}_{0.875}\text{Pu}_{0.125}\text{O}_2$ is compared with HT-XRD determined values of ThO_2 , $\text{Th}_{0.96}\text{Ce}_{0.04}\text{O}_2$ and $\text{Th}_{0.92}\text{Ce}_{0.08}\text{O}_2$ MOX. MD values are calculated in the 300-3000 K temperature range in 100 K interval.

our calculations are not affected from porosity, impurity effects, *etc.* Nuclear fuel designers need thermal expansion data generated by dilatometer for estimating the fuel clad gap during fuel operating conditions under normal and hot spot conditions. So, Table 8.1 also enlists α values measured using dilatometry in this study.

Experimental studies using dilatometer indicated that the CTE of $(\text{Th},\text{Pu})\text{O}_2$ increases with an increasing PuO_2 content due to higher CTE of PuO_2 arising from its lower melting point compared to that of ThO_2 and similar observations have been largely reported on $(\text{Th},\text{Ce})\text{O}_2$ system [140, 141]. The CTE values observed in our study showed deviation on the higher side compared to the extrapolated values for similar compositions of $(\text{Th},\text{Ce})\text{O}_2$ in the study conducted by Tyagi *et al.* [127]. The deviation in CTE values might be due to the different heat treatment during fabrication and extent of homogeneity in the samples.

Table 8.1: MD Calculated and experimentally measured thermal expansion coefficients of ThO₂ and (Th,Pu)O₂ MOX are compared with available experimental data for (Th,Ce)O₂ MOX. ThO₂-5wt%CeO₂ and ThO₂-8wt%CeO₂ corresponds to compositions Th_{0.9253}Ce_{0.0747}O₂ and Th_{0.8823}Ce_{0.1177}O₂, respectively. (TD=Theoretical Density)

Thermal Expansion Coefficients α (10^{-6} K ⁻¹)	Remarks
ThO₂	
10.29 (300-1800 K)	MD present study
9.99 (300-1450 K)	Dilatometry, present study, ThO ₂
9.04 (293-1123 K)	Dilatometry, 96% TD [141]
9.54 (293-1173 K)	HT XRD [141]
Th_{0.9375}Pu_{0.0625}O₂ MOX	
10.55 (300-1800 K)	MD present study
10.56 (873-1773 K)	Dilatometry, CAP, ThO ₂ -5wt%CeO ₂ (Air)
10.35 (873-1773 K)	Dilatometry, POP, ThO ₂ -5wt%CeO ₂ (Air)
10.65 (873-1773 K)	Dilatometry, CAP, ThO ₂ -5wt%CeO ₂ (Ar-H ₂)
10.44 (873-1773 K)	Dilatometry, POP, ThO ₂ -5wt%CeO ₂ (Ar-H ₂)
9.35 (293-1123 K)	Th _{0.96} Ce _{0.04} O ₂ , Dilatometry, 83% TD [141]
9.76 (293-1173 K)	Th _{0.96} Ce _{0.04} O ₂ , HT XRD [141]
9.49 (293-1123 K)	Th _{0.92} Ce _{0.08} O ₂ , Dilatometry, 83% TD [141]
9.96 (293-1173 K)	Th _{0.92} Ce _{0.08} O ₂ , HT XRD [141]
Th_{0.875}Pu_{0.125}O₂ MOX	
10.90 (300-1800 K)	MD present study, BMM model
10.69 (300-1773 K)	Dilatometry, CAP, present study, ThO ₂ -8wt%CeO ₂
10.50 (300-1773 K)	Dilatometry, POP, present study, ThO ₂ -8wt%CeO ₂
9.50 (293-1123 K)	Th _{0.9} Ce _{0.1} O ₂ , Dilatometry, 85% TD [140]

8.3.2 Thermal Conductivity

The calculated thermal conductivity of pure ThO₂ and Th_{0.9375}Pu_{0.0625}O₂ MOX as a function of temperature (300-2000 K range) is shown in Figure 8.2 along with our experimentally measured thermal conductivities of ThO₂ and ThO₂-6%PuO₂ MOX between 873-1513 K and previously reported experimental values by Cozzo *et al.* [142]. In order to compare with the reported experimental data, a density (porosity) correction was applied to the MD calculated values as the latter were calculated for 100% TD. The porosity effect incorporated thermal conductivity (κ) is related with

the 100% TD thermal conductivity (κ_0) by Maxwell-Eucken equation [294]:

$$\kappa = \kappa_0 \frac{1 - p}{1 + \beta p} \quad (8.1)$$

where $\beta = 0.5$, p is the porosity ($p = 0.05$ for this study) and $\kappa/\kappa_0 = 0.92683$. In other words, 5% porosity incorporated MD calculated thermal conductivity (κ) is lower compared to κ_0 by $(1 - 0.92683) \times 100\% = 7.32\%$ at all temperature. The MD calculated values decreases with an increase of temperature, which reflects lowering of thermal conductivity by the phonon-phonon scattering. Moreover, our MD calculated values for ThO₂ are an overestimation of experimental results of Cozzo *et al.* [142] throughout the temperature range. Our MD calculated values are underestimated compared to those measured using laser flash technique in the 900-1100 K temperature range but match very well (within $\pm 1\%$) in the 1200-1600 K temperature range. Our MD calculated values for Th_{0.9375}Pu_{0.0625}O₂ MOX overestimate experimental results of Cozzo *et al.* [142] in the 500-900 K temperature range. But in the high temperature range (>1000 K), the MD calculated values match very well (with in $\pm 1\%$) with our laser-flash measured values for ThO₂-6wt.%PuO₂ and previous experimental values for ThO₂-3wt.%PuO₂ and ThO₂-8wt.%PuO₂ [142]. Importantly, a significant decrease in MD calculated thermal conductivity values as a result of Pu addition to ThO₂ lattice, particularly at low temperatures, is due to phonon mean free path reduction from lattice-phonon scattering associated with non-uniform cation sublattice. However, at high temperatures the decrease in MD calculated values upon Pu addition is less as the phonon mean free path at high temperatures is governed by the dominant phonon-phonon scattering mechanism.

It is important, therefore, to consider the temperature range over which the fuel will be operated in the AHWR. The average operating temperature of AHWR is 700-800 K at the periphery of the pellet and centre line temperature is around 900-1000 K. Our MD calculated results show that the TC of Th_{0.9375}Pu_{0.0625}O₂ exhibits a reduction in the range of 21-13% relative to that of pure ThO₂ in the 700-1000 K temperature interval. For higher temperature reactors, such as the Advanced gas-cooled reactor (AGR), where the temperature at the periphery of the fuel pellet may reach 900-1000 K, the TC of Th_{0.9375}Pu_{0.0625}O₂ is found to be 20% lower than that of ThO₂. Also, at the peak center line temperature of about 1650 K, the degradation of TC of Th_{0.9375}Pu_{0.0625}O₂ is about 14% relative to pure ThO₂. Our laser-flash measured TC showed a decrease of 26% and 20% compared to pure ThO₂ at 973 K and 1613 K, respectively.

For ceramic oxide systems, the behavior of thermal conductivity with tem-

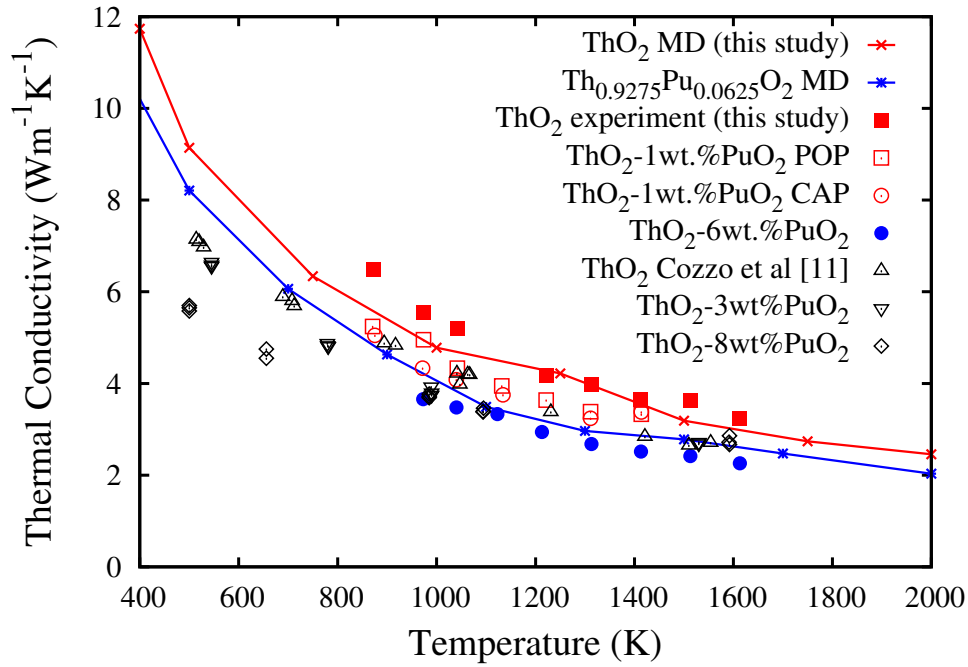


Figure 8.2: Thermal conductivity calculated by MD simulations as a function of temperature for ThO_2 and $\text{Th}_{0.9275}\text{Pu}_{0.0625}\text{O}_2$ compared with our experimental values of ThO_2 , ThO_2 -1 wt.% PuO_2 (POP and CAP pellets) and ThO_2 -6 wt.% PuO_2 POP pellet (95% TD). These values are also compared with reported values of ThO_2 , ThO_2 -3 wt.% and ThO_2 -8 wt.% PuO_2 by Cozzo *et al.* [142]. Solid lines are only for visual guidance.

perature is governed by two factors: (i) the phonon-phonon interactions and (ii) the density of defects (phonon scattering centers) in the lattice. For temperatures below 1900 K, the contribution of the free electrons on the thermal conductivity can be neglected for electronically insulator materials [6, 295]. In view of this, the MD calculated thermal conductivity data was fitted to the standard relation with phonon conduction, as given below,

$$\kappa = \frac{1}{A + BT} \quad (8.2)$$

where, ‘A’ represent scattering due to the presence of impurities, representing defect thermal resistivity and is independent of temperature and ‘B’ represents scattering due to phonons and is a function of temperature. The influence of substituted impurities on the thermal conductivity is attributed to an increase of the parameter ‘A’. This results from interaction of phonon with lattice imperfections, impurities, isotopic, or other mass differences as well as bulk defects such as grain boundaries

in the sample. Parameter ‘B’ remains constant theoretically and the second term, namely ‘B.T’, represents the intrinsic lattice thermal resistivity caused by phonon-phonon scattering. As the temperature increases, this term becomes predominant.

Table 8.2: Constants A and B of the equations $\kappa = \frac{1}{A+BT}$ for ThO₂ and (Th,Pu)O₂ MOX calculated from MD simulations and experimental measurements.

System	A (m K/W)	B (m/W) $\times 10^{-4}$
MD this study		
ThO ₂	0.00315	1.88
Th _{0.9375} Pu _{0.0625} O ₂	0.00451	2.24
ThO ₂ , Expt. This study	0.02000	1.34
ThO ₂ -6wt.% PuO ₂ (POP), Expt. this study	0.00424	2.74
ThO ₂ , Cozzo <i>et al.</i> [142]	0.010	2.30
ThO ₂ -3wt.%PuO ₂ , Cozzo <i>et al.</i> [142]	0.035	2.20
ThO ₂ -3wt.%PuO ₂ , Cozzo <i>et al.</i> [142]	0.099	1.69

The MD calculated thermal conductivity data was fitted to the standard relation with phonon conduction, as shown in Equation 8.2. One pair of A and B constants is obtained for each composition of solid solution by polynomial fitting of the thermal resistivity versus temperature data. Table 8.2 shows the determined values of A and B constants from our MD calculated and experimentally measured thermal conductivity variation as a function of temperature along with those values as determined by Cozzo *et al.* [142]. Figure 8.2 shows thermal conductivity values of ThO₂, ThO₂-1wt.%PuO₂ for CAP and POP pellets and ThO₂-6wt.%PuO₂ POP pellet. It is evident from Table 8.2 that our MD calculated B constants are almost independent of composition of solid solutions which is in accordance with experimental measurements of Cozzo *et al.* [142]. On the other hand, the values of constant A continuously increase with PuO₂ concentration in agreement with the experimental trend. This is attributed to the scattering of the phonons occurring due to mass and size difference between substituted and host atoms.

8.4 (Th,U)O₂ MOX

This study is performed to determine thermal properties of ThO₂ and (Th,U)O₂ MOX using an empirical potential comprises of Buckingham, Morese and Many-body (BMM) interactions as described in **Chapter 7, section 7.2.1**. A similar

methodology as described in **section 8.2** is adopted to perform MD simulations using BMM potentials. MD calculated values are further validated by performing experimental measurements, such as, high temperature XRD and dilatometry to measure thermal expansion as well as laser flash method to determine thermal diffusivity. A brief description of the sample preparation, sample characterization techniques and thermal property measurements techniques are given in **Appendix C**.

We performed multiple equivalent simulations with different initial conditions, evaluated each of them separately and took average of them to present in this study. Five equivalent simulations for thermal expansion (TE) and three equivalent simulations for thermal conductivity (TC) were performed at each temperature the error-bars for TE and TC calculated values are $\pm 0.0008 \text{ \AA}$ and from ± 0.1 to $\pm 0.3 \text{ Wm}^{-1}\text{K}^{-1}$ range in the whole temperature range, respectively.

8.4.1 Experiments

ThO_2 and $\text{ThO}_{2-x} \text{ wt\% UO}_2$ ($x = 6, 13, 25$ and 30) MOX pellets were analyzed for its trace impurities using high resolution sequential inductively coupled plasma-atomic emission spectroscopy (ICP-AES) to understand the effect of impurities in the thermal expansion and thermal conductivity behavior of (Th,U) O_2 MOX. Elaborate details of the ICP-AES sample preparation, experimental procedure and operating conditions are given in **Appendix C**. Using this method, the transition metal and lanthanides were examined. In our study, we found similar results for all the samples and Table 8.3 presents results of only pure ThO_2 and $\text{ThO}_{2-6\%}\text{UO}_2$. Table 8.3 clearly indicates almost all the elements were found to be in the range 0.3-260 ppm with a precision of maximum $\pm 7.3\%$ root mean square deviation (RSD) which confirm a near total purity of the sample with respect to the above impurities. Therefore, chemical analysis results indicate complete removal of binder-cum-lubricants added and absence of any extraneous contamination due to process operations. So, thermal properties of these samples are not expected to influence by the trace impurities.

Figure 8.3 shows room temperature XRD patterns of ThO_2 and $\text{ThO}_{2-x} \text{ wt\% UO}_2$ ($x = 6, 13, 25$ and 30) MOX powders. The measured lattice parameters (a_0) of ThO_2 and (Th,U) O_2 MOX are given in Table 8.4. Our measured a_0 for ThO_2 , $\text{ThO}_{2-6\%}\text{UO}_2$ and $\text{ThO}_{2-13\%}\text{UO}_2$ are 5.5967 \AA , 5.5885 \AA and 5.5800 \AA , respectively, matches very well with previous measurement of 5.599 \AA , 5.585 \AA [127] and 5.58 \AA [129] at respective compositions. The O/M ratio of the POP pellets

Table 8.3: Impurity content analysis by ICP-AES

Elements	Impurity contains of ThO ₂		Impurity contains of ThO ₂ -6%UO ₂	
	ppm	rsd	ppm	rsd
Zn	58.00	3.41	37.00	2.72
Cu	13.35	1.51	8.48	1.21
Ni	9.45	4.58	8.10	3.72
Co	1.54	0.37	1.23	1.60
Fe	252.53	7.00	179.46	5.13
Mn	8.2	4.19	3.57	3.55
Cr	35.7	4.66	25.96	5.02
Ca	103.83	0.01	31.57	0.03
Mg	78.16	4.25	28.23	3.08
Sr	55.76	0.31	7.24	1.23
Ba	5.65	1.33	4.63	1.32
Li	0.34	1.72	0.10	5.06
Na	235.14	5.66	183.86	2.75
K	78.73	1.04	21.53	3.70
B	67.35	7.38	16.87	4.03
Al	49.05	3.62	56.59	2.86
Ga	169.78	4.62	149.12	2.74
In	4.89	4.02	3.03	3.21
Cd	3.90	3.82	1.47	2.94
Ag	5.04	3.01	3.86	3.02
Pb	13.75	7.28	11.61	6.15

were determined by thermogravimetry (TG) method (described in **Appendix C**). The change in weights (gain/loss) before and after the experiment measured by TG corresponds to the extent of hypo/hyper-stoichiometry and the calculated O/M ratio was found to be in the range 2.002 to 2.007 with a measurement accuracy of ± 0.002 . Therefore, our thermal expansion values of (Th,U)O₂ MOX powders are not affected by the hypo-/hyper-stoichiometry of the samples.

8.4.2 Thermal Expansion

(a) HT-XRD

Typical XRD patterns of ThO₂-6wt.% UO₂ powder for different temperatures are given in Figure 8.4. The unit cell parameters were determined as a function of temperature in the 293 to 1273 K range. Lattice parameters were measured with an accuracy of ± 0.0005 nm. The lattice parameters of each sample at different temperatures are given in Table 8.4. The experimental thermal expansion data was least squares fitted to a third degree polynomial equation for each sample. The fitting errors for all these compositions were within $\pm 1\%$. The recommended percentage thermal expansion data in the temperature range from 293 to 1273 K

for $\text{ThO}_2\text{-}x \text{ wt.}\% \text{UO}_2$ ($x = 0, 6, 13, 25$ and 30) is given below:

ThO_2 :

$$\Delta a/a_0 \times 100(\%) = -0.17719 + 0.45880 \times 10^{-3} \times T + 2.52793 \times 10^{-7} \times T^2 + 0.67866 \times 10^{-10} \times T^3$$

$\text{ThO}_2 - 6\text{wt.}\% \text{UO}_2 (\text{Th}_{0.9413}\text{U}_{0.0587}\text{O}_2)$:

$$\Delta a/a_0 \times 100(\%) = -0.15033 + 0.29546 \times 10^{-3} \times T + 8.18691 \times 10^{-7} \times T^2 + 3.27958 \times 10^{-10} \times T^3$$

$\text{ThO}_2 - 13\text{wt.}\% \text{UO}_2 (\text{Th}_{0.8725}\text{U}_{0.1275}\text{O}_2)$:

$$\Delta a/a_0 \times 100(\%) = -0.21292 + 0.71674 \times 10^{-3} \times T - 1.57198 \times 10^{-7} \times T^2 + 2.84777 \times 10^{-10} \times T^3 \quad (8.3)$$

$\text{ThO}_2 - 25\text{wt.}\% \text{UO}_2 (\text{Th}_{0.7542}\text{U}_{0.2458}\text{O}_2)$:

$$\Delta a/a_0 \times 100(\%) = -0.54082 + 2.30035 \times 10^{-3} \times T - 23.1553 \times 10^{-7} \times T^2 + 11.3387 \times 10^{-10} \times T^3$$

$\text{ThO}_2 - 30\text{wt.}\% \text{UO}_2 (\text{Th}_{0.7047}\text{U}_{0.2953}\text{O}_2)$:

$$\Delta a/a_0 \times 100(\%) = -0.51630 + 2.34762 \times 10^{-3} \times T - 25.8682 \times 10^{-7} \times T^2 + 13.2255 \times 10^{-10} \times T^3$$

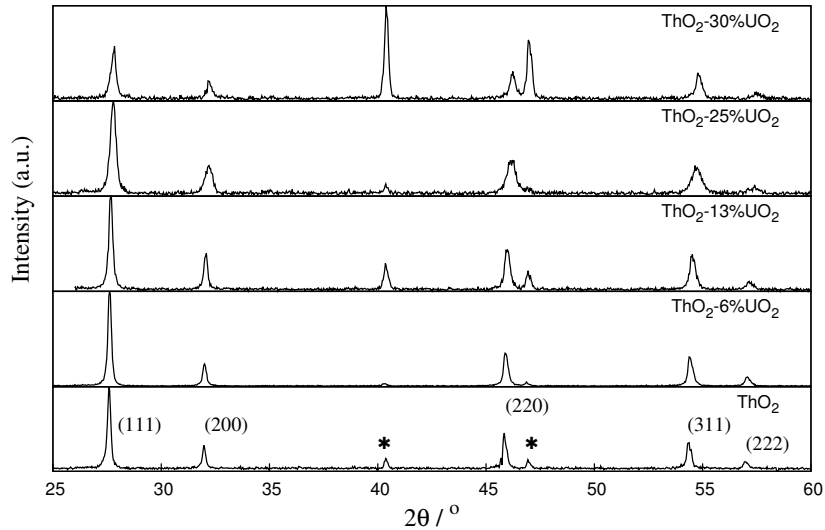


Figure 8.3: XRD patterns of $\text{ThO}_2\text{-}x \text{ wt.}\% \text{UO}_2$ ($x = 0, 6, 13, 25$ and 30) MOX at room temperature. Lines at 40.47° and 47.12° are due to Pt-Rh sample carrier (marked as \star in the figure).

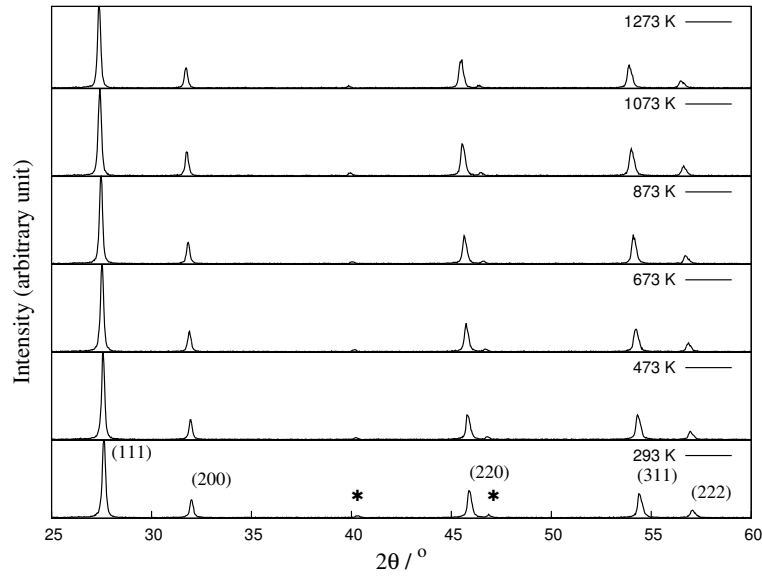


Figure 8.4: XRD patterns of ThO₂-6wt.% UO₂ (POP) at different temperatures. Lines at 40.47° and 47.12° are due to Pt-Rh sample carrier.

Table 8.4: Variation of lattice parameter a (Å) for ThO₂ and ThO₂- x wt.%UO₂ MOX ($x = 6, 13, 25$ and 30) with temperature as measured using HT-XRD.

Temperature (K)	Lattice parameter variation of (Th,U)O ₂ MOX				
	ThO ₂	ThO ₂ -6%UO ₂	ThO ₂ -13%UO ₂	ThO ₂ -25%UO ₂	ThO ₂ -30%UO ₂
293	5.5967 (7)	5.5885 (0)	5.5800 (0)	5.5590 (0)	5.5501 (0)
373	5.5970 (8)	5.5916 (17)	5.5826 (23)	5.5595 (15)	5.5534 (14)
473	5.6012 (7)	5.5967 (7)	5.5867 (23)	5.5686 (13)	5.5601 (23)
573	5.6063 (14)	5.6014 (22)	5.5904 (11)	5.5709 (15)	5.5636 (22)
673	5.6110 (4)	5.6056 (4)	5.5955 (19)	5.5755 (14)	5.5681 (33)
773	5.6162 (9)	5.6122 (13)	5.6024 (14)	5.5787 (14)	5.5694 (25)
873	5.6227 (3)	5.6169 (15)	5.6074 (27)	5.5883 (18)	5.5747 (17)
973	5.6283 (8)	5.6224 (16)	5.6130 (11)	5.5898 (12)	5.5819 (19)
1073	5.6343 (13)	5.6274 (23)	5.6206 (35)	5.5957 (25)	5.5886 (32)
1173	5.6401 (7)	5.6342 (10)	5.6275 (27)	5.5993 (27)	5.5938 (12)
1273	5.6506 (18)	5.6448 (31)	5.6383 (25)	5.6180 (33)	5.6095 (32)

(b) Dilatometry

The O/M ratio of the CAP pellet was determined by TG method as described previously. The change in weights (gain/loss) before and after the experiment measured by TG corresponds to the extent of hypo/hyper-stoichiometry and the calculated O/M ratio is shown in Table 8.5. Table 8.5 also compares density, porosity and O/M values of ThO₂-6%UO₂ POP and CAP pellets sintered in Ar-8%H₂ atmosphere. ThO₂-6wt% UO₂ powder (CAP pellet) was analyzed chemically for its trace impurities using high resolution sequential ICP-AES and similar results

were found as shown in Table 8.5.

The typical variation of the linear thermal expansion (%) as a function of temperature (300-1773 K) as measured by dilatometer for ThO₂ and ThO₂-6%UO₂ MOX (CAP and POP pellets). The experimental thermal expansion data are least squares fitted to a third degree polynomial equation for each sample. The fitting errors for all these compositions are within $\pm 1\%$. The recommended percentage thermal expansion data in the temperature range from 300 to 1773 K for CAP and POP pellets is given below (T in K):

ThO₂ :

$$(\Delta L/L_0) \times 100(\%) = -0.19730 + 5.6599 \times 10^{-4} \times T + 3.54902 \times 10^{-7} \times T^2 - 7.4276 \times 10^{-11} \times T^3$$

ThO₂ – 6%UO₂(POP) :

$$(\Delta L/L_0) \times 100(\%) = 0.01716 - 1.56136 \times 10^{-4} \times T + 1.2326 \times 10^{-7} \times T^2 - 3.9263 \times 10^{-10} \times T^3$$

ThO₂ – 6%UO₂(CAP) :

$$(\Delta L/L_0) \times 100(\%) = -0.20084 + 5.21632 \times 10^{-4} \times T + 4.36863 \times 10^{-7} \times T^2 - 1.08349 \times 10^{-10} \times T^3$$

(8.4)

Table 8.5: Characteristics of experimental pellets used for thermal property studies.

Fabrication route	Sintering atmosphere	Density (g/cc)	O/M	Prosity (% TD)
POP	Ar-8%H ₂	9.464	2.002	5.9
CAP	Ar-8%H ₂	9.354	2.013	7.0

(c) MD Simulations

The MD calculated average lattice parameters ($a(T)$) of ThO₂ are plotted as a function of temperature (300-2000 K range) for 10×10×10 supercell in Figure 8.5 (a). The error bar due to initial conditions in lattice parameter calculation at desired temperature was $\pm 0.0008 \text{ \AA}$. This figure also compares MD calculated $a(T)$ with other experimentally determined $a(T)$ by HT-XRD [128, 130, 296, 297] and show very good agreement with the predictions of the potential model. Figure 8.6 compares MD calculated $a(T)$ as a function of temperature for Th_{1-x}U_xO₂ (x = 0, 0.0625, 0.125, 0.1875, 0.25 and 0.3125) with our HT-XRD measured $a(T)$ for ThO₂-x wt% UO₂ (x = 0, 6, 13, 25 and 30) in the temperature range of 300 and 1300 K.

The calculated decrease in lattice parameter as a function of U^{4+} concentration can be attributed to small ionic radii of U^{4+} (0.997 Å) compared to Th^{4+} (1.05 Å) in eight-fold coordination. Our MD calculated $a(T)$ for $Th_{1-x}U_xO_2$ ($x = 0, 0.0625$ and 0.125) exactly matches with HT-XRD measured values for ThO_2 , ThO_2 -6wt.% and 13wt.% UO_2 samples. On the other hand, our MD calculated $a(T)$ for $Th_{1-x}U_xO_2$ ($x = 0.2500$ and 0.3125) slightly overestimates our HT-XRD measured $a(T)$ for ThO_2 -25wt.% and 30wt.% UO_2 samples. Therefore, our potential model along with SQS model is capable of reproducing lattice thermal expansion behavior of ThO_2 and $(Th,U)O_2$ MOX in the temperature range of 300 K and 1300 K.

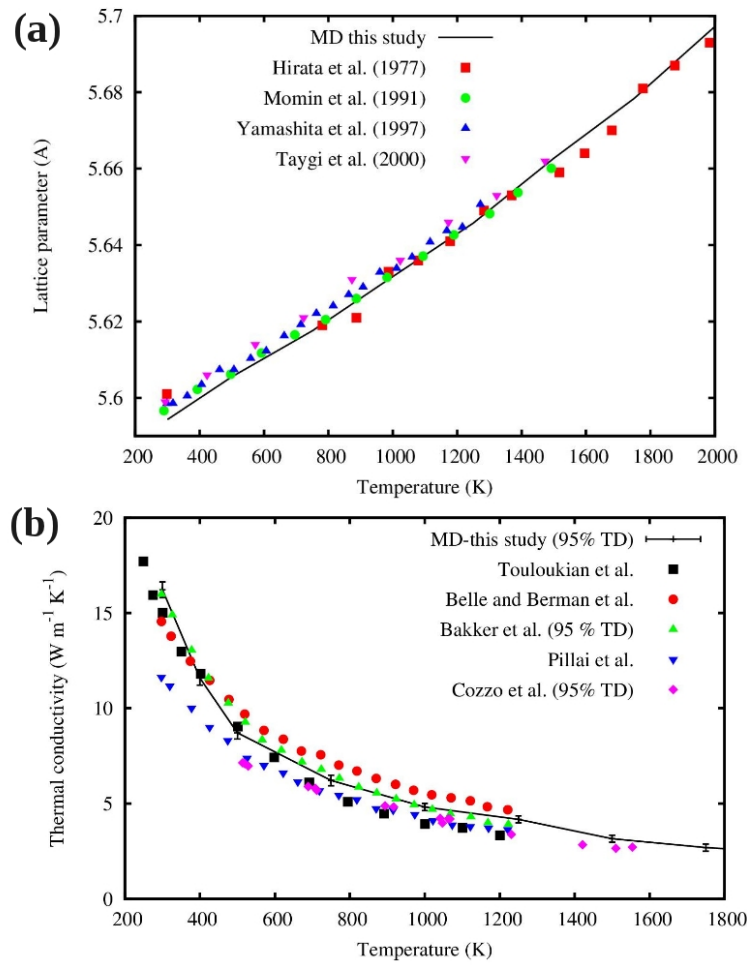


Figure 8.5: Comparison of lattice parameter (a) and thermal conductivity (b) variation as a function of temperature of pure ThO_2 calculated by classical MD simulation and reported experimental values. The lattice parameters are calculated from 300-3000 K in 100 K interval and the error bars in the calculated lattice parameters are ± 0.0008 Å. The thermal conductivity values are calculated at 300, 400, 500, 750, 1000, 1250, 1500, 1750 and 2000 K temperature.

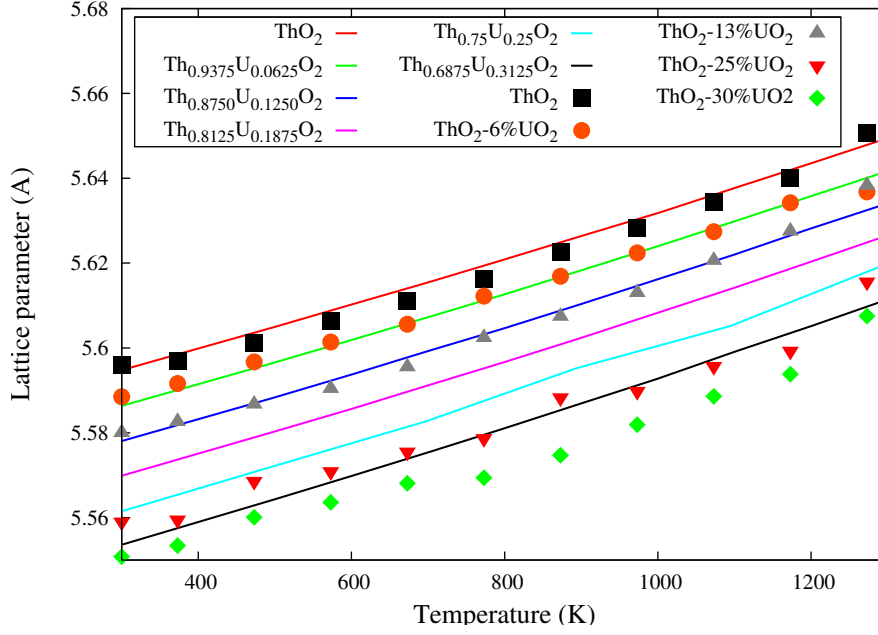


Figure 8.6: Variation of lattice parameter of $\text{Th}_{1-x}\text{U}_x\text{O}_2$ ($x = 0, 0.0625, 0.125, 0.1875, 0.25$ and 0.3125) in the 300-1300 K temperature range along with our HT-XRD data. The lattice parameters are calculated from 300-3000 K in 100 K interval and the error bars in the calculated lattice parameters are $\pm 0.0008 \text{ \AA}$.

Figure 8.7 shows the increase in the lattice parameter as a function temperature of $5 \times 5 \times 5$ supercell of SQS (96 atom unit cell) for compositions $\text{Th}_{1-x}\text{U}_x\text{O}_2$ ($x = 0.0625, 0.1250, 0.1875, 0.2500$ and 0.3125) in the temperature range between 300 K and 3000 K. Experimentally measured HT-XRD data for $\text{Th}_{0.94}\text{U}_{0.06}\text{O}_2$ [127] and $\text{Th}_{0.87}\text{U}_{0.13}\text{O}_2$ [129] are also included in the same figure and show very good agreement with the MD calculated values. Even though the HT-XRD measured value of $a(T)$ at room temperature for $\text{Th}_{0.80}\text{U}_{0.20}\text{O}_2$ [130] is matching well with our MD calculated value for $\text{Th}_{0.8125}\text{U}_{0.1875}\text{O}_2$, the behavior of $a(T)$ for $\text{Th}_{0.80}\text{U}_{0.20}\text{O}_2$ [130] is significantly different at high temperature compared to our MD calculated values. It is important to note that, the variation of $a(T)$ measured using HT-XRD by Momin *et al.* [130] for $\text{Th}_{0.8}\text{U}_{0.2}\text{O}_2$ is also significantly different from the other HT-XRD values for $\text{Th}_{0.94}\text{U}_{0.06}\text{O}_2$ [127] and $\text{Th}_{0.87}\text{U}_{0.13}\text{O}_2$ [129]. This can also be understood by the fact that thermal expansion coefficient value of $\text{Th}_{0.8}\text{U}_{0.2}\text{O}_2$ (within 300-1600 K temperature range) is lower to pure ThO_2 which is in contradiction to other HT-XRD study [127, 129]. Figure 8.7 also illustrates a significant increase in $a(T)$ for all compositions of solid solution as well as for the pure systems at high temperatures (2300-3000 K). This prediction, covering temperature range both at operating temperatures and at extreme temperatures approaching the melting point, is important to reactor fuel applications.

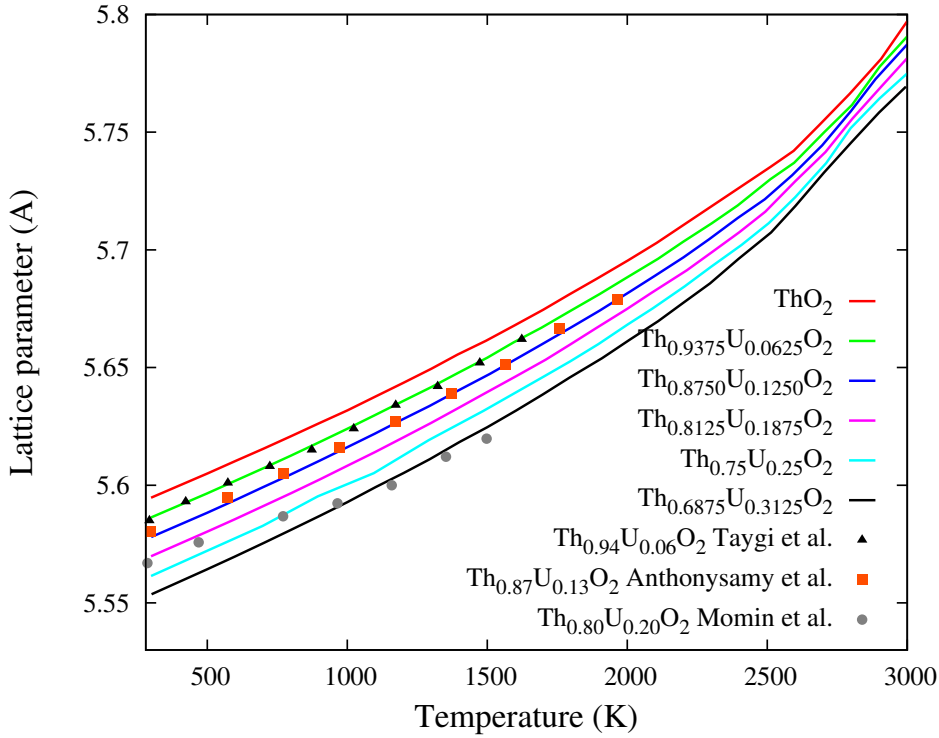


Figure 8.7: Variation of lattice parameter of $\text{Th}_{1-x}\text{U}_x\text{O}_2$ ($x = 0, 0.0625, 0.125, 0.1875, 0.25$ and 0.3125) in the 300-3000 K temperature range along with HT-XRD data of $\text{Th}_{0.94}\text{U}_{0.06}\text{O}_2$ [127], $\text{Th}_{0.87}\text{U}_{0.13}\text{O}_2$ [129] and $\text{Th}_{0.80}\text{U}_{0.20}\text{O}_2$ [130]. The lattice parameters are calculated from 300-3000 K in 100 K interval and the error bars in the calculated lattice parameters are ± 0.0008 .

In order to analyze further the thermal expansion behavior of ThO_2 and $(\text{Th},\text{U})\text{O}_2$ MOX, the MD calculated and experimentally measured (by HT-XRD and dilatometry) thermal expansion coefficients (α) are listed in Table 8.6 along with other literature data. Generally, the numerical value of MD calculated α is always greater than the experimentally measured α values. This can be attributed to the fact that our MD calculations are performed on a ideal solid-solution model system not incorporating the effects of porosity, impurity, intrinsic defects, *etc.*. In contrast, the experimental samples are not devoid of these effects where some part of the lattice thermal expansion may be accommodated in the porosity of the samples. Table 8.6 also clearly illustrates that with increase in UO_2 concentration α values of $(\text{Th},\text{U})\text{O}_2$ MOX is increasing as the melting point of UO_2 (~ 3073 K) is lower than that of ThO_2 (~ 3573 K) [3, 4, 6]. Similar observation have already been reported by various authors [126–129, 131] except for Momin *et al.* [130].

Our HT-XRD measured α values for ThO_2 match very well with previous HT-XRD and our dilatometry measured α values. Our HT-XRD measured α values

Table 8.6: MD Calculated and experimentally measured thermal expansion coefficients of ThO₂ and (Th,U)O₂ MOX compared with available experimental data in the literature.

Thermal Expansion Coefficients α (10^{-6} K ⁻¹)	Remarks
ThO₂	
10.28 (300-1800 K)	MD present study
9.78 (293-1273 K)	HT-XRD, present study
9.99 (300-1773 K)	Dilatometry, present study
9.67 (293-1623 K)	HT XRD [128]
9.54 (293-1173 K)	HT XRD [141]
Th_{0.9375}U_{0.0625}O₂	
10.47 (300-1800 K)	MD present study, Th _{0.9375} U _{0.0625} O ₂
10.33 (293-1273 K)	HT-XRD, present study, ThO ₂ -6wt%UO ₂
10.10 (300-1773 K)	Dilatometry, present study, POP, ThO ₂ -6wt%UO ₂
10.14 (300-1773 K)	Dilatometry, present study, CAP, ThO ₂ -6wt%UO ₂
10.37 (293-1623 K)	HT-XRD, Th _{0.94} U _{0.06} O ₂ [127]
(Th,U)O₂	
10.66 (300-1800 K)	MD present study, Th _{0.875} U _{0.125} O ₂
10.66 (293-1273 K)	HT-XRD present study, ThO ₂ -13wt.%UO ₂
10.33 (293-1973 K)	HT-XRD, Th _{0.87} U _{0.13} O ₂ [129]
10.76 (300-1800 K)	MD present study, Th _{0.8125} U _{0.1875} O ₂
10.93 (300-1800 K)	MD present study, Th _{0.75} U _{0.25} O ₂
10.83 (293-1273 K)	HT-XRD present study, ThO ₂ -25wt.%UO ₂
11.05 (300-1800 K)	MD present study, Th _{0.6875} U _{0.3125} O ₂
10.94 (293-1273 K)	HT-XRD present study, ThO ₂ -30wt.%UO ₂

for ThO₂-6wt.% and 13wt.%UO₂ match very well with previous HT-XRD measured values. But the α measured from dilatometer for ThO₂-6wt.%UO₂ (both POP and CAP pellets) is lower than HT-XRD values. This can be attributed to the fact that density of the ThO₂-6wt.%UO₂ MOX pellets are lower (by 6-7%) compared to theoretical density due to porosity. Nuclear fuel designers require thermal expansion data generated by dilatometer for estimating the fuel clad gap during fuel operating conditions under normal and hot spot conditions and importantly this estimation is a key information (among the many other) to calculate effective heat transfer from fuel to clad. It is also important to note that the α measured from dilatometer for ThO₂-6wt.%UO₂ for both POP and CAP pellets is very similar. Therefore, our

thermal expansion study indicates CTE is almost independent of inhomogeneity and porosity effect of the pellets.

8.4.3 Thermal Conductivity

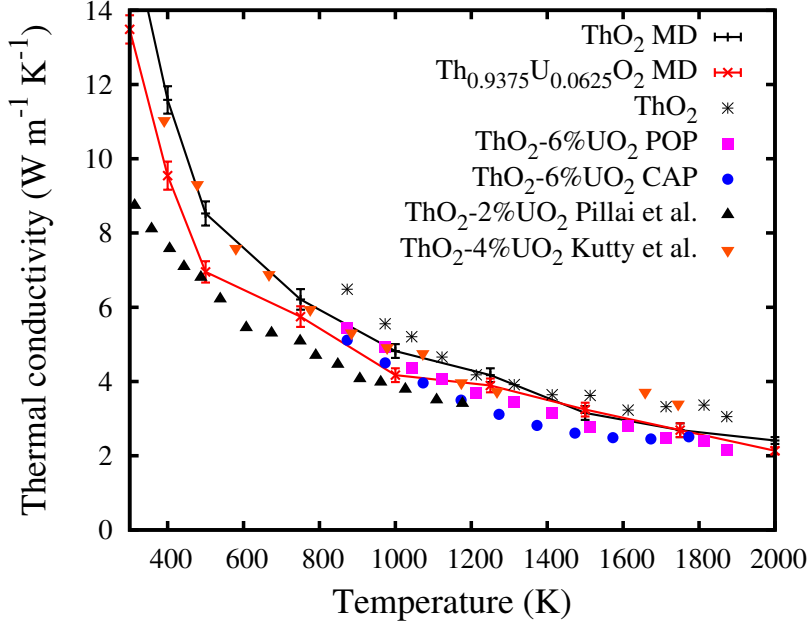


Figure 8.8: Thermal conductivity as calculated by MD simulations as a function of temperature for ThO_2 and $\text{Th}_{0.9375}\text{U}_{0.0625}\text{O}_2$ compared with our experimental values of ThO_2 and ThO_2 -6wt.% UO_2 (POP and CAP) pellet (both corrected to 95 % TD). These values are also compared with reported values of ThO_2 -2wt.% UO_2 by Pillai *et al.* [132]. The thermal conductivity values are calculated at 300, 400, 500, 750, 1000, 1250, 1500, 1750 and 2000 K temperature and solid lines are only for visual guidance.

The MD calculated thermal conductivity of ThO_2 as a function of temperature (300-1800 K range) are shown in Figure 8.5 (b). The error bar due to initial conditions in thermal conductivity calculation at desired temperature was ± 0.1 to $\pm 0.35 \text{ Wm}^{-1}\text{K}^{-1}$ range. In order to compare with the reported experimental data, a density (porosity) correction was applied to the MD calculated values as these were obtained for 100% TD. The porosity effect incorporated thermal conductivity (κ) is related with the 100% TD thermal conductivity (κ_0) by Maxwell-Eucken equation (Equation B.2). In other words, 5% porosity incorporated MD calculated thermal conductivity (κ) is lower compared to κ_0 by $(1 - 0.92683) \times 100\% = 7.32\%$ at all temperature. The MD calculated values decreases with an increase of temperature, which reflects lowering of thermal conductivity by the phonon-phonon scattering.

Table 8.7: Constants A and B of the equations $\kappa = \frac{1}{A+BT}$ for ThO₂ and (Th,U)O₂ MOX calculated from MD simulations and experimental measurements.

System	A (m K/W)	B (m/W) $\times 10^{-4}$
ThO ₂ , MD, this study	0.0032	1.879
Th _{0.9375} U _{0.0625} O ₂ , MD, this study	0.0174	1.784
ThO ₂ , Expt. This study	0.0307	1.611
ThO ₂ -6wt.% UO ₂ (POP), Expt. this study	0.0514	2.649
ThO ₂ -6wt.% UO ₂ (CAP), Expt. this study	0.0547	2.548
ThO ₂ , Kutty <i>et al.</i> [126]	0.0334	1.374
ThO ₂ -4wt.%UO ₂ , Kutty <i>et al.</i> [126]	0.0497	1.475
ThO ₂ , Bakker <i>et al.</i> [6]	0.0004	2.248
ThO ₂ -6wt.%UO ₂ , Bakker <i>et al.</i> [6]	0.0509	1.848

On the other hand, plenty of experimental thermal conductivities measurements are available in the literature for ThO₂ [6, 122, 142, 298] and these are also plotted in Figure 8.5 (b). It is evident that, the calculated thermal conductivities are in good agreement with the experimental data within $\pm 1 \text{ Wm}^{-1}\text{K}^{-1}$ in the whole temperature range.

In Figure 8.8, the MD calculated thermal conductivity of Th_{1-x}U_xO₂ (x = 0 and 0.0625) are plotted (corrected to 95% TD) as a function of temperature (400-2000 K range) along with our experimentally measured values of pure ThO₂ and ThO₂-6wt.%UO₂ (Th_{0.9413}U_{0.0587}O₂) in the 873-1873 K temperature range for POP and CAP pellets. At low temperatures, the thermal conductivity of the (Th,U)O₂ MOX decreases with an increase of the UO₂ content. It is also evident that the decrease in thermal conductivity with UO₂ concentration at 500 K is larger than that at 1500 K. At higher temperatures (above 1200 K), the thermal conductivity of Th_{0.9375}U_{0.0625}O₂ is lower compared to ThO₂ in the 0.5-0.1 Wm⁻¹K⁻¹ range. It is also important to note that experimentally measured κ values for POP pellet is higher than the CAP pellets though the difference is within 5%. It further emphasizes that cumulative effects of porosity majorly and inhomogeneity are affecting the thermal conductivity properties of the CAP pellets. Figure 8.8 also includes experimentally determined thermal conductivity values of Pillai *et al.* [132] for Th_{0.98}U_{0.02}O₂ which show lower thermal conductivity values compared to ThO₂-6wt.%UO₂ (CAP and POP pellets). At this point it is important to note, Pillai *et al.* [132] used a static configuration technique in contrast to dynamical configuration technique (this study) to estimate thermal conductivity and the density for which

thermal conductivity values were reported was also not mentioned in [132].

The MD calculated thermal conductivity values are fitted to the equation 8.2 and Table 8.7 enlists A and B values obtained from the MD calculated and experimentally measured κ versus temperature data along with those values determined by Kutty *et al.* [126] and suggested by Bakker *et al.* [6]. Our MD calculated A value shows an order of magnitude increase for $\text{Th}_{0.9375}\text{U}_{0.0625}\text{O}_2$ compared to ThO_2 and B value remains almost constant. This general feature of increasing A value with increasing UO_2 concentration is matching well with reported data by Kutty *et al.* [126] and suggested by Bakker *et al.* [6]. It can be noted that determined A values for CAP pellet is higher than POP pellet and this can be attributed to inhomogeneous distribution of UO_2 in ThO_2 matrix. So inhomogeneous distribution is creating more lattice defect centers resulting in higher phonon-lattice scattering cross-section.

8.5 Summary

MD simulations were performed on ThO_2 , $(\text{Th,Pu})\text{O}_2$ and $(\text{Th,U})\text{O}_2$ MOX using Buckingham-Morse-Manybody type potential functions to systematically evaluate thermal expansion and thermal conductivity of MOX. The variation of calculated lattice parameters as a function of temperature for MOX solid solutions are in good agreement with HT-XRD data which validates our potential parameters used in this study.

Our combined MD simulations and dilatometry measurements indicate that incorporation of PuO_2 in ThO_2 systematically increases coefficient of thermal expansion. Similarly, MD calculated and laser-flash measured thermal conductivity values indicate that incorporation of PuO_2 in ThO_2 (by 6 wt.%) reduces thermal conductivity values in the 0.6-1.2 $\text{Wm}^{-1}\text{K}^{-1}$ range for the 973-1613 K temperature interval compared to ThO_2 .

Our combined MD simulations and HT-XRD measurements indicate that incorporation of UO_2 in ThO_2 systematically increases coefficient of thermal expansion but the rate of increase is higher in low UO_2 composition range (<13 wt.%). Similarly, MD calculated and laser-flash measured thermal conductivity values indicate that incorporation of UO_2 in ThO_2 (by 6 wt.%) reduces thermal conductivity values in the 0.5-1.1 $\text{Wm}^{-1}\text{K}^{-1}$ range for the 873-1873 K temperature interval compared to ThO_2 . These values are of immense interest for fuel designers of AHWR-LEU.

Chapter 9

Conclusions and Future Scopes

The focus of this thesis can, therefore, be divided into two areas. One that aimed to improve the understanding of detailed atomistic mechanism of phase transformations of displacive, mixed-mode (replacive-cum-displacive), superionic nature and melting in pure Zr, Zr₂Al-Nb alloys and ThO₂ based mixed oxides. Second that aimed to determine basic thermal properties (enthalpy, density, thermal expansion, thermal conductivity, melting temperatures) of ThO₂ based mixed oxides.

9.1 Summary of Results and Conclusions

9.1.1 Phase Transformation Pathways

This study presents a systematic theoretical investigation to determine most energetically favorable atomistic transformation pathways (TP's) for $\alpha \rightarrow \omega$ transformation in pure Zr. Our first-principles study finds direct $\alpha \rightarrow \omega$ TP proposed by SG has a C2/c common space group along the TP and lowest enthalpy barrier (of 22 meV/atom at 0 K) compared to other TP's. The lowest barrier pathway is a suitable combination of small strains and relative atomic shuffle compared to the nearest neighbor distances, an essential criterion for diffusionless displacive transformation. Our calculations also show that phase transformation is associated with softening of the shear elastic constant (C_{44}) and Γ point transverse optical phonon frequency (E_{2g}) with pressure. Application of pressure in α Zr changes the effective potential landscape for the E_{2g} phonon at Γ point of the Brillouin zone. It is also found that topological change in band structure around special k-point 'M' is a precursor to this transformation.

In mixed-mode transformations displacive part is intimately connected with

diffusive part. In Zr_2Al , Zr_3Al_2Nb and Zr_4AlNb alloys, mixed-mode phase transformation pave the path to form chemically ordered ω phase. Here, the disordered bcc lattice (β) is transformed into the hexagonal ω -structure by a periodic displacement of lattice planes while the decoration of the ω -lattice by different atomic species occurs through diffusional atom movements. In this study, the quantitative determination of thermodynamic tendencies for diffusive *vis-a-vis* displacive processes at different stages of the transformation delineates the actual pathway on the free energy surface. In this thesis, ab-initio estimation of formation energies of chemically disordered and ordered Zr_2Al , Zr_3Al_2Nb and Zr_4AlNb alloys shows that ω like collapse (displacive part) is not energetically favorable for chemically disordered β phase at these compositions. DFT calculated ground state energy suggested that for the ω like collapse to occur, a certain degree of chemical ordering is a prerequisite. Moreover, mechanical stability analysis predicts both ω - Zr_3Al_2Nb and $B8_2$ - Zr_2Al are mechanically stable phases with very poor ductility properties. But degree of directional bonding in $B8_2$ - Zr_2Al is higher and it reduces with addition of Nb in ω - Zr_3Al_2Nb . In contrast, being mechanically stable and having less pronounced directional bonding makes ω - Zr_4AlNb ductile. It is also established that, an interplay between relative number of Zr-Al, Zr-Nb and Nb-Al bonds promotes formation of ω phase in these alloys.

The “superionic transitions” is characterized by the rapid diffusion of a significant fraction of one of the constituent species (oxygen for ThO_2) within an essentially rigid framework formed by the other species. A combined first-principles and classical molecular dynamics (MD) simulations were used to investigate “superionic” transition in ThO_2 . Our GGA, LDA+ U and MD calculated ground state properties of ThO_2 agree well with experimental and previous theoretical calculations. Phonon dispersion curves along symmetry directions, calculated using first principles approaches, are in good agreement with reported experimental data at room temperature. With increasing dilational lattice strain (ϵ), GGA and LDA+ U calculated B_{1u} and E_u phonon mode frequencies soften at the X point. These decrease nonlinearly so that the B_{1u} mode frequencies become smaller compared to E_u mode frequencies in the range $0.05 > \epsilon > 0.04$. This is associated with sharp increase in the narrow peak of the phonon density of states when the B_{1u} and E_u modes cross each other (or are about to cross) at the X point. With further increase of temperature, B_{1u} phonon mode continues to soften and become imaginary at a temperature of 3430 K (below melting temperature of ~ 3600 K). Moreover, the calculated diffusion barriers indicate that $\langle 001 \rangle$ is the easy direction for anion migration in superionic state. The calculated temperature variation of single crystal

elastic constants show the fluorite phase of ThO_2 remains elastically stable up to the superionic regime, though the B_{1u} phonon mode is imaginary in that state. This leads to anionic disorder in the elevated temperature. Tracking of anion positions in the superionic state as a function of time suggests a hopping model in which the oxygen ions migrate from one tetrahedral site to another.

Classical MD calculated melting temperatures (MT) of ThO_2 , UO_2 and PuO_2 are in good agreement with previously reported experimental data. The MD calculated change in enthalpy ($H(T)-H(300\text{ K})$) values of defect-free UO_2 upon heating match very well upto 2000 K. The underestimation of values from 2000 K to melting can be attributed to the Schottky defects and contribution from the electronic defects, which is not taken into account explicitly in these MD simulations. Enthalpy of fusion values for ThO_2 , UO_2 and PuO_2 are calculated from the width of the enthalpy discontinuity and calculated values are lower than experimental values as the lattice and electronic defect contribution to the enthalpy is not taken into account in our one-phase simulations. The MD calculated MT of $(\text{Th,U})\text{O}_2$ and $(\text{Th,Pu})\text{O}_2$ MOX show good agreement with the ideal solidus line in the Th rich part of the phase diagram. The ideal solidus line is, however, underestimated by ~ 50 K for $(\text{Th,U})\text{O}_2$ in the UO_2 rich parts of the phase diagram. Importantly, our study would be consistent with a minima occurring around 5 atom% of ThO_2 in the high temperature phase diagram of $(\text{Th,Pu})\text{O}_2$ MOX. Equations were developed and fitted to the MD data that were able to describe enthalpy increment and density variation of solid and liquid phases of $(\text{Th}_{1-x}\text{Pu}_x)\text{O}_2$ and $(\text{Th}_{1-x}\text{U}_x)\text{O}_2$ MOX from 300 to 6000 K. These values are of importance for AHWR fuel design, performance modeling and safety analysis.

Hence, the work presented here contributes to a clearer understanding of actual atomistic pathways which are operative in displacive, diffusive *vis-a-vis* displacive, superionic and melting type phase transformations. This study also elaborates the associated change in physical and thermal properties accompanying the phase transformations.

9.1.2 Thermodynamic Parameters of ThO_2 based MOX

Present study adopts a two-pronged theoretical and experimental approach to determine thermal expansion and thermal conductivity (TC, κ) of $\text{Th}_{1-x}\text{Ce}_x\text{O}_2$, $\text{Th}_{1-x}\text{Pu}_x\text{O}_2$ and $\text{Th}_{1-x}\text{U}_x\text{O}_2$ MOX as a function of temperature.

The TC decreases with the increase of CeO_2 concentration and the decrease in TC at 500 K is larger than that at 1500 K. At higher temperatures (above 900

K), the TC of (Th,Ce)O₂ MOX is almost independent of the concentration of CeO₂. Our MD calculated κ values of ThO₂ overestimates (within 2-0.3 Wm⁻¹K⁻¹ range) experimentally reported values by Cozzo *et al.* [142] in the 500-1573 K temperature range but matches well (within 1-0.1 Wm⁻¹K⁻¹ range) with our experimentally determined values. MD calculated κ values of Th_{0.9375}Ce_{0.0625}O₂ and Th_{0.875}Ce_{0.125}O₂ also are in good agreement (within 1-0.1 Wm⁻¹K⁻¹ range) with ThO₂-3%PuO₂ and ThO₂-8%PuO₂ values, respectively, reported by Cozzo *et al.* [142]. Our combined MD simulations and dilatometry measurements indicate that incorporation of PuO₂ in ThO₂ systematically increases coefficient of thermal expansion. Similarly, MD calculated and laser-flash measured TC values indicate that incorporation of PuO₂ in ThO₂ (by 6 wt.%) reduces TC values in the 0.6-1.2 Wm⁻¹K⁻¹ range for the 973-1613 K temperature interval compared to ThO₂.

It is important, therefore, to consider the temperature range over which the fuel will be operated in the AHWR. The average operating temperature of AHWR is 700-800 K at the periphery of the pellet and the center line temperature is around 900-1000 K. Our MD calculated results show that the TC of Th_{0.9375}Pu_{0.0625}O₂ exhibits a reduction in the range of 21-13% relative to that of pure ThO₂ in the 700-1000 K temperature interval. For higher temperature reactors, such as the Advanced gas-cooled reactor (AGR), where the temperature at the periphery of the fuel pellet may reach 900-1000 K, the TC of Th_{0.9375}Pu_{0.0625}O₂ is found to be 20% lower than that of ThO₂. Also, at the peak center line temperature of about 1650 K, the degradation of TC of Th_{0.9375}Pu_{0.0625}O₂ is about 14% relative to pure ThO₂. Our laser-flash measured TC showed a decrease of 26% and 20% compared to pure ThO₂ at 973 K and 1613 K, respectively.

Coefficient of thermal expansion (CTE) has been measured for (Th,U)O₂ MOX (with 0, 6, 13, 25 and 30 wt.% UO₂) by high temperature XRD in the 293-1273 K temperature range and this experimental study is extended by calculating CTE in the 300-3000 K temperature range using classical MD simulations. Our combined MD simulations and HT-XRD measurements indicate that incorporation of UO₂ in ThO₂ systematically increases CTE but the rate of increase is higher in low UO₂ composition range (<13 wt.%). Similarly, MD calculated and laser-flash measured TC values indicate that incorporation of UO₂ in ThO₂ (by 6 wt.%) reduces TC values in the 0.5-1.1 Wm⁻¹K⁻¹ range for the 873-1873 K temperature interval compared to pure ThO₂. These values are of immense interest for fuel designers of AHWR. MD calculated thermal property values of ThO₂ and (Th,U)O₂ MOX essentially reproduce experimentally determined values without taking into account effects like, porosity, inhomogeneity, *etc.*. Using this state-of-the-art MD simulation

methodology thermal properties of ThO_2 and $(\text{Th,U})\text{O}_2$ MOX can be predicted over a wide temperature and composition range.

The thermal conductivity of the ThO_2 rich $(\text{Th}_{1-x}\text{Ce}_x)\text{O}_2$, $(\text{Th}_{1-x}\text{Pu}_x)\text{O}_2$ and $(\text{Th}_{1-x}\text{U}_x)\text{O}_2$ solid solutions was found to be highly non linear as a function of composition. Deviations from the perfect end member compositions introduced phonon scattering due to the non-uniform cation sub-lattice, thereby reducing the phonon mean free path and the thermal conductivity of the system. The concentration and scattering strength of defects governs the extent to which the phonon mean free path is reduced. The degradation of thermal conductivity was more significant for $(\text{Th}_{1-x}\text{Ce}_x)\text{O}_2$ than for $(\text{Th}_{1-x}\text{Pu}_x)\text{O}_2$ and $(\text{Th}_{1-x}\text{U}_x)\text{O}_2$ due to the large lattice parameter mismatch of the end members. Equations were developed and fitted to the MD data that were able to describe $(\text{Th}_{1-x}\text{Ce}_x)\text{O}_2$, $(\text{Th}_{1-x}\text{Pu}_x)\text{O}_2$ and $(\text{Th}_{1-x}\text{U}_x)\text{O}_2$ thermal conductivity from 300 to 2000 K in a composition range which is of importance for AHWR fuels. Understanding how differing cation sizes alters thermal conductivity in these systems is useful for the development of mixed oxide fuels. However, as the breeding of U^{233} from Th^{232} is the primary reason for incorporating Th into the fuel cycle, the fuel conductivity would be expected to degrade as transmutation proceeds. Being able to predict the rate and extent of this degradation would be useful to aid in optimizing fuel core performance.

9.2 Limitations and Future Scope of this work

An atomistic model of the phase transformation provides an clear picture of the transformations irrespective of the mechanism involved in the transformation (displacive, replacive-displacive and superionic). In this study, the energies of the intermediate structures that arises during phase transformations (displacive and/or diffusive type) are calculated using the first-principles calculations and hence the energies are calculated at 0 K. The transformations are experimentally observed at high temperatures. The vibrational entropy effects are not included in the calculation of PT energy landscapes. So this study captures inherent chemical and thermodynamical tendencies in a displacive and replacive-displacive PT. It is expected that thermal entropy is going to alter PT energy landscape and this study does not give any estimation for that. Although, the study of superionic transition in ThO_2 considers thermal expansion effect indirectly by performing series of phonon calculations at elongated lattice parameters.

Experimentally prepared $(\text{Th,U})\text{O}_2$ and $(\text{Th,Pu})\text{O}_2$ MOX pellets always con-

tain certain amount of porosity, non-stoichiometry, grain-boundaries and certain amount of inhomogeneous distribution of UO_2 and PuO_2 in ThO_2 matrix. MD simulation methodologies adopted in this thesis to study thermal properties does not account for any of these effects explicitly. Although, porosity effects are considered in the MD calculated thermal conductivity values by Maxwell-Eucken equation.

Even though, the MD interatomic potential developed for ThO_2 and CeO_2 works reasonably well to predict thermal expansion and thermal conductivity values in the 300-2000 K range, the melting temperature is overestimated. These potential set need further refinement to include very high temperature behavior.

This study can be treated as a template to systematically find an atomistic pathway, verifying it and applying it to calculation of transformation barrier. Applying this approach to the understanding of other displacive and/or diffusional transformation in element or alloys, has great potential to expand the boundaries of both physics and materials science. Moreover, clear understanding of phase transformation pathway enables us to go a step forward by predicting change in phase transformation behavior due to impurities and/or alloying. Mapping competing phases and the associated phase transformation with pressure, temperature and impurities can provide predictive design for improved control of alloy properties.

The metastability of the high pressure transformation in Zr (Fig. 4.4) is clearly seen by the decrease of the activation barrier with increasing pressure. Low pressure transformations are thermally inhibited by an activation energy. Moreover, the transient bcc phase has not been seen in equilibrium experiments. Experimental works on Zr or Zr-2.5%Nb alloy by Perez-Prado *et al.* [299,300] does see the β phase at lower pressure and this observation is supported by the non-uniform (shear) stress applied to the sample [301]. More detailed theoretical works on pathway under shear stress and experiments at high hydrostatic pressure are needed to further understand the metastability.

This work was undertaken to partially fulfill the objective of determining phase equilibrium in actinide MOX systems that is initially required to start the fission chain reaction. The chemical compositions of the actinide MOX will definitely be changed during the “burn-up” process in the reactors and initial actinides (Th, U and Pu) will transmute to minor actinides such as Np, Am and Cm. The results of this work are important in understanding phase equilibrium in the $(\text{Th,U})\text{O}_2$ and $(\text{Th,Pu})\text{O}_2$ MOX, which provides phase stability information at a particular point in the temperature-composition space. However, as mentioned above, the nuclear fuels being developed are multi-component alloys (or MOX), and under irradiation, they transmute to minor actinide elements, which opens up a range of possibilities

of MOX formation during this process. Thus, it becomes important to integrate the thermodynamic results obtained from this study, for other binary MOX to obtain phase equilibrium in ternary or multi-component systems, such as (Th,U,Np)O₂, (Th,U,Am)O₂, (Th,Pu,Np)O₂, (Th,Pu,Am)O₂, *etc.*.

According to previous high temperature melting experiments [102, 104, 110, 121, 123], low additions of ThO₂ to UO₂ result in a slight decrease of the solidification temperature and this behavior would be consistent with a minimum at 3098 K around a composition of 5 mol.% ThO₂. The solid/liquid transition temperature was thereafter observed to increase with increasing ThO₂ fraction. At high temperatures UO₂ can accommodate in the fcc lattice both oxygen interstitials and vacancies over a wide stoichiometry range (at least, $1.5 \leq O/U \leq 2.25$). The variations of the melting point with stoichiometry are expected in conjunction with the appearance of an oxygen solubility gap when solid solutions UO_{2±x} are melted [275]. The minimum in the uranium rich side of ThO₂-UO₂ phase diagram is an overall outcome of the abrupt increase of specific heat due to formation of Frankel pairs and order-disorder pre-melting transitions, non-stoichiometry effect *etc.*. Incorporation of all these effects in the current state of the MD simulation methodologies is difficult. Two-phase simulations employed in this study to calculate melting temperature of ThO₂, UO₂ and MOX indirectly incorporate the effect of lattice defects (mostly Frankel defects). Non-stoichiometry effect requires U⁺³-O and U⁺⁵-O interactions to be incorporated in the potential data set efficiently. This will allow us to predict the melting temperature variation as a function of non-stoichiometry. Similar behavior can also be studied for (Pu,Th)O₂ MOX.

Understanding thermal property changes of nuclear fuels under extreme radiation conditions will provide actual performance of the fuel in the operating stage and this has been a subject of great interests for decades in UO₂ based fuels [119, 302–305]. On the contrary less attention has been paid to ThO₂ based fuels. In order to improve the modeling capability to predict fuel performance, effect of micro-structural changes on phonon and thermal carrier transport within domains and at grain boundaries of ThO₂ need to be studied separately. Therefore, thermal property changes of ThO₂ having different boundary-to-volume ratios can be appropriately modeled as a function of burnup levels. It is well known that interfacial resistance of grain boundaries dramatically influences thermal conductivity of polycrystalline solids [306]. Therefore, this study can be extended further to calculate thermal conductivity of ThO₂ based fuels in the presence of grain boundaries and radiation related defects.

Appendices

Appendix A

Superionic Transition in ThO_2

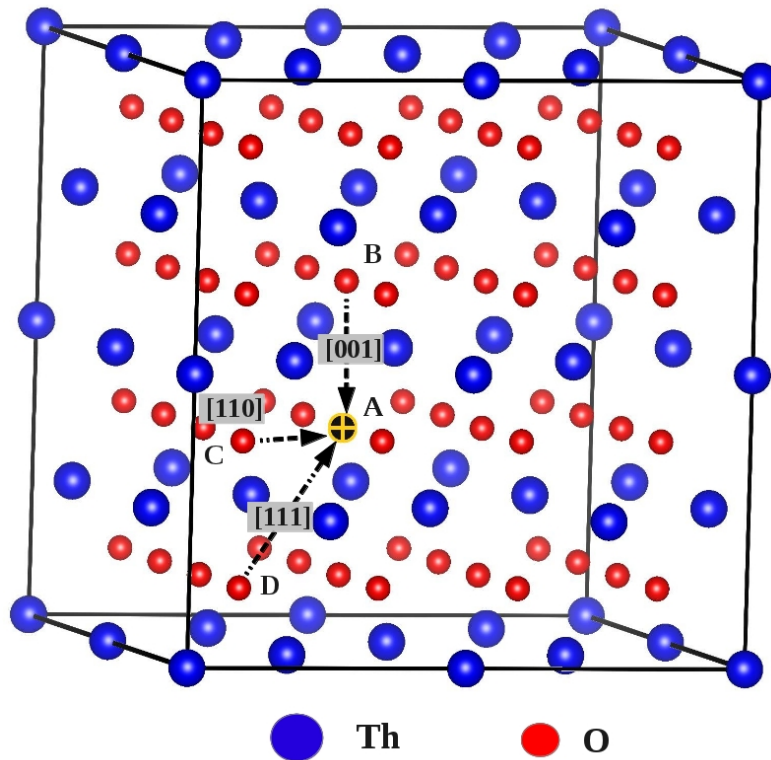


Figure A.1: Illustration of oxygen migration directions towards a vacant oxygen site A (black atom) in a $2 \times 2 \times 2$ supercell (96 atoms). Atoms B, C and D migrate to position A along $[001]$, $[110]$ and $[111]$ directions, respectively. This supercell is taken only to show 3 migration direction and actual calculation was performed in a $10 \times 10 \times 10$ supercell (12000 atoms).

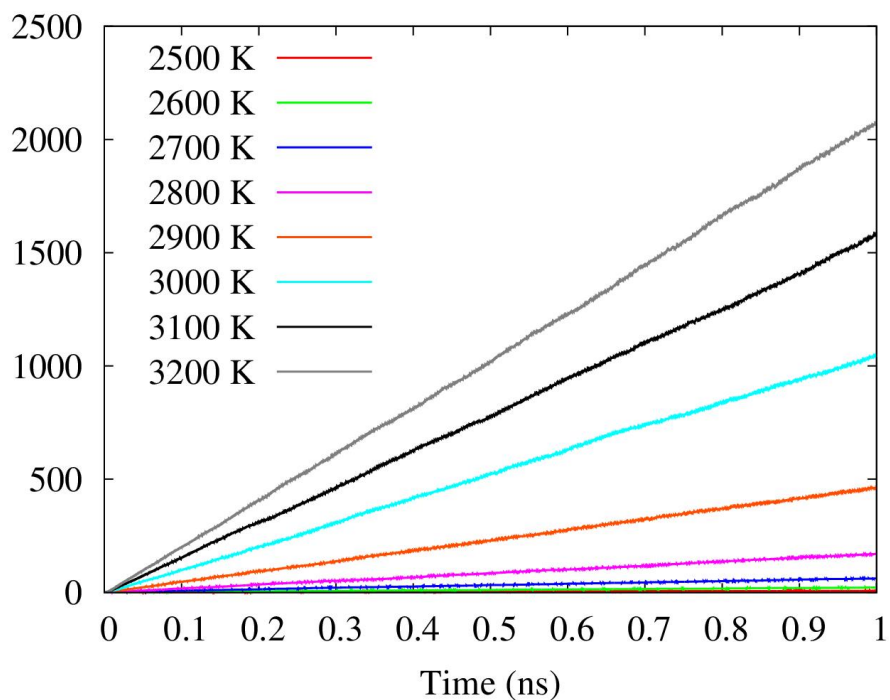


Figure A.2: MD calculated MSD curve for oxygen between 2500 K and 3200 K (100 K interval). Superionic transition is visible above 2900 K.

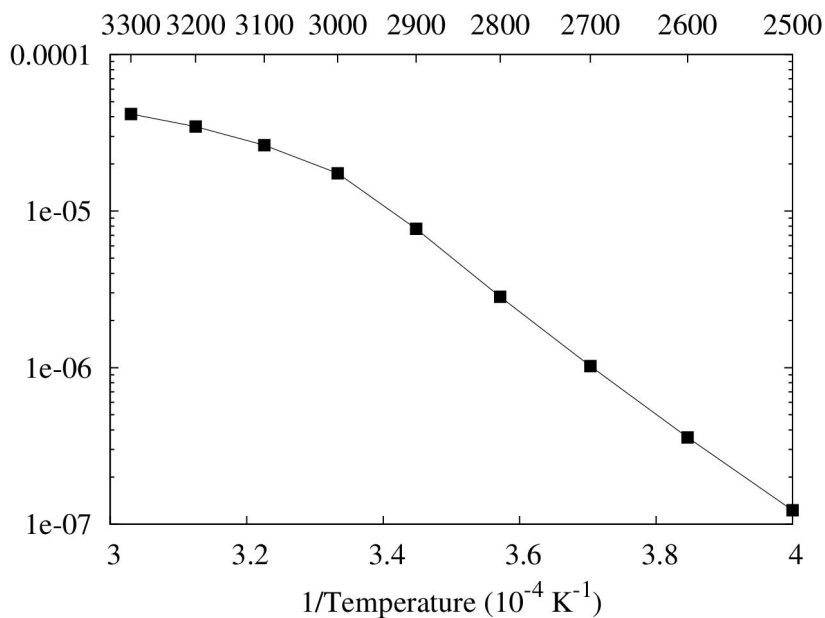


Figure A.3: MD calculated diffusivity plot for oxygen between 2500 K and 3300 K (100 K interval). The jump in the diffusivity value appears at 3000 K and above.

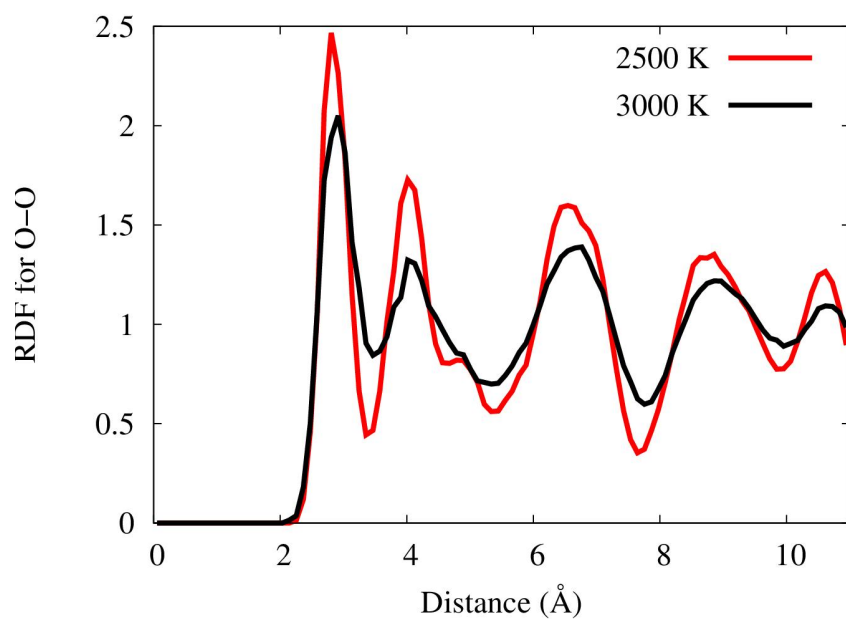


Figure A.4: MD calculated RDF plot for O-O pair at 2500 K and 3000 K. Below the fast ionic regime, simulated at 2500 K, RDF of O-O show succession of well-defined peaks, while in the fast ionic regime O-O RDF peaks are less-well defined from 2nd nearest neighbours onwards. This indicates a diffuse O sub-lattice because of intensive ionic motion.

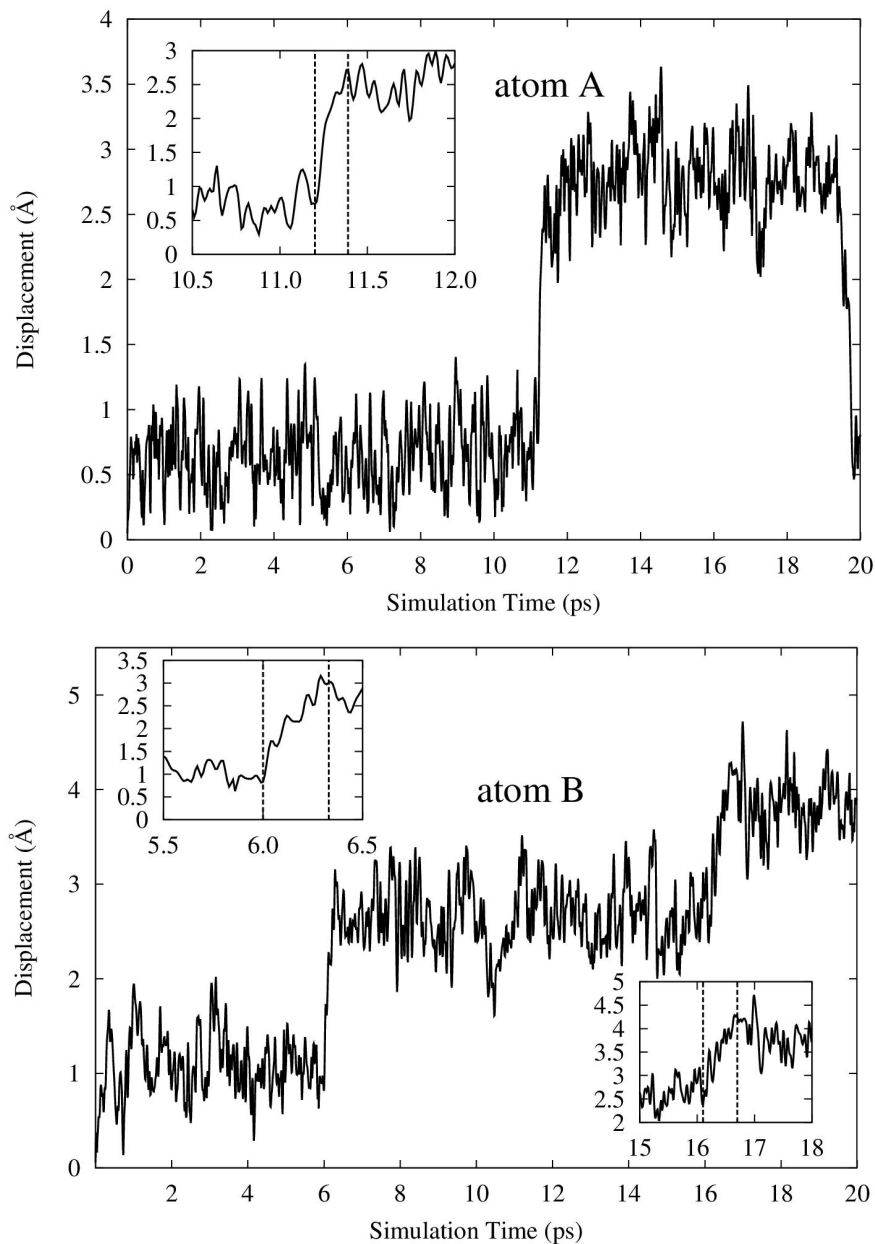


Figure A.5: MD calculated total displacement ($\sqrt{(dx^2 + dy^2 + dz^2)}$) from equilibrium position is plotted as a function of simulation time for atom A (upper panel) and atom B (lower panel) at 3000 K temperature. Inset figures show simulation time corresponding to which anionic transition occurs from one tetrahedral position to the other.

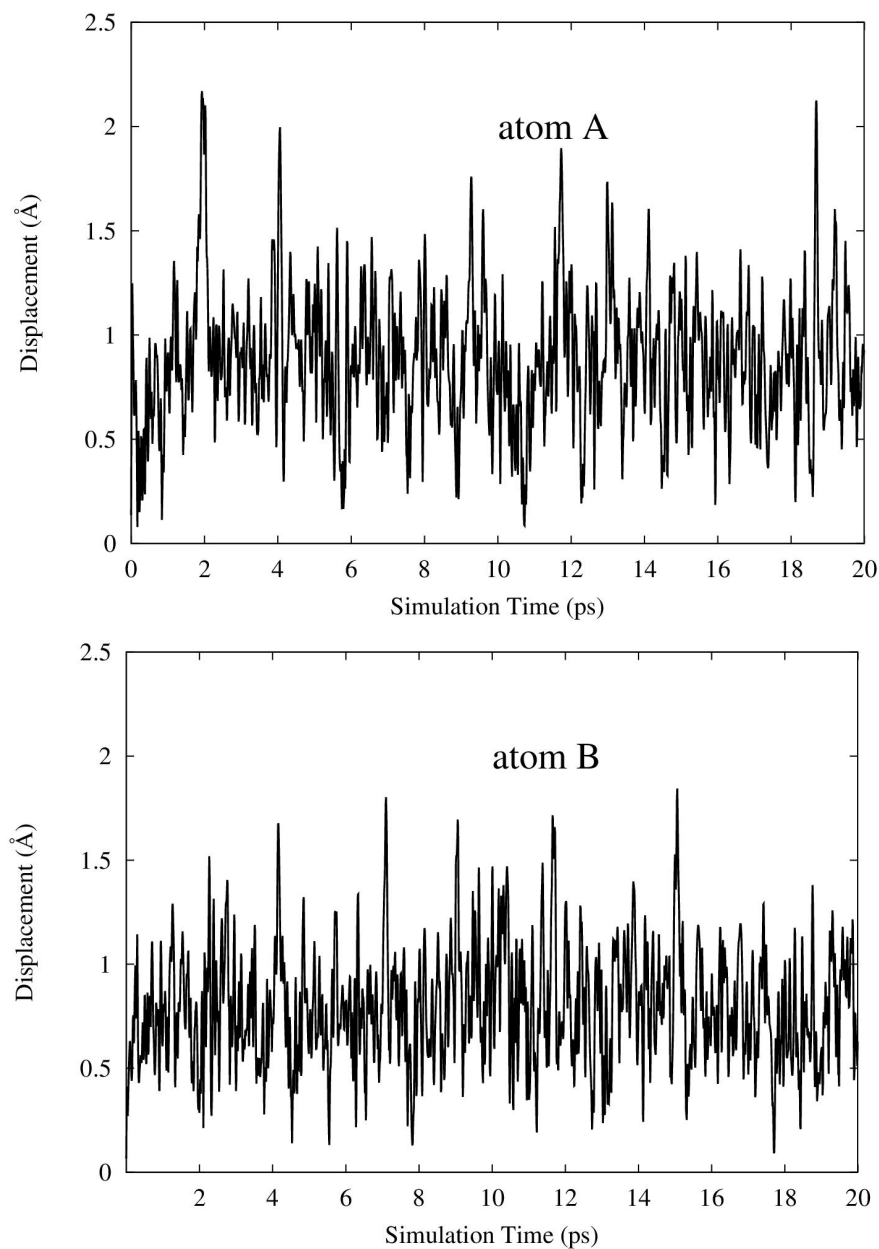


Figure A.6: MD calculated total displacement ($\sqrt{(dx^2 + dy^2 + dz^2)}$) from equilibrium position is plotted as a function of simulation time for atom A (upper panel) and atom B (lower panel) at 2900 K temperature. Inset figures show simulation time corresponding to which anionic transition occurs from one tetrahedral position to the other.

Appendix B

Thermal Properties of (Th,Ce)O₂ MOX

B.1 Determination of Buckingham-type (Th,Ce)O₂ MOX Interatomic Potentials

The MD calculations of thermal expansion and thermal conductivity of (Th,Ce)O₂ MOX were performed using Buckingham (Buck) and Buckingham-Morse-manybody (BMM) potential models. A description of the BMM potential model is given in section 7.2.2. A description to determine potential parameters of Buck potential model is given below.

In order to determine the interatomic potential functions for ThO₂ and CeO₂, we applied Born model of ionic solid, where the ions within the system are considered to be a series of charged interacting particle with a partial ionic charge. In this model, an effective ionicity, Z_{α}^{eff} is introduced to replace the formal charges of the ions with effective charges, $q_{\alpha} = Z_{\alpha}^{eff}|e|$. The pair interaction potential of two particles i and j, separated by r_{ij} in this system consists of long-range Coulomb and short range Buckingham type repulsive contributions:

$$\phi_{\alpha\beta}(r_{ij}) = \frac{q_{\alpha}q_{\beta}}{4\pi\epsilon_0 r_{ij}} + A_{\alpha\beta} \exp\left(-\frac{r_{ij}}{b_{\alpha\beta}}\right) - \frac{C_{\alpha\beta}}{r_{ij}^6} \quad (\text{B.1})$$

where α and β are used to label the species of atom i and j, respectively. $A_{\alpha\beta}$, $b_{\alpha\beta}$ and $C_{\alpha\beta}$ are empirical parameters that describes Buckingham potentials between atom i and j. An ionic bonding of 67.5% is assumed for each ion in the present study, *i.e.*, $Z_{\alpha}^{eff} = 2.7$ for the tetravalent cations and $Z_{\alpha}^{eff} = -1.35$ for the

oxygen anions. The potential parameters of O^{2-} were obtained from the earlier work [147, 289]. Firstly, we determined the potential parameters of Th^{4+} ions to reduce the difference between calculated and measured properties (*i.e.*, thermal expansion and bulk modulus). The thermal expansion of ThO_2 with a fluorite structure had been measured in several studies [6, 127, 130, 140, 141]. In addition, the bulk modulus was also experimentally estimated to be 198 GPa [259]. Figure B.1 (a) shows that the thermal expansion as obtained from our MD calculations is in good agreement with the literature data. The volume-pressure relationships of ThO_2 are shown in Figure B.1(b). The bulk modulus obtained from our MD calculations was estimated to be 216 GPa using a third order polynomial equation of state.

Secondly, the potential parameters of Ce^{4+} ions were determined based on the experimental thermal expansion [140] and the bulk modulus [307] in the same way as those of Th^{4+} ions. The thermal expansion and volume-pressure relationship calculated using the optimized potential parameters of Ce^{4+} are shown in Figure B.2 (a and b), respectively. The calculated thermal expansion is a little larger than the literature data at high temperatures [140]. On the other hand, the calculated bulk modulus of 208 GPa, is slightly larger than the experimental value of 204 GPa [307]. In general, to further improve the reproducibility of mechanical properties, the interatomic potential function with a high flexibility, *e.g.*, by including the Morse term, should be provided. But in the present study, we show that our potential model is sufficient to reproduce thermal properties of ThO_2 , CeO_2 and $(Th,Ce)O_2$ MOX from room temperature to 1750 K. The potential parameters thus obtained for Th^{4+} and Ce^{4+} ions as well as oxygen ions are summarized in Table B.1.

Table B.1: Parameters of the pair-wise interactions described by equation B.1.

Interaction Type	A (eV)	b (\AA)	C (eV \AA^6)
Th-O	26300	0.224857	12.8
Ce-O	7390	0.250	12.8
O-O	919.17	0.332	17.36

The reliability of the generated potential parameters can be cross checked by systematic study of phase stability of ThO_2 and CeO_2 . Phase stability is a crucial issue for the simulation of nuclear fuel materials as they are subjected to high temperature and pressure during applications. We studied ground state phase stability of ThO_2 and CeO_2 in a variety of AB_2 structures at zero pressure and temperature. The different phases considered are fluorite (cubic, space group: $Fm\bar{3}m$

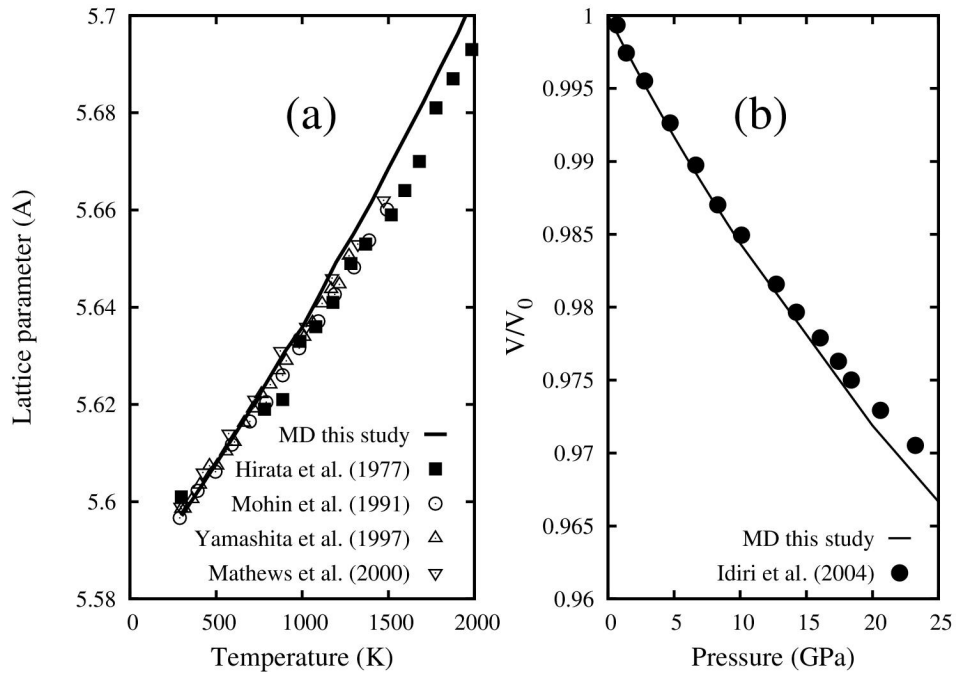


Figure B.1: Calculated (a) Thermal expansion and (b) isothermal compressibility of ThO_2 is compared with available experimental data in the literature [130, 141, 259, 296, 297].

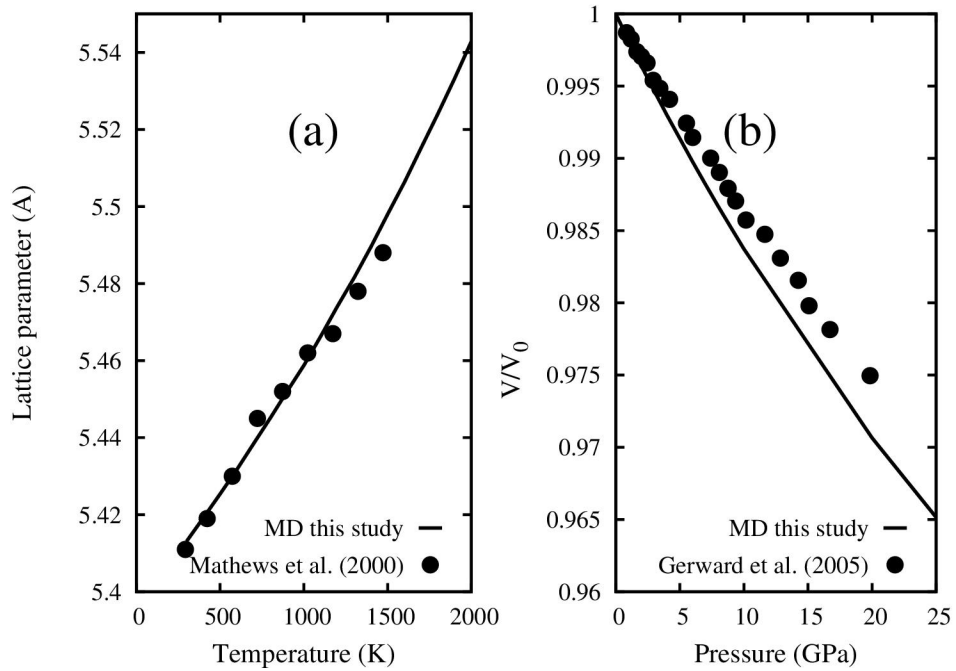


Figure B.2: Calculated (a) Thermal expansion and (b) isothermal compressibility of CeO_2 is compared with available experimental data in the literature [141, 307].

(225)), anatase (tetragonal, space group: $I4_1/amd$ (141)), rutile (tetragonal, space group: $P4/2mnm$ (136)), pyrite (cubic, space group: $Fm\bar{3}m$ (205)), cotunnite

Table B.2: Relative lattice energies of different AB_2 polymorphs with respect to fluorite structure calculated from our interaction parameters for ThO_2 and CeO_2 in eV/atom. ‘F’ indicates the structures optimized to the same energy as the fluorite structure.

Structure	Fluorite	Anatase	Rutile	Pyrite	Cotunnite	Coulombite	Brookite
ThO_2	0.0	0.205	0.158	F	0.669	0.488	0.176
CeO_2	0.0	0.065	0.017	F	0.477	0.381	0.409

(orthorhombic, space group: $Pnma$ (62)), columbite (orthorhombic, space group: $Pbcn$ (60)) and brookite (orthorhombic, space group: $Pbca$ (61)). Table B.2 reports the calculated phase stability (with respect to fluorite phase) of ThO_2 and CeO_2 with our determined potential parameters. A positive value of the relative energy indicates the structure to be less favorable than fluorite. Our determined potential parameters correctly predict the fluorite structure to be the ground state structure. In these calculations, the pyrite phase was found to have the same energy as that of the fluorite phase (Table B.2).

B.2 Thermal Expansion

The MD calculated average lattice parameters ($a(T)$) of ThO_2 , $Th_{1-x}Ce_xO_2$ ($x = 0.0625$ and 0.125) are plotted as a function of temperature (300-3000 K range) in Figure B.3. The HT-XRD studies of ThO_2 and $Th_{1-x}Ce_xO_2$ MOX are also shown in the figure. The calculated $a(T)$ for $Th_{0.9375}Ce_{0.0625}O_2$ matches well with experimentally measured polycrystalline $a(T)$ for $Th_{0.96}Ce_{0.04}O_2$ and $Th_{0.92}Ce_{0.08}O_2$ MOX in the temperature range of 300-1500 K. It can be seen that the calculated $a(T)$ for ThO_2 is also matching well with experimental measurements in the same temperature range. The calculated decrease in lattice parameter as a function of Ce^{4+} concentration can be attributed to small ionic radii of Ce^{4+} compared to Th^{4+} in eight-fold coordination. Therefore, the generated potential parameters as well as SQS models are not only capable of predicting exact behavior of $a(T)$ for ThO_2 , but also can efficiently estimate $a(T)$ for small CeO_2 doping in ThO_2 matrix. We extended our study by estimating $a(T)$ for ThO_2 , $Th_{0.9375}Ce_{0.0625}O_2$ and $Th_{0.875}Ce_{0.125}O_2$ in the temperature range of 300-3000 K. This allowed useful predictions to be made, both at operating temperatures and at extreme temperatures approaching the melting point in reference to reactor fuel applications.

In order to further analyze the thermal expansion behavior of ThO_2 and $Th_{1-x}Ce_xO_2$ MOX, the MD calculated and experimentally measured thermal ex-

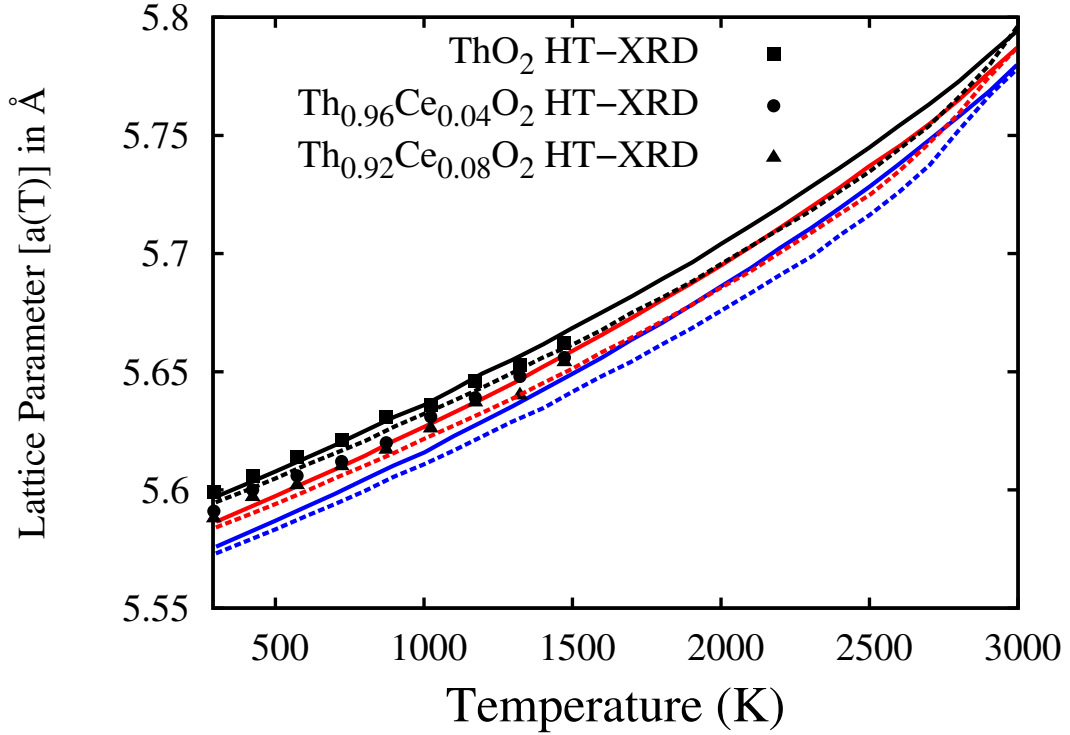


Figure B.3: MD calculated (using Buck (solid line) and BMM (dotted line) model) unit cell dimension of pure ThO_2 , $\text{Th}_{0.9375}\text{Ce}_{0.0625}\text{O}_2$ and $\text{Th}_{0.875}\text{Ce}_{0.125}\text{O}_2$ MOX in the 300-3000 K temperature range is compared with HT-XRD data [141]. The lattice parameters are calculated from 300-3000 K in 100 K interval. Black, red and blue lines are for ThO_2 , $\text{Th}_{0.9375}\text{Ce}_{0.0625}\text{O}_2$ and $\text{Th}_{0.875}\text{Ce}_{0.125}\text{O}_2$ MOX, respectively.

pansion coefficients (α) are listed in Table B.3 along with experimental data. Thermal expansion of ThO_2 and ThO_2 -5 and 8 wt% CeO_2 pellets (POP and CAP pellets) have been measured using a dilatometer. In all previous experimental studies, the mixed oxide pellets were generally prepared by the conventional powder metallurgy route of powder processing and pelletization (POP) technique to perform laboratory scale experiments. A Coated Agglomerate Pelletization (CAP) process, with certain added advantage over conventional powder metallurgy route [126, 135], can be implemented directly in making MOX fuel pellets to be later used in AHWR operated in India and other countries. Details of the pellet preparations and characterizations are described in **Appendix C**.

The numerical value of MD calculated α is always greater than the experimentally measured α values. This can be attributed to the fact that our MD calculations are performed on a model system with homogeneous distribution of CeO_2 in ThO_2 matrix and with no incorporation of porosity, impurity effects, *etc.*. In con-

Table B.3: MD Calculated and experimentally measured thermal expansion coefficients of ThO_2 and $(\text{Th,Ce})\text{O}_2$ MOX are compared with available experimental data in the literature. ThO_2 -5wt% CeO_2 and ThO_2 -8wt% CeO_2 corresponds to compositions $\text{Th}_{0.9253}\text{Ce}_{0.0747}\text{O}_2$ and $\text{Th}_{0.8823}\text{Ce}_{0.1177}\text{O}_2$, respectively. The Buckingham (Buck) and Buckingham-Morese-manybody (BMM) models correspond to the potential model employed in those calculations

Thermal Expansion Coefficients α (10^{-6} K^{-1})	Remarks
ThO_2	
10.61 (300-1800 K)	MD present study, Buck model
10.29 (300-1800 K)	MD present study, BMM model
9.99 (300-1450 K)	Dilatometry, present study, ThO_2
9.04 (293-1123 K)	Dilatometry, 96% TD [141]
9.54 (293-1173 K)	HT XRD [141]
$\text{Th}_{0.9375}\text{Ce}_{0.0625}\text{O}_2$ MOX	
10.78 (300-1800 K)	MD present study, Buck model
10.42 (300-1800 K)	MD present study, BMM model
10.56 (873-1773 K)	Dilatometry, CAP, ThO_2 -5wt% CeO_2 (Air)
10.35 (873-1773 K)	Dilatometry, POP, ThO_2 -5wt% CeO_2 (Air)
10.65 (873-1773 K)	Dilatometry, CAP, ThO_2 -5wt% CeO_2 (Ar- H_2)
10.44 (873-1773 K)	Dilatometry, POP, ThO_2 -5wt% CeO_2 (Ar- H_2)
9.35 (293-1123 K)	$\text{Th}_{0.96}\text{Ce}_{0.04}\text{O}_2$, Dilatometry, 83% TD [141]
9.76 (293-1173 K)	$\text{Th}_{0.96}\text{Ce}_{0.04}\text{O}_2$, HT XRD [141]
9.49 (293-1123 K)	$\text{Th}_{0.92}\text{Ce}_{0.08}\text{O}_2$, Dilatometry, 83% TD [141]
9.96 (293-1173 K)	$\text{Th}_{0.92}\text{Ce}_{0.08}\text{O}_2$, HT XRD [141]
$\text{Th}_{0.875}\text{Ce}_{0.125}\text{O}_2$ MOX	
10.93 (300-1800 K)	MD present study, Buck model
10.57 (300-1800 K)	MD present study, BMM model
10.69 (300-1773 K)	Dilatometry, CAP, present study, ThO_2 -8wt% CeO_2
10.50 (300-1773 K)	Dilatometry, POP, present study, ThO_2 -8wt% CeO_2
9.50 (293-1123 K)	$\text{Th}_{0.9}\text{Ce}_{0.1}\text{O}_2$, Dilatometry, 85% TD [140]

trast, the experimental samples are not devoid of these effects where some part of the lattice thermal expansion may be accommodated in the porosity of the samples. Nuclear fuel designers need thermal expansion data generated by dilatometer for estimating the fuel clad gap during fuel operating conditions under normal and hot spot conditions. Experimental studies using dilatometer indicated that the thermal expansion coefficient of $(\text{Th,Ce})\text{O}_2$ increases with an increasing CeO_2 content due

to higher thermal expansion coefficient of CeO_2 arising from its lower melting point compared to that of ThO_2 .

B.3 Thermal Conductivity

The lattice thermal conductivity of ThO_2 was calculated using a supercell comprising $8 \times 8 \times 8$ fluorite unit cells using Green-Kubo formalism. In Figure B.4, the normalized HCACF $C_{xx}(t)$ is presented for ThO_2 at $T = 500$ K and 1500 K. Analogous result can be obtained for $C_{yy}(t)$ and $C_{zz}(t)$. A distinctive feature of these curves is their rapid and regular oscillation around $t = 0$ ps and the amplitude is getting smaller gradually with the elapsed time. This kind of oscillatory behavior is usual in these ceramic oxides [289]. This figure also shows that the amplitude of HCCF for 500 K is larger than that for 1500 K. In addition, the relaxation time of the correlation between $J(t)$ and $J(0)$ is longer at the lower temperature. In the present study, the thermal conductivity was considered to be the value when the amplitude of fluctuation of the normalized HCCF became almost zero for every temperature. Similarly, normalized HCCF is presented for CeO_2 at $T = 500$ K and 1500 K in Figure B.5

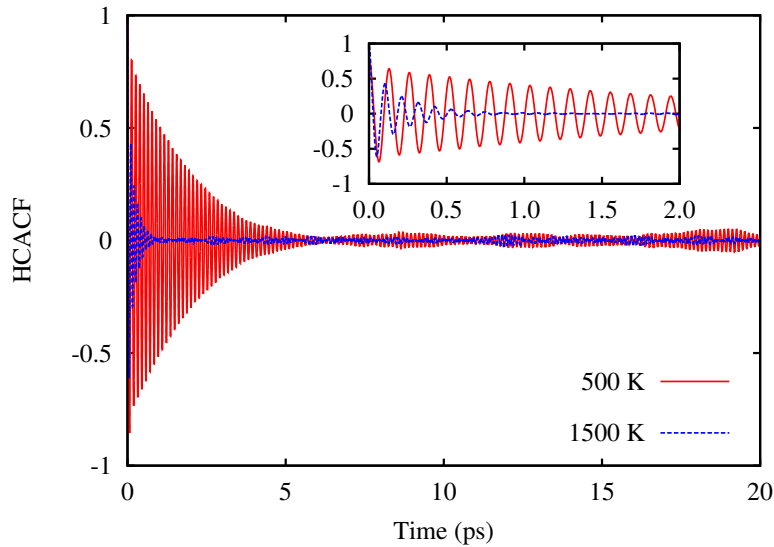


Figure B.4: Normalized heat current auto correlation function (HCACF) for C_{xx} as a function of time for ThO_2 at 500 K and 1500 K.

The calculated thermal conductivities of ThO_2 and CeO_2 as a function of temperature (300-2000 K range) are shown in Figure B.6 and B.7, respectively. These calculated values decrease with an increase of temperature, which reflects lowering of thermal conductivity by the phonon-phonon scattering. On the other

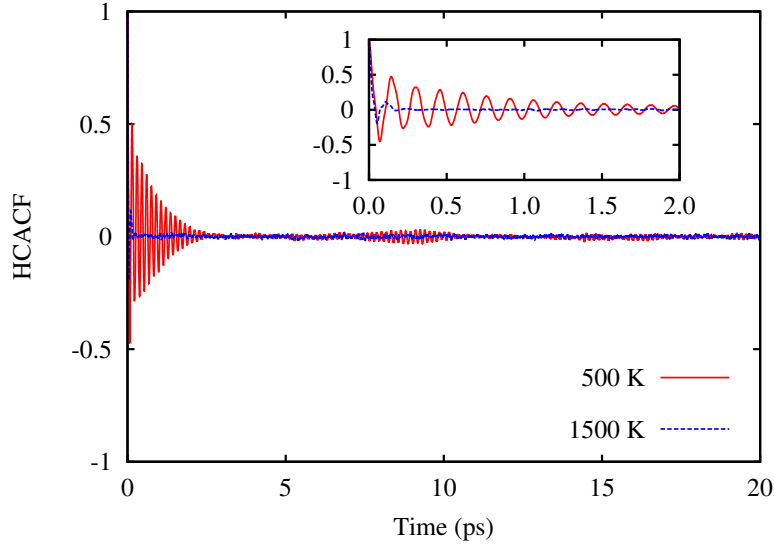


Figure B.5: Normalized heat current auto correction function (HCACF) for C_{xx} as a function of time for CeO_2 at 500 K and 1500 K.

hand, a number of experimental thermal conductivities measurements are available in the literature for ThO_2 [6, 122, 132, 142, 298] and these are also plotted in Figure B.6. In order to compare with the reported experimental data, a density (porosity) correction was applied to the MD calculated values as these were obtained for 100% TD. The porosity effect incorporated thermal conductivity (κ) is related to the 100% TD thermal conductivity (κ_0) by Maxwell-Eucken equation:

$$\kappa = \kappa_0 \frac{1 - p}{1 + \beta p} \quad (\text{B.2})$$

where $\beta = 0.5$ and p is the porosity ($p = 0.05$ for this study) [294]. As shown in Figure B.6, the calculated thermal conductivities are in good agreement with the experimental data within $\pm 1 \text{ W m}^{-1} \text{ K}^{-1}$ for temperatures greater than 750 K. While on the lower temperature side ($< 750 \text{ K}$), our calculated values are, in general, slightly overestimated compared to the experimental data. For CeO_2 , the calculated thermal conductivities (corrected for 95 % TD) are shown in Figure B.7 along with reported experimental values for CeO_2 and PuO_2 [142, 308–310]. Our MD calculated thermal conductivities for CeO_2 are generally underestimated (between 0.5 to 3 $\text{W m}^{-1} \text{ K}^{-1}$ over the temperature range) as compared to the experimental measurement of Cozzo *et al.* [142]. It is also important to note that the experimental measurements of thermal conductivities by Cozzo *et al.* [142] for PuO_2 in the 500-1750 K range is significantly larger compared to other experimental measurements [308–310].

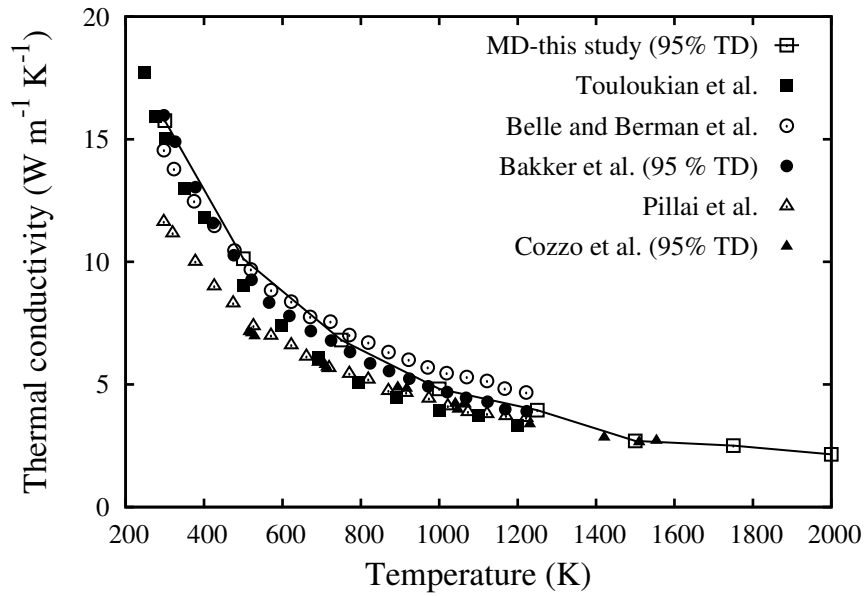


Figure B.6: Thermal conductivity calculated by MD simulations as a function of temperature for ThO_2 compared with experimental values. Solid line is only for visual guidance.

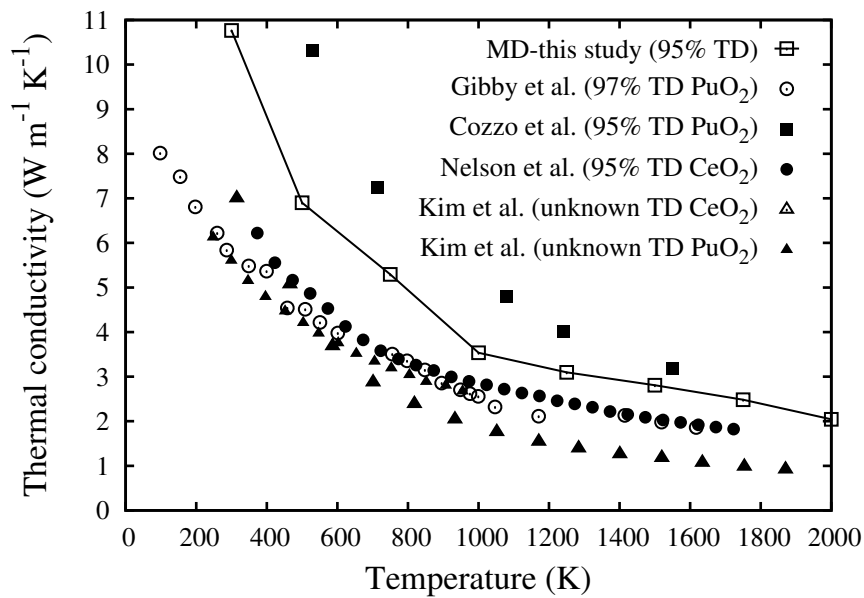


Figure B.7: Thermal conductivity calculated by MD simulations as a function of temperature for CeO_2 compared with experimental values. Solid line is only for visual guidance.

The thermal conductivities of ThO₂, CeO₂ and MOX solid solutions as calculated for 8×8×8 supercells are shown in Figures B.6 and B.7. To check for dependence of supercell size on the calculation of thermal conductivity, those of ThO₂ were calculated at 1250 K for different supercell sizes. The calculated thermal conductivity values are listed in Table B.4, which shows these values to converge for 8×8×8 supercell.

Table B.4: Supercell size dependence of thermal conductivity of ThO₂ at 1250 K.

Supercell size (unit cells)	Thermal conductivity (W m ⁻¹ K ⁻¹)
5×5×5	3.87
6×6×6	4.65
7×7×7	3.95
8×8×8	3.97

In Figure B.8, the MD calculated thermal conductivity of pure ThO₂, Th_{1-x}Ce_xO₂ (x = 0.0625 and 0.125) are plotted as a function of temperature (300-2000 K range) along with experimental results for pure ThO₂, 3wt% and 8wt% PuO₂ doped ThO₂ [142]. Our experimentally measured thermal conductivity values for ThO₂-5wt% CeO₂ (Th_{0.9253}Ce_{0.0747}O₂) pellets in the 873-1613 K temperature range for POP and CAP pellets sintered under different conditions (Ar+7%H₂ and Air) are also presented in Figure B.8 for comparison. At low temperatures, the thermal conductivity of the ThO₂-MOX decreases with an increase of the CeO₂ content in the range between 0-12.5 at.% CeO₂. As shown in Figure B.8, the thermal conductivity decreases with the increase of CeO₂ concentration and this decrease in thermal conductivity is larger at 500 K than that at 1500 K. This is attributed to the scattering of the phonons occurring due to mass and size difference between substituted and host atoms. Experimental observations on conductivity studies show that the pellets fabricated by CAP process exhibited lower thermal conductivity compared to pellets fabricated by conventional route (POP) in general. At higher temperatures (above 900 K), the thermal conductivity of ThO₂-MOX is almost independent of the concentration of CeO₂.

For ceramic oxide systems, the behavior of thermal conductivity with temperature is governed by two factors: (i) the phonon-phonon interactions and (ii) the density of defects (phonon scattering centers) in the lattice. For temperatures below 1900 K, the contribution of the free electrons on the thermal conductivity can be neglected for electronically insulator materials [6, 295]. In view of this, the MD calculated thermal conductivity data was fitted to the standard relation with

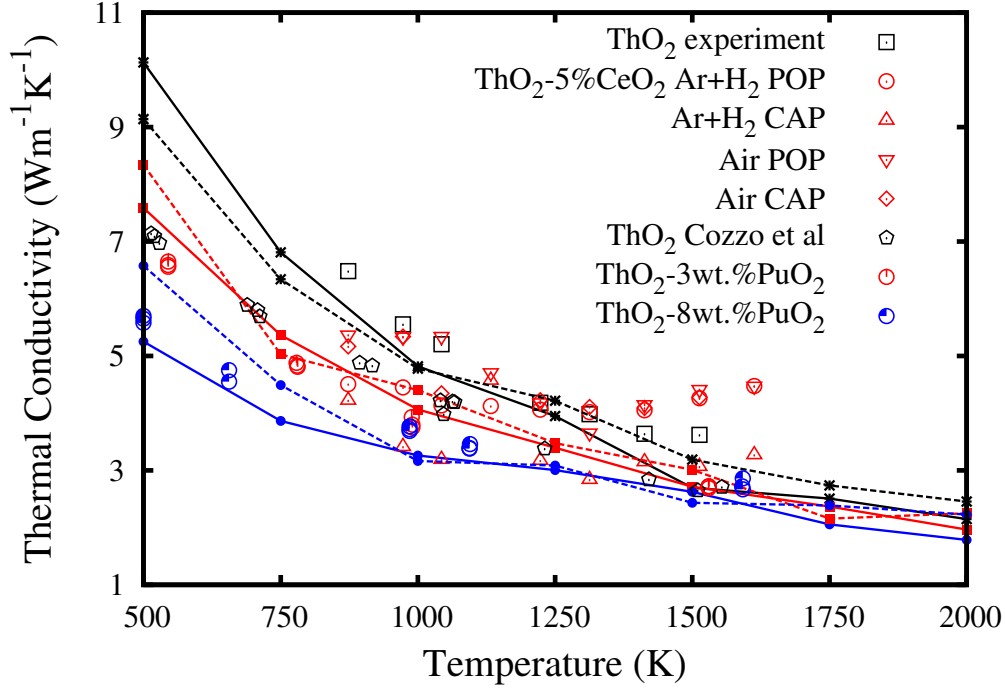


Figure B.8: Thermal conductivity calculated by MD simulations as a function of temperature for ThO_2 , $\text{Th}_{0.9275}\text{Ce}_{0.0625}\text{O}_2$ and $\text{Th}_{0.875}\text{Ce}_{0.125}\text{O}_2$ compared with our experimental values of ThO_2 and ThO_2 -5wt% CeO_2 for POP as well as CAP pellets sintered in $\text{Ar}+\text{H}_2$ and Air atmosphere (95 % TD). These values are also compared with reported values of ThO_2 , ThO_2 -3wt% and ThO_2 -8wt% PuO_2 by Cozzo *et al.* [142]. Lines are only for visual guidance. Black, red and blue lines show MD calculated values of ThO_2 , $\text{Th}_{0.9275}\text{Ce}_{0.0625}\text{O}_2$ and $\text{Th}_{0.875}\text{Ce}_{0.125}\text{O}_2$ MOX. Solid and dotted lines show MD calculated values using Buckingham and BMM potential.

phonon conduction, as given below,

$$\kappa = \frac{1}{A + BT} \quad (\text{B.3})$$

where, ‘A’ represent scattering due to the presence of impurities, representing defect thermal resistivity and is independent of temperature and ‘B’ represents scattering due to phonons and is a function of temperature. The influence of substituted impurities on the thermal conductivity is attributed to an increase of the parameter ‘A’. This results from interaction of phonon with lattice imperfections, impurities, isotopic, or other mass differences as well as bulk defects such as grain boundaries in the sample. Parameter ‘B’ remains constant theoretically and the second term, namely ‘B.T’, represents the intrinsic lattice thermal resistivity caused by phonon-phonon scattering. As the temperature increases, this term becomes predominant.

One pair of A and B constants can be obtained for each composition of solid solution by polynomial fitting of the thermal resistivity versus temperature data. Table B.5 shows the determined values of A and B constants from our MD calculated and experimentally measured thermal conductivity variation as a function of temperature along with those values as determined by Cozzo *et al.* [142]. Figure B.8 shows thermal conductivity values of ThO₂ and ThO₂-5%CeO₂ for CAP and POP pellets sintered at different atmospheres along with the polynomial fitted curve used to determine the values of constants A and B. It is evident from Table B.5 that our MD calculated B constants are almost independent of composition of solid solutions which is in accordance with experimental measurements of Cozzo *et al.* [142]. On the other hand, the values of constant A continuously increase with CeO₂ concentration in agreement with the experimental trend. This is attributed to the scattering of the phonons occurring due to mass and size difference between substituted and host atoms.

Table B.5: Constants A and B of the equations $\kappa = \frac{1}{A+BT}$ for ThO₂ and (Th,Ce)O₂ MOX calculated from MD simulations and experimental measurements.

System	A (m K/W)	B (m/W) $\times 10^{-4}$
MD this study, Buck model		
ThO ₂	0.00254	2.44
Th _{0.9375} Ce _{0.0625} O ₂	0.00825	2.41
Th _{0.875} Ce _{0.125} O ₂	0.06460	2.29
MD this study, BMM model		
ThO ₂	0.00315	1.88
Th _{0.9375} Ce _{0.0625} O ₂	0.00794	2.05
Th _{0.875} Ce _{0.125} O ₂	0.05363	1.97
ThO ₂ , Expt. This study	0.02000	1.34
ThO ₂ -5wt.% CeO ₂ (POP) Ar-H ₂ , Expt. this study	0.20519	0.08
ThO ₂ -5wt.% CeO ₂ (CAP) Ar-H ₂ , Expt. this study	0.22145	1.00
ThO ₂ -5wt.% CeO ₂ (POP) Air, Expt. this study	0.08605	0.90
ThO ₂ -5wt.% CeO ₂ (CAP) Air, Expt. this study	0.07449	0.90
ThO ₂ , Cozzo <i>et al.</i> [142]	0.010	2.30
ThO ₂ -3wt.%PuO ₂ , Cozzo <i>et al.</i> [142]	0.035	2.20
ThO ₂ -3wt.%PuO ₂ , Cozzo <i>et al.</i> [142]	0.099	1.69

Appendix C

Experimental Techniques

C.1 Preparation of ThO_2 -X wt% CeO_2 (X = 0, 5 and 8) solid solutions

ThO_2 and CeO_2 powders were used for fabrication of $(\text{Th,Ce})\text{O}_2$ pellets. The individual powders were characterized for their physical properties and chemical purity. The O/M ratio of both the powders was 2.00 and the total chemical impurities analyzed in ThO_2 and CeO_2 powders were found to be <1700 ppm and <500 ppm, respectively. The $(\text{Th,Ce})\text{O}_2$ green pellets for the study were prepared by the following routes:

1. Conventional powder metallurgy of powder processing and pelletization (POP) technique, and
2. Coated agglomerate pelletization (CAP) technique.

POP technique consisted of weighing of powders and mixing in requisite proportion, milling of powders along with admixed lubricant-cum-binder (Oleic acid and polyethylene glycol) in high energy ball mill, pre-compaction of mixed powders at 120-150 MPa, granulation in an oscillatory granulator, sieving and final compaction at 300-360 MPa. The CAP technique involved milling of ThO_2 powder, emulsion addition to the powder, extrusion through an extruder and spheroidization, drying of spheroids in an oven at 70°C , coating with second phase powder and final compaction at 300-360 MPa. The green pellets of ThO_2 , ThO_2 -3 wt% CeO_2 , ThO_2 -5wt% CeO_2 and ThO_2 -8wt% CeO_2 were fabricated by both the POP and CAP processes for further experimental studies. The density of the green pellets was in the range of $64 \pm 2\%$ of theoretical density (TD). For comparison, the pellets

of the experimental batches were sintered together under two different conditions, viz., i) at 1650°C in Ar-8%H₂ (reducing atmosphere) and ii) in air (oxidizing atmosphere) for 4 hours in a batch type resistance heating furnace. Intermediate temperature soak of 2 hours at 400°C was provided during sintering operation to ensure complete removal of binder-cum-lubricants (liquid) added. No additional procedures, techniques or parametric changes were carried out during experimental fabrication to influence degree of homogeneity of CeO₂ in ThO₂ powders and other properties of pellets.

Pellets were, further, characterized for properties which might influence the thermal properties of the pellets. Density measurement of pellets was carried out using Archimedes principle. Pore distribution was observed by optical microscopy on metallographically prepared samples. Oxygen to metal (O/M) ratio in the thorium-actinide solid solutions was determined by thermogravimetry (TG) method. Thermogravimetric studies for the sintered pellets were carried out in Mettler Thermo Analyser (Model: TGA-SDTA LT/1600 MT5) equipment. The powder of a pellet ~2g was loaded in TG and heated at 1273 K and held isothermally for 3 hrs in a flowing Ar-8%H₂ gas (flow rate: 50 cm³/min) with a heating rate of 10 K/min over saturated moisture (H₂O) content with defined oxygen potential (-100 kcal/mol) which ensured perfect oxygen stoichiometry to 2.0. Thus, the change in weights (gain/loss) before and after the experiment measured by TG corresponded to the extent of hypo-/hyper-stoichiometry from which the O/M ratio was calculated and buoyancy correction was applied to correct the weight changes.

C.2 Preparation of ThO₂ -X wt% UO₂ (X = 0, 6, 13, 25 and 30) solid solutions

The (Th,U)O₂ green pellets for the study were prepared by conventional powder metallurgy of powder processing and pelletization (POP) technique using ThO₂ and UO₂ powders as starting material. The characteristics of the starting ThO₂ and UO₂ powders used in this study are given in Table C.1. Fabrication of pellets by POP route involves weighing of powders for required composition, mixing and milling of powders along with admixed lubricant-cum-binder (Oleic acid and polyethylene glycol), pre-compaction, granulation, sieving and final compaction of (Th,U)O₂ mixed oxide granules at 300-360 MPa.

The green pellets of ThO₂, ThO₂-MOX were fabricated by the POP techniques and were further processed for further experimental studies. The density

of the green pellets was in the range of $60\pm 2\%$ of theoretical density (TD). For maintaining similar experimental conditions, all the experimental pellets were sintered together at 1923 K in Ar-8% H_2 reducing atmosphere for 4 hours at a rate of 2 K/min.. For removal of binder-cum-lubricants (liquid), intermediate temperature soak of 2 hours at 400°C was provided during sintering operation. No additional procedures, techniques or parametric changes were carried out during experimental fabrication to influence degree of homogeneity of UO_2 in ThO_2 powders and other properties of pellets.

Table C.1: Characteristics of starting ThO_2 and UO_2 powders.

Characteristics	ThO_2	UO_2
Apparent density (g/cc) (by Hall flow meter)	0.70	1.30
Specific Surface area (m^2/g) (by BET method)	1.53	3.00
Theoretical density (g/cc)	10.00	10.96
Oxygen to metal ratio (O/M) (by thermogravimetry)	2.00	2.18
Total impurities (ppm) (by ICP-AES analysis)	<1200	<700

C.3 ICP-AES

Chemical analysis of impurity contents of $(Th,U)O_2$ sintered pellets was carried out by Inductively Coupled Plasma-Atomic Emission Spectroscopy (ICP-AES).

C.3.1 Sample preparation for ICP analysis

The reagents used *e.g.*, TBP, tri-n-octyl phosphine oxide (TOPO), CCl_4 and HF were of analytical reagent grade and HNO_3 was of suprapure grade. All glassware used were made of quartz. Two ThO_2 trace element standards namely ThO_2 and ThO_2 -13% UO_2 were analyzed for their trace element contents by ICP-AES after separating thorium AND Uranium by TBP extractions. For separation of thorium and uranium, weighed quantities of ThO_2 and ThO_2 -13% UO_2 were taken in 100 mL capacity high purity platinum dish. Approximately 10 mL of suprapure conc. HNO_3 was added to the sample taken in the dish and the resultant mixture was boiled gently on a hot plate. In the boiling mixture 1.5 mL of 0.5 solution of HF was added to get clear solution. This solution was evaporated to almost dryness. The residue obtained was dissolved in 1 mL of conc. suprapure HNO_3 and evaporated to dryness. This process of dissolution and evaporation was repeated further for four times so that HF is completely removed after which, the residue was dissolved in

10 mL of 4 M HNO_3 . All these dissolution and evaporation operations were carried using a hood connected to suction so that corrosive vapors are safely collected in an aqueous medium and not left in the atmosphere. The volumes of the solutions obtained after the dissolution of ThO_2 and $\text{ThO}_2\text{-13\%UO}_2$ were made up to 15 mL with 4 M HNO_3 . These solutions were extracted four times with equal volume of 40% solution of TBP in CCl_4 and later two times with 0.2 M TOPO in CCl_4 to assure that most of the Th and U ions were extracted from the solution leaving behind only the impurities in the aqueous phase. The aqueous portion was carefully separated and made up to 25 mL with milli Q water and was analyzed by ICP-AES and the results were given in **section 8.4.1**.

C.3.2 Instrument and operating conditions

The analysis was carried out using Atomic Emission Spectrometer (AES), ARCOS, procured from Germany, with inductively coupled argon plasma as excitation source and capacitive coupled device (CCD) as a detector system. Instrumental specifications and optimized operating conditions are given elsewhere [311].

C.4 Thermogravimetry

Oxygen to metal (O/M) ratio in the (Th,U) O_2 solid solutions was determined by thermogravimetry (TG) method. Thermo-gravimetric studies for the sintered pellets were carried out in Mettler Thermo Analyser (Model: TGA-SDTA LT/1600 MT5) equipment. The powder of a pellet $\sim 2\text{g}$ was loaded in TG and heated at 1273 K and held isothermally for 3 hours in a flowing Ar-8% H_2 gas (flow rate: 50 cm^3/m) with a heating rate of 10 K/min over saturated moisture (H_2O) content with defined oxygen potential (-100 kcal/mol) which ensured perfect oxygen stoichiometry to 2.0. Thus, the change in weights (gain/loss) before and after the experiment measured by TG corresponded to the extent of hypo/hyper-stoichiometry from which the O/M ratio was calculated and buoyancy correction was applied to correct the weight changes.

C.5 High Temperature XRD

Thermal expansion measurements were performed using High Temperature X-ray Diffraction (HT-XRD) and Dilatometry. The HT-XRD studies were carried out

using STOE Diffractometer (theta-theta geometry), fitted with HDK-2.4 high temperature attachment having Platinum-Rhodium (Pt-Rh) sample carrier under high vacuum. The well ground powder samples were mounted on the Pt-Rh sample carrier, spot welded at the bottom with a Pt/Pt-13% Rh thermocouple for temperature measurement. The temperature of the sample was controlled by a PID type temperature controller within ± 1 K. Silicon and Platinum-Rhodium stages were used as standards to calibrate the instrument. The HT-XRD patterns were recorded at different temperatures, from ambient to 1273 K in the 2θ range of 20-60° using monochromatised Cu $K_{\alpha 1}$ radiation (0.15406 nm). The samples were heated at the rate of 15 K min⁻¹ and measurements were made at 100 K intervals. The measurements were carried out in vacuum (1x10⁻⁵ mbar). At each temperature, the sample was soaked for 15 min to stabilize the temperature.

C.6 Dilatometry

Bulk thermal expansion studies were also carried out using a Setaram vertical Dilatometer. The thermal expansion measurements of ThO₂ and ThO₂-6wt.%UO₂ MOX sintered pellets fabricated by both POP and CAP routes were carried out at a heating rate of 2 K/min from room temperature to 1773 K in high purity Ar atmosphere. The accuracy of the measurement of change in length was within ± 0.1 μ m. Dilatometer was calibrated with respect to both expansion values as well as temperature. The expansion data measured were corrected using expansion data from standard run. The coefficient of thermal expansion (CTE) was calculated by a software package attached to the dilatometer. The CTE between two temperatures T_1 and T_2 was calculated using the relation:

$$CTE_{(T_1-T_2)} = \frac{L_2 - L_1}{L_0(T_2 - T_1)} \quad (C.1)$$

where L_0 is the initial length of the specimen at room temperature, L_1 and L_2 are the lengths at temperatures T_1 and T_2 respectively.

C.7 Thermal Conductivity Measurements

Thermal diffusivity measurements of ThO₂ and ThO₂-6%UO₂ sintered pellets fabricated by both POP and CAP routes were done by laser flash method (Ulvac, Sinku-Riko, Japan). For the thermal diffusivity measurements, the sintered pellet

was sliced into discs of about 2 mm thickness. Graphite coating was given on the surfaces of the specimen. A pulse of laser was projected on to the surface of the pellet and the temperature rise on the opposite surface of the pellet was recorded as a transient signal by using an infrared detector. The thermal diffusivity (α) was calculated from the following relationship:

$$\alpha = WL^2/\pi t_{1/2} \quad (\text{C.2})$$

where $t_{1/2}$ is the time required in seconds to reach half of the maximum temperature rise at the rear surface of the sample and L is the sample thickness in millimeter and W is a dimensionless parameter which is a function of the relative heat loss from the sample during the measurement.

Thermal diffusivity studies were carried out in the temperature range between 873 K to 1613 K on the reference ThO₂ pellet and ThO₂-6wt.%UO₂ pellets (POP and CAP). Thermal conductivity was determined from the experimental values of thermal diffusivity, specific heat and density of the sample using the following relation:

$$\kappa_m = \alpha C_p \rho \quad (\text{C.3})$$

where κ_m is measured thermal conductivity in W/mK, α is the thermal diffusivity in m²/s, C_p is the specific heat in J/(Kg K) and ρ is the density of the sample in Kg/m³. Thermal conductivity values were calculated for (Th,U)O₂ samples and were normalized to 95% theoretical density using Eucken and Maxwell correction factor [294] for porosity and values of β , including its temperature dependence, reported by Notley and McEwan [312]. For the calculation of the thermal conductivity, the heat capacity values of pure oxides were taken from Barin *et al.* [313], and heat capacity of the MOX were calculated from these values using the Neumann Kopp's rule:

$$C_p(\text{Th}_{1-x}\text{U}_x\text{O}_2) = (1-x).C_p(\text{ThO}_2) + x.C_p(\text{UO}_2) \quad (\text{C.4})$$

Bibliography

- [1] E. Gerstner, *Nature* **460** (2009) 25-28.
- [2] S. Banerjee and T.R. GovindanKutty, *Functional Materials. Nuclear Fuels* **10** (2012) 387-466.
- [3] IAEA-TECDOC-1450: “*Thorium fuel cycle- Potential benefits and challenges*”, International Atomic Energy Agency, Vienna, May 2005.
- [4] IAEA-TECDOC-1496: “*Thermophysical properties database of materials for light water reactors and heavy water reactors*”, International Atomic Energy Agency, Australia, June 2006.
- [5] R.K. Sinha, A. Kakodkar, *Nucl. Eng. Des.* **236** (2006) 683-700.
- [6] K. Bakker, E.H.P. Cordfunke, R.J.M. Konings, R.P.C. Schram, *J. Nucl. Mater.* **250** (1997) 1-12.
- [7] S. Glasstone, A. Sesonske in “*Nuclear Reactor Engineering*”, Vol. 1 and 2, Van Nostrand Reinhold Company, United States (1994).
- [8] E.M. Schulson, *J. Nucl. Mater.* **83** (1979) 239.
- [9] E.M. Schulson, M.L. Swanson and S.R. MacEwen, *Phil. Mag. A* **37** (1978) 575.
- [10] E.M. Schulson, “*Zr₃Al: A Potential Nuclear Reactor Structural Materials*”, Intermetallic Compounds, Vol. 2, Editors J.H. Westbrook and R.L. Fleischer, John Eiley and Sons Ltd., 133 (1994).
- [11] E.M.Schulson and J.A. Roy, *J. Nucl. Mater.* **71** (1977) 124.
- [12] A.D. Schwoppe and W. Chuble, *J. of Metals* **4** (1942) 1138.
- [13] H.E. Rosinger and B.J.S. Wilkins, *J. Nucl. Mater.* **89** (1980) 347-353.

- [14] P. Mukhopadhyay, V. Raman, S. Banerjee, R. Krishnan, *J. Nucl. Mater.* **82** (1979) 227.
- [15] D. Faulkner, H.E. Rosiner, R.C. Styles, *J. Nucl. Mater.* **90** (1980) 256.
- [16] R. Tewari, G.K. Dey, R.K. Fotedar, T.R.G. Kutty, N. Prabhu, *Metall. Mater. Trans. A* **35** (2004) 189.
- [17] S. Banerjee, P. Mukhopadhyay, “*Phase transformations: examples from titanium and zirconium alloys*”, Pergamon Materials Series, Elsevier, Amsterdam (2007).
- [18] S.K. Sikka, Y.K. Vohra, R. Chidambaram, *Prog. Mater. Sci.* **27** (1982) 245.
- [19] P.D. Frost, W.M. Parris, L.L. Hirsch, J.R. Doig, and C.M. Schwartz, *Trans. Am. Soc. Met.* **46** (1954) 231.
- [20] I. Bakonyi, H. Ebert, and A. I. Liechtenstein, *Phys. Rev. B* **48** (1993) 7841.
- [21] G.B. Grad, P. Blaha, J. Luitz and K. Schwarz, *Phys. Rev. B* **62** (2000) 12743.
- [22] S. Banerjee, R. Tewari, P. Mukhopadhyay, *Prog. Mater. Sci.* **42** (1997) 109.
- [23] S. Banerjee, R.W. Cahn, *Acta Metall.* **31** (1983) 1721.
- [24] R. Tewari, P. Mukhopadhyay, S. Banerjee and L. A. Bendersky, *Acta Metall.* **47** (1999) 1307.
- [25] C.N.R. Rao and K.J. Rao, “*Phase Transitions in Solids: An approach to the study of the chemistry and physics of solids*”, McGraw-Hill International Book Company (1978).
- [26] S.G. Song and G.T. Gray, *Phil. Mag. A* **71** (1995) 275.
- [27] E. Cerreta, G.T. Gray III, R.S. Hixson, P.A. Rigg and D.W. Brown, *Acta Mater.* **53** (2005) 1751.
- [28] D.A. Keen, *J. Phys.: Condens. Matter.* **14** (2002) R819-R857.
- [29] S. Hull, *Rep. Prog. Phys.* **67** (2004) 1233-1314.
- [30] J.B. Boyce and B.A. Huberman, *Phys. Rep.* **51** (1979) 189.
- [31] K. Funke, *Prog. Solid State Chem.* **11** (1976) 345.
- [32] S. Chandra, “*Superionic Solids*”, North-Holland, Amsterdam (1981).

- [33] P. Haasen, “*Physical Metallurgy*”, third edition, translated by J. Mordike, Cambridge University Press, Cambridge, UK (1996).
- [34] A. Jayaraman, W. Klement Jr. and G.C. Kennedy, *Phys. Rev.* **131** (1963) 644.
- [35] J.C. Jamison, *Science* **140** (1963) 72.
- [36] J.C. Jamison, “*Metallurgy at High Pressures and Temperature*”, editors K.A. Gschneidner Jr., M.T. Hepworth and N.A.D. Parlee, p. 201, Gordon and Breach, New York (1964).
- [37] V.A. Zilbershtein, N.P. Chistotina, A.A. Zharov, N.S. Grishina and E.I. Estrin, *Fiz. Metal Metalloved* **39** (1975) 445.
- [38] A.R. Kustar and V.N. German, Proceedings of Pulsed Pressures, Moscow, No. 44(74), p. 166,(1979).
- [39] R.G. McQueen, S.P. Marsh, J.W. Taylor, J. N. Fritz and W.J. Carter, “*High Velocity Impact Phenomenon*”, Editor R. Kinslow, p. 293, Academic Press, New York and London (1970).
- [40] Y. Zhao, J. Zhang, C. Pantea, J. Qian, L.L. Daemen, P.A. Rigg, R.S. Hixson, G.T. Gray III, Y. Yang, L. Wang, Y. Wang and T. Uchida, *Phys. Rev. B* **71** (2005) 184119.
- [41] W. Liu, B. Li, L. Wang, J. Zhang and Y. Zhao, *J. App. Phys.* **104** (2008) 076102.
- [42] M.P. Usikov and V.A. Zilbershtein, *Phys. Stat. Solidi (a)* **19** (1973) 53.
- [43] A. Rabinkin, M. Talianker and O. Botstein, *Acta Metall.* **29** (1981) 691-698.
- [44] J.M. Silcock, *Acta Metall.* **6** (1958) 481.
- [45] A. R. Kutsar, I. V. Lyasotski, A. M Podurets and A. F Sanches-Bolinches, *High Pressure Research* **4** (1990) 475.
- [46] G. Jyoti , K.D. Joshi , Satish C. Gupta and S.K. Sikka, *Phil. Mag. Let.* **75** (1997) 291.
- [47] H. Olijnyk and A. P. Jephcoat, *Phys. Rev. B* **56** (1997) 10751.
- [48] H. Olijnyk and A. P. Jephcoat, *Solid State Commun.* **115** (2000) 335.

- [49] H. Xia, S. J. Duclos, A. L. Ruoff, and Y. K. Vohra, *Phys. Rev. Lett.* **64** (1990) 204.
- [50] S.A. Ostanin and V. Yu. Trubitsin, *Phys. Rev. B* **57** (1998) 13485.
- [51] Yan-Jun Hao, Lin Zhang, Xiang-Rong Chen, Ling-Cang Cai, Qiang Wu and Dario Alfe, *Phys. Rev. B* **78** (2008) 134101.
- [52] I. Schnell and R.C. Albers, *J. Phys.: Cond. Mat.* **18** (2006) 1483-1494.
- [53] Yan-Jun Hao, Lin Zhang, Xiang-Rong Chen, Ying-Hua Li and Hong-Liang He, *J. Phys.: Cond. Mat.* **20** (2008) 235230.
- [54] F. Jona and P.M. Marcus, *J. Phys.: Condens. Matter* **15** (2003) 5009.
- [55] Cui-E. Hu, Zhao-Yi Zeng, Lin Zhang, Xiang-Rong Chen, Ling-Cang Cai, *Comp. Mater. Science* **50** (2011) 835-840.
- [56] L. Delaey, J. Perkins and T. B. Massalski, *J. Mater. Sci.* **7** (1972) 1197.
- [57] C. L. Correy and K. M. Tetteff, *Scripta Metall.* **10** (1976) 909.
- [58] H. Kubo, A. Hamabe and K. Shimizu, *Scripta Metall.* **10** (1976) 547.
- [59] A. Fourdeux, H. Bruyas, D. Weber, M. Meurton, M. Roth and P. Lesbats, *Scripta Metall.* **14** (1980) 485.
- [60] O. Ortiz and D. E. Epperson, *Scripta Metall.* **13** (1979) 237.
- [61] W. Sha, A. Cerezo and G.D.W. Smith, *Metall. Trans. A* **24** (1993) 1241.
- [62] C. Servant, N. Bouzid and O. Lyon, *Phil. Mag. A* **56** (1987) 565.
- [63] C. Servant and N. Bouzid, *Acta Metall.* **36** (1988) 2771.
- [64] C.W. Dawson, S.L. Sass, *Metall Trans* **1** (1970) 2225.
- [65] S.L. Sass, *J. Less Common Metals* **28** (1972) 157.
- [66] B.S. Hickman, *J. Met Science* **4** (1969) 554.
- [67] A.L.J. Chang, S.L. Saaa, W. Krakow, *Acta Metall.* **24** (1976) 29.
- [68] A.J. Perkins, P.E. Yafee, R.F. Hehemann, *Metallography* **4** (1971) 303.
- [69] L.E. Rehn, P.R. Okamoto, J. Pearson, R. Bhadra, R. Grimsditch, *Phys. Rev. Lett.* **59** (1987) 2987.

- [70] L.A. Bendersky, W.J. Boettinger, B.P. Burton and F.S. Biancaniello, *Acta Metall. Mater.* **38** (1990) 931.
- [71] F.A. Sadi and C. Servant, *Phil. Mag. A* **80** (2000) 639.
- [72] F. A. Sadi and C. Servant, *Z. Metallkd.* **91** (2000) 504.
- [73] C.B. Shoemaker, D.P. Shoemaker and L.A. Bendersky, *Acta Crystallogr., Sect. C: Cryst. Struct. Commun.* **46** (1990) 374.
- [74] T.H. Yu and C.H. Koo, *Mater. Sci. Eng. A* **239-240** (1997) 694.
- [75] R. Strychor, J.C. Williams and W.A. Soffa, *Metall. Trans. A* **19** (1988) 225.
- [76] C.P. Chang and M.H. Loretto, *Phil. Mag. A* **63** (1991) 389.
- [77] R.G. Hansen and A. Raman, *Z. Metallkd.* **61** (1970) 115.
- [78] D. Nguyen-Manh, D.G. Pettifor, G. Show, A.P. Miodownik, A. Pesturel, *Phil. Mag. A* **74** (1996) 1385.
- [79] M. Sanati, R.C. Albers, F.J. Pinski, *J. Phys.: Condens. Matter.* **13** (2001) 5387.
- [80] M. Sanati, D. West, R.C. Albers, *Phys. Rev. B* **76** (2007) 174101.
- [81] M. Sanati, D. West and R.C. Albers, *J. Phys.: Cond. Mater.* **20** (2008) 465206.
- [82] S. Nag, A. Devaraj, R. Srinivasan, R.E.A. Williams, N. Gupta, G. B. Viswanathan, J. S. Tiley, S. Banerjee, S. G. Srinivasan, H. L. Fraser and R. Banerjee, *Phys. Rev. Lett.* **106** (2011) 245701.
- [83] H.Y. Xiao, Y. Zhang and W.J. Weber, *Phys. Rev. B* **86** (2012) 054109.
- [84] O.J. Staun, L. Gerward, V. Kanchana and G. Vaitheeswaran, *J. Alloy. Compd.* **381** (2004) 37-40.
- [85] R.C. Linares, *J. Phys. Chem. Solids* **28** (1967) 1285.
- [86] B.T.M. Willis, *Proc. R. Soc. Lond. A* **274** (1963) 134 (part II).
- [87] K. Clausen, W. Hayes, J. E. Macdonald and R. Osborn, *Phys. Rev. Lett.* **52** (1984) 1238.
- [88] M.T. Hutchings, *J. Chem. Soc., Faraday Trans. II* **83** (1987) 1083-1103.

- [89] M. H. Dickens, W. Hayes, M. T. Hutchings and C. Smith, *J. Phys. C: Solid State Phys.* **15** (1982) 4043.
- [90] D.F. Fischer, *J. Nucl. Mater.* **102** (1981) 220-222.
- [91] H. Nafe, *Solid State Ionics* **13** (1984) 255-263.
- [92] D.K. Hohnke, *Solid State Ionics* **5** (1981) 531-534.
- [93] C. Mo, Y. Yang, W. Kanga and P. Zhang, *Phys. Lett. A* **380** (2016) 1481-1486.
- [94] P. Martin, D. J. Cooke and R. Cywinski, *J. Appl. Phys.* **112** (2012) 073507.
- [95] N.R. Williams, M. Molinari, S.C. Parker and M.T. Storr, *J. Nucl. Mater.* **458** (2015) 45-55.
- [96] S. I. Potashnikov, A. S. Boyarchenkov, K. A. Nekrasov and A. Ya. Kupryazhkin, *J. Nucl. Mater.* **433** (2013) 215-226.
- [97] Neelima Prasad, Anek Kumar, Umasankari Kannan, Arvind Kumar, P.D. Krishnani and R.K.Sinha, IAEA-CN-184/207, N. Prasad, A. Kumar, P.D. Krishnani and R.K.Sinha - 2010 - inis.iaea.org.
- [98] R. Benz, *J. Nucl. Mater.* **29** (1969) 43-49.
- [99] M.H. Rand, “*Thorium: physico-chemical properties of its compounds and alloys*”, *Atom Energy Rev.* **5** (1975) 35.
- [100] W.A. Lambertson, M.H. Mueller, F.H. Gunzel, *J. Am. Ceram. Soc.* **36** (1953) 397-399.
- [101] C. Ronchi, J.P. Hiernaut, *J. Alloys Compd.* **240** (1996) 179-185.
- [102] R. Böhler, A. Quaini, L. Capriotti, P. Cakir, O. Benes, K. Boboridis, A. Guiot, L. Luzzi, R. Konings, D. Manara, *J. Alloys Compd.* **616** (2014) 5-13.
- [103] W.L. Lyon, W.E. Baily, *J. Nucl. Mater.* **22** (1967) 332-339
- [104] R.E. Latta, R.E. Fryxell, *J. Nucl. Mater.* **35** (1970) 195-210.
- [105] C. Ronchi, J.P. Hiernaut, R. Selfslag, G.J. Hyland, *Nucl. Sci. Eng.* **113** (1993) 1-19.
- [106] M.G. Adamson, E.A. Aitken, R.W. Caputi, *J. Nucl. Mater.* **130** (1985) 349-365.

- [107] D.T. Hagrman, “*MATPRO-A library of materials properties for Light Water Reactor accident Analysis*”, SCDAP/RELAP5/MOD 3.1/Code manual, Vol. 4, MATPRO, USNRC Report NUREG/CR-6150 (EGGG-2720) (1995).
- [108] J. Komatsu, T. Tachibana, K. Konashi, *J. Nucl. Mater.* **154** (1988) 38-44.
- [109] S.G. Popov, J.J. Carbajo, V.K. Ivanov, G.L. Yoder, “*Thermophysical properties of MOX and UO₂ fuels including its effects of irradiation*”, ORNL/TM-2000/351, Oak Ridge National Laboratory, Oak Ridge.
- [110] R. Böhler, M. Welland, D. Prieur, P. Caker, T. Vitova, T. Pruessmann, I. Pidchenko, C. Hennig, C. Gueneau, D. Manara, *J. Nucl. Mater.* **448** (1-3) (2014) 330-339.
- [111] M. Kato, K. Morimoto, H. Sugata, K. Konashi, M. Kashimura, T. Abe, *J. Nucl. Mater.* **373** (2008) 237-245.
- [112] F. De Bruycker, K. Boboridis, P. Pöml, R. Eloirdi, R.J.M. Konings, D. Manara, *J. Nucl. Mater.* **416** (2011) 166-172.
- [113] M. Hoch and H. L. Johnston, *J. Phys. Chem.* **65** (1961) 1184.
- [114] R. Agarwal, R. Prasad, and V. Venugopal, *J. Nucl. Mater.* **322** (2003) 98.
- [115] S. Dash, S. C. Parida, Z. Singh, B. K. Sen, and V. Venugopal, *J. Nucl. Mater.* **393** (2009) 267.
- [116] J. K. Fink, M. G. Chasanov, and L. Leibowitz, Technical Report ANLCEN-RSD 77-1, Argonne National Laboratory (1977).
- [117] A.C. Momin and Karkhanvala, *High Temp. Sci.* **10** (1978) 45.
- [118] J.K. Fink, M.G. Chasanov, and L. Leibowitz, *J. Nucl. Mater.* **102** (1981) 17-25.
- [119] J.K. Fink, *J. Nucl. Mater.* **279** (2000) 1-18.
- [120] A. E. Ogard, “*Plutonium and Other Actinides*”, Metallurgical Society of the American Institute of Mining, New York, p. 78 (1970).
- [121] R.E. Latta, E.C. Duderstadt and R.E. Fryxell, *J. Nucl. Mater.* **35** (1970) 347-349.

- [122] J. Belle, R.M. Berman, “*Thorium dioxide: properties and nuclear applications*”, Naval Reactors Office, United State Department of Energy, Government Printing Office, Washington (1984).
- [123] R. Böhler, P. Cakr, O. Beneš, H. Hein, R.J.M. Konings, D. Manara, *J. Chem. Thermodynamics* **81** (2015) 245-252.
- [124] O.S. Valu, O. Bene, R.J.M. Konings, H. Hein, *J. Chem. Thermodynamics* **68** (2014) 122-127.
- [125] M.W.D. Cooper, S.T. Murphy, P.C.M. Fossati, M.J.D. Rushton, R.W. Grimes, *Proc. R. Soc. Lond. A* **470** (2014) 20140427.
- [126] T.R.G. Kutty, K.B. Khan, P.S. Somayajulu, A.K. Sengupta, J.P. Panakkal, Arun Kumar, H.S. Kamath, *J. Nucl. Mater.* **373** (2008) 309.
- [127] A.K. Tyagi, M.D. Mathews, B.R. Ambekar, R. Ramachandran, *Thermochimica Acta* **421** (2004) 69.
- [128] A.K. Tyagi, M.D. Mathews, *J. Nucl. Mater.* **278** (2000) 123.
- [129] S. Anthonysamy, G. Panneerselvam, Santanu Bera, S.V. Narasimhan, P.R. Vasudeva Rao, *J. Nucl. Mater.* **281** (2000) 15.
- [130] A.C. Momin, *J. Nucl. Mater.* **185** (1991) 308.
- [131] P. Rodriguez, C.V. Sundaram, *J. Nucl. Mater.* **100** (1981) 227.
- [132] C.G.S. Pillai, P. Raj, *J. Nucl. Mater.* **277** (2000) 116.
- [133] R.J.M. Konings, P.J.A.M. Blankenvoorde, E.H.P. Cordfunke, K. Bakker, “*Evaluation of thorium based nuclear fuels: chemical aspects*”, ECN-R-95-007, Netherlands Energy Research Foundation, ECN (1995).
- [134] U. Basak, A.K. Sengupta, C. Ganguly, *J. Mater. Sci. Lett.* **8** (1989) 449.
- [135] T.R.G. Kutty, K.B. Khan, P.S. Somayajulu, A.K. Sengupta, J.P. Panakkal, Arun Kumar, H.S. Kamath, *J. Nucl. Mater.* **373** (2008) 299.
- [136] C. Ronchi, J.P. Ottaviani, C. Degueldre, R. Calabrese, *J. Nucl. Mater.* **320** (2003) 54.
- [137] D. Barrier, A.A. Bukaemskiy, G. Modolo, *J. Nucl. Mater.* **352** (2006) 357-364.

- [138] J.C. Marra, A.D. Cozzi, R.A. Pierce, J.M. Pareizs, A.R. Jurgensen, D.M. Missimer, *Ceram. Trans.* **132** (2002) 381.
- [139] S. Hubert, J. Purans, G. Heisbourg, P. Moisy and N. Dacheux, *Inorg. Chem.* **45** (2006) 3887-3894.
- [140] M.D. Mathews, B.R. Ambekar, A.K. Tyagi, *J. Nucl. Mater.* **288** (2001) 83-85.
- [141] M.D. Mathews, B.R. Ambekar, A.K. Tyagi, *J. Nucl. Mater.* **280** (2000) 246-249.
- [142] C. Cozzo, D. Staicu, J. Somers, A. Fernandez, R.J.M. Konings, *J. Nucl. Mater.* **416** (2011) 135-141.
- [143] H.Y. Xiao, Y. Zhang, W.J. Weber, *Acta Mater.* **61** (2013) 467-476.
- [144] K. Govers and M. Verwerft, *J. Nucl. Mater.* **438**(2013) 134-143.
- [145] K. Govers, S. Lemehov, M. Hou and M. Verwerft, *J. Nucl. Mater.* **366** (2007) 161-177.
- [146] K. Govers, S. Lemehov, M. Hou and M. Verwerft, *J. Nucl. Mater.* **376** (2008) 66-77.
- [147] R. Behera and C. Deo, *J. Phys.: Condens. Matter* **24** (2012) 215405.
- [148] M.W.D. Cooper, M.J.D. Rushton, R.W. Grimes, *J. Phys. Condens. Matter* **26** (2014) 105401.
- [149] R. M. Martin, *Electronic structure basic theory and practical methods*, Cambridge (2004).
- [150] L. D. Landau and E. M. Lifshitz, *Quantum Mechanics: Non-relativistic Theory*, Butterworth-Heinemann (1981).
- [151] P. Hohenberg and W. Kohn, *Phys. Rev.* **136** (1964) B864.
- [152] W. Kohn and L. J. Sham, *Phys. Rev.* **140** (1965) A1133.
- [153] E. Kaxiras, *Atomic and Electronic Structure of Solids*, Cambridge University Press, ISBN 9780521523394 (2003).
- [154] D.M. Ceperley and B.J. Alder, *Phys. Rev. Lett.* **45** (1980) 566.
- [155] J.P. Perdew and A. Zunger, *Phys. Rev. B* **23** (1981) 5048.

- [156] J.P. Perdew and Y. Wang, *Phys. Rev. B* **33** (1986) 8800.
- [157] J.P. Perdew, J.A. Chevary, S.H. Vosko, K.A. Jackson, M.R. Pederson, D.J. Singh and C. Fiolhais, *Phys. Rev. B* **46** (1992) 6671.
- [158] J.P. Perdew, K. Burke and M. Ernzerhof, *Phys. Rev. Lett.* **77** (1996) 3865.
- [159] A. Svane and O. Gunnarsson, *Phys. Rev. Lett.* **65** (1990) 114.
- [160] S. Massida, M. Posternak and A. Baldereschi, *Phys. Rev. B* **48** (1993) 5058.
- [161] L. Hedin, *Phys. Rev.* **139** (1965) A796.
- [162] V.I. Anisimov, F. Aryasetiawan and A.I. Lichtenstein, *J. Phys. Condens. Matter* **9** (1997) 767.
- [163] A.D. Becke, *J. Chem. Phys.* **98** (1993) 1372.
- [164] J. Perdew, M. Ernzerhof, K. Burke, *J. Chem. Phys.* **105** (1997) 9982.
- [165] J.P. Perdew, M. Ernzerhof and K. Burke, *J. Chem. Phys.* **105** (1996) 9982.
- [166] J. Heyd, G.E. Scuseria and M. Ernzerhof, *J. Chem. Phys.* **118** (2003) 8207.
- [167] J. Heyd, G. E. Scuseria and M. Ernzerhof, *J. Chem. Phys.* **124** (2006) 219906.
- [168] T. Leininger, H. Stoll, H.J. Werner and A. Savin, *Chem. Phys. Lett.* **275** (1997) 151.
- [169] A.V. Krukau, O.A. Vydrov, A.F. Izmaylov and G.E. Scuseria, *J. Chem. Phys.* **125** (2006) 224106.
- [170] O. K. Andersen, *Phys. Rev. B* **12** (1975) 3060.
- [171] J. C. Slater, *Phys. Rev.* **51** (1937) 846.
- [172] J. Korrynga, *Physica* **13** (1947) 393.
- [173] W. Kohn and N. Rostocker, *Phys. Rev.* **94** (1954) 111.
- [174] D. R. Hamann, M. Schlter and C. Chiang, *Phys. Rev. Lett.* **43** (1979) 1494.
- [175] D. Vanderbilt, *Phys. Rev. B* **41** (1990) R7892.
- [176] P.E. Blöchl, *Phys. Rev. B* **50** (1994) 17953.

- [177] G. Kresse and J. Furthmüller, *Comput. Mater. Sci.* **6** (1996) 15; *Phys. Rev. B* **54** (1996) 11169.
- [178] Charles Kittel, “*Introduction to solid state physics*”, Wiley (1995).
- [179] W. Heisenberg, “*The Physical Principles of Quantum Theory*”, University of Chicago Press (1930).
- [180] M. Born and K. Huang, “*Dynamical Theory of Crystal Lattices*”, Oxford University Press (1954).
- [181] S. Baroni, S. de Gironcoli, A. Dal Corso, and P. Giannozzi, *Rev. Mod. Phys.* **73** (2001) 515.
- [182] X. Gonze, and J.P. Vigneron, *Phys. Rev. B* **39** (1989) 13120.
- [183] N. W. Ashcroft and N. D. Mermin, “*Solid state physics*”, Thomson Learning Inc. (1976).
- [184] D. Alfe, *Comput. Phys. Commun.* **180** (2009) 2622.
- [185] S. A. Teukolsky, W. T. Vetterling and B. P. Flannery, “*Numerical Recipes*”, W. H. Press, Cambridge: University Press, Cambridge, p. 670 (1992).
- [186] I. Newton and J. Machin, “*The mathematical principles of natural philosophy*”, Benjamin Motte, London (1729).
- [187] W.C. Swope, *J. Chem. Phys.* **76** (1982) 637.
- [188] L. Verlet, *Phys. Rev.* **159** (1967) 98.
- [189] K. Govers, and M. Verwerft, *J. Nucl. Mater.* **438** (2013) 134.
- [190] M. Born and J. Mayer, *Z. Phys.* **75** (1932) 1.
- [191] M. Born and J. Mayer, *J. Chem. Phys.* **1** (1933) 270.
- [192] P.P. Ewald, *Ann. Phys.* **64** (1921) 253.
- [193] M. Born, “*Atomic Physics*”, Blackie and Son Ltd., 6th ed. (1956).
- [194] D.C. Rapaport, “*The Art of Molecular Dynamics Simulation*”, 2nd ed., Cambridge University Press, Cambridge (1995).
- [195] P.M. Morse, *Phys. Rev.* **34** (1929) 57.

- [196] R.A. Buckingham, *Proc. R. Soc. Lond. Ser. A* **168** (1938) 264.
- [197] H.C. Hamaker, *Physica* **4** (1937) 1058.
- [198] I.J. Fritz, *J. Appl. Phys.* **47** (1976) 4353.
- [199] M.S. Daw, S.M. Foiles and M.I. Baskes, *Mater. Sci. Reports* **9** (1993) 251.
- [200] M.S. Daw and M.I. Baskes, *Phys. Rev. B* **29** (1984) 6443.
- [201] D. J. Evans and G. Morriss, “*Statistical Mechanics of Nonequilibrium Liquids*”, 2nd ed., Cambridge University Press, Cambridge (2008).
- [202] T. Höhr, P. Pendzig, W. Dieterich and P. Maass, *Phys. Chem. Chem. Phys.* **4** (2002) 3168-3172.
- [203] H. J. C. Berendsen, J. P. M. Postma, W. F. van Gunsteren, A. DiNola and J. R. Haak, *J. Chem. Phys.* **81** (1984) 3684-3690.
- [204] S. Nose, *J. Chem. Phys.* **6** (1984) 511-519.
- [205] R. Kubo, *J. Phys. Soc. Jpn.* **12** (1957) 570-586.
- [206] D. A. Greenwood, *Proc. Phys. Soc.* **71** (1958) 585-596.
- [207] G.B. Olson, M. Cohen, *Metall. Trans. A* **7** (1976) 1897.
- [208] H.J. Monkhorst and J.D. Pack, *Phys. Rev. B* **13** (1979) 5188.
- [209] M. Methfessel and A.T. Paxton, *Phys. Rev. B* **40** (1989) 3616.
- [210] J.F. Nye, “*Physical Properties of Crystals*”, Oxford University Press, Oxford (1957).
- [211] W.G. Burgers, *Physica (Utrecht)* **1** (1934) 561.
- [212] H. T. Stokes, D. M. Hatch and B.J. Campbell (2007) ISOTROPY software package, <http://stokes.byu.edu/isotropy.html>.
- [213] H. T. Stokes and D. M. Hatch, *Phys. Rev. B* **65** (2002) 144114.
- [214] S.L. Qie, F. Apostol and P.M. Marcas, *J. Phys.: Cond. Mat.* **17** (2005) 2121.
- [215] E.A. Brandes, “*Smithells Metals Reference Book*”, Butterworth, London (1983).
- [216] R. Roberge, *J. Less-Common Met.* **40** (1975) 161.

- [217] P.M. Sutton, *Phys. Rev.* **91** (1953) 816.
- [218] G.N. Kemm, G.A. Alers, *J. Appl. Phys.* **35** (1964) 327.
- [219] J. Vallin, J.M. Mongy, K. Salama, O. Beckman, *J. Appl. Phys.* **35** (1964) 1825.
- [220] L. Goldak, L.T. Loyed, C.S. Barrett, *Phys. Rev.* **144** (1966) 468.
- [221] E.S. Fisher, C.J. Renken, *Phys. Rev.* **135** (1964) A482.
- [222] C.G. Wilson, D. Sams, *Acta Crystallogr.* **14** (1961) 71.
- [223] M. Potzschke, K. Schubert, *Z. Metalkde.* **53** (1962) 548.
- [224] M. Asta, G. Ghosh, *Acta Mater.* **53** (2005) 3225.
- [225] M. Alatalo, M. Weinert, R.E. Watson, *Phys. Rev. B* **5** (1998) R2009.
- [226] F.D. Murnaghan, *Proc. Natl. Acad. Sci. U.S.A.* **30** (1944) 2344.
- [227] M. Sanati, D. West and R. C. Albers, *J. Phys.: Cond Mater.* **20** (2008) 465206.
- [228] G. Shao and P. Tsakirooulos, *Mater. Sci. Eng. A* **914** (2002) 329.
- [229] G. Shao, A.P. Miodownik and P. Tsakirooulos, *Phil. Mag. A* **71** (1995) 1389.
- [230] K.J. Carroll, *J. Appl. Phys.* **36** (1965) 3689.
- [231] G. Ghosh, A. van de Walle, M. Asta and G.B. Olson, *Calphad* **26** (2002) 491.
- [232] M.J. Mehl, D.A. Papaconstantopoulos, *Phys. Rev. B* **41** (1990) 10311.
- [233] L. Fast, J.M. Wills, B. Johansson, O. Eriksson, *Phys. Rev. B* **51** (1995) 17431.
- [234] J. Zhao, J.M. Winey and Y.M. Gupta, *Phys. Rev. B* **75** (2007) 094105.
- [235] X.L. Yuan, D.Q. Wei, X.R. Chen, Q.M. Zhang and Z.Z. Gong, *J. Alloys. Comp.* **509** (2011) 769.
- [236] R. Hill, *Proc. Phys. Soc. London* **65** (1952) 349.
- [237] W. Voigt, *Ann. Phys. (Leipzig)* **38** (1889) 573.
- [238] A. Reuss, *Z. Angew. Math. Phys.* **9** (1929) 49.

- [239] S.F. Pugh, *Phil. Mag* **45** (1953) 823.
- [240] R.A. Johnson, *Phys Rev B* **37** (1988) 3924.
- [241] S. Kamran, K. Chen, L. Chen, *Phys. Rev. B* **79** (2009) 024106.
- [242] V.V. Bannikov, I.R. Shein, A.L. Ivanovskii, *Solid State Commun.* **149** (2009) 1807.
- [243] I.R. Shein, A.L. Ivanovskii, *Mater. Lett.* **63** (2009) 2413.
- [244] M.T. Hutchings, *J. Phys. C: Solid State* **17** (1984) 3903.
- [245] B. Voronin and S. Volkov, *J. Phys. Chem. Solids* **62** (2001) 1349.
- [246] C.R.A. Catlow, *Solid State Phys.* **9** (1980) 157.
- [247] A. Chadwick, *Solid State Ionics* **8** (1983) 209.
- [248] A.R. Allnatt, A.V. Chadwick and P.W.M. Jacobs, *Proc. R. Soc. A* **410** (1987) 385.
- [249] B. Voronin, *J. Phys. Chem. Solids* **56** (1995) 839.
- [250] C.R.C. Catlow, *Proc. R. Soc. Lond. A* **353** (1977) 533.
- [251] Xiao-Dong Wen, R.L. Martin, T.M. Henderson and G.E. Scuseria, *Chem. Rev.* **113** (2013) 1063-1096.
- [252] S.L. Dudarev, G.A. Botton, S.Y. Savrasov, C.J. Humphreys, A.P. Sutton, *Phys. Rev. B* **57** (1998) 1505.
- [253] M. Marsman, J. Paier, A. Stroppa, G. Kresse, *J. Phys. Condens Matter* **20** (2008) 064201.
- [254] A. Togo, F. Oba and I. Tanaka, *Phys. Rev. B* **78** (2008) 134106.
- [255] R.M. Pick, M.H. Cohen and R.M. Martin, *Phys. Rev. B* **1** (1970) 910.
- [256] P. Giannozzi, S. de Gironcoli, P. Pavone, and S. Baroni, *Phys. Rev. B* **43** (1991) 7231.
- [257] X. Gonze and C. Lee, *Phys. Rev. B* **55** (1997) 10355.
- [258] S. Plimpton, *J. Comput. Phys.* **117** (1995) 1-19.

- [259] M. Idiri, T. Le Bihan, S. Heathman, J. Rebizant, *Phys. Rev. B* **70** (2004) 014113.
- [260] P.M. Macedo, W. Capps and J.B. Watchman, *J. Am. Ceram. Soc.* **47** (1964) 651.
- [261] K. Clausen, W. Hayes, E.J. Macdonald, R. Osborn and G.P. Schnabel, *J. Chem. Soc., Faraday Trans. II* **83** (1987) 1109.
- [262] J.D. Axe and G.D. Pettit, *Phys. Rev.* **151** (1966) 676-680.
- [263] Y. Lu, Y. Yang and P. Zhang, *J. Phys.: Condens. Matter* **24** (2012) 225801.
- [264] C. Sevik and T. Cagin, *Phys. Rev. B* **80** (2009) 014108.
- [265] A. Jayaraman, G.A. Kourouklis and L.G. Van Uitert, *Pramana J. Phys.* **30** (1988) 225-231.
- [266] J.L. Gavartin, C.R.A. Catlow, A.L. Shluger, P.W.M. Jacobs, Z.A. Rycerz, *Radiat. Defects Solids* **134** (1995) 107.
- [267] A. Nakano, *Comp. Phys. Commun.* **176** (2008) 280.
- [268] G. Henkelman, H.A. Jonsson, *J. Chem. Phys.* **113** (2000) 9978.
- [269] G. Henkelman, B.P. Uberuaga, H. Jonsson, *J. Chem. Phys.* **113** (2000) 9901.
- [270] J.X.M. Zheng-Johannson and R.L. McGreevy, *Solid State Ionics* **83** (1996) 35.
- [271] K. Ihata and H. Okazaki, *J. Phys.: Condens. Matter* **9** (1997) 1477.
- [272] J. von Pezold, A. Dick, M. Friak, J. Neugebauer, *Phys. Rev. B* **81** (2010) 094203.
- [273] M.W.D. Cooper, S.T. Murphy, M.J.D. Rushton, R.W. Grimes, *J. Nucl. Mater.* **461** (2015) 206-214.
- [274] L.S.I. Liyanage, S.G. Kim, J. Houze, S. Kim, M.A. Tschopp, M.I. Baskes, M.F. Horstemeyer, *Phys. Rev. B* **89** (2014) 094102.
- [275] D. Manara, C. Ronchi, M. Sheindlin, M. Lewis, M. Brykin, *J. Nucl. Mater.* **342** (2005) 148-163.

- [276] M.J. Qin, M.W.D. Cooper, E.Y. Kuo, M.J.D. Rushton, R.W. Grimes, G.R. Lumpkin and S.C. Middleburgh, *J. Phys.: Condens. Matter* **26** (2014) 495401.
- [277] J.H. Harding, P. Masri, A.M. Stoneham, *J. Nucl. Mater.* **92** (1980) 73-78.
- [278] C. Ronchi, G.J. Hyland, *J. Alloys Compd.* **213/214** (1994) 159.
- [279] K. Gofryk, S. Du, C. Stanek, J. Lashley, X.Y. Liu, R. Schulze, J. Smith, D. Safarik, D. Byler, K. McClellan, B. Uberuaga, B. Scott, D. Andersson, *Nat. Commun.* **5** (2014) 4551.
- [280] R.J.M. Konings, O. Benes, *J. Phys. Chem. Solids* **74** (2013) 653-655.
- [281] M. Chollet, J. Lechelle, R.C. Belin, J.C. Richaud, *J. Appl. Cryst.* **47** (2014) 1008-1015.
- [282] C. Ronchi, M. Sheindlin, M. Musella, G. Hyland, *J. Appl. Phys.* **85** (1999) 776-789.
- [283] A.V. Lunev, B.A. Tarasov, *J. Nucl. Mater* **415** (2011) 217-221.
- [284] S.N. Luo, A. Strachan, D.C. Swift, *J. Chem. Phys.* **120** (2004) 11640.
- [285] W. Zhang, Y. Peng, Z. Liu, *AIP Adv.* **4** (2014) 057110.
- [286] H. Xiao, C. Long, X. Tian, H. Chen, *Mater. Des.* **96** (2016) 335-340.
- [287] D.F. Fischer, J.K. Fink, L. Leibowitz, *J. Nucl. Mater.* **118** (1983) 342-348.
- [288] H. Idriss, *Surf. Sci. Rep.* **65** (2010) 67-109.
- [289] T. Arima, S. Yamasaki, Y. Inagaki, K. Idemitsu, *J. Alloys Compd.* **400** (2005) 43.
- [290] K. Yamada, K. Kurosaki, M. Uno, S. Yamanaka, *J. Alloys Compd.* **307** (2000) 10.
- [291] S. Nichenko, D. Staicu, *J. Nucl. Mater.* **433** (2013) 297.
- [292] M.J. Wan, L. Zhang, J.G. Du, D.H. Huang, L.L. Wang, G. Jiang, *Phys. Rev. B* **407** (2013) 4595.
- [293] K. Kurosaki, K. Yamada, M. Uno, S. Yamanaka, K. Yamamoto, T. Namekawa, *J. Nucl. Mater.* **294** (2001) 160.

- [294] IAEA-TECDOC-59: “*Thermal Conductivity of Uranium Dioxide*”, International Atomic Energy Agency, Vienna, 1966.
- [295] P. Klemens, “*Thermal Conductivity and Lattice Vibrational Modes*”, vol. 7, Academic Press, New York (1959).
- [296] K. Hirata, K. Moria, Y. Waseda, *J. Mater. Science* **12** (1977) 838.
- [297] T. Yamashita, N. Nitani, T. Tsuji, H. Inagaki, *J. Nucl. Mater.* **245** (1997) 72-78
- [298] Y.S. Touloukian, “*Thermal Conductivity: Nonmetallic Solids*”, Vol 2, Ed. R.W. Powell, C.Y. Ho and P.G. Klemens, New York:IFI/Plenum (1970).
- [299] M.T. Perez-Prado and A.P. Zhilyaev, *Phys. Rev. Lett.* **102** (2009) 175504.
- [300] A.P. Zhilyaev, A.V. Sharafutdinov and M.T. Perez-Prado, *Adv. Eng. Mater.* **12** (2010) 754.
- [301] H. Zong, T. Lookman, X. Ding, C. Nisoli, D. Brown, S. R. Niezgodá and J. Sun, *Acta Mater.* **77** (2014) 191.
- [302] J.B. Conway, R.M. Fencil Jr., R.A. Hein, *Trans. Am. Nucl. Soc.* **6** (1963) 153.
- [303] T. Watanabe, S.B. Sinnott, J.S. Tulenko, R.W. Grimes, P.K. Schelling, S.R. Phillpot, *J. Nucl. Mater.* **375** (2008) 388-396.
- [304] P. Jund, R. Jullien, *Phys. Rev. B* **59** (1999) 13707.
- [305] J.A. Webb, I. Charit, *J. Nucl. Mater.* **427** (2012) 87.
- [306] E.T. Swartz, R.O. Pohl, *Rev. Mod. Phys.* **61** (1989) 605.
- [307] L. Gerward, J. Staun Olsen, L. Petit, G. Vaitheeswaran, V. Kanchana, A. Svane, *J. Alloys Comp.* **400** (2005) 56.
- [308] H.S. Kim, C.Y. Joung, B.H. Lee, J.Y. Oh, Y.H. Koo, P. Heimgartner, *J. Nucl. Mater.* **378** (2008) 98.
- [309] A.T. Nelson, D.R. Rittman, J.T. White, J.T. Dunwoody, M. Kato and K.J. McClellan, *J. Am. Ceram. Soc.* **97** (2014) 3652-3659.
- [310] R.L. Gibby, *J. Nucl. Mater.* **38** (1971) 163.

- [311] N. Pathak, V.C. Adya, S.K. Thulasidas, A. Sengupta, T.K. Seshagiri, and S.V. Godbole, *At. Spectrosc.* **35(1)** (2014) 17-24.
- [312] M.J.F. Notley, J.R. McEwan, *Nucl. Appl. Technol.* **2** (1966) 117.
- [313] Ihsan Barin, “*Thermochemical Data of Pure Substances*”, third ed., VCH publication (1995).